



**CZECH TECHNICAL
UNIVERSITY
IN PRAGUE**

F7

**Faculty of Biomedical Engineering
Department of Biomedical Technology**

Ph.D. Thesis

Noninvasive Localization of the Focus of Ectopic Ventricular Activation

MSc. Elena Deutsch

Kladno, October 2018

Supervisor: doc. Ing. Milan Tyšler, CSc.

Supervisor-Specialist: prof. Ing. Peter Kneppo, DrSc.

Ph.D. Programme: Biomedical and Clinical Technology

Branch of study: Biomedical and Clinical Technology

Acknowledgement / Declaration

I would like to thank doc. Milan Tyšler, Ing. CSc for the priceless discussions, advises and encouragement. Every consultation was very sophisticated, intense and made me look at things from a different angle.

My special thanks belong to prof. Peter Kneppo, Ing. DrSc the head of the Department of Biomedical Technology FBMI, for the opportunity of working at the Faculty, his advice, suggestions for designing the experiments. Without his guidance and organizational support, this research would not be possible.

My grateful thanks belong to colleagues doc. MD. Pavel Osmančík, PhD, Ing. Jana Žďárská from 3rd Faculty of Medicine, Charles University and Cardiocenter, University Hospital Kralovske Vinohrady for cooperation in the clinical measurements and kind permission to use the data in this study.

I value cooperation with prof. V. Maksymenko, MD. DrSc., doc. Ye. Bilynsky, MD. DrSc., MD. V. Zalevsky, MD. B. Kravchuk, PhD., and MSc. M. Sychyk, PhD., O. Stychynsky, DrSc., MD. B. Batsak from “National M. Amosov Institute of Cardiovascular Surgery AMSU”.

Notably, I would like to thank Ing. Jana Švehlíková, PhD from Institute of Measurement Science SAS (Bratislava, Slovakia) for her invaluable counseling and friendship.

I thank MSc. Ksenia Sedova, PhD, Ing. Richard Grünes, PhD, MSc. Svitlana Strunina, who helped to perform the measurements.

The financial support from Department of BMT 17110/122/1222100G000 and CTU SGS13/229/OHK4/3T/17 is gratefully appreciated.

I appreciate my family and friends, who supported me in everything.

Prohlašuji, že jsem doktorskou práci s názvem “Neinvazivní lokalizace ohniska ektopické komorové aktivace” vypracovala samostatně a použila k tomu úplný výčet citací použitých pramenů, které uvádím v seznamu přiloženém k doktorské práci.

Nemám závažný důvod proti užití tohoto školního díla ve smyslu §60 Zákona č. 121/2000 Sb., o právu autorském, o právech souvisejících s právem autorským a o změně některých zákonů (autorský zákon).

I hereby declare that I have completed this thesis with the topic “*Noninvasive localization of the focus of ectopic ventricular activation*” independently, and that I have attached an exhaustive list of citations of the employed sources to the Doctoral thesis.

I do not have a compelling reason against the use of the thesis within the meaning of Section 60 of the Act No.121 / 2000 Coll., on copyright, rights related to copyright and amending some laws (Copyright Act).

.....

Abstrakt /

Časté (více než 20%) předčasné komorové extrasystoly (KES) mohou vést k rozvoji dysfunkce levé komory. Možnou léčbou těchto pacientů je radiofrekvenční ablace (RFA) počátečního místa (ohniska) ektopické aktivity, která se provádí během invazivní elektrofyziologické (EP) studie. Přesná lokalizace ohniska KES je nejdůležitějším faktorem úspěšnosti RFA. Cílem dizertační práce je předoperační neinvazivní lokalizace ohniska KES s použitím EKG mapování z povrchu hrudníku (BSP) a individualizovaného modelu hrudníku, vyhodnocení a výběr nejlepších vstupních parametrů inverzního řešení pro přesnou lokalizaci ohniska KES.

Pacienti s KES podstoupili mapování BSP, CT skenování a EP studii s RFA. Pro určení optimálních vstupních dat byl u každého pacienta zpracován počáteční časový interval 30 ms z 5 KES komplexů v rámci tohoto intervalu bylo vypočteno 21 integrálových (IBSPM) a 31 okamžikových BSP map (TIBSPM) pro každý z pěti komplexů. Individualizovaná TIBSPM byla vybrána na základě maximální průměrné korelace mezi TIBSPMs z celého sledovaného časového intervalu. CT vyšetření byly použity k získání modelů torza pacienta s různou úrovní uvažování nehomogenit: homogenní model H, nehomogenní model V (obsahující plíce a srdeční komory) a nehomogenní model AV (obsahující plíce, srdeční komory, atria a výtokové cesty). Po skončení RFA byla lékařem vyznačena poloha ablačních lézí pomocí čísla segmentu podle doporučení AHA pro segmentaci levé komory, která byla rozšířena také pro segmentaci pravé komory, nebo pomocí 12-hodinového dělení pro ablační léze v místě odtokových traktů.

Pro nalezení jediného dipólu reprezentujícího ohnisko KES byl vyřešen

inverzní problém pro všech 156 možných kombinací vstupních parametrů, pro 5 KES u deseti pacientů. Dipól byl vybrán na základě kritéria minimální relativní zbytkové chyby (RRE) mezi vstupní BSP mapou a mapou generovanou tímto dipólem. Pouze inverzní řešení s hodnotou RRE menší nebo rovnou 0,3 byla považována za relevantní. Relevantní výsledek byl považován za správný (SRV) pokud se jeho umístění shodovalo se segmentem označeným lékařem.

Byl vyhodnocen vliv vstupních dat inverzního řešení na jeho přesnost a stabilitu. Nejvyšší počet — 61.3% SRV bylo dosaženo při použití vstupní mapy IBSPM 0–15 ms bez ohledu na použitý model hrudníku ($p < 0.01$); nebo 62.9% SRV když byl jako vstupní data použit homogenní model hrudníku H bez ohledu na použitou BSP mapu ($p < 0.01$). Když byly jako vstupní data použity kombinace homogenního modelu torza H a TIBSPM z 8., 9. nebo 10. ms byl dosažen nejvyšší počet SRV — 77,4% ($p < 0,01$). Použití individualizovaných vstupních dat nevedlo k signifikantně vyššímu počtu SRV.

Stabilita inverzního řešení v závislosti na funkci RRE a fluktuace vstupních dat ukázala, že funkce RRE je prostorově stabilní, ale vysoké fluktuace EKG mohou zhoršovat inverzní řešení.

Získané výsledky naznačují, že navržená metoda neinvazivní lokalizace ohniska KES může být použita před operací pro zkrácení EP studie při zásahu pomocí RFA.

Klíčová slova: mapování potenciálu povrchu těla; inverzní problém elektrokardiografie; ektopická aktivita; předčasné komorové extrasystoly; model nehomogenního trupu; neinvazivní lokalizace.

Abstract /

Frequent (more than 20%) premature ventricular complexes (PVCs) can lead to the development of left ventricular dysfunction. Possible treatment of such patients is radiofrequency ablation (RFA) of the initial site (focus) of the ectopic activity, which is performed during invasive electrophysiological (EP) study. PVC focus accurate localization is the most important factor for the RFA success. The aim of the thesis is preoperative noninvasive localization of the PVC focus using ECG body surface potential (BSP) mapping and patient-specific torso geometry, evaluation and selection of the best input parameters of the inverse problem for accurate PVC focus localization.

Patients with PVCs underwent BSP mapping, CT scanning, and EP study with RFA. To find optimal input data, in each patient, initial 30 ms time interval of 5 PVC signals were processed and within this interval 21 integral BSP maps (IBSPMs) and 31 time instant BSP maps (TIBSPMs) were computed for each of the five beats. Patient-specific TIBSPM was selected based on the maximum averaged correlation between the TIBSPMs from the whole studied time interval. CT images were used to obtain patient torso models with different levels of torso complexity: homogeneous model H, inhomogeneous model V (with lungs, and heart ventricles), and inhomogeneous model AV (with lungs, heart ventricles, atria and outflow tracts). After successful RFA the clinician assigned the localization of the ablation lesions by a segment number according to AHA recommendations of LV division and its extension to the RV, or using a 12 segment clock-like-division for ablation lesions with outflow tract locations.

The inverse problem was solved for all 156 possible combinations of the input data, for 5 PVCs in ten patients to find a single dipole representing the PVC focus. It was selected using the criterion of minimal relative residual error (RRE) between the input BSP map and the map generated by the dipole. Only inverse solutions with RRE less or equal 0.3 were considered as relevant. Relevant result was considered correct (CRR) if its location matched with the segment assigned by the clinician.

Impact of the input data on the accuracy and stability of the inverse problem was evaluated. The highest number — 61.3% of CRR was obtained when IBSPM from 0–15 ms was used as input data, regardless of the used torso model ($p < 0.01$); or 62.9% of CRR when the homogeneous torso model H was used as input data, regardless of the used BSP map ($p < 0.01$). In combinations, the homogeneous torso model H and one of the TIBSPM computed in 8 ms, 9 ms, or 10 ms led to the highest number of CRR — 77.4% ($p < 0.01$). The use of patient-specific input data did not yield significantly higher number of CRRs.

Stability of the inverse solution depending on RRE function and fluctuations in input data showed that the RRE function is spatially stable but high fluctuations in ECG can hinder the inverse solution.

The obtained results suggest that the proposed method for noninvasive localization of the PVC focus can be used pre-operationally for shortening of the EP study with the RFA intervention.

Keywords: body surface potential mapping; inverse problem of electrocardiography; ectopic activity; premature ventricular complexes; inhomogeneous torso model; noninvasive localization.

Contents /

Abbreviations and symbols	1
1 State of art	3
1.1 Heart as part of cardiovascular system	3
1.2 Electrical activity of the heart ..	4
1.2.1 Conduction system of the heart	4
1.2.2 Cellular electrophysiology	5
1.3 Cardiac arrhythmias	6
1.3.1 Premature ventricular complexes	9
1.4 Treatment of the cardiac arrhythmias	9
1.4.1 Pharmacotherapy	10
1.4.2 Surgical therapy	10
1.4.3 Device therapy	10
1.4.4 Catheter ablation	10
1.4.5 Treatment of the PVCs..	14
1.5 Measurement of the cardiac electrical field	14
1.5.1 Intracardiac electrograms	14
1.5.2 Standard 12-lead electrocardiogram	16
1.5.3 Multichannel ECG	19
1.6 Mapping of the cardiac electrical field	21
1.6.1 Intracardial mapping	21
1.6.2 Body surface potential mapping	23
1.7 Modelling of the cardiac electrical activity	27
1.7.1 Forward problem of electrocardiography	28
1.7.2 Source models	29
1.7.3 Modelling of the torso volume conductor	31
1.7.4 Numerical methods	33
1.7.5 Inverse problem of electrocardiography	34
1.7.6 Noninvasive electrocardiographic imaging ...	35
2 Aim and goals of the thesis	36
3 Selected processing and evaluation methods	37
3.1 Inverse method	37
3.1.1 Selection of the electrical generator and the computational method...	37
3.1.2 Inverse solution with one dipole	38
3.1.3 Number of ECG leads for the inverse solution ..	39
3.1.4 Required resolution of the inverse solution	41
3.2 ECG measurement and processing	42
3.2.1 Selection of the processed time interval in ECG	42
3.2.2 Correction of the ECG baseline	43
3.2.3 Definition of the PVC onset in the ECG	45
3.2.4 Filtering of the ECG	46
3.3 CT data processing	47
3.4 Correctness of the inverse solution	48
3.5 Evaluation of the inverse solution results	50
3.5.1 Used statistical terms and tests	50
3.5.2 Selection of the relevant results using relative residual error criterion	52
3.5.3 Evaluation of the input BSP maps impact on inverse solution	52
3.5.4 Search of the patient-specific time instant for TIBSPM computation ...	53
3.5.5 Evaluation of the impact of the torso model complexity on the inverse solution	55
3.5.6 Search of the best combination of input data for the inverse solution ..	55

3.5.7 Evaluation of the stability of the inverse solution	56	6 Discussion	83
4 Experimental evaluation of the proposed methods	58	6.1 Measurement-related issues ...	83
4.1 Selection and description of the patient group	58	6.2 Golden truth of the PVC location and precision of the inverse solution.....	86
4.2 Measurement procedures	58	6.3 Analysis of the patients with small number of relevant results	88
4.2.1 Multichannel ECG measurement and processing	58	6.4 Input parameters for the inverse solution.....	90
4.2.2 CT data processing	62	6.5 Stability of the inverse solution	91
4.2.3 Electrophysiological study	64	7 Conclusions	92
4.3 Inverse solution setting	65	Summary of achieved results and fulfillment of the goals	94
5 Results	66	References	96
5.1 Selection of the relevant results using relative residual error criterion	66	A Patient group description	117
5.2 Evaluation of the input BSP maps impact on the inverse solution.....	67	B Patient's informed consent protocol	118
5.3 Search of the patient-specific time instant for TIBSPM computation.....	70	C Contingency tables	121
5.4 Evaluation of the impact of the torso model complexity on the inverse solution.....	70	D Pat004	130
5.5 Search of the best combination of the input data for the inverse solution.....	74	E Pat005	134
5.6 Evaluation of the stability of the inverse solution	75	F Pat006	138
5.6.1 Stability of the inverse solution using the best combination of input parameters based on the minimal RRE value .	75	G Pat007	142
5.6.2 Stability of the inverse solution in dependence on the BSP map variability.....	77	H Pat008	146
5.6.3 Stability of the inverse solution in dependence on the torso model complexity	77	I Pat009	150
		J Pat010	154
		K Pat011	158
		L Pat015	162
		M Pat016	166
		N List of author's publications	170
		Papers in journals related to the Thesis	170
		Conference contributions related to the Thesis	170
		Projects	172
		Further author's publications	172

Tables /

1.1. Comparison of three-dimensional mapping systems .	24
1.2. Comparison of ECG and BSP mapping	25
4.1. Twenty-one sub-intervals used to compute IBSPMs.....	60
5.1. Contingency table showing how many correct/incorrect inverse results were observed among results with $RRE \leq 0.3$	66
5.2. Contingency table showing how many correct inverse solutions were observed using IBSPM from 0–15 ms time interval versus all the other BSP maps	68
5.3. Contingency table showing how many correct inverse solutions are expected (assuming independency of the inverse solution correctness from input BSP map) using IBSPM from 0–15 ms time interval versus all the other BSP maps	68
5.4. Contingency table showing how many correct relevant inverse solutions were observed using torso model with selected complexity.....	72
5.5. Contingency table showing how many correct inverse solutions are expected (assuming independency of the inverse solution correctness from the torso model complexity) using torso model with selected complexity	73
5.6. Contingency table showing how many correct relevant inverse solutions were observed using torso model with selected complexity.....	73
5.7. Contingency table showing how many correct inverse solutions are expected (assuming independency of the inverse solution correctness from the torso model complexity) using torso model with selected complexity	73
5.8. Contingency table showing how many correct relevant inverse solutions were observed using the selected combination of the used body surface potential map and torso model with selected level of complexity	75
5.9. Contingency table showing how many correct inverse solutions are expected (assuming independency of the inverse solution correctness from the used input combination) using the selected combination of the used body surface potential map and torso model with selected level of complexity	75
A.1. Patient group description	117
C.1. Contingency table showing how many correct inverse solutions were observed using BSP map generated for the selected time interval or time instant	121
C.2. Contingency table showing how many correct inverse solutions are expected (assuming independency of the inverse solution correctness from input BSP map) using body surface potential map generated for the selected time interval or time instant..	123
C.3. Contingency table showing how many correct relevant inverse solutions were observed using selected combination of the input parameters (torso	

model and time interval or time instant for BSP map) ...	124
C.4. Contingency table showing how many correct inverse solutions are expected (as- suming independency of the inverse solution correctness from the used input combi- nation) using combination of selected body surface po- tential map and torso model with selected level of com- plexity	127



Figures /

1.1.	The anatomy of the heart and associated vessels	3
1.2.	The conduction system of the heart	4
1.3.	Activation sequence of ventricular myocardium	4
1.4.	Action potential in cardiac contractile cells	5
1.5.	Action potential of the sinus node	6
1.6.	Types of afterdepolarizations	8
1.7.	Thermal injury of myocardium caused by resistive and conductive heating	12
1.8.	Catheter approach for electrophysiological study	13
1.9.	Multipolar diagnostic catheters	13
1.10.	Ablation catheters	13
1.11.	Generation of the unipolar and bipolar recordings	15
1.12.	Creating zero potential using driving reference	16
1.13.	ECG electrodes placement	17
1.14.	ECG represents heart activity ..	18
1.15.	Normal ECG signal	18
1.16.	Example of 2 PVCs	18
1.17.	Lead systems	20
1.18.	CardioInsight vest	20
1.19.	Computation of departure BSP map	26
1.20.	Types of BSP maps	27
1.21.	Forward and inverse problems of electrocardiography	28
3.1.	Diagram of ablation lesions dimensions for different radiofrequency ablation modes ..	41
3.2.	Assumptions of the single dipole model representing PVC focus ablation	43
3.3.	Example of the ECG baseline wander	44
3.4.	Examples of artifacts caused by different sources	46
3.5.	Relative power spectra of an QRS complex, P and T waves, muscle noise and motion artifacts	47
3.6.	Torso models with different degree of included inhomogeneities	48
3.7.	Heart geometries obtained using 3D navigation system and CT	49
3.8.	Segmentation of the ventricles ..	49
3.9.	Segmentation of the outflow tract	50
3.10.	Correlations between TIB-SPMs	54
3.11.	Average correlation of the TIBSPMs for each time instant	55
4.1.	ProCardio 8 mapping system ..	59
4.2.	Patient with 96 lead system ...	59
4.3.	Initial manual selection of the processed interval	60
4.4.	Redefinition of baseline times and manual setting of the Zero-time	61
4.5.	Allocation of the final PVC onset and time markers defining sub-intervals	61
4.6.	Example of IBSPM	62
4.7.	Whole torso CT scan in AP projection	62
4.8.	CT image with contours of the torso structures	63
4.9.	3D structures of the torso model	63
4.10.	Electroanatomic mapping of the RV of Pat004	64
4.11.	RV endocardium model merged with RV 3D model reconstructed from CT	65
5.1.	Percentage of the relevant inverse solutions with $RRE \leq 0.3$ in each patient	66
5.2.	Percentage of the correct relevant inverse solutions out of all relevant solutions with $RRE \leq 0.3$ in each patient	67

<p>5.3. Correctness of the inverse solutions in each patient with respect to the RRE value 67</p> <p>5.4. Percentage of correct inverse results for the selected 52 BSP maps 68</p> <p>5.5. Percentage of the obtained correct inverse results from 21 input IBSPMs for each patient separately 69</p> <p>5.6. Percentage of the obtained correct inverse results from 31 input TIBSPMs for each patient separately 69</p> <p>5.8. Number of the total and correct relevant inverse results obtained using patient-specific TIBSPM and one of three torso models 70</p> <p>5.7. Averaged correlations of the TIBSPMs in each time instant for each of the five PVCs for each patient 71</p> <p>5.9. Amount of correct relevant inverse solutions (in %) obtained using integral and time instant BSP maps generated for five PVCs in each patient for three torso models with different inhomogeneities . 72</p> <p>5.10. Percentage of obtained correct relevant inverse results for three levels of torso model complexity for each patient separately 72</p> <p>5.11. Percentage of the correct relevant inverse results for the combinations with more than 60% success..... 74</p> <p>5.12. Box-and-whisker plot of the distances between the positions of the first five dipoles of the inverse solution with minimal RRE and their gravity center in each patient 76</p>	<p>5.13. Positions of the five dipoles of the inverse solutions with minimal RREs obtained for single PVC using TIBSPM in time instant 8 ms and homogeneous torso model H 76</p> <p>5.14. Box-and-whisker plot of the distances between the positions of the twenty-five dipoles of the inverse solutions and their gravity center in each patient 77</p> <p>5.15. Positions of the twenty-five dipoles of the inverse solutions with minimal RRE..... 78</p> <p>5.16. Mean and standard deviation of the positions of the five dipoles from their gravity center obtained for the inverse solutions with minimal RRE values computed for individual patients 78</p> <p>5.17. Mean and standard deviation of the positions of the five dipoles from their gravity center obtained for the inverse solutions with minimal RRE values computed for all 10 patients 79</p> <p>5.18. Box-and-whisker plot of the distances between the positions of the five dipoles of the inverse solution and their gravity center in each patient. Torso model H and IBSPM 0–15 ms 79</p> <p>5.19. Box-and-whisker plot of the distances between the positions of the five dipoles of the inverse solution and their gravity center in each patient. Torso model V and IBSPM 0–15 ms 80</p> <p>5.20. Box-and-whisker plot of the distances between the positions of the five dipoles of</p>
---	---

the inverse solution and their gravity center in each patient. Torso model AV and IBSPM 0–15 ms	80	6.2. Electrode displacement in female patient	84
5.21. Positions of first five dipoles with minimal RRE value of the inverse solution for one BSP map (IBSPM 0–15 ms) and homogeneous torso model H	80	6.3. Rendering of the CT scan for Pat005	84
5.22. Positions of first five dipoles with minimal RRE value of the inverse solution for one BSP map (IBSPM 0–15 ms) and inhomogeneous torso model V	81	6.4. Box-and-whisker plot of the noise-per-second value	85
5.23. Positions of first five dipoles with minimal RRE value of the inverse solution for one BSP map (IBSPM 0–15 ms) and inhomogeneous torso model AV	81	6.5. Geometries of the left cavities for Pat006	87
5.24. Distances between gravity centers of the five inverse solution positions obtained for IBSPM 0–15 ms and torso models of different complexity .	82	6.6. Merged geometries of the intraoperational endocardial RV with 3D model of the RV reconstructed from CT of the Pat008	87
5.25. Biggest distances between the gravity centers of the five dipole positions obtained for inverse solutions with IBSPM 0–15 ms and each of three input torso models in the ventricular myocardium of the Pat007	82	6.7. Right ventricle + right atrium + pulmonary artery 3D models of the Pat008	88
5.26. The smallest distances between the gravity centers of the five dipole positions obtained for inverse solutions with IBSPM 0–15 ms and each of three input torso models in the ventricular myocardium of the Pat016	82	6.8. 3D models of the RV with ablation points. AP view	88
6.1. Patient P2 from a pilot study with Amsterdam lead system..	83	6.9. Torso models of the patients with RRE less than 40%	89
		6.10. Mean and standard deviation of the relative residual error of the inverse solutions for Pat006 and Pat009	90
		6.11. Percentage of correct relevant inverse results for one of the torso models in combination with patient-specific TIBSPM or best map (IBSPM 0–15 ms), and best combination of the input parameters — homogenous torso model H and TIBSPM 8 ms .	91
		6.12. Percentage of obtained relevant inverse results for best methods for each patient separately	91
		D.1. Torso models of patient Pat004	130
		D.2. BSP maps of patient Pat004 .	130
		D.3. Results for Pat004	130
		D.4. Positions of the inverse solutions for IBSPM 0–15 ms in combination with one of the torso models for Pat004	131

D.5. Positions of the inverse solutions for torso model H and patient-specific TIBSPM for Pat004.....	131		
D.6. Positions of the inverse solutions for torso model V and patient-specific TIBSPM for Pat004.....	131		
D.7. Positions of the inverse solutions for torso model AV and patient-specific TIBSPM for Pat004.....	131		
D.8. Positions of the inverse solutions for torso model H in combination with one of 52 BSP maps for Pat004	132		
D.9. Positions of the inverse solutions for torso model H and TIBSPM 8 ms for Pat004	132		
D.10. Positions of the first five dipoles of the inverse solution with minimal RRE for best combination of the input parameters. Pat004	132		
D.11. Positions of the 25 dipoles of the inverse solution with minimal RRE using combination of input parameters: homogeneous torso model H and 5 TIBSPMs 8 ms for Pat004.....	132		
D.12. Positions of first five dipoles with minimal RRE value of the inverse solution for one IBSPM 0–15 ms and homogeneous torso model H for Pat004.....	133		
D.13. Positions of first five dipoles with minimal RRE value of the inverse solution for one IBSPM 0–15 ms and inhomogeneous torso model V for Pat004.....	133		
D.14. Positions of first five dipoles with minimal RRE value of the inverse solution for one IBSPM 0–15 ms and inhomogeneous torso model AV for Pat004.....	133		
D.15. Gravity centers of the five dipoles positions derived for inverse solution for IBSPM 0–15 ms and each of the three input torso models in the ventricular myocardium of the Pat004.....	133		
E.1. Torso models of patient Pat005.....	134		
E.2. BSP maps of patient Pat005	134		
E.3. Results for Pat005	134		
E.4. Positions of the inverse solutions for IBSPM 0–15 ms in combination with one of the torso models for Pat005	135		
E.5. Positions of the inverse solutions for torso model H and patient-specific TIBSPM for Pat005.....	135		
E.6. Positions of the inverse solutions for torso model V and patient-specific TIBSPM for Pat005.....	135		
E.7. Positions of the inverse solutions for torso model AV and patient-specific TIBSPM for Pat005.....	135		
E.8. Positions of the inverse solutions for torso model H in combination with one of 52 BSP maps for Pat005	136		
E.9. Positions of the inverse solutions for torso model H and TIBSPM 8 ms for Pat005	136		
E.10. Positions of the first five dipoles of the inverse solution with minimal RRE for best combination of the input parameters. Pat005	136		
E.11. Positions of the 25 dipoles of the inverse solution with minimal RRE using combination of input parameters:			

homogeneous torso model H and 5 TIBSPMs 8 ms for Pat005.....	136	patient-specific TIBSPM for Pat006.....	139
E.12. Positions of first five dipoles with minimal RRE value of the inverse solution for one IBSPM 0–15 ms and homogeneous torso model H for Pat005.....	137	F.8. Positions of the inverse solutions for torso model H in combination with one of 52 BSP maps for Pat006	140
E.13. Positions of first five dipoles with minimal RRE value of the inverse solution for one IBSPM 0–15 ms and inhomogeneous torso model V for Pat005.....	137	F.9. Positions of the inverse solutions for torso model H and TIBSPM 8 ms for Pat006	140
E.14. Positions of first five dipoles with minimal RRE value of the inverse solution for one IBSPM 0–15 ms and inhomogeneous torso model AV for Pat005.....	137	F.10. Positions of the first five dipoles of the inverse solution with minimal RRE for best combination of the input parameters. Pat006	140
E.15. Gravity centers of the five dipoles positions derived for inverse solution for IBSPM 0–15 ms and each of the three input torso models in the ventricular myocardium of the Pat005.....	137	F.11. Positions of the 25 dipoles of the inverse solution with minimal RRE using combination of input parameters: homogeneous torso model H and 5 TIBSPMs 8 ms for Pat006.....	140
F.1. Torso models of patient Pat006.....	138	F.12. Positions of first five dipoles with minimal RRE value of the inverse solution for one IBSPM 0–15 ms and homogeneous torso model H for Pat006.....	141
F.2. BSP maps of patient Pat006	138	F.13. Positions of first five dipoles with minimal RRE value of the inverse solution for one IBSPM 0–15 ms and inhomogeneous torso model V for Pat006.....	141
F.3. Results for Pat006	138	F.14. Positions of first five dipoles with minimal RRE value of the inverse solution for one IBSPM 0–15 ms and inhomogeneous torso model AV for Pat006.....	141
F.4. Positions of the inverse solutions for IBSPM 0–15 ms in combination with one of the torso models for Pat006	139	F.15. Gravity centers of the five dipoles positions derived for inverse solution for IBSPM 0–15 ms and each of the three input torso models in the ventricular myocardium of the Pat006.....	141
F.5. Positions of the inverse solutions for torso model H and patient-specific TIBSPM for Pat006.....	139		
F.6. Positions of the inverse solutions for torso model V and patient-specific TIBSPM for Pat006.....	139		
F.7. Positions of the inverse solutions for torso model AV and			

G.1. Torso models of patient Pat007	142	G.13. Positions of first five dipoles with minimal RRE value of the inverse solution for one IBSPM 0–15 ms and inhomogeneous torso model V for Pat007	145
G.2. BSP maps of patient Pat007 .	142	G.14. Positions of first five dipoles with minimal RRE value of the inverse solution for one IBSPM 0–15 ms and inhomogeneous torso model AV for Pat007	145
G.3. Results for Pat007	142	G.15. Gravity centers of the five dipoles positions derived for inverse solution for IBSPM 0–15 ms and each of the three input torso models in the ventricular myocardium of the Pat007	145
G.4. Positions of the inverse solutions for IBSPM 0–15 ms in combination with one of the torso models for Pat007	143	H.1. Torso models of patient Pat008	146
G.5. Positions of the inverse solutions for torso model H and patient-specific TIBSPM for Pat007	143	H.2. BSP maps of patient Pat008 .	146
G.6. Positions of the inverse solutions for torso model V and patient-specific TIBSPM for Pat007	143	H.3. Results for Pat008	146
G.7. Positions of the inverse solutions for torso model AV and patient-specific TIBSPM for Pat007	143	H.4. Positions of the inverse solutions for IBSPM 0–15 ms in combination with one of the torso models for Pat008	147
G.8. Positions of the inverse solutions for torso model H in combination with one of 52 BSP maps for Pat007	144	H.5. Positions of the inverse solutions for torso model H and patient-specific TIBSPM for Pat008	147
G.9. Positions of the inverse solutions for torso model H and TIBSPM 8 ms for Pat007	144	H.6. Positions of the inverse solutions for torso model V and patient-specific TIBSPM for Pat008	147
G.10. Positions of the first five dipoles of the inverse solution with minimal RRE for best combination of the input parameters. Pat007	144	H.7. Positions of the inverse solutions for torso model AV and patient-specific TIBSPM for Pat008	147
G.11. Positions of the 25 dipoles of the inverse solution with minimal RRE using combination of input parameters: homogeneous torso model H and 5 TIBSPMs 8 ms for Pat007	144	H.8. Positions of the inverse solutions for torso model H in combination with one of 52 BSP maps for Pat008	148
G.12. Positions of first five dipoles with minimal RRE value of the inverse solution for one IBSPM 0–15 ms and homogeneous torso model H for Pat007	145	H.9. Positions of the inverse solutions for torso model H and TIBSPM 8 ms for Pat008	148

H.10.	Positions of the first five dipoles of the inverse solution with minimal RRE for best combination of the input parameters. Pat008	148
H.11.	Positions of the 25 dipoles of the inverse solution with minimal RRE using combination of input parameters: homogeneous torso model H and 5 TIBSPMs 8 ms for Pat008	148
H.12.	Positions of first five dipoles with minimal RRE value of the inverse solution for one IBSPM 0–15 ms and homogeneous torso model H for Pat008	149
H.13.	Positions of first five dipoles with minimal RRE value of the inverse solution for one IBSPM 0–15 ms and inhomogeneous torso model V for Pat008	149
H.14.	Positions of first five dipoles with minimal RRE value of the inverse solution for one IBSPM 0–15 ms and inhomogeneous torso model AV for Pat008	149
H.15.	Gravity centers of the five dipoles positions derived for inverse solution for IBSPM 0–15 ms and each of the three input torso models in the ventricular myocardium of the Pat008	149
I.1.	Torso models of patient Pat009	150
I.2.	BSP maps of patient Pat009 .	150
I.3.	Results for Pat009	150
I.4.	Positions of the inverse solutions for IBSPM 0–15 ms in combination with one of the torso models for Pat009	151
I.5.	Positions of the inverse solutions for torso model H and patient-specific TIBSPM for Pat009	151
I.6.	Positions of the inverse solutions for torso model V and patient-specific TIBSPM for Pat009	151
I.7.	Positions of the inverse solutions for torso model AV and patient-specific TIBSPM for Pat009	151
I.8.	Positions of the inverse solutions for torso model H in combination with one of 52 BSP maps for Pat009	152
I.9.	Positions of the inverse solutions for torso model H and TIBSPM 8 ms for Pat009	152
I.10.	Positions of the first five dipoles of the inverse solution with minimal RRE for best combination of the input parameters. Pat009	152
I.11.	Positions of the 25 dipoles of the inverse solution with minimal RRE using combination of input parameters: homogeneous torso model H and 5 TIBSPMs 8 ms for Pat009	152
I.12.	Positions of first five dipoles with minimal RRE value of the inverse solution for one IBSPM 0–15 ms and homogeneous torso model H for Pat009	153
I.13.	Positions of first five dipoles with minimal RRE value of the inverse solution for one IBSPM 0–15 ms and inhomogeneous torso model V for Pat009	153
I.14.	Positions of first five dipoles with minimal RRE value of the inverse solution for one	

	IBSPM 0–15 ms and inhomogeneous torso model AV for Pat009	153
I.15.	Gravity centers of the five dipoles positions derived for inverse solution for IBSPM 0–15 ms and each of the three input torso models in the ventricular myocardium of the Pat009	153
J.1.	Torso models of patient Pat010	154
J.2.	BSP maps of patient Pat010 .	154
J.3.	Results for Pat010	154
J.4.	Positions of the inverse solutions for IBSPM 0–15 ms in combination with one of the torso models for Pat010	155
J.5.	Positions of the inverse solutions for torso model H and patient-specific TIBSPM for Pat010	155
J.6.	Positions of the inverse solutions for torso model V and patient-specific TIBSPM for Pat010	155
J.7.	Positions of the inverse solutions for torso model AV and patient-specific TIBSPM for Pat010	155
J.8.	Positions of the inverse solutions for torso model H in combination with one of 52 BSP maps for Pat010	156
J.9.	Positions of the inverse solutions for torso model H and TIBSPM 8 ms for Pat010	156
J.10.	Positions of the first five dipoles of the inverse solution with minimal RRE for best combination of the input parameters. Pat010	156
J.11.	Positions of the 25 dipoles of the inverse solution with minimal RRE using combination of input parameters:	
	homogeneous torso model H and 5 TIBSPMs 8 ms for Pat010	156
J.12.	Positions of first five dipoles with minimal RRE value of the inverse solution for one IBSPM 0–15 ms and homogeneous torso model H for Pat010	157
J.13.	Positions of first five dipoles with minimal RRE value of the inverse solution for one IBSPM 0–15 ms and inhomogeneous torso model V for Pat010	157
J.14.	Positions of first five dipoles with minimal RRE value of the inverse solution for one IBSPM 0–15 ms and inhomogeneous torso model AV for Pat010	157
J.15.	Gravity centers of the five dipoles positions derived for inverse solution for IBSPM 0–15 ms and each of the three input torso models in the ventricular myocardium of the Pat010	157
K.1.	Torso models of patient Pat011	158
K.2.	BSP maps of patient Pat011 .	158
K.3.	Results for Pat011	158
K.4.	Positions of the inverse solutions for IBSPM 0–15 ms in combination with one of the torso models for Pat011	159
K.5.	Positions of the inverse solutions for torso model H and patient-specific TIBSPM for Pat011	159
K.6.	Positions of the inverse solutions for torso model V and patient-specific TIBSPM for Pat011	159
K.7.	Positions of the inverse solutions for torso model AV and	

patient-specific TIBSPM for Pat011	159	L.1. Torso models of patient Pat015	162
K.8. Positions of the inverse solutions for torso model H in combination with one of 52 BSP maps for Pat011	160	L.2. BSP maps of patient Pat015 ..	162
K.9. Positions of the inverse solutions for torso model H and TIBSPM 8 ms for Pat011	160	L.3. Results for Pat015	162
K.10. Positions of the first five dipoles of the inverse solution with minimal RRE for best combination of the input parameters. Pat011	160	L.4. Positions of the inverse solutions for IBSPM 0–15 ms in combination with one of the torso models for Pat015	163
K.11. Positions of the 25 dipoles of the inverse solution with minimal RRE using combination of input parameters: homogeneous torso model H and 5 TIBSPMs 8 ms for Pat011	160	L.5. Positions of the inverse solutions for torso model H and patient-specific TIBSPM for Pat015	163
K.12. Positions of first five dipoles with minimal RRE value of the inverse solution for one IBSPM 0–15 ms and homogeneous torso model H for Pat011	161	L.6. Positions of the inverse solutions for torso model V and patient-specific TIBSPM for Pat015	163
K.13. Positions of first five dipoles with minimal RRE value of the inverse solution for one IBSPM 0–15 ms and inhomogeneous torso model V for Pat011	161	L.7. Positions of the inverse solutions for torso model AV and patient-specific TIBSPM for Pat015	163
K.14. Positions of first five dipoles with minimal RRE value of the inverse solution for one IBSPM 0–15 ms and inhomogeneous torso model AV for Pat011	161	L.8. Positions of the inverse solutions for torso model H in combination with one of 52 BSP maps for Pat015	164
K.15. Gravity centers of the five dipoles positions derived for inverse solution for IBSPM 0–15 ms and each of the three input torso models in the ventricular myocardium of the Pat011	161	L.9. Positions of the inverse solutions for torso model H and TIBSPM 8 ms for Pat015	164
		L.10. Positions of the first five dipoles of the inverse solution with minimal RRE for best combination of the input parameters. Pat015	164
		L.11. Positions of the 25 dipoles of the inverse solution with minimal RRE using combination of input parameters: homogeneous torso model H and 5 TIBSPMs 8 ms for Pat015	164
		L.12. Positions of first five dipoles with minimal RRE value of the inverse solution for one IBSPM 0–15 ms and homogeneous torso model H for Pat015	165

<p>L.13. Positions of first five dipoles with minimal RRE value of the inverse solution for one IBSPM 0–15 ms and inhomogeneous torso model V for Pat015 165</p> <p>L.14. Positions of first five dipoles with minimal RRE value of the inverse solution for one IBSPM 0–15 ms and inhomogeneous torso model AV for Pat015 165</p> <p>L.15. Gravity centers of the five dipoles positions derived for inverse solution for IBSPM 0–15 ms and each of the three input torso models in the ventricular myocardium of the Pat015 165</p> <p>M.1. Torso models of patient Pat016 166</p> <p>M.2. BSP maps of patient Pat016 . 166</p> <p>M.3. Results for Pat016 166</p> <p>M.4. Positions of the inverse solutions for IBSPM 0–15 ms in combination with one of the torso models for Pat016 167</p> <p>M.5. Positions of the inverse solutions for torso model H and patient-specific TIBSPM for Pat016 167</p> <p>M.6. Positions of the inverse solutions for torso model V and patient-specific TIBSPM for Pat016 167</p> <p>M.7. Positions of the inverse solutions for torso model AV and patient-specific TIBSPM for Pat016 167</p> <p>M.8. Positions of the inverse solutions for torso model H in combination with one of 52 BSP maps for Pat016 168</p> <p>M.9. Positions of the inverse solutions for torso model H and TIBSPM 8 ms for Pat016 168</p>	<p>M.10. Positions of the first five dipoles of the inverse solution with minimal RRE for best combination of the input parameters. Pat016 168</p> <p>M.11. Positions of the 25 dipoles of the inverse solution with minimal RRE using combination of input parameters: homogeneous torso model H and 5 TIBSPMs 8 ms for Pat016 168</p> <p>M.12. Positions of first five dipoles with minimal RRE value of the inverse solution for one IBSPM 0–15 ms and homogeneous torso model H for Pat016 169</p> <p>M.13. Positions of first five dipoles with minimal RRE value of the inverse solution for one IBSPM 0–15 ms and inhomogeneous torso model V for Pat016 169</p> <p>M.14. Positions of first five dipoles with minimal RRE value of the inverse solution for one IBSPM 0–15 ms and inhomogeneous torso model AV for Pat016 169</p> <p>M.15. Gravity centers of the five dipoles positions derived for inverse solution for IBSPM 0–15 ms and each of the three input torso models in the ventricular myocardium of the Pat016 169</p>
---	--

Abbreviations and symbols

aVF	■ augmented left leg lead
aVL	■ augmented left arm lead
aVR	■ augmented right arm lead
$bspm$	■ body surface potential map
D	■ single dipole
$dbspm$	■ body surface potential map, generated by the single dipole
df	■ degrees of freedom
$D(t)$	■ equivalent heart generator
I	■ examined time interval
LA	■ left arm electrode
LL	■ left leg electrode
m	■ number of measured points on the torso (leads)
n	■ number of single dipoles in the pre-defined positions in the myocardium
RA	■ right arm electrode
t	■ time instant
χ^2	■ chi-square
ϕ_i	■ potentials on the body surface measured in i points
RRE	■ relative residual error
B	■ transfer matrix
AAD	■ antiarrhythmic drug
AF	■ atrial fibrillation
AHA	■ American Heart Association
AO	■ aorta
AP	■ anterior-posterior
AT	■ atrial tachycardia
AV	■ atrioventricular
BEM	■ boundary element method
BSP	■ body surface potential
CMS	■ common mode sense electrode
DC	■ direct current
DRL	■ driven right leg electrode
ECG	■ electrocardiogram
ECGI	■ electrophysiological imaging
EDL	■ equivalent double layer
EP	■ electrophysiological
FDM	■ finite difference method
FEM	■ finite element method
FVM	■ finite volume method
GDF	■ general data format for biomedical signals
I	■ standard ECG lead I
IBSPM	■ integral body surface potential map



- II ■ standard ECG lead II
- III ■ standard ECG lead III
- IQR ■ interquartile range
- LA ■ left atrium
- LV ■ left ventricle
- LVOT ■ left ventricular outflow tract
- PA ■ posterior-anterior
- PVC ■ premature ventricular complex
- RA ■ right atrium
- RFA ■ radiofrequency ablation
- RMS ■ root mean square
- RV ■ right ventricle
- RVOT ■ right ventricular outflow tract
- SNR ■ signal-to-noise ratio
- SVD ■ singular value decomposition
- TIBSPM ■ time instant body surface potential map
- UDL ■ uniform double layer
- VT ■ ventricular tachycardia
- WCT ■ Wilson's Central Terminal

Chapter 1

State of art

1.1 Heart as part of cardiovascular system

Heart is a functional organ, a part of the circulation system, which pumps blood via blood vessels. In humans, it has four chambers: **right (RA)** and **left atrium (LA)**, **right (RV)** and **left ventricle (LV)** (Fig. 1.1). RA receives deoxygenated blood from systematic circulation through inferior and superior vena cava and pumps it to the RV via the tricuspid valve. From the RV the blood is pumped via the **right ventricular outflow tract (RVOT)** through the pulmonary valve to the pulmonary artery. After passing through the pulmonary capillary beds, where the blood is oxygenated, the blood is returned via pulmonary veins to the LA and ejected to the LV through the mitral valve. From the LV the blood is pumped through the **left ventricular outflow tract (LVOT)** and is ejected through the aortic valve to the **aorta (AO)**. From AO it is distributed to the organs of the body. The movement of the blood from the right to the left heart (through the lungs) is called pulmonary circulation. And the movement to and from the rest of the body is called systematic circulation.

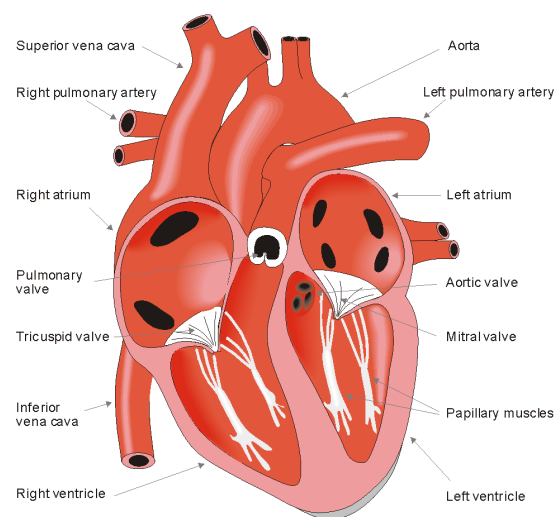


Figure 1.1: The anatomy of the heart and associated vessels. From [1]

The main function of the heart is to pump the blood through the blood vessels of the circulatory system and is gained by contractions of the heart. Each heart cycle consists of two phases: relaxation (diastole) and contraction (systole) of the chambers. During the diastole, the ventricles are filled with blood, and during the systole, they eject the blood into the large vessels. The contraction of the heart is controlled by the electrical activity of the myocardial cells.

include catheter ablation and implantable cardioverter-defibrillator (for primary and secondary prevention of sudden cardiac death) [7].

■ 1.4.1 Pharmacotherapy

All cardiac tachyarrhythmias are caused by localized or generalized changes in action potential regardless of underlying mechanism (abnormal automaticity, reentry or channelopathies). Therefore, principle of **antiarrhythmic drugs (AAD)** is based on a change of the shape of the action potential. This is achieved by the altering of the ionic channels in the cardiac cell membrane and in this way controlling the ionic fluxes through it. Modifying the action potential shape, the conductivity and refractory period of the cardiac cell is changed. As stated in [22], in practice AAD are relatively ineffective in automatic arrhythmias or channelopathies treatment, but they are highly used in the treatment of reentrant arrhythmias [22].

According to the latest guidelines on AAD there was no significant improvement in clinical pharmacology for arrhythmias over the last decades [23]. Because of severe cardiac and extracardiac adverse effects, the AAD is not a neutral medication and should be used only when arrhythmias are significantly symptomatic or life-threatening [24]. Studies focused on discovering target-specific AAD try to improve safety and decrease complex drug-drug interactions. Currently, decision-making when starting AAD focus on the patient's clinical condition, structural and functional substrate, arrhythmia mechanism at the cellular and molecular level. Patient-centered decision making is also explained by interference of multiple factors (such as race, gender, genetics, temperature, drug-drug interaction, triggering factors, neurohormonal changes, disease state and severity, disease-induced substrate remodeling, etc.) with drug effects [23].

■ 1.4.2 Surgical therapy

Because pharmacological therapy may not be adequate and/or may be associated with significant proarrhythmic effects, the preferred treatment of the arrhythmia is destruction or removal of the tissue responsible for arrhythmia [25]. Thus, catheter ablation (see sec. 1.4.4) and surgical procedures are helpful in arrhythmia treatment [24, 26]. For instance, reentrant circuits can be mapped and disrupted surgically; and arrhythmias caused by cardiac ischemia often respond to coronary artery bypass.

■ 1.4.3 Device therapy

Permanent artificial pacemakers are used to increase the heart rhythm in patients with bradyarrhythmias. The pacemaker consists of a source of electrical current that is connected to the cardiac muscle by a wire (lead) and is controlled by an integrated circuit. The pacemaker stimulates the heart if it is not generating intrinsic electrical impulses often enough. If a disorder of conducting system present, pacemakers also can be used to coordinate contraction of the atria and ventricles or between ventricles.

In patients with malignant ventricular tachyarrhythmias implantable cardioverter defibrillators are used to deliver a large defibrillating current (shock) in order to terminate the arrhythmia. It is common knowledge that implantable defibrillators have prevented sudden cardiac death in many patients with lethal ventricular arrhythmias [24].

■ 1.4.4 Catheter ablation

One of the most important advance in the electrophysiology field, which happened over the past three decades, is that an **electrophysiological (EP)** study evolved from largely diagnostic therapy to mainly therapeutic one [24]. Currently, many arrhythmias can

be treated by means of catheter ablation techniques instead of potentially toxic drugs or cardiac surgery.

Catheter ablation is an invasive procedure performed during the EP study in a catheterization laboratory. The basic idea behind is using a catheter to destroy pathological tissue or disrupt the pathways required for pathological tachyarrhythmias, and create an electrically inert discrete scar. Obviously, to perform successful ablation it is important to know the precise position of the pathological tissue/pathway, understand the physiology of the involved electrical pathways, have the technology for precise positioning of the catheter, and technology to create a lesion of the desired size at critical location [24].

From the first successful ablation in human in 1982 until 1989, **direct current (DC)** shocks were used for ablation [24]. The electrode catheter was connected to a conventional defibrillator and delivered the shocks of 200–300 J [27]. The shock was delivered between the distal catheter electrode and the surface electrode, which was used as a sink [26]. DC shocks resulted in several forms of potentially damaging energy — heat, light, pressure, and electrical current. Only electrical current energy created desired damage, whereas all the other forms of energy increased the possibility of complications [24]. Therefore, low energy DC shocks (up to 40 J) were used [27]. Also, the DC shocks often created lesions with patchy borders, which were potentially proarrhythmic [24, 28]. Hence, ablation using DC shocks had traumatic nature and limited usage [26]. In the 1990's it was replaced with **radiofrequency ablation (RFA)** [24, 26].

Oppositely to ablation using DC shocks, radiofrequency ablation allowed to create discrete lesions, perform the procedure on conscious patients, terminate lesion formation in case of complication occurrence [26]. Radiofrequency current has the ability to heat the tissue and create hyperthermic injury (lesion/scar) without stimulation of the cardiac and skeletal muscles, avoiding arrhythmia induction and decreasing the pain for the patient [9]. Radiofrequency generators deliver alternating continuous low voltage (typically 40 V) [27] current with a frequency between 300–1000 kHz [7, 26], which causes resistive and conductive heating (Fig. 1.7). Resistive heating damages the tissues in direct contact with the catheter and the conductive heating — the deeper and surrounding tissues. Irreversible damage occurs when myocardial tissue reaches temperatures around 48–50°C. It usually takes 5–20 s to achieve a steady state between current delivery and heat dissipation by tissue and blood [27]. Therefore, the electrophysiological effect is continuously monitored and proper actions can be taken. If the observed change in electrocardiogram is desired, the ablation continues for at least 30 s, otherwise it is disrupted immediately with the hope of avoiding permanent damage. The radiofrequency current is delivered between the tip of the catheter electrode and a large (surface area 100–250 cm²) dispersive/indifferent electrode applied to the skin [29].

There are also other kinds of arrhythmia ablation — microwave energy, laser energy, and cryoablation. Microwave ablation, similarly to RFA, uses thermal energy to create damage. In this case, the tissue heating is achieved by the molecular oscillations of dipoles within polar molecules (such as water) [9, 29]. These oscillations are caused by the electromagnetic field created with the microwave antenna, which can be designed with various lengths (915 MHz–2450 MHz) and pattern of delivering energy. Microwave energy allows performing deeper and more even tissue damage with less surface heating, but requires closer monitoring of lesions [30]. Light amplification by stimulated emission of radiation (laser) produces a monochromatic phase-coherent beam at a specific wavelength [9]. Absorption of the photon energy causes photothermal effect and heats

■ 1.4.5 Treatment of the PVCs

For many years wrong assumption existed that anti-arrhythmic drug therapy can improve the risk of sudden death associated with PVCs [22, 32]. However, numerous clinical trials [33–36] examined this question and showed that it is not appropriate to treat patients with AAD for the purpose of improving the patients' survival [22, 37]. But, in symptomatic patients AAD can be used and an appropriate choice of the AAD depends on the patient's clinical condition [22]. For example, to reduce symptomatic PVCs in patients with prior myocardial infarctions or heart failure beta-blockers could be used (because of the significant improvement in survival they impart to these patients) [22].

In case of high frequency PVCs or if they are symptomatic and do not respond to pharmacological treatment, they are indicated for catheter radiofrequency ablation according to the ESC2015 ESC Guidelines for the management of patients with ventricular arrhythmias and the prevention of sudden cardiac death [38–39]. According to the guidelines, radiofrequency ablation is recommended for three groups of patients:

1. patients with symptomatic PVC;
2. symptomatic or asymptomatic patients with frequent PVC plus left ventricular dysfunction;
3. asymptomatic patients with very frequent extrasystoles (more than 20%), to prevent the development of left ventricular dysfunction. Following successful catheter ablation, the symptoms of PVC disappear and in patients with decreased ejection fraction, the function of the left ventricle can normalize [40–42].

Accurate localization of the PVC focus is the most important factor for the success rate of the ablation that reached 77% in a long-term follow-up [43]. The anatomical origin of PVCs can be anywhere in the ventricles and adjacent structures with a predominant location in the right and left outflow tracts. Less common PVC foci locations include the myocardium around the aortic (Valsalva) sinus, aortic cusps, the region between the aortic and mitral valves (the aortomitral continuity), and the region of coronary sinus [44]. Approximately 70% of them are in the RVOT [45]. Several algorithms have been developed to determine the site of PVC origin using a 12-lead ECG [46], however, even the best algorithm has only 90% positive predictive value. This means, that in 10% of patients intracardial mapping procedure is prolonged jointly with longer fluoroscopy time.

Therefore, noninvasive localization of the position of the ectopic focus would accelerate and simplify intracardial mapping.

■ 1.5 Measurement of the cardiac electrical field

Cardiac electrical field can be measured invasively using intracardial catheters or noninvasively using electrodes placed on the body surface. Signals obtained from invasive intracardial measurements are referred to as *intracardiac electrograms* (see sec. 1.5.1), and signals measured noninvasively on the body surface are called **electrocardiograms (ECGs)** (see sec. 1.5.2, 1.5.3).

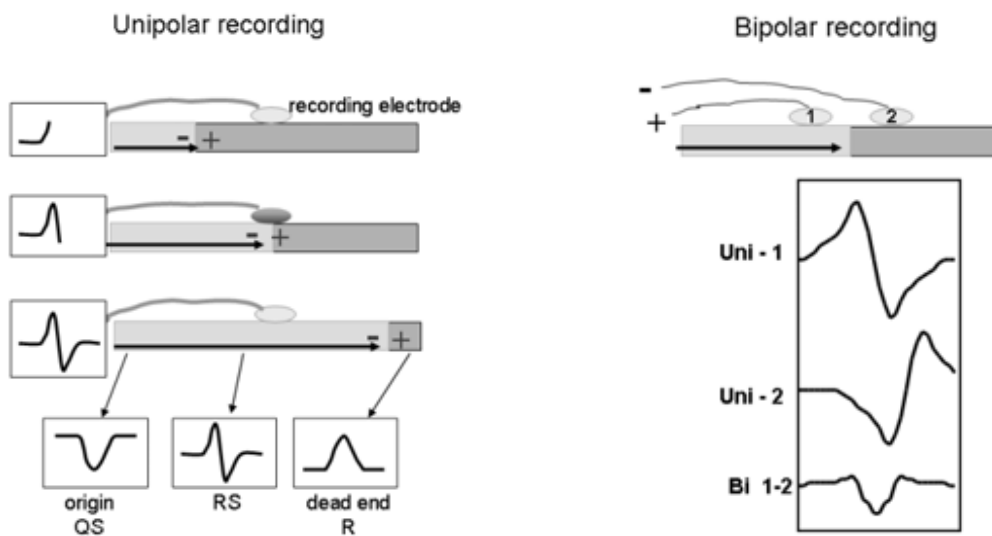
■ 1.5.1 Intracardiac electrograms

The electrical activity of the local cardiac tissue recorded by the electrode catheter is called *intracardiac electrogram*. As was mentioned before in sec. 1.2.2, the cardiac action potential reflects cardiac activation and majority of the electrical activity is generated within individual myocardial cells and some net charge flow in the extracellular space.

In general, clinicians are interested in the rapid depolarization phase (phase 0) of the cardiac tissue [9].

In order to record an electrogram, two electrodes are used. One is positive and one is negative. Electrogram is derived by subtraction of the information at the negative electrode from the information at the positive electrode. Intracardiac electrograms can be divided into *unipolar* and *bipolar recordings*.

Unipolar recordings use one electrode in the heart and a reference electrode, distant from the heart (Fig. 1.11a). One of the ways to create a reference electrode with zero potential is by using a driving reference. It means that input at one electrode is summarized with its inverse signal, resulting in a zero potential (Fig. 1.12). Unipolar recordings provide information about the direction of impulse propagation. The major disadvantage of unipolar recordings is that they contain substantial far-field signals generated by depolarization of tissue remote from the recording electrode [9].



(a) Unipolar recording. From the top schematic, as the wavefront propagates toward the electrode a positive deflection, an R wave, is inscribed. As the wavefront propagates past the recording electrode, an S wave is inscribed and thus an RS complex occurs (middle schematic). Recording from the initial site of depolarization (origin at the left side of the tissue) produces a QS complex as the wavefront moves away from the recording electrode. Recording at the right side of the tissue (dead end) produces a monophasic R wave

(b) Bipolar recording. Electrode 1 is connected to the positive input of the amplifier and electrode 2 is connected to the negative input. Electrograms created by a mathematical simulation are shown below the schematic. Compared to the signal from electrode 1 (Uni-1), the signal from electrode 2 (Uni-2) is slightly delayed (because the wavefront reaches it later) and is inverted because it is attached to the negative input of the recording amplifier. Adding these two signals together generates the bipolar signal (Bi 1-2) that removes much of the far-field signal

Figure 1.11: Generation of the unipolar and bipolar recordings. Horizontal bars that represent a sheet of myocardium with depolarization propagating from left to right (arrow). The potential in front of the wavefront is positive and that behind the wavefront is negative, generating a vector that points toward the positive potential. Electrodes resting on the tissue are shown as grey circles. Theoretical electrograms are shown in boxes. From [47]

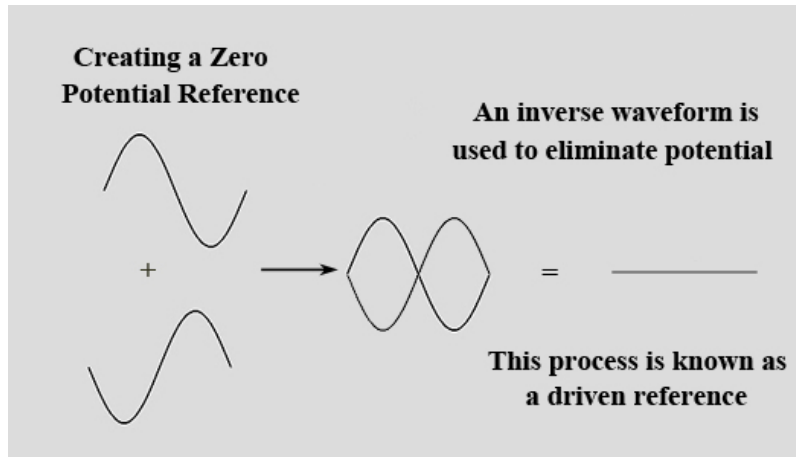


Figure 1.12: Creating zero potential using driving reference

Bipolar recordings use two electrodes located in the area of interest (Fig. 1.11b). The bipolar recording is generated as a summation of the potential at the positive electrode and inverted potential of the negative electrode. Bipolar electrograms obtained from the catheter with small interelectrode distance are almost unaffected by the far-field.

Unipolar electrograms provide information regarding the local and distant electrical activity (which are decreasing in proportion to the square of the distance from the electrode). Bipolar electrodes provide information only about local activity and are sensitive to the direction of the activation front [48]. Therefore, intracardiac electrogram provides precise, localized data on the heart's electrical impulse [24]:

- the time of the activation (local activation time) of the myocardium bordering with the recording electrode relative to the reference;
- direction of the propagation of the electrical impulse;
- complexity of the myocardial activation within the field of view of the recording electrode.

1.5.2 Standard 12-lead electrocardiogram

The method, which is widely used in the clinical practice thanks to its quick, simple, harmless, noninvasive procedure and diagnostic efficiency is called electrocardiography and uses 12-lead ECG. Surface ECG represents the electrical activity of the entire heart. It is the sum of all of the action potentials of all of the cardiac cells. Thus, an ECG provides information about the sequence of cardiac depolarization and repolarization across the entire heart [49].

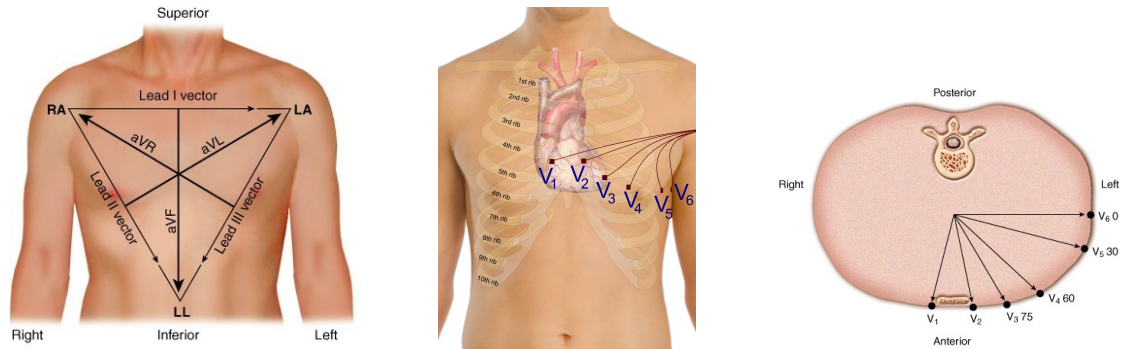
To record standard ECG, the electrodes are placed on the limbs and chest (Fig. 1.13). Standard leads are denoted I, II, III and are obtained by measuring the difference between electrodes placed on the arms and left leg (*right arm (RA)*, *left arm (LA)*, *left leg (LL)*) in the following combinations:

$$I = LA - RA \quad (1.1)$$

$$II = LL - RA \quad (1.2)$$

$$III = LL - LA. \quad (1.3)$$

Standard leads form a triangle with a heart in its centre. Besides the bipolar leads, the 12-lead ECG method also includes unipolar leads: *augmented limb leads* and *precordial*



(a) Torso model in frontal view with limb electrodes: right arm (RA), left arm (LA), left leg (LL)
 (b) Torso model in frontal view with chest electrodes (V_1 – V_6)
 (c) Torso model in superior view with chest electrodes (V_1 – V_6)

Figure 1.13: Placement of the ECG electrodes on the torso

leads. Augmented leads are obtained from the limb electrodes using the Goldberger's central terminal for the reference [49]. Using the Goldberger's central terminal as a negative pole is a combination of the two voltages from the other two limb electrodes. *Augmented* voltages of the *right arm* (aVR), *left arm* (aVL) and *leg* (aVF) can be obtained using the following equations [50]:

$$aVR = RA - \frac{LA + LL}{2} \quad (1.4)$$

$$aVL = LA - \frac{RA + LL}{2} \quad (1.5)$$

$$aVF = LL - \frac{RA + LA}{2}. \quad (1.6)$$

In order to represent the electrical activity of the heart in the frontal plane, six unipolar precordial electrodes are used (Fig. 1.13b, c). The V_1 – V_2 electrodes represent information in the anterosseptal region of the heart, V_3 – V_4 in the anteroapical and V_5 – V_6 in the anterolateral accordingly. The precordial electrodes are measured relative to **Wilson's central terminal** (**WCT**), which is an average of the potentials of the three limb electrodes:

$$\text{WCT} = \frac{RA + LA + LL}{3}. \quad (1.7)$$

The ECG waveforms represent the depolarization and repolarization of the heart (Fig. 1.14), where the depolarization of the atria is reflected by the **P wave**, depolarization of the ventricles by the **QRS complex**, repolarization of the ventricles by the **T wave** and sometimes also **U wave** (Fig. 1.15). Atrial repolarization is obscured by the much larger QRS complex; thus, it is not typically visible as a discrete event in the ECG. The duration of the wave is defined by the two time instants at which the wave crosses the baseline or significantly deviates from it [50].

Since this work will be focusing on the pathological premature ventricular activity, it is important to mention that generally, the ventricular activity during ectopic firing is easily distinguished in the ECG by the presence of a premature broad QRS complex, generally with QRS duration ≥ 120 ms without a preceding P wave (Fig. 1.16).

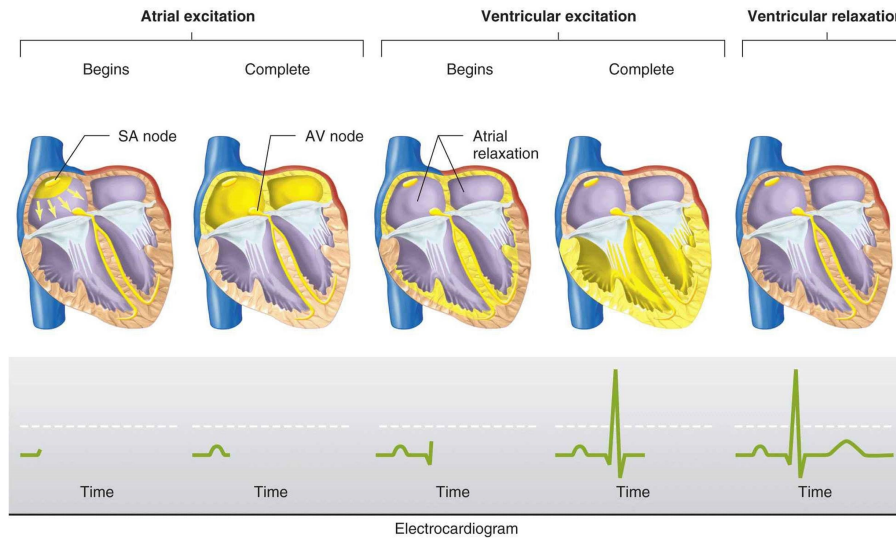


Figure 1.14: Electrocardiogram represents the depolarization and repolarization of the heart

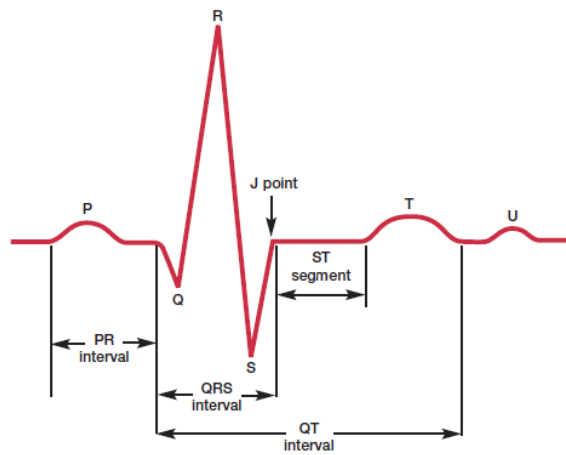


Figure 1.15: The basic pattern of the normal ECG signal. From [51]

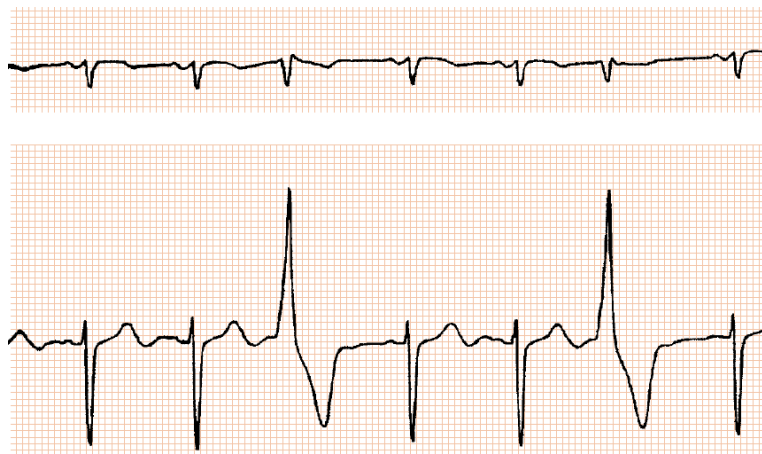


Figure 1.16: Simultaneous recording of leads V_1 (upper graph) and V_2 (lower graph). The third and sixth beats are unifocal PVCs. Their ventricular origin is not apparent in lead V_1 but is obvious in V_2 . From [52]

■ 1.5.3 Multichannel ECG

Besides the clinically widely used standard 12-lead ECG, also systems that contain a higher number of electrodes distributed on the patient's torso are used especially for experimental and research purposes. After the pioneering work of Taccardi [53], many research centers around the world became interested in the simultaneous recording of multichannel electrocardiograms that enabled detailed representation of the electrical potential distribution on the torso using **body surface potential (BSP)** mapping techniques discussed in more detail in section 1.6.2. The possibilities of the research groups that used the sequential measurement of few leads and manual map construction were limited until the late 1960s when the mini computers were invented and could be used for automated simultaneous multilead ECG recording, fast data processing, and easy displaying of obtained maps [4]. Almost each research group has developed its own mapping system, what resulted in wide diversity between the measuring systems, used numbers of leads, electrodes locations on the torso and the way of their organization (individual electrodes, strips or vests with electrodes), methods of signal processing, analysis and interpretation of results and evaluation of errors.

Since little was known on the spatial variability of the surface potentials and, mapping systems starting from technically feasible 24 electrodes up to 219 electrodes covering the whole torso were developed and tested in order to obtain as much information on the potential distribution as possible [54–56]. Some developed lead systems ordered according to increasing number of electrodes are presented in Fig. 1.17. The number of leads for each of the lead systems is given in brackets.

Generally, in BSP map the torso surface is displayed as a rectangle representing an unfolded elliptical cylinder constituting the human torso model. The height of the rectangle usually extends from the jugular or suprasternal notch to umbilicus [55]. Electrode positions are usually marked by individual points or points in strips or grids. Their number and placement have a direct influence on data processing. Lead systems with a large number of electrodes evenly covering the whole surface of the torso are called *full systems* and simple bilinear or spline interpolation is usually used to construct the potential distribution in the map. Lead systems with a small number of electrodes, usually with irregular electrode placement are called *reduced systems*. They use mostly advanced interpolation methods based on analytical functions approximating the potential changes between the electrodes or a priori information on the correlation between torso potentials obtained from full lead measurements [55].

The impracticality of the time-consuming electrode application and hardware expenses limited BSP mapping in fact to research purposes and it was not implemented in clinical daily routine. It is obvious that a higher number of electrodes provides more detailed information about the distribution of the electrical potential on the torso [57]. Nevertheless, it is important to keep the method convenient in usage and tolerable for the patients. An ideal number of mapping electrodes should fulfill the demands of clinical practice that requires low cost, minimal time and effort for their application and maximum of useful diagnostic information of the body surface potential distribution. That is why some systems used strips or vests (in order to decrease the time of electrode placement).

Last year a commercial system CardioInsight Noninvasive 3D Mapping System (Medtronic) [58] received permission in the USA to be used in clinical practice. This system uses a vest of 252 electrodes, which is presented in Fig. 1.18.

The possible influence of the lead system on the accuracy of the potential field representation as well the impact of electrode displacements on the map patterns was

extensively studied both, in models and experiments, in normal subjects and in patients.

One of the first studies on the selection of the number of measuring electrodes [59] showed that 24 properly located electrodes selected out of a grid of 150 (10×15) are enough to describe body surface potential distribution to an acceptable degree of accuracy. However, the authors recommend to extend this number for clinical practice. It is obvious that due to the specificity of the individual patient torso geometry, heart position and orientation, the optimal position of electrodes can vary between the patients and affects the number of required leads. Therefore, mapping systems with a higher number of measured leads might be recommended to obtain a more precise description of the individual body surface potential distribution. However, an evaluation by Lux et al. [60–61] showed some redundancy in the ECG measured by cumbersome mapping systems with 100–200 electrodes and suggested 32 lead system with optimal placement of the electrodes for practical clinical diagnostics. Later, the same research group proposed a sequential algorithm for optimal recording sites selection and confirmed that 32 leads are sufficient for diagnostically acceptable reconstruction of the body surface potential distribution [62]. Nevertheless, the study highlighted that suggested configuration of the lead system was optimized only for capturing of the signal information and was not considered as best diagnostic information.

Besides the analysis of the impact of the electrode number and position, it was also shown in a computer model how the electrode displacement can cause substantial changes in the map patterns [56].

A detailed overview of the most cited works regarding the selection of the number and positioning of recording leads based on the signal or diagnostic information criteria is given by Donnelly et al. [63]. A comprehensive description of the research studies performed by Kornreich during more than 20 years highlighted the complexity of the issue to define optimal number and placement of the recording leads.

■ 1.6 Mapping of the cardiac electrical field

■ 1.6.1 Intracardial mapping

In order to obtain a general understanding of the activation sequence in the heart or selected chamber, a methodology of cardiac electrical mapping is performed by recording intracardiac electrograms (see sec. 1.5.1). Initially, this method was used in order to understand the normal heart activation, but later it was more used to study the underlying pathophysiological mechanisms of the arrhythmias, their initiation, and sustenance [7]. Conventional cardiac mapping techniques can be divided into [30, 48]:

1. Activation sequence mapping

defines the localization of the earliest electrical activation (the time difference between the onset of the signal on the mapping catheter and the onset of PVC on a 12-lead ECG should be the longest). This technique is highly used for ablation of focal arrhythmias [30]. Usage of the electroanatomical mapping systems allows creating color-coded activation maps.

2. Pace mapping

compares the morphology of the paced P wave or paced QRS complex (in sinus rhythm) with the morphology of the complex during tachycardia in all ECG leads. If they have an exact match, it is presumed that the pacing was performed from the location of the arrhythmia origin.

3. Entrainment mapping

is usually used to define the characteristics of the reentrant circuit. Entrainment mapping continuously resets the reentrant circuit. It is possible if the reentrant circuit has an excitable gap at each point of the circuit, which is defined by the time between the recovery from the last depolarization and the time of arrival of the next excitation wavefront. Shortly, the method checks whether the applied stimulus or train of extrastimuli are inside or outside of the reentrant circuit.

4. Miscellaneous pacing procedures

In order to determine the mechanism of arrhythmia, a useful maneuver is to perform atrial or ventricular pacing during the sinus rhythm or tachycardia.

5. Voltage mapping and fractional local electrogram

determine the amplitudes of the local electrocardiograms in the heart cavities. In order to perform voltage mapping, electroanatomical 3D mapping systems are used to distinguish the viable regions from the scar in the presumed reentry circuit.

Cardiac mapping is the bedrock of the radiofrequency ablation and intracardiac intervention. Spatial information about anatomical structures combined with electrophysiological information from the electrograms is crucial for successful ablation. For this purpose alternative cardiac mapping systems were developed. Long before these systems were elaborated, an article by Idecker et al. [64] stated four assumptions for construction and use of the isochronal cardiac maps, which should be fulfilled by cardiac mapping system in order it to be used for diagnostic purposes. “These assumptions include the following:

1. the location of the recording electrodes is known with sufficient accuracy to determine the mechanism of an arrhythmia or to guide therapy;
2. a single, discrete activation time can be assigned to each recording electrode location;
3. the presence or absence of activation at an electrode site can be reliably ascertained, and when activation is present, the time of activation can be determined with sufficient accuracy to specify the mechanism of an arrhythmia or to guide therapy;
4. the recording electrodes are close enough together that the activation sequence can be estimated with sufficient accuracy to determine the mechanism of an arrhythmia or to guide therapy.” [64]

There are two types of the cardiac mapping systems: *sequential mapping systems* and *continuous mapping systems* [7]. The sequential mapping system collects electrophysiological information from the tip of the catheter simultaneously with the tip location point by point. This allows to create a 3D surface geometry, representing the studied chamber and depict the electrical activation of the heart [65]. Therefore, these sequential systems CARTO™(Biosense Webster) [66], LocaLisa®(Medtronic) [67], Realtime Position Management (RPM™, Boston Scientific) [68], and NavX System (Endocardial Solutions) [69]) are also referred as *electroanatomical*. Continuous mapping systems use basket mapping [70] and noncontact catheter mapping [71] with many simultaneously recording electrodes to obtain the global information about the rhythm from one or two cardiac beats. These systems are ideally suited for mapping complex and poorly tolerated arrhythmias (e.g. infarct-related VT).

Electroanatomical mapping systems and noncontact mapping systems provide following advantages [30]:

- global view of the activation;
- nonfluoroscopic catheter navigation;

- precise tagging of the ablation sites and ability to renavigate ablation catheter to the sites of prior current application or close to it.

Limitations of the sequential mapping lie in the assumption that the impulse spreads in exactly the same way during each heartbeat. Therefore, it is not applicable in patients with complex arrhythmias and during rapid electrophysiological changes as those associated with ischemia and reperfusion [72].

Noncontact mapping systems also have limitations. The multielectrode array might be difficult to position in the left atrium or in ventricles [30]. For distances greater than 4 mm virtual electrograms deteriorate and require multielectrode repositioning. The system has difficulties to delineate borders of activation zones not bordered by anatomic structures. Noncontact mapping also does not reliably identifies ventricular scarring. A detailed comparison of the cardiac mapping systems is given in Tab. 1.1 [73].

Over the past few years, the technology has evolved allowing integration with CT and MRI data sets [65]. CARTO-UNIVU™ (Biosense Webster) integrates electroanatomical mapping and live fluoroscopy into a single view [74]. A comprehensive review of the electroanatomical mapping systems and their development is given in [74].

■ 1.6.2 Body surface potential mapping

One of the novel noninvasive methods for cardiac diagnostics is body surface potential mapping. As it was already mentioned in sec. 1.5.3, this method uses multichannel ECGs records from the torso surface to obtain significant physiologic and prognostic information [4, 72, 75].

A detailed comparison of ECG and BSP mapping is given in Tab. 1.2 [76]. Among valuable advantages of the BSP mapping compared with 12-lead ECG are:

- possibility to explore entire chest surface potential distribution and provide all the information on the cardiac electric field available at the body surface;
- higher sensitivity of the local electrical activity (ventricular recovery heterogeneities or local conduction disturbances);
- besides temporal and amplitude values has additional spatial component, whereas the 12-lead ECG scalar waveforms only present the voltage variation in time at a given site.

On the other hand, disadvantages of the BSP mapping include [77]:

- **Technical aspect:** time-consuming application of a large number of electrodes on the thoracic surface and the collection of large amounts of data for further processing and analysis.
- **Clinical aspect:** perception by medical staff that other techniques (echocardiography, radionuclide imaging, CT-scan, SPECT, PET, Doppler, etc.) provide more useful or more accurate clinical information.
- **User-friendliness:** novel data representation — unfamiliarity of physicians and cardiologists with the new methodology — map format of body surface potential representation.

BSP mapping is a technique with controversial demands. Nevertheless, it allows receiving more information from body surface potential electrodes, the procedure is noninvasive and nonfluoroscopic, and can provide highly useful diagnostic information without substantially loading the patient. In comparison with the invasive intracardiac electrophysiological study, the BSP mapping does not introduce additional risks for the patient such as bleeding, damage of the vessel, infection, perforation of the heart etc.

Feature/Mapping System	Catheter localization system			
	CARTO	EnSite	NavX	RPM
				LocalLisa
Replicates anatomy without distortion	+++	++	++	++
Multiple chamber/structure rendering (simultaneous)	+++	-	++	-
Pulmonary vein, superior vena cava/inferior vena cava display	Rendered anatomy or pulled tubes	Cut outs/juxtaped spheres	Cut outs/juxtaped spheres	-
Esophagus annotation	No	Direct localization	Direct localization	+
Interstructure delineation without interpolation obliteration	++	Fixed points required	Fixed points required	No surface geometry
Spatial accuracy (mm)	1	< 1	< 1	2
Temporal accuracy (sampling rate)	0.1 K	1.2 K	1.2 K	3 K
Simultaneous onscreen map view windows	2	2	2	2
Virtual cardioscope views	+++	+++	+++	+
Ease of map display user interface	+++	++	++	++
“Transparency”view	No	Yes	Yes	Yes
Activation time mapping	+++	++	++	+++
Voltage mapping	+++	+++	+++	+
High-resolution electrogram mapping.	+	+++	+	+
Nonsustained AT/VT-APC/VPC mapping	With effort	+++	With effort	With effort
Unstable AT/VT mapping	No	+++	No	No
Robust intervention annotation (abl. dots)	+++	+++	+++	+++
Detection of low-amplitude signals	+++	+++	+++	+++
Repolarization mapping	+	+++	No	-
Mapping using alternative signal content	In development	In development	In development	No
Mechanical/contraction mapping	Yes NOGA	No	No	No
Preablation map-based intervention planning	+++	+	+	No
Click and point electrogram recall	+++	+++	+++	No
Catheter tip/tissue contact visualization	+++	++	+	++
Multiple chamber mapping (synchronized)	+++	-	++	-
Geometry “learning”during mapping and ablation	+++	+	+	-
Ablation catheter use	Specific	Any	Any	Any
Navigation/electrograms during ablation	Yes	Yes	Yes	Yes
Respiratory compensation	+	+++	+++	No
Simultaneous electrode recordings	26	Array +4	64	? N/A

Table 1.1: Comparison of three-dimensional mapping systems. From [73]

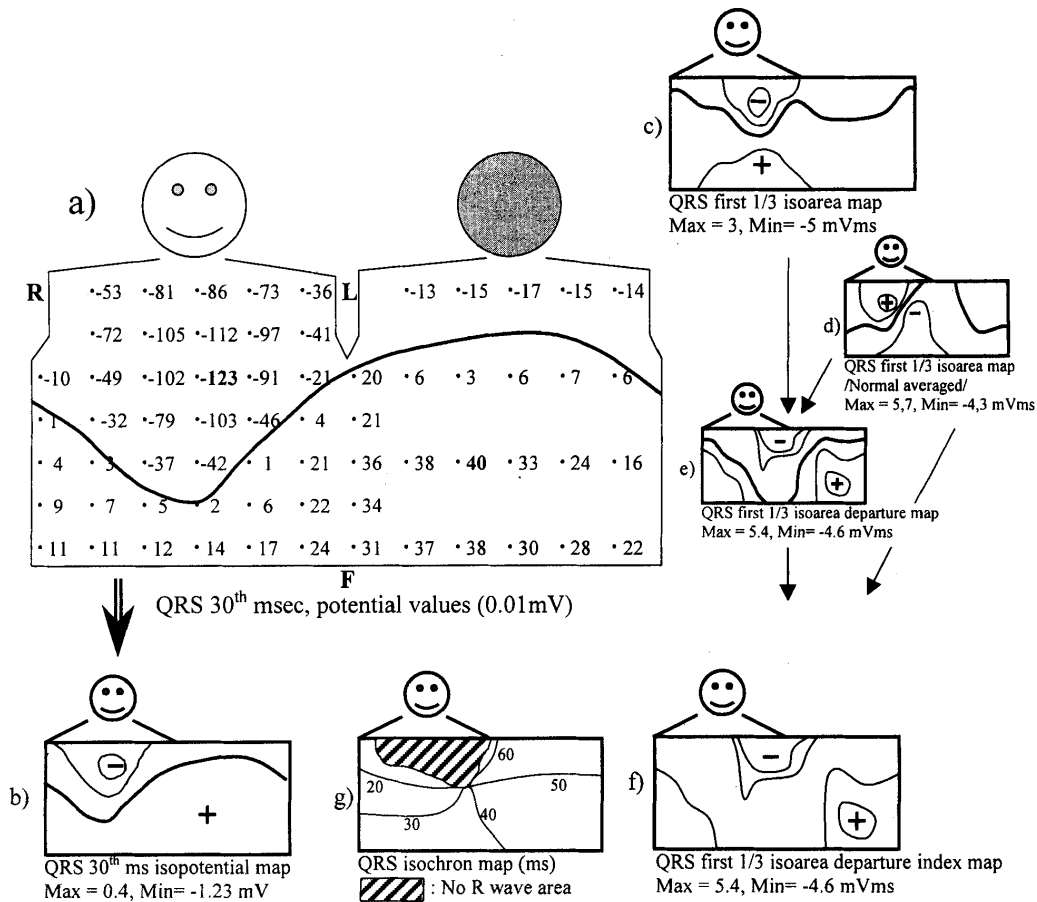


Figure 1.20: Presentation of various map-types in a schematic form (old anterior infarction, using the Montreal configuration). (a) potential values on the sites of the electrodes at the 30th ms after QRS onset; (b) the corresponding isopotential map/instantaneous or time instant BSP map (TIBSPM); (c) isoarea map or integral BSP map (IBSPM) of the first 30 ms of the QRS from the same patient; (d) averaged isoarea map of the first 30 ms of the QRS in normal group (24 patients) for computation of departure maps; (e) isoarea departure map of the first 30 ms of the QRS (c–d); (f) isoarea departure index map of the first 30 ms of the QRS (like “e” but only those sites are assigned, where the difference is more than 2 SD of the normal group); (g) isochrone map during the QRS also from the same patient. In (b–f), the maximum and minimum values are given and their location is indicated by a + or a – sign on the map. Difference between isopotential lines in (b): 0.5 mV; the difference between isoarea lines in (c–f): 2.2 mVms. From [76]

1.7 Modelling of the cardiac electrical activity

Living organisms are functioning based on cross-correlating mechanisms and therefore not all measurements can be performed during the experiment. In order to study dependences, interactions, mechanisms, and behavior in the living organisms, hypotheses are checked on the simplified mathematical models. Models are adjusted to represent the experimental measurements and controlled by the basic science laws [1].

Mathematical models of physiological bioelectrical processes are usually constructed to perform experiments, which are not possible to conduct with living tissues. They contain some simplifications and assumptions, but they are required to accurately represent the natural behavior [1, 86].

The ECG record represents the electrical activity of the internal bioelectrical source, but does not provide its unique specification as different electrical sources might generate the same distribution of the electrical potential on the body surface. Forward (see sec. 1.7.1) and inverse (see sec. 1.7.5) problems help to understand the processes of cardiac electrical activity more deeply from qualitative and quantitative points of view.

Modelling of the cardiac electrical field in the heart (or on its surface) and on the body surface and its relation with the sources is known as the *forward* and *inverse problem of electrocardiography* (Fig. 1.21) [1]. The forward problem determines the electrical field from the known source and conductor. Whereas the inverse problem determines the source from the known field and conductor.

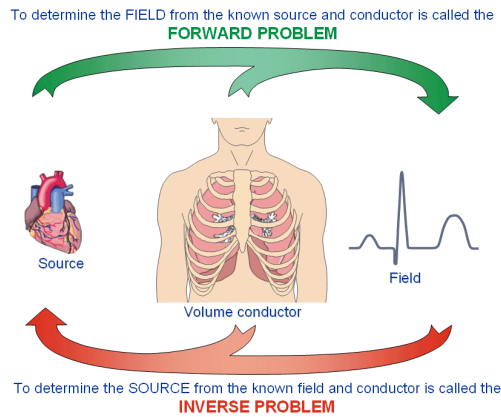


Figure 1.21: Schematic principle of the forward and inverse problems of electrocardiography. From [1]

The forward problem has a unique solution whereas the inverse problem mathematically has several solutions [87–88]. Hermann von Helmholtz firstly described this fact in the theoretical paper in 1853 [89].

In order to solve the forward and inverse problem, several assumptions are accepted. The electrical activity of the heart is represented by equivalent electrical source (see sec. 1.7.2) and since the body is a three-dimensional conducting medium, it is referred to as a volume conductor (see sec. 1.7.3).

■ 1.7.1 Forward problem of electrocardiography

The forward problem has fundamental role as it must grasp and describe the relationship between the electrical sources and distant cardiac bioelectrical activity [4]. A complete forward solution would include information from the scale of ion-channel protein to the complete human thorax, and from nanosecond to minutes or even hours of time [4]. Thus, the multiscale nature of the problem and constraints of the computational resources requires a division of the problem into several components [90]:

- cellular electrophysiology (protein membrane biochemistry, genetics, pharmacological impact, kinetics of membrane ion currents),
- tissue level (cell-to-cell coupling, tissue structure modelling, activation sequence),
- organ level (heart geometry, tissue types, heart activation sequence),
- whole body level (geometry and structure of the thorax, electrical field in volume conductor).

Generally, the forward problem of electrocardiography can be expressed using a matrix formulation [91]. Discretization of the electric source strength of N generator

elements at T subsequent time instances, produces a matrix \mathbf{S} , which represents the entire source with elements $s_{n,t}$, $n = 1 \dots N$; $t = 1 \dots T$. Similarly, effect of the volume conductor might be represented by a transfer matrix \mathbf{A} with $a_{l,n}$ elements, where each element represents the potential in the lead l generated by a unit source element n of unit strength. Therefore, the computation of the forward problem can be represented by matrix multiplication:

$$\Phi_{[L \times T]} = \mathbf{A}_{[L \times N]} \cdot \mathbf{S}_{[N \times T]}, \quad (1.12)$$

where

$\Phi_{[L \times T]}$ — represents potentials at L lead positions at T discrete time instants. The matrix formulation of the forward problem can be viewed as a mapping of the information about the heart sources onto the images on the body surface [91].

Forward problem was solved using various approaches [87, 92] in simulation [93–95], animal [96–98] and patient studies [93, 99–101]. The latest revision of the conducted studies is presented in [86, 102–103].

■ 1.7.2 Source models

There are various source models, which can be used to represent the electrical activity of the heart: discrete source models (dipole, moving dipole, multiple dipoles and multipole), epicardial potentials, uniform and equivalent double layer models [1, 4, 92].

A huge advantage of the discrete source models of the heart is the small number of parameters required for the source description, which results in simplicity of the associated forward (and inverse) problems. The biggest disadvantage of the discrete source models is the absence of clear physiological and physical links between the discrete sources and true sources (that they represent) or any directly measurable quantities [4].

■ Dipole

The simplest and the best-known model of the cardiac electrical generator is a single dipole [91]. This model is defined by a single dipole moment with fixed location and variable orientation and magnitude. Therefore, the dipole has three independent components: in Cartesian coordinates it is $D_x; D_y; D_z$ and in spherical coordinate system it is the magnitude D and two direction angles θ and ϕ [1]. This model is used in vectorcardiography as an equivalent generator during the QRST interval to analyze the trajectory of the electrical depolarization and repolarization [4, 104]. In spite of its simplicity, dipole model is widely used in solving forward and inverse problems.

■ Moving dipole

Moving dipole model means that the dipole can have variable location at different time instants. It has three variables defining the location and three variables defining the dipole moment itself. Therefore, it has six independent variables in total [1, 105].

■ Multiple dipoles

The heart volume with electrical sources can be divided into smaller regions and each region can be represented by a dipole. The dipoles are in fixed positions and have varying magnitude and orientation. Therefore, if the number of dipoles is N , then $3 \times N$ independent variables are necessary to characterize the multiple dipole. If the orientation of the dipoles is fixed, then each dipole can be characterized by only one independent variable — the magnitude [1, 87].

■ Multipole

Multipole is an expansion of the dipole model, formed by higher orders of monopoles [1, 91, 106]. While the dipole is formed from two equal and opposite

monopoles, the quadrupole is formed by two equal and opposite dipoles. Continuing adding the source configurations in this way a higher order source can be formed. The multipole is described by the coefficients as well as the dipole. The dipole, as it was already mentioned, is characterized by three coefficients; the quadrupole can be defined using five coefficients, an octopole by seven, and so on [1, 91, 107–108].

■ Epicardial potentials

The model describing the equivalent cardiac generator as electric potentials on the surface of the epicardium is based on the theoretical unique one-to-one relationship between the voltage on the cardiac surface and voltage on the outer body surface [87, 91]. The following preconditions should be met: the internal surface should be closed and no primary sources should be present between the cardiac and body surfaces, assuming that all the representing sources are lying within the internal surface [4]. In this model only the outer epicardial surface is taken into account, therefore there is no need in the exact knowledge of the inner heart geometry or impact of the intracardiac blood masses [4]. A significant benefit of this model is the possibility of the experimental validation. The epicardial potentials can be measured during the open chest surgery or in the studies with animal hearts placed in the electrolytic tanks [109].

■ Uniform and equivalent double layer models

The source model based on the two assumptions of elementary dipoles lined up with the direction of the wavefront propagation and having uniform strength is known as the **uniform double layer (UDL)** [4]. This model is restricted to describing the major sources during depolarization only [91].

An extended variant of the UDL uses current sources of the double layer type and is referred as **equivalent double layer (EDL)** model [4]. It represents the depolarization wavefronts in the myocardium using surfaces carrying elementary current dipoles and separating the resting (polarized) and excited (depolarized) regions. This model has the potential of describing the cardiac electrical generator during the depolarization phase as well as during the repolarization phase of the cardiac cycle, both in the manner that is related to the underlying electrophysiology [4]. There is a direct link between the UDL and EDL source model, which is based on the solid angle formulation of body surface potential description caused by the cardiac electrical activity [110]. EDL model was highly used to explain the ECG waveforms [91].

■ Bidomain model

Besides abovementioned source models, it is important to mention another technique used for the description of the cardiac activity — *bidomain model*. The actual structure of myocytes connected to each other by gap junctions, forming branching and intertwining muscle fibers embedded in an interstitial fluid and interspersed with capillaries and other structures, is abstracted by two continuous domains. There are the *intracellular domain*, representing the myocytes and gap junctions, and the *extracellular domain*, representing all other tissue components. Each domain is characterized by an electrical conductivity that is greater along than across the fibers and changes from place to place, to account for the variable fiber orientation in the heart. The two domains are coupled through the cell membrane [4, 111]. The membrane includes the ionic channels, which are represented by voltage- and time-dependent currents, that generate action potential within the cell. The currents flowing from the extracellular space into extramyocardial volume conductor ultimately form BSP on the torso [4].

This enables to investigate not only the effect of the drugs on cellular electrophysiology, but on action potential propagation, and arrhythmia. Special notice should be given to the point that the bidomain model allows simulating the application of external stimuli and defibrillation currents because it distinguishes intracellular and extracellular current flows. The bidomain model developed by Potse et al. [112] consists of 12 million cells and allows to consider not only anisotropy, but also rotating fiber direction, early activation times of the specialized conduction system.

The bidomain model has been used in the most biophysically detailed approach for ECG computation [113]. Despite technological improvements in computers and modalities of the parallel processing over the last twenty years it still takes too long time in order to simulate a single heart beat with such model. This fact complicates the possibility of the implementation of this method in clinics [100, 113].

A simplified bidomain model, referred as *monodomain model*, sets extracellular potentials to zero and was shown to be good enough compared to the bidomain model for propagation studies and computation of the full cardiac cycle [112].

■ 1.7.3 Modelling of the torso volume conductor

In practice, in order to solve the forward (see sec. 1.7.1) or inverse problem (see sec. 1.7.5) of electrocardiography usually it is necessary to use numerical methods (see sec. 1.7.4). Generally, these methods require a discrete description of the torso geometry, which is achieved by segmentation of scans from imaging modalities and results in mesh generation. Mesh generation usually starts with surface representation based on triangles or quadrilaterals [4]. Depending on the numerical method, the resulting mesh will be either a surface or volume mesh [86].

There are two types of the torso models depending on the level of volume conductor complexity. If the torso model has the same conductivity between the heart and body surface, then this model is *homogeneous*. If the torso model includes various regions with different conductivities, then the volume conductor is described as *inhomogeneous*. The electrical conductivity of the selected region in the model can be constant (*isotropic*) or can vary with the direction (*anisotropic*) [1].

The human heart is filled with blood, which has high conductivity, and the myocardium itself has about one-third conductivity of the blood. The heart is located between the lungs, filled with air, and therefore region with low conductivity. The lungs are surrounded by the high conductivity skeletal muscle layer, which in turn is surrounded by the low conductivity subcutaneous fat [1, 114]. It is obvious that the electrical field of the heart will be modified on the outer body surface after passing the regions with different conductivities due to the secondary sources, which appear at the interfaces between these regions [114].

Simulation study of the torso inhomogeneities effect on the body surface potentials was performed by Gulrajani [115] using realistic heart and torso models. Simulations were performed for four torso models:

1. homogeneous;
2. with muscle layer;
3. with muscle layer and lungs;
4. with muscle layer, lungs, and blood masses.

They confirmed that inhomogeneities of the torso model does not change the general pattern of the potential distribution and tend to smooth out the activation details. Therefore, the effect of the blood masses will override the effect of the muscle layer and

biological imaging (see sec. 1.7.6) and main anatomical parameters of the heart (size, it's position and orientation) provide feasible results of the inverse solution.

Evaluation of the cardiac phase and torso inhomogeneities impact on the reconstruction of the body surface potentials was evaluated in [132]. It was shown that cardiac phase did not have significant affect on the reconstruction performance, whereas the difference in torso conductivities (homogeneous/inhomogeneous) did. Ramanathan concluded in [133] that in clinical application it is not necessary to include torso inhomogeneities in noninvasive electrophysiological imaging, but Zemzemi showed in [134] that using inhomogeneities in combination with low noise ECGs improves the accuracy of the inverse solution. Attempt to define ST-elevated myocardial infarction area using 12-lead ECGs and gender-dependent generalized torso model was performed in [135]. It was shown, that accurate patient-specific model is required to obtain a correct inverse solution, which corresponds with [136]. Summarizing, it is fair to say that the problem of the impact of the torso model complexity on the accuracy of the inverse solution remains open.

■ 1.7.4 Numerical methods

Most bioelectric field problems can be formulated in terms of either the Poisson or the Laplace equation for electrical conduction [137]. Numerical methods are used to solve the governing equations written in the form of ordinary and partial differential equations, approximately [4]. These are **boundary element method (BEM)**, **finite difference method (FDM)**, **finite element method (FEM)** and **finite volume method (FVM)** [137–138].

BEM assumes that different torso regions have isotropic conductivities and takes into account only the boundaries between different torso regions. FDM, FEM, FVM represent numerically the whole torso model in three-dimensional space using usually a combination of tetrahedral and hexahedral elements. In order to represent incorporation of the regions with varying conductivity only these methods can be used.

The BEM uses integral equations (boundary integral form) to solve the partial differential equations [86]. The surface integrals are computed on the surfaces with homogeneous conductivity. As it was mentioned previously, the unknown potential values are defined only on the surfaces.

The FDM is based on the application of a local Taylor expansion to approximate the differential equations. The partial derivatives are approximated by the finite differences creating sparse diagonal dominant matrix. FDM uses a regular structured three-dimensional grid to discretize the torso geometry. Since FDM is using topologically square network of lines, it is hard to represent complex biological geometries precisely. Therefore, the grid should have a smaller step near the boundaries of the different conductivities. As the grid should have the regular structure in the whole torso, the amount of the nodes will increase significantly and slower down the solution process [138].

FEM divides the torso regions into small subdomains referred to as “finite elements”. Interpolation function is used to describe each element relatively to its nodes. Finite elements can have different size resulting in a possibility to use irregular mesh near the regions with local refinement and keeping a relatively small amount of nodes. It also allows to represent the torso regions with similar conductivities and little solution variations by larger finite elements and reduce computing time [4, 138].

FVM is similar to the FEM, but without a priori assumption of the potential variation within an element, therefore a high level of discretization should be used for higher

by Tyšler using single dipole generator [163–164] and multiple dipole generator [75]. Inverse solution defining the last activated area in the ventricles was performed in the simulation study on the ECGSIM heart model using one and two dipole models [165].

Group of Bin He performed several studies in well-controlled intact pigs to localize the endocardial pacing site using single moving dipole model [96], to obtain single moving dipole trajectories originated near the pacing site [97] and to localize endocardial pacing site using current density reconstruction method [166]. Results of the applied approaches showed that the localization of the pacing sites was in a good agreement with the actual position of the pacing electrode.

Summarizing, there are various approaches to solve the inverse problem. Since the inverse solution can be influenced by various factors as torso inhomogeneities, electrode displacement, method of signal processing, accuracy of the CT/MRI segmentation, best representing equivalent source model, etc. the selection of the inverse method should be performed carefully in order to reduce the ambiguity of the obtained results.

■ 1.7.6 Noninvasive electrocardiographic imaging

Available imaging methods as computer tomography and magnetic resonance tomography allow combining computing and modelling methods with real patient measurements. **Electrocardiographic imaging (ECGI)** represents new noninvasive imaging modality for cardiac electrophysiology, which allows reconstructing electrical activity of the heart using information about electrical data recorded on the body surface together with cardiac CT or MRI imaging that provides accurate electrode positions and the heart-surface morphology and structure of the patient chest.

ECGI has great perspective benefits and might be helpful in treating cardiac arrhythmias, assessment of the drug effect on the cardiac conduction system, estimate the arrhythmogenic areas prior to the operation [167]. Formulation of the inverse approach [168] to define the epicardial potentials from BSP and to reconstruct the activation sequence has received considerable attention [169]. Numerous studies [98, 170–172] based on EDL model evaluated epicardial [104, 169, 173] and endocardial [100] activity.

Rudy et al group [174] studied, tested and validated their technique formulated in [168, 175] experimentally using isolated canine hearts in torso-tank models [176] and in humans [177]. In particular, studies have successfully provided images of cardiac activation and repolarization during normal excitation [177–178], during ventricular pacing [176, 179–180], in the presence of conduction disturbances [181], during atrial fibrillation [179], and ventricular tachycardia [174, 182–183]. It was shown by Cochet et al. [128] in patients with VT, WPW, atrial fibrillation, and scar-related ventricular fibrillation that fusion of the BSP mapping and imaging modalities enables comprehensive noninvasive assessment of cardiac arrhythmias to guide mapping and ablation. ECGI results have been compared with intraoperative mapping in patients undergoing cardiac surgery and have demonstrated the spatial accuracy of 6–10 mm in locating focal activity initiated by pacing [174, 184–185].

Summarizing, ECGI provides the same information (or its close approximation) that could be obtained invasively with a multi-electrode sock placed over the heart or with a basket catheter inside the heart, but without the need to open the chest. However, to date ECGI is not being used as a primary clinical tool for arrhythmia diagnosis and management [104, 186]. “To enter the clinical arena, the physical validity of the simulations and robustness of individual methods must be undisputed.” [104].

Chapter 2

Aim and goals of the thesis

Aim:

Proposal of a diagnostic method for noninvasive localization of the ventricular ectopic beat focus using body surface potential mapping, 3D model of the torso structure from an imaging method and suitable solution of the inverse problem of electrocardiology.

Goals:

1. Overview of existing noninvasive diagnostic methods for ventricular ectopic beat focus localization.
2. Suggestion of a diagnostic method based on inverse solution and using appropriate electrical equivalent source, representing the pathological ventricular ectopic beat.
3. Verification of the proposed method in patients.
4. Experimental study of the selection of the evaluated body surface potential map on stability and accuracy of the inverse solution.
5. Study of the influence of torso model complexity on stability and accuracy of the inverse solution.

Practical impact:

The noninvasive method should supply pre-operational information about the localization of the ectopic focus enabling to decrease the time required for the invasive electrophysiological study and the ablation therapy.

Chapter 3

Selected processing and evaluation methods

3.1 Inverse method

As shown in sections 1.7.5 and 1.7.6, pre-operational noninvasive localization of the premature ventricular complex focus can be obtained by solving the inverse problem of electrocardiography. To solve the inverse problem in this particular case, several partial tasks have to be accomplished:

- proper formulation of the electrical generator that represents the pathological electrical heart activity during the PVC has to be selected and appropriate method for the inverse solution yielding its parameters has to be proposed,
- suitable methods for measurement and processing of the surface ECG have to be proposed that allow to obtain sufficient data on the cardiac electrical field and extract the specific information needed for the inverse solution,
- appropriate model of the torso volume conductor has to be created that represents the heart and other organs and tissues within the torso and leads to a sufficiently accurate and numerically stable inverse solution.

For all that, proper methods have to be proposed that allow evaluation of the success rate, accuracy and stability of the obtained inverse solution and estimation or identification of optimal parameters for proposed methods for processing of electrical and geometrical data.

These partial tasks are discussed in following chapters.

3.1.1 Selection of the electrical generator and the computational method

Premature ventricular complexes represent early activation of the ventricles, which is caused by pathological depolarization initiated in a small region of cardiac cells — in the PVC focus. As the main aim of this work is finding of the focus as the target for the catheter ablation, we propose not to look for an inverse solution reconstructing the whole depolarization/repolarization sequence but to concentrate on the beginning of the depolarization what leads to simpler formulation of the equivalent electrical generator that will make the inverse solution easier. To represent a small activated region, a single dipole model can be used as an equivalent cardiac generator. Single dipole model offers benefits of simplicity, robustness, and quick computation.

Finding of such a single dipole model, commonly known as the “moving dipole” [1, 94, 187–188], requires determination of six parameters: three components of the dipole moment and three coordinates of its position. However, solving of this task leads to a nonlinear problem with respect to the dipole coordinates. Moreover, it can happen that the resultant position of the dipole will not coincide with real region in the ventricular tissue but can be found only in its vicinity.

To avoid solving of the nonlinear problem and to guarantee the position of the dipole in the ventricular myocardium, an alternative approach, originally proposed in [189] is

suggested in this work. This “brute force” approach takes the advantage of today’s fast computers and calculates only three dipole moment components of “fixed dipoles” [1, 187] in all possible positions within the ventricular myocardium, what is a fast and linear task. Then a dipole in a position where it generates the distribution of surface potentials that best resembles the really measured BSP map is selected as the inverse solution.

■ 3.1.2 Inverse solution with one dipole

To find the inverse solution, possible positions of the dipole are predefined within the whole ventricular myocardium. A straightforward method of defining these positions is to place them in a regular rectangular grid. The *grid step* should be selected depending on the desired resolution of the inverse solution (see sec. 3.1.4).

Let’s assume that there are n single dipoles in the pre-defined positions in the myocardium. Then the dipole generator D , representing a single point equivalent heart generator, creates in each time instant t a potential distribution on the body surface torso, which can be described by the equation:

$$bspm(t) = \mathbf{B} \cdot D(t), \quad (3.1)$$

where

$bspm_{[m \times t]}$ — is a body surface potential map measured in m leads on the torso, generated by the heart generator D .

$\mathbf{B}_{[m \times 3]}$ — is a transfer matrix representing the relation between the single dipole D and potentials on the torso. This matrix is time independent with size $[m \times 3]$, where m is the number of measured points on the torso and 3 is the number of single dipole moments. Computation of the transfer matrix is performed using boundary element method [190].

$D(t)_{[3 \times t]}$ — is the equivalent heart generator in the form of a single dipole with 3 dipolar moment components each in instant time t .

For each pre-defined position of the single dipole an inverse problem is calculated, therefore a matrix \mathbf{B}_n , corresponding to the n -th position of the single dipole, is computed. If we know the input BSP map, the unknown components of the single dipole D can be computed using the formula

$$D = \mathbf{B}_n^{-1} \cdot bspm, \quad (3.2)$$

where

\mathbf{B}_n^{-1} — is a pseudoinverse matrix of the \mathbf{B}_n .

D — is a single dipole with three dipole moments, which best represents the input BSP map.

The inverse of the submatrix \mathbf{B}_n can be obtained using **singular value decomposition (SVD)** method [191]. Application of the SVD method to Eq. (3.2) will factorize the matrix \mathbf{B}_n into the form:

$$\mathbf{B}_n = \mathbf{U} \times \mathbf{\Sigma} \times \mathbf{V}^T \quad (3.3)$$

where

$\mathbf{\Sigma} = \text{diag}\{\lambda_i\}$ — is a diagonal matrix with non-negative singular values λ_i . Columns of the \mathbf{V} and \mathbf{U} are singular vectors, that define orthonormal basis of the dipole space and BSP map space. The singular vectors are unit vectors, therefore, each singular value λ_i is a scaling coefficient of the corresponding basis vector (i -th column of \mathbf{V}) for the

dipole D . Since both of the matrices \mathbf{V} and \mathbf{U} are orthonormal, their inverses can be computed through the transposition:

$$\mathbf{U}^{-1} = \mathbf{U}^T \quad (3.4)$$

$$\mathbf{V}^{-1} = \mathbf{V}^T \quad (3.5)$$

Hence,

$$\begin{aligned} \mathbf{B}_n^{-1} &= (\mathbf{U} \times \mathbf{\Sigma} \times \mathbf{V}^T)^{-1} = (\mathbf{V}^T)^{-1} \times \mathbf{\Sigma}^{-1} \times \mathbf{U}^{-1} = \\ &= (\mathbf{V}^{-1})^{-1} \times \mathbf{\Sigma}^{-1} \times \mathbf{U}^T = \mathbf{V} \times \mathbf{\Sigma}^{-1} \times \mathbf{U}^T, \end{aligned} \quad (3.6)$$

where $\mathbf{\Sigma}^{-1} = \text{diag}\left(\frac{1}{\lambda_i}\right)$. Singular values λ_i in matrix \mathbf{B}_n are arranged in decreasing sequence. For small values of the λ_i , the inverse value $1/\lambda_i$ causes numerical instability. Therefore, generally the matrix B_n is inverted through the so-called truncated SVD, using only singular vectors with large enough singular values [191–192]. In our case of defining three dipole moments only first 3 singular values are used. Therefore, the inverse \mathbf{B}_n^{-1} is numerically stable.

Inverse solution for a single dipole in each pre-defined position results in defining its dipole moments D for each position n . BSP map generated by this dipole $dbspm$ in m measuring points on the torso can be computed using:

$$dbspm = \mathbf{B}_n \cdot D, \quad (3.7)$$

where the sizes of the matrices are: $[m \times 1] = [m \times 3] \cdot [3 \times 1]$

To select the best single dipole D , a criterion of the **relative residual error** (RRE) between the input BSP map ($bspm$) and map computed from the inversely calculated dipole ($dbspm$) is evaluated for each dipole position:

$$\text{RRE} = \sqrt{\frac{\sum_{i=1}^m (bspm_i - dbspm_i)^2}{\sum_{i=1}^m bspm_i^2}} \quad (3.8)$$

The single dipole D with minimal RRE value is selected as the resulting single dipole that can represent the small initially activated area of the myocardium during the PVC.

■ 3.1.3 Number of ECG leads for the inverse solution

As it was discussed in sec. 3.1.2, one of the inputs for the inverse solution is the BSP map. Existing variety of the lead systems (characterized in sec. 1.5.3) raises the question what is the sufficient number of ECG leads for an accurate inverse solution.

This issue was addressed already by one of the pioneer studies on BSP mapping [59]. It showed that 24 properly placed leads with measuring points located mostly on the left anterior torso (in close proximity to the heart) and several measuring points scattered widely on the rest of the torso are sufficient for acceptable description of the body surface potential distribution over time. However, Lux et al. [60, 193] and Puurtinen et al. [194–195] studies indicated necessity to use 32 leads with high electrode density in precordial region in order to obtain reliable inverse solution.

Since required number of measuring electrodes can be dependent on the used inverse method, studies on sufficient leads number from the inverse solution performance viewpoint was evaluated in simulation studies [196–197]. More recent study by Gharbalchi et al. [197] compares mapping systems consisting of 771, 192, 64 and 32 electrodes. It confirms that reduced lead systems with optimal placement of electrodes can be used for the inverse solution.

Our method selected for the inverse solution in sec. 3.1.2 was used in a simulation study by Tysler et al. [164] that compared the accuracy of the inverse solution depending on the used lead system for BSP map computation. It showed that localization error of the inverse solution obtained using 32 leads [61] was twice smaller compared to the localization error of the inverse solution using 24 leads. And their later study [163] suggests to increase the number of measuring leads to improve accuracy of the inverse solution, which is also supported in [55, 198] recommending to use more than 64 leads for the inverse solution to obtain meaningful results. Use of the reduced lead systems requires high precision while positioning the electrodes on the body surface because electrode dislocation leads to unsatisfactory inverse solution with low accuracy of the source localization [194–195, 199].

Though the question of the sufficient number of the measuring electrodes for accurate inverse solution was never resolved, many research groups used 62–65 leads in their patient studies for PVC focus localization [81, 150], optimization of the biventricular pacing in [200], identification of the heart regions with changed repolarization [75], and validation of the sinus rhythm reconstruction [201–202]. Worth mentioning, that the inverse solution aiming to reconstruct the whole activation sequence of the heart requires high number of about 192 measuring leads [196] (evenly distributed around torso) and up to 224 and 252 measuring leads placed on the vest, which was intensively studied by Rudy research group [128, 177, 181].

Summarizing, when selecting desired lead system the following should be considered:

- To obtain reliable results of the inverse solution using single dipole model, the lead system should include more than 62 electrodes.
- To avoid lengthy application of individual electrodes, the lead system should be organized in stripes (of several electrodes) or should be placed on a vest. Lead system organized in a vest will require several vest sizes due to vast variability of the torso geometry among patients. It also can be difficult to use this system in larger-breasted female patients. So, lead system organized in stripes is preferable thanks to its flexibility.
- Because patient’s torso geometry and heart position within the torso is individual, it will be challenging to find optimal placement [197] of the electrodes. Thus, electrodes should have even distribution around the torso (regular grid).
- For patient’s convenience the electrodes application should take less than 5 min.

Existing lead systems were described in sec. 1.5.3. Four of them have even distribution of the electrodes organized in stripes: *Bath*, 80 *Regular*, 96 *Regular* and *Lux* – 192. *Bath* system uses 43 electrodes, which is not enough for reliable inverse solution. Oppositely, for our purpose *Lux* – 192 has redundant number of electrodes. Such a high number of leads is generally used for activation computation or studies in atria.

As can be seen in Fig. 1.17, 80 *Regular* has 16 stripes with 5 electrodes each and 96 *Regular* has 12 stripes with 8 electrodes each. The 96 *Regular* should be selected because it has smaller amount of stripes, which will be applied quicker. At the same

time this lead system has higher amount of electrodes, which will provide more detailed description of the BSP distribution.

■ 3.1.4 Required resolution of the inverse solution

It is obvious that due to the use of simplified equivalent electrical generator, unavoidable presence of noise in the ECG measurements, simplification and geometrical uncertainties of the torso model, and imprecision of numeric calculations, the accuracy of the inverse solution will be affected. As this accuracy is not known in advance, the needed or desired resolution of the inverse solution may be estimated from the main goal — successful ablation of the PVC focus. The diameter of the tip of the electrode on the cardiac catheter used for the destruction of the pathological source is 5–7 Fr (1.67–2.33 mm, Fig. 1.10); and the diameter of the ablation lesion depends on the applied power, temperature, orientation of the electrode, irrigation of the electrode [48] and can be about 10 to 15 mm. As can be seen from the Fig. 3.1, the smallest ablation depth 4.7 ± 0.6 mm is observed during the constant voltage mode.

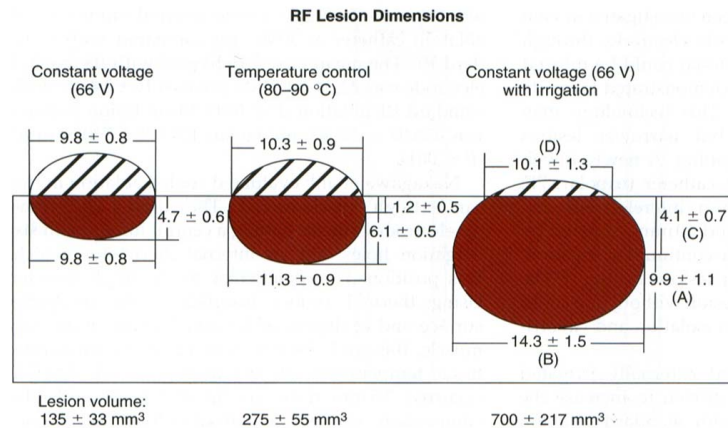


Figure 3.1: Diagram of ablation lesions dimensions for different radiofrequency ablation modes. **A** indicates maximal lesion depth; **B** maximal lesion diameter; **C** depth at maximal lesion diameter; **D** lesion surface diameter. Lesion volume was calculated by use of the formula for an oblate ellipsoid, by subtracting the volume of the “missing cap” (hatched area). From [48]

Therefore, the resolution of the method (i.e. the grid step of possible dipole positions) should be less than 5 mm to hit the PVC focus safely in all ablation modes. Meanwhile, because the size of the ablation electrode is around 2 mm, setting the spatial resolution less than 2 mm is redundant. Summarizing, the selected grid step should be in the range 2–5 mm.

To select the resolution of the inverse solution it is important to keep in mind that preoperational localization of the PVC focus is highly important for cases with septal localization of the focus. Correct discern between right and left ventricle approach is possible only if the thickness of the septum will be bigger than the grid step of the possible dipole positions. According to Marcomichelakis et al. [203] interventricular septum thickness increases with age and according to Am Soc Echocardiography [204] in normal the thickness of the interventricular septum is 6–10 mm [204–206]. Therefore, by selecting grid step of the possible dipole positions twice smaller than the normal interventricular septum results in value of 3 mm.

3.2 ECG measurement and processing

3.2.1 Selection of the processed time interval in ECG

When localizing the focus of the premature activity, we are not interested in the electrical activity of the whole ventricular myocardium but only in its initial part, right after the onset of the ectopic QRS [189], [J3, C12], and appropriate time interval from the ECG signal should be selected.

Careful selection of the used time interval of the BSP map used as input data for the inverse solution is necessary to obtain correct inverse result. When selecting the proper time interval, we are facing two contradictory requirements:

1. The interval should be taken so that the recorded electrical activity is strong enough to be clearly distinguishable from the noise present in the ECG signal, what effectively means that the evaluated interval should be taken “as late as possible” after the PVC onset.
2. The interval should be taken very early, “as soon as possible” after the PVC onset to fulfill the condition that the activated area is small enough and can be represented with a reasonable accuracy by a single dipole – i.e. a point source.

It also means that selection of the interval can depend on the actual position of the PVC focus in the heart influencing

- the amplitudes of electrical signals projected to different ECG leads and the **signal-to-noise ratio (SNR)**, and
- the possibly asymmetric spread of the activation front due to the anatomy or anisotropy of the myocardium near the PVC focus.

A closer look on the last condition is provided in example in Fig. 3.2. If the PVC focus is located in point **F**, the volume activated during a short time interval **T1** will be still nearly symmetric and the equivalent dipole generator will be located in point **D1** at the gravity center of the activated zone, near the PVC focus. In this case the ablation electrode placed in position **E1** can safely destroy the focus. However, after a longer time interval **T2** the activated volume can be highly asymmetric due to the local tissue shape or anisotropy. In this case the equivalent dipole generator located at the gravity center of the activated zone in point **D2** is far from the PVC focus and the area ablated by the electrode placed in position **E2** will not “hit” the PVC focus.

Taking into account that the velocity of the activation front in isotropic working myocardium is about 0.6 to 0.75 m/s [207–208], within the first 15 ms after the PVC onset the activated area will reach a diameter of 18 to 22.5 mm which in this work will be supposed to be:

- large enough to generate ECG signals clearly distinguishable from the noise,
- small enough to be represented by a single equivalent dipole placed in its center of gravity and yielding position of the dipole so close to the PVC focus that it will fall within the ablation lesion of 14.3 ± 1.5 mm diameter caused by application of the constant voltage RFA via an irrigating catheter (according to Fig. 3.1).

To select the best time interval for accurate PVC focus localization based on the results of the inverse solution (described in more detail in sec. 3.5.3) several time intervals will be studied. For this purpose a longer initial time interval (twice longer than 15 ms) will be considered and several sub-intervals will be tested for IBSPM computations (see sec. 1.6.2, Eq. (1.9)). The use of too long or late sub-intervals can lead to evaluation

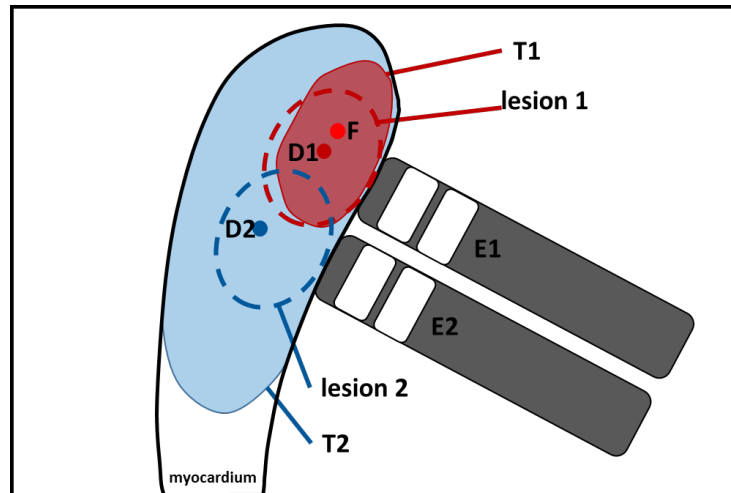


Figure 3.2: Example of the possible influence of the evaluated time interval after the activation onset on the inversely obtained dipole position and its impact on the ablation success. **F** — PVC focus position. Red — area activated in time **T1** yielding equivalent dipole in position **D1** and enabling successful ablation by electrode placed in position **E1**. Blue — area activated in longer time **T2** yielding equivalent dipole in position **D2** preventing successful ablation by electrode placed in position **E2**

of larger activated part of the myocardium which can not be correctly represented by a dipole. On the other side, the use of too short or early sub-intervals can lead to evaluation ECG signals with low SNR. In both cases, the inverse solutions obtained using IBSPM from these sub-intervals may lead to incorrect inverse results. Evaluation of correct and incorrect inverse solution results will allow to select the optimal time interval which should be used to represent the PVC focus by a single dipole.

The question still remains if BSP map from a single time instant or some “smoothed” ECG from a longer time interval should be used to improve the signal-to-noise ratio. In this work it is suggested to test both, using BSP maps from individual time instants and integral BSP maps from different sub-intervals within the whole evaluated ECG interval. Also, in order to study the consistency/stability of the obtained inverse solution from beat to beat, five PVCs are analyzed in each patient. This amount is based on practical reasons that the multichannel ECG measurement should be fast and should not be tiresome for the patient due to “PVC expectation”.

Thus, for each of the five ectopic beats, the BSP maps will be computed within the initial 30 ms time interval of the PVC. The TIBSPMs will be calculated for each millisecond within this interval, resulting in 31 TIBSPMs. Then also IBSPMs for 21 sub-intervals of the initial 30 ms interval will be computed.

■ 3.2.2 Correction of the ECG baseline

During the ECG measurement, namely patient’s movements and breathing cause changes of skin-electrode contacts and electrode polarizing voltages leading to ECG baseline wandering (Fig. 3.3). Correction of the ECG baseline should be performed before the PVC onset can be selected and desired time interval in the ECG is evaluated.

The baseline wander is localized in low frequencies and is not limited in a specific band [209]. The periodic respiration movements (15 respirations/min) generate a cycle of 4 seconds and fundamental component of 0.25 Hz [210]. The baseline noise spectrum is usually not higher than 1 Hz but in most cases overlaps with the ST segment spectrum. According to [210] interpretation of the ST segment should be performed only

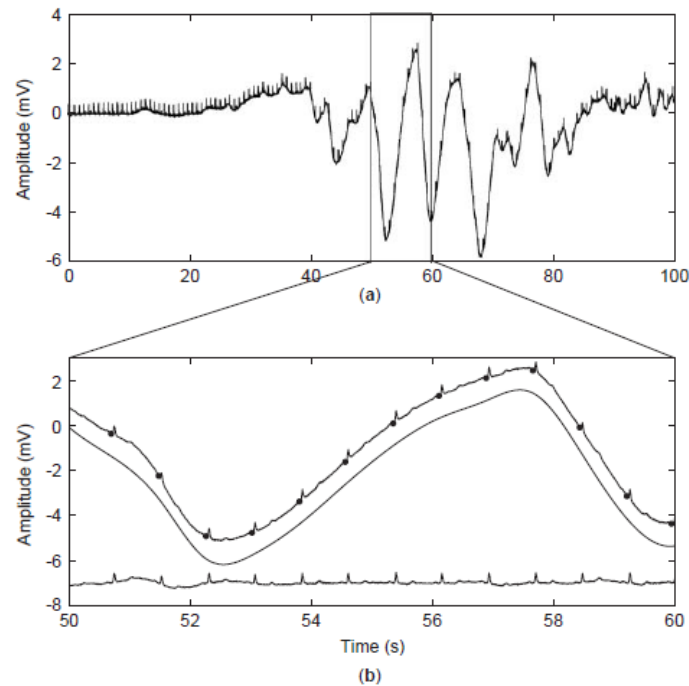


Figure 3.3: (a) Example of the ECG baseline wander due to sudden body movements. The amplitude of the baseline wander is considerably larger than that of the QRS complexes. (b) ECG signal frame (a) magnified ($10\times$), the estimated baseline obtained by fitting a cubic spline to the series of knots (indicated by dots), and the corrected ECG signal. From [209]

using high-pass filters with cut-off frequency of 0.05 Hz or lower. AHA recommendations [211] also state that 0.5-Hz low-frequency cut-off introduces considerable distortion into the ECG, particularly with respect to the level of the ST segment. Therefore, baseline wander is considered less distorting than the main interference, but more difficult to be removed or even reduced. The specified requirement of the baseline drift in the standard of the Association for the Advancement of Medical Instrumentation [212] is $10\mu\text{V/s}$.

In this study small time interval (its selection is described in sec. 3.2.1) of the initial QRS signal will be processed. As in this case artefacts from sudden body movements are rare, a linear 2-point baseline correction using points in the electrically still intervals after the T wave and before the P wave, will be used. It will not affect the small deviations of the signal, but will enable to correct the baseline sway without the use of a high-pass filter which can yield phase shift [210, 213].

As a rule, the baseline correction is performed in two steps using 2-point baseline correction. First, the baseline is roughly corrected along a longer time interval with two normal beats, that have longer baseline after the preceding T wave. This longer interval between the beats guarantees unbiased selection of two time markers. One of them marks the baseline before the normal complex preceding the PVC complex. The second one marks the baseline after the normal complex following the ectopic beat. The markers are placed on the time interval with undeniable absence of cardiac activity.

After the first/rough baseline correction, both time markers will be re-defined. The first one will be set to mark the baseline immediately before the ectopic complex and the second one right after it. Using this setting, the 2-point baseline correction will be performed once more.

■ 3.2.3 Definition of the PVC onset in the ECG

In order to find in the ECG signal the beginning of the premature ventricular activation (“Zero-time”), a semi-automatic approach will be used after the baseline correction. Zero-time will be at first defined manually and then re-defined after using the algorithm estimating the SNR. Because the Zero-time (or PVC onset) represents the premature activation of the ventricles, initial part of the QRS complex representing activation of the ventricles will be analyzed.

To define the onset of the QRS more precisely, a derivative (reflecting fast change) of the reference lead will be used. Multichannel ECG measurement has the advantage of more dense coverage of the surface potential compared to the 12-lead ECG. To use this advantage, **root mean square (RMS)** signal which reflects the “energy” in all measured signals is calculated using the formula:

$$\text{RMS} = \sqrt{\frac{\sum_{i=1}^m \text{sig}_i^2}{m}}, \quad (3.9)$$

where

RMS — root mean square signal,

sig_i — signal of the i -th measured lead,

m — number of measured leads.

Manual definition of the Zero-time will be based on the morphology of three graphs: *the reference lead, it's derivative* and *RMS*; so that the Zero-time will be the time instant of the strict simultaneous change (increase/decrease) in all of them. Manual selection of the Zero-time can be biased as it does not take into account the overall noise in the signals. Therefore, an automated approach evaluating the signal-to-noise ratio will be applied to improve the initial manual definition of the Zero-time.

To estimate the level of the overall noise in the measured signals, the following assessment might be considered. Two windows of the same duration (their length is chosen at the end of this sub-chapter) will be selected. The first window, assumingly, will contain only *noise* and the second window, will contain useful *signal with noise*.

Assuming that there is no useful signal between the T (or U) and P waves, the first window should be considered as pure noise and selected on the isoelectric line between the end of the T (or U) wave and the onset of the P wave. Its root mean square signal $\text{RMS}_{\text{Noise}}$ will be calculated from all measured chest leads.

Then the second window should be selected prior to the manually defined Zero-time and its $\text{RMS}_{\text{Signal}}$ value will be computed also from all measured chest leads. To compare the level of noise in the previously selected $\text{RMS}_{\text{Noise}}$ signal with $\text{RMS}_{\text{Signal}}$, a ratio is evaluated from these two signals of similar duration:

$$\text{Ratio} = \frac{\sum_{i=1}^t \text{RMS}_{\text{Signal}}(t)}{t} \bigg/ \frac{\sum_{i=1}^t \text{RMS}_{\text{Noise}}(t)}{t} = \frac{\sum_{i=1}^t \text{RMS}_{\text{Signal}}(t)}{\sum_{i=1}^t \text{RMS}_{\text{Noise}}(t)}. \quad (3.10)$$

If the ratio is less or equal to 1, it means that the selected time interval (second window) does not contain any useful signal. The window of the *Signal* can be shifted for 1 ms towards Zero-time and evaluation can be repeated iteratively until the ratio is

more than 1.5. The middle of this selected time window *Signal* will be defined as the Zero-time (PVC onset).

Since the new Zero-time will be placed in the middle of the window, it is assumed that the signal from this new Zero-time is significantly higher than the noise. Therefore, a mean from window containing noise and useful signal should be higher than 1. Selecting relatively low ratio of 1.5 will guarantee not to “miss” early activation.

In order to select the duration of the window (which is identical for the first and second window), it is important to keep in mind that real measurements often contain disturbances of various nature (in more detail, see sec. 3.2.4). A mean of the signal, evaluated from longer time interval, is more precise. At the same time, the suggested method sets the new Zero-time in the middle of the window and too wide window could shift results incorrectly. To remove 50 Hz noise caused by power lines, the length of the window should be some multiple of 20 ms duration, and in this study 20 ms will be selected.

Because the Manual definition of the Zero-time is influenced by the human judgment, the algorithm should start evaluation earlier than the actual Zero-time. As the length of the window is 20 ms, evaluation can be 50 ms prior to the manually defined Zero-time.

■ 3.2.4 Filtering of the ECG

Additional method to improve the signal quality is filtering of the signal. The main sources of disturbances in ECG (Fig. 3.4), besides baseline wandering, are noise from the power lines (50 or 60 Hz) and myopotentials (35–45 Hz) [49, 209]. Unfortunately, both these disturbances are in the spectrum of useful ECG signals (Fig. 3.5), which is considered 0.05–150 Hz according to recommendations of **American Heart Association (AHA)** [212, 214] and the Association for the Advancement of Medical Instrumentation [215].

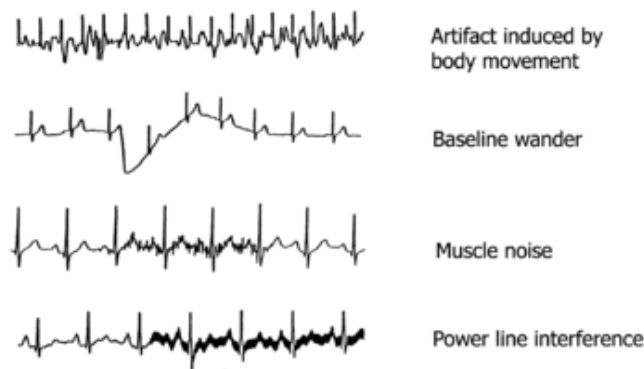


Figure 3.4: Examples of artifacts caused by different sources. From [216]

For this reason, filtering of these frequencies will also distort the useful signal and should be used only if unavoidable, i.e. if the disturbances are present and strong. For power line interference a notch filter can be used, but it may alter the ECG components around the power line frequency (50 or 60 Hz). To avoid this issue adaptive filters can be used, but they are not effective in cases of ectopic beats and arrhythmia in general because they require an adaptation period after every abrupt change in the ECG signal [209]. The electromyogram noise is produced by many sources and therefore can be treated as random. Since it overlaps with the ECG spectrum its filtering in many cases is not effective [209]. In this work Pipberger filter will be used in cases with signal

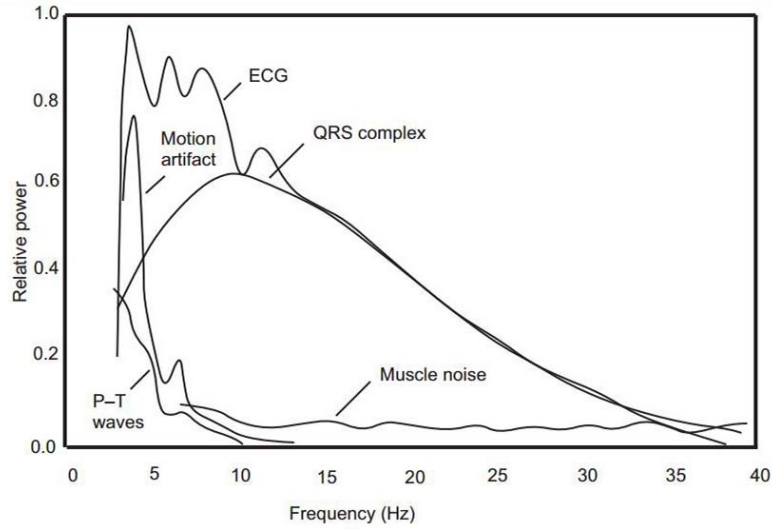


Figure 3.5: Relative power spectra of an QRS complex, P and T waves, muscle noise and motion artifacts based on an average of 150 beats. From [49]

highly disturbed by the noise. It is a low pass filter with cut-off at 25 Hz and zero transfer at 50 Hz and its higher harmonics.

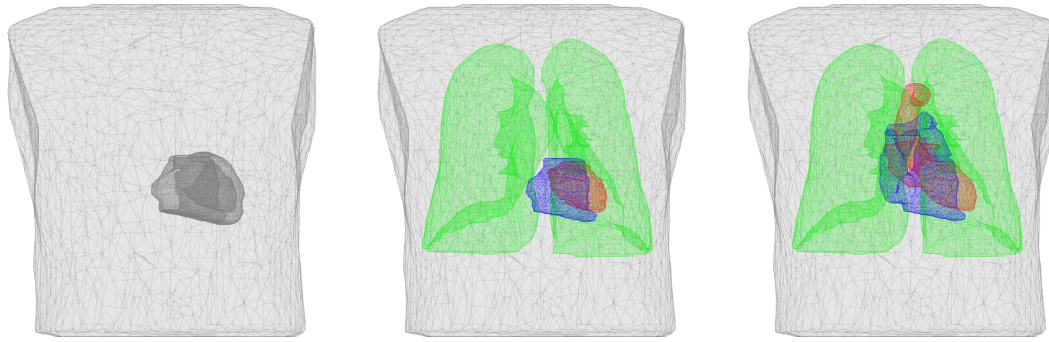
3.3 CT data processing

Because the heart and torso geometry varies from patient to patient, a patient-specific torso model should be created using some imaging method. As it was mentioned in sec. 1.7.3, accuracy of the torso model is of high importance. And so, CT scanning providing high-resolution spatial images is used to create 3D torso models. These torso models are formed by closed surfaces (boundaries) that separate internal regions of the torso volume conductor with different conductivities, while each considered region is assumed to be homogeneous. To use BEM for the forward and inverse solution, the torso models should be described by triangulated surfaces.

The selection of the CT as imaging method is also based on the necessity to know exact positions of measuring electrodes relatively to the patient's torso [217–219] for an accurate inverse solution.

However, the optimal *complexity* of the torso model used for the inverse solution, i.e. the inclusion of regions with different conductivities within defined boundaries, is to date an open question. According to Cuffin et al.[220], impact of the torso inhomogeneities on the inverse solution is negligible unless the cardiac cavities are closely located to the lung tissue. It was shown in [221] that such inhomogeneities as lungs and intracavitary blood masses cause noticeable effect on the torso potential distribution.

In order to study the impact of the torso model complexity on the inverse solution, in this work three types of torso models are constructed for each patient. They vary in the degree of included inhomogeneities. The first model is *homogeneous torso* without any considered internal regions with different conductivities (**torso model H** — Fig. 3.6 a). The second torso model is *inhomogeneous torso* with lungs, right and left ventricle (**torso model V** — Fig. 3.6 b). The third torso model has the *biggest complexity*; it is also *inhomogeneous* and includes torso, lungs, heart ventricles and atria, aorta, and pulmonary artery (**torso model AV** — Fig. 3.6 c).



(a) torso model H

(b) torso model V

(c) torso model AV

Figure 3.6: Torso models with different degree of included inhomogeneities

The second torso model (V) includes inhomogeneities in close proximity to the myocardium, which are lungs and ventricular cavities filled with blood. The third torso model (AV) includes lungs and more detailed heart cavities filled with blood. The heart cavities of right ventricle, right atrium and pulmonary artery are joined into one internal region with the same conductivity. Similarly, combined cavities of the left ventricle, left atrium and aorta form one internal region. Therefore, the V and AV torso models have the same number of regions with inhomogeneities but in the AV torso model the heart cavities include also corresponding atrium and outflow tract.

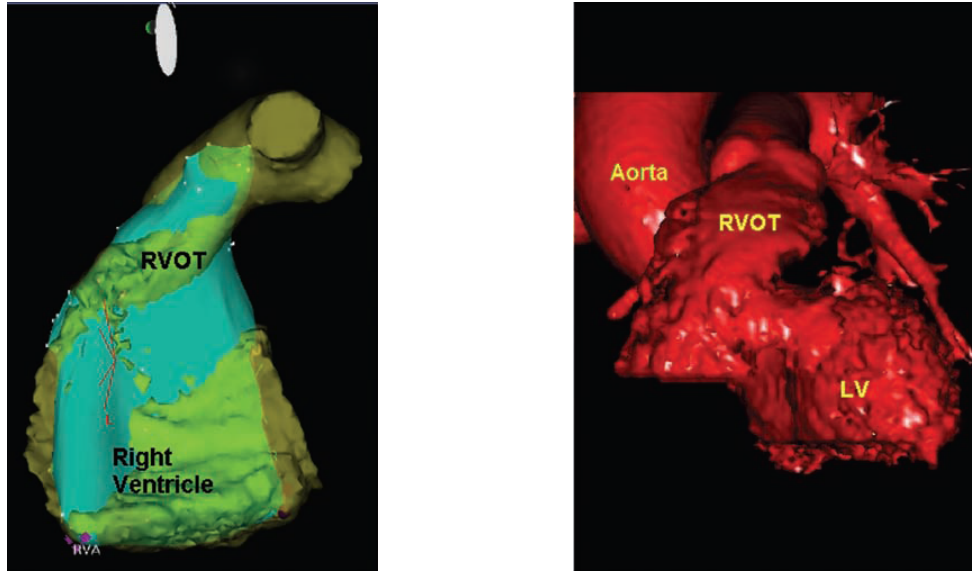
3.4 Correctness of the inverse solution

In order to verify the correctness of the inverse solution, the results of the inverse solution are compared with the results of the clinical invasive electrophysiological study. During an EP intervention, the origin of the PVC activity is defined by the physician according to the standard protocol of the EP study using intracardiac mapping techniques described in sec. 1.6.1. To obtain spatial information about the PVC focus location, the cardiac mapping is performed by the use of a 3D navigation system.

During the mapping, a 3D model of the endocardial surface of the investigated chamber is constructed by mapping of the catheter electrode tip positions. This model is merged with the 3D model of the heart constructed from the CT images using a build in tool of the navigation system and a few reference points (Fig. 3.7). The reference points are selected by the clinician performing the EP study depending on the studied heart cavity and patient-specific anatomy. Thus, merge of these two geometries provides clinician with additional and more reliable knowledge of the patient-specific heart anatomy enabling precise mapping of the activation and safe radiofrequency ablation of the PVC focus.

As it was mentioned in sec. 1.4.4, 1.4.5, application of the radiofrequency current to the myocardium, where the PVC focus is located, destroys the pathological tissue and creates a lesion. Ablation lesions are marked by the 3D navigation system automatically on the 3D model of the investigated chamber by vinous markers. Thus, if the ablation procedure was successful, locations of these ablation lesions in the 3D model are assumed as real PVC focus location. Then, locations of these ablation lesion markers can be compared with the PVC focus localization obtained from the inverse solution.

In order to keep the study unbiased, the designation of the heart area with ablation lesion markers is performed by the clinician without knowledge of the inverse solution results. After the EP study, the clinician evaluates the positions of the ablation markers



(a) Merged geometries of the intraoperation endocardial geometry of the right ventricle (cyan color) with 3D model of the reconstructed from CT images right ventricle and pulmonary artery geometry (moss color). Left view

(b) 3D reconstruction of the heart showing the posterior superior course of the RVOT. Antero-posterior view

Figure 3.7: Heart geometries obtained using 3D navigation system and CT [31]

within the heart regions and assigns them to particular heart segments in agreement with clinical conventions. Region assignment is performed depending on the location of the ablation lesion within the right/left myocardium or near the outflow tracts. If the lesions are located in the LV myocardium, the recommendations of the American Heart Association [222] are used and the name of the ablation lesion position is given according the division of the LV myocardium into 17 segments. The recommendations of the AHA for the LV segmentation are extended to create corresponding segmentation of the RV, by mirroring the LV segmentation with regard to septum (Fig. 3.8). If the ablation lesions are near the outflow tract of the RV or LV, the outflow tract in superior view is divided into 12 segments as on the clock without mirroring for the RVOT (Fig. 3.9).

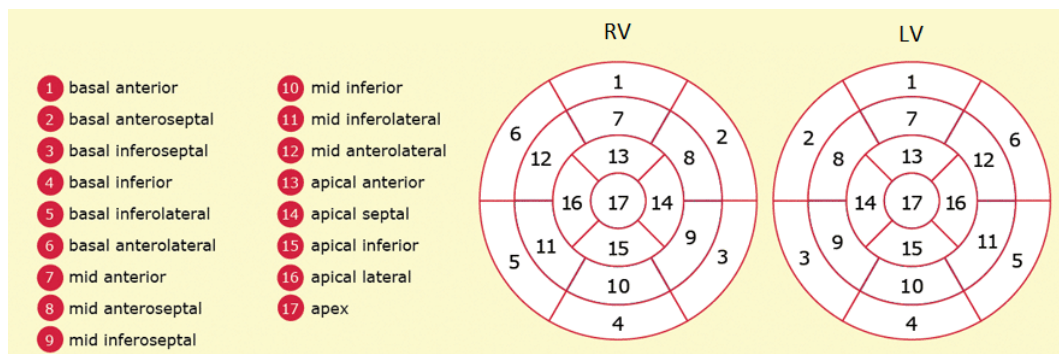


Figure 3.8: LV division into 17 segments according to the AHA recommendations [222] (right) and its extension to RV segmentation (left). Apex to base view

Considering the computed results of the inverse solution we use the same segmentation of the heart as physicians and, similarly to clinicians to stay unbiased, we assign

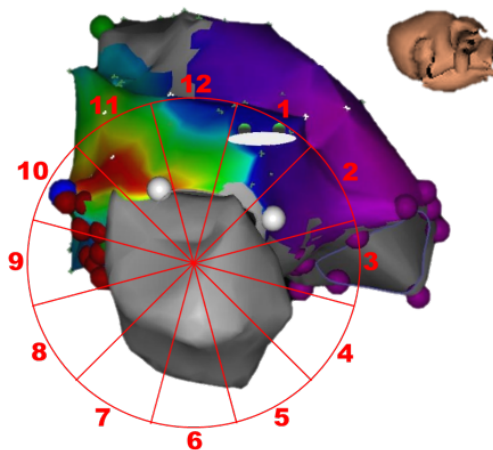


Figure 3.9: Example of the superior view of the RV with the RVOT and its division into 12 segments

the appropriate anatomical region to the inverse results without knowing the EP study findings.

Later, the anatomical region assigned to the inverse solution by us will be compared to the region assigned by the clinicians. If the anatomical region is the same, the result of the inverse solution will be marked as **CORRECT**. If the anatomical region of the inverse solution is different from the region assigned by physician, the inverse solution will be marked as **INCORRECT**.

3.5 Evaluation of the inverse solution results

3.5.1 Used statistical terms and tests

To describe and analyze the measured/evaluated data, commonly known statistical terms are used: mean, median, deviance, variance/dispersion, standard deviation and **interquartile range (IQR)**. As it was described in sec. 3.4, the obtained result of the inverse solution is evaluated as *correct* or *incorrect*. Therefore, the evaluation of the inverse solution result, which has only two possible values, is a categorical data type.

In this work, different types of BSP map and torso model are used as input data for the inverse solution. In order to study whether different types of these input data have impact on correctness of the inverse solution the Pearson's chi-square test will be used [223]. It will test whether:

- the type of the BSP map has impact on the inverse solution;
- the torso model complexity has impact on the inverse solution;
- there is the best combination of the input BSP map and torso model in order to obtain correct inverse solution.

The Pearson's chi-square tests the null hypothesis that the variables are independent. The test compares the observed frequencies in certain categories to the expected frequencies you might get in those categories by chance. The $expected_{ij}$ frequencies for each of the categories can be calculated using the equation [223]:

$$expected_{ij} = \frac{rowtotal_i \times columntotal_j}{k}, \quad (3.11)$$

where

$rowtotal_i$ — is the sum of the frequencies in the i -th row of the contingency table

$$\sum_{j=1}^n a_{ij},$$

$columnntotal_j$ — is the sum of the frequencies in the j -th column of the contingency

$$table \sum_{i=1}^m a_{ij},$$

i — is the number of row in the contingency table,

j — is the number of column in the contingency table,

k — is the total number of the observations ($\sum a_{ij}$).

Pearson's chi-square test standardizes the deviation for each observation. Sum of these standardized observations results in Pearson's chi-square (χ^2) [223]:

$$\chi^2 = \sum \frac{(\text{observed}_{ij} - \text{expected}_{ij})^2}{\text{expected}_{ij}}. \quad (3.12)$$

The obtained Pearson's chi-square χ^2 is checked against a chi-square distribution with known properties. Degrees of freedom df are calculated as

$$df = (m - 1)(n - 1), \quad (3.13)$$

where

df — degrees of freedom,

m — is the number of rows in the contingency table,

n — is the number of columns in the contingency table.

Then, the observed value of the chi-square distribution χ^2 is compared against the critical value for the chi-square distribution with df and significance value p . If the observed value of the chi-square distribution χ^2 is bigger than the critical value, the null hypothesis is rejected and the categorical variables are assumed to be dependent [223].

In order to find patient-specific time instant for TIBSPM computation, which represents the initial part of the ectopic activation and at the same time has high signal-to-noise ratio, a *correlation coefficient* r will be used [223]. It can be calculated using the expression:

$$r = \frac{\sum (x_i - \bar{x}) \cdot (y_i - \bar{y})}{(n - 1) \cdot s_x \cdot s_y}, \quad (3.14)$$

where

r — correlation coefficient;

s_x — is the standard deviation of the first variable x ;

s_y — is the standard deviation of the second variable y ;

x_i — values of the first variable x ;

y_i — values of the second variable y ;

\bar{x} — is mean of the first variable x ;

\bar{y} — is mean of the second variable y ;

n — number of observations.

The absolute value of the correlation coefficient shows the relationship strength and can be any value from -1 to $+1$. The larger the number — the stronger the relationship. The values of correlation coefficient less than ± 0.5 represent a weak relationship, and values greater than ± 0.8 is generally described as strong relationship.

To compare the stability of the inverse solution results obtained when torso models of different complexity were used, the dispersions of the positions of the inverse results

are evaluated using the *F-test of equality of variances* [223–224]. Usually, *F*-test is used to test the null hypothesis that the two variables x and y with normal distribution have the same variance. The *F*-test can be one-tailed or two-tailed test. If the test is one-tailed, it checks only in one direction, which means that the variance σ_x^2 of the first variable x is either greater than or less than the variance σ_y^2 of the second variable y . If the test is two-tailed, it checks the alternative that the variances are not equal. The definition of the *F hypothesis* can be described as [224]:

$$\begin{aligned} \mathbf{H}_0 : & \quad \sigma_x^2 = \sigma_y^2 \\ \mathbf{H}_1 : & \quad \sigma_x^2 < \sigma_y^2 \quad \text{for a lower one – tailed test;} \\ & \quad \sigma_x^2 > \sigma_y^2 \quad \text{for an upper one – tailed test;} \\ & \quad \sigma_x^2 \neq \sigma_y^2 \quad \text{for a two – tailed test.} \end{aligned}$$

The tested statistics is $F = \frac{s_x^2}{s_y^2}$, where the s_x^2 , s_y^2 are the sample variances, and the presumption that they have Fisher-Snedecor distribution with degrees of freedom $(n_1 - 1, n_2 - 1)$ and significance level α . The more this **F ratio** deviates from **1**, the stronger is the evidence of the unequal variances of the two variables. The hypothesis that two variances are equal is rejected if:

$$\begin{aligned} F < F_{1-\alpha, n_1-1, n_2-1} & \quad \text{for a lower one-tailed test;} \\ F > F_{\alpha, n_1-1, n_2-1} & \quad \text{for an upper one-tailed test;} \\ F < F_{1-\frac{\alpha}{2}, n_1-1, n_2-1} \quad \text{or} \quad F > F_{\frac{\alpha}{2}, n_1-1, n_2-1} & \quad \text{for a two-tailed test;} \end{aligned}$$

where F_{α, n_1-1, n_2-1} is the critical value of the *F*-distribution with $n_1 - 1, n_2 - 1$ degrees of freedom and a significance level of α [224].

■ 3.5.2 Selection of the relevant results using relative residual error criterion

The main criterion of the relevancy of the inverse solution is the **relative residual error**, which is described in more detail in sec. 3.1.2. RRE shows the deviation of the BSP map computed from the inversely estimated dipole from the input BSP map used for the inverse solution. The dipole with minimal RRE value is selected as the resulting single dipole of the inverse solution. If the value of the RRE is higher than a selected threshold value the result is assumed as not relevant, i.e. the measured BSP map cannot be satisfactorily represented by a single dipole.

In this study all results of the inverse solution which have RRE value *higher than 0.3* are considered **not relevant** and excluded from the later evaluation. The inverse results with RRE value *less or equal to 0.3* are referred as **relevant results**.

■ 3.5.3 Evaluation of the input BSP maps impact on inverse solution

One of the inputs for the inverse solution is body surface potential map. In this work two types of BSP maps are used – time instant BSP maps (TIBSPMs) and integral BSP maps (IBSPMs). The difference between these types of maps, as it was already mentioned in sec. 1.6.2, is that the TIBSPM displays the potential distribution over the torso at a particular time instant, while the IBSPM displays the distribution of potential integrated over the defined period of time (interval).

To determine whether the type of the BSP map has an impact on the inverse solution a Pearson’s chi-square test is used. The test checks the null hypothesis that the

correctness of inverse solution is independent of the used BSP map. The first category represents independently used BSP maps (TIBSPMs and IBSPMs) for all five measured PVCs and the second category represents the correctness of the inverse solution (correct, incorrect).

If the null hypothesis is rejected, a new Pearson's chi-square test is performed to check whether the BSP map, which gave the highest amount of correct results, is better compared to all the other BSP maps joined into one category. In other words, compared to the previous test, instead of separate categories of BSP maps (for each time interval or time instant), we assume that there might be two categories of BSP maps. The first one is the BSP map, which provided the highest amount of the correct results, and the second category consists of all the other BSP maps. In this case, the Pearson's chi-square test checks the null hypothesis that the highest amount of the correct inverse results is independent of the used BSP map.

■ 3.5.4 Search of the patient-specific time instant for TIBSPM computation

Keeping in mind, that PVC may arise in any part of the ventricles and that ectopic focus position varies from patient to patient, the PVC beat morphology also varies from patient to patient. It means that there is a high chance that the best time interval for computing the most proper BSP map for the inverse solution can vary from patient to patient. That is why an approach to determine patient-specific time instant for the input BSP map is required. In order to define/find this time instant a study of the correlations between the TIBSPMs is performed.

The theoretical background behind this test lies in two presumptions:

- The first one is that the TIBSPM, best representing the premature ventricular activity, contains only the initial activation of the pathological cardiac tissue.
- The second presumption is that the signal-to-noise ratio for this TIBSPM is sufficiently high (typically higher than 3), which is very hard to achieve in the very initial time instant in real measurements.

Because the TIBSPMs, computed from the nearby time instants depict similar electrical change, they should be highly correlated. The TIBSPMs obtained from the beginning of the initial time interval represent the very initial part of the activation, but might be more corrupted by the noise; and the TIBSPMs for the latest part of the selected time interval are less disrupted by the noise, but represent much larger part of the activated myocardium, which cannot be correctly represented by single dipole in the inverse solution. A TIBSPM, which has the highest correlation with the TIBSPMs obtained from both, the beginning and ending of the selected time interval represents the compromise between the small area of activation and high signal-to-noise ratio.

In order to find such TIBSPM, correlations between all TIBSPMs within the studied initial 30 ms are calculated (Fig. 3.10).

After computing the correlations within the whole selected time interval, an average of the correlations is calculated for each time instant. The time instant with maximal value of the obtained average correlation is selected as the best "patient-specific" input TIBSPM (Fig. 3.11).

The inverse results obtained for these 5 best TIBSPMs with the highest average correlation coefficient are evaluated separately with respect to 3 torso models with different complexity. Only relevant results with RRE less than or equal to 0.3 are taken into account.

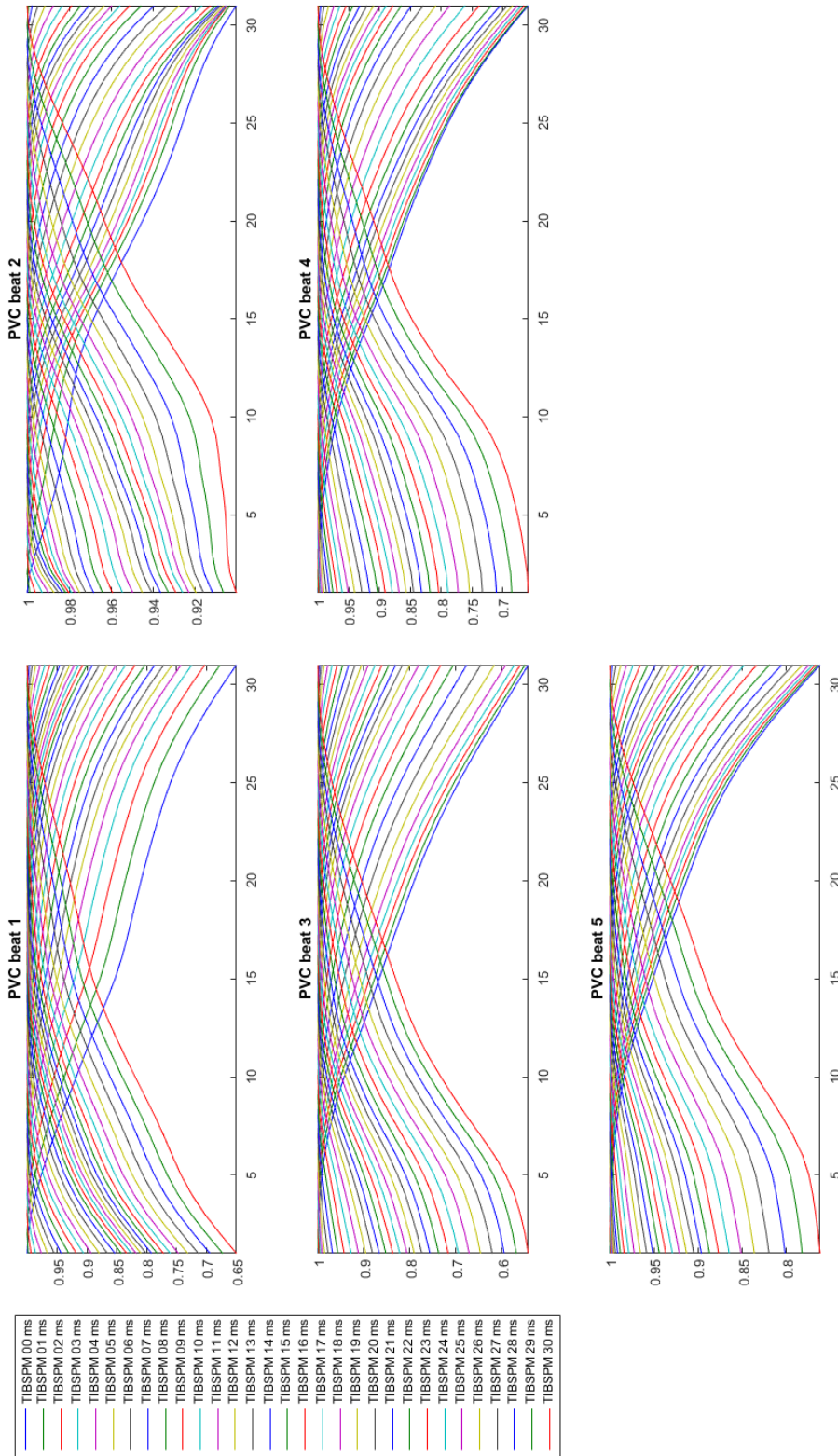


Figure 3.10: Correlations between TIBSPMs, computed for initial 30ms time interval for each out of 5 selected PVCs for Pat007. Each line represents correlations of one TIBSPM with the other 30 TIBSPMs. There are 31 lines on each of the five graphs as there are 31 TIBSPMs

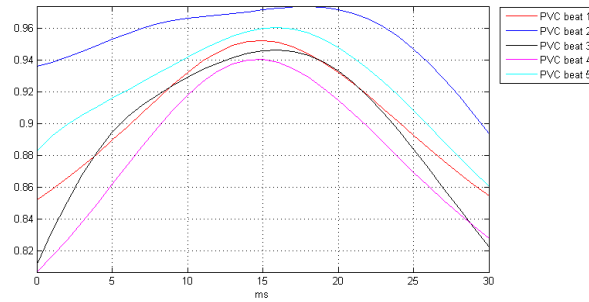


Figure 3.11: Average correlation of the TIBSPMs for each time instant of the selected initial 30 ms time interval. Five lines represent five PVCs from Fig. 3.10

Then the hypothesis whether such TIBSPM can be assumed as the optimal input map for the selected PVC for the specific patient is tested.

■ 3.5.5 Evaluation of the impact of the torso model complexity on the inverse solution

As it was described in sec. 3.3, three types of torso models are constructed for each of the patients. The torso models vary in completeness/degree of inclusion of the inhomogeneities. To evaluate whether the inclusion of torso inhomogeneities has impact on the inverse solution a Pearson's chi-square test is used. The first category represents the degree of inclusion of torso inhomogeneities and the second category describes the correctness of the inverse solution. In this case the Pearson's chi-square test checks the null hypothesis that the correctness of inverse solution is independent of the used torso model.

If the null hypothesis is rejected, a new Pearson's chi-square test is performed to check whether the torso model, which gave the highest amount of the correct result, is better compared to the other two torso models joined in one category. The Pearson's chi-square test checks the null hypothesis that the highest amount of correct results using selected torso model is independent of the used torso model.

■ 3.5.6 Search of the best combination of input data for the inverse solution

As it was already discussed in sec. 3.5.3–3.5.5, selection and processing of the input data for the inverse solution can have impact on the correctness of the inverse results. In this chapter, we describe the testing whether there is the best combination of the BSP map and torso model data, which generates the correct inverse results with higher probability than some other combinations.

In order to do this, we will perform the Pearson's chi-square test to check the null hypothesis that the correctness of the inverse results is independent of the used combination of the input parameters for the inverse solution. As there are various BSP maps (several IBSPMs and 31 TIBSPMs) and 3 torso models (homogeneous H, inhomogeneous V, and inhomogeneous AV), there is a total amount of possible combinations. These combinations are used to compute the correct or incorrect inverse solution for each out of five ectopic beats in each patient. Only relevant inverse results are taken into account.

If the null hypothesis is rejected and the inverse solution is dependent on the used combination of the input parameters, a further analysis is performed to define the best combination of input parameters for the inverse solution. The combination with highest amount of correct inverse results is compared against all the other combinations joined

together. Here, the Pearson's chi-square test checks the null hypothesis that the best combination of input parameters provides the highest amount of correct inverse results by chance.

■ 3.5.7 Evaluation of the stability of the inverse solution

Two aspects of the stability of the inverse solutions are studied. First, the spatial stability of the inverse solution obtained according sec. 3.5.6 is computed using the best combination of the input torso model with one input BSP map based on the minimal value of the RRE parameter. Second, the stability of results obtained from slightly different input data is evaluated.

The inverse problem of electrocardiography is ill-posed, therefore small inaccuracy in the input data can cause significant change of the obtained inverse result. In practical applications, it is important to know how the result will be affected by the input data fluctuations/errors, because it can be challenging to reduce them in real measurements.

To evaluate whether the RRE function, which is the main criterion of the selected inverse method, provides inverse solutions with steady and consistent dipole localization within the ventricles, the localizations of the first five dipoles with minimal RREs will be studied. If the positions of these dipoles are located close to each other, we can suppose, that the minimal RRE value indicates a spatially stable solution. On the other hand, if the positions of these first five dipoles are located far from each other in different parts of the ventricular myocardium, the inverse solution found according the minimal RRE value is spatially unstable and unreliable. In this study the best combination of input parameters selected in sec. 3.5.6 is used for the inverse computations.

In order to assess the abovementioned spatial stability of the inverse solutions, the following steps are performed:

1. Instead of one dipole with the smallest RRE value, five dipoles with the smallest RRE values are evaluated.
2. For these five dipoles a gravity center is computed.
3. Distances between this gravity center and each of the five dipoles are calculated.
4. Mean, standard deviation and quartiles of the obtained distances are determined and used as measures of the spatial stability of the inverse solution.

Stability of the inverse solution can be also dependent on the fluctuations of the input data. In our case, the input data for the inverse solution are BSP map and homogeneous or inhomogeneous torso geometry. Therefore, the stability of the inverse solution depending on the fluctuations of both of them is analyzed.

The stability of the inverse solution in dependence on the fluctuations of the BSP map is assessed using the above suggested evaluation method of the stability and the same combination of input parameters as selected in sec. 3.5.6 but in this case it is used for all 5 PVCs in each patient. Therefore, results of the inverse solution for each patient include 25 dipoles from 5 PVCs in total. After estimation of the gravity center of these 25 dipoles, mean and dispersion of the distances to each dipole from this gravity center is calculated. The smaller the dispersion of the positions of the inverse results, the more stable is the inverse solution depending on the BSP map fluctuations.

To assess the stability of the inverse solution in dependence on the selected torso model the same method as for evaluation of the RRE stability is used. Only one ectopic beat is used for the inverse solution jointly with each of the three torso models. BSP map computed for this one PVC is selected in sec. 3.5.3. For each of the three combinations, first five dipoles with minimal RRE value are obtained as the result of

the inverse solution. For these 5 dipoles a gravity center is computed. Then, mean and dispersion of the dipole distances from the gravity center are evaluated for each of the three combinations.

In order to compare the stability of the inverse results when different torso models are used, obtained dispersions are evaluated using the F -test of equality of variances, described in sec. 3.5.1. This comparison of dispersions gives an understanding how consistent are the positions of the inversely obtained dipoles when using each of the combinations with different degree of inclusion of the torso inhomogeneities. Besides this, the analysis of the distances between gravity centers, obtained for each of the combinations, provides information how the inverse results shift when different torso models are used.

Chapter 4

Experimental evaluation of the proposed methods

4.1 Selection and description of the patient group

The experimental measurements were performed in cardiologic departments of University Hospital Kralovske Vinohrady (Prague, Czech Republic). Characteristics of the eighteen measured patients is given in Tab. A.1. The patients with frequent monomorphic PVCs were selected by the clinicians of the cardiologic department. The data from patients were collected after obtaining their informed consent (Appendix B). All used methods and applied procedures were approved by the Ethic Committee of the University Hospital Kralovske Vinohrady. From the total amount of 18 measured patients, 10 patients were evaluated after excluding patients with less than 5 PVCs during the ECG recording (3 patients), wrong selection of the ECG sampling frequency (1 patient), cancelled EP study due to atrial fibrillation (1 patient), or CT data of poor quality (3 patients).

4.2 Measurement procedures

Patients underwent up to 30 minutes of multichannel ECG recording. Right after the ECG recording the cables were unplugged from the electrodes and the patients underwent whole torso CT scanning with electrodes remaining on their chests. This enabled to obtain precise positions of electrodes respectively to the torso directly from the CT scan. An intracardiac electrophysiological study with catheter ablation using a 3D navigational system was performed on the same or the next day.

4.2.1 Multichannel ECG measurement and processing

ProCardio 8 system [83, 225–226] (Fig. 4.1) was used for multichannel ECG recording. The system consists of a set of lead cables with active electrode adapters, data acquisition unit powered by a rechargeable Li-ion battery and connected to a personal computer by an optical USB cable. The system can be configured for simultaneous recording of limb leads and up to 128 chest leads according to the user requirements.

Driven right leg (DRL) is used and all ECG signals are measured relatively to a **common mode sense (CMS)** electrode (that can be placed in selected position on the body) to minimize the unwanted common mode signal. After the measurement all leads are recomputed relatively to the Wilson's Central Terminal (see Eq. (1.7)) by the software [226–227].

In this work 96 chest electrodes organized in 12 strips of 8 electrodes (Fig. 4.2) evenly distributed around the patient's thorax together with four limb electrodes and a CMS electrode were used for the multichannel ECG measurements. The signals were recorded using disposable Ag/AgCl electrodes with active adapters and sampled at

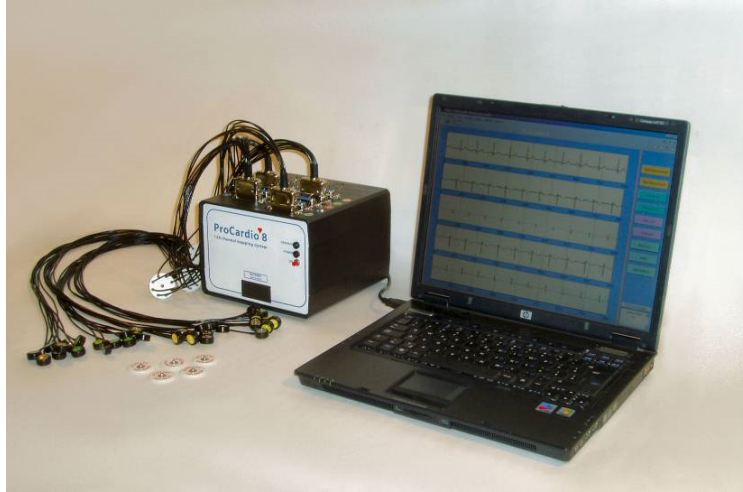
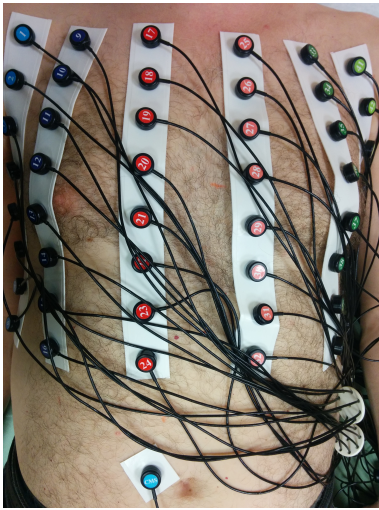
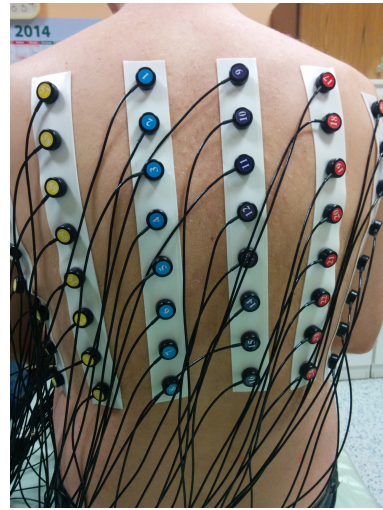


Figure 4.1: ProCardio 8 — BSP mapping system



(a) Anterior-posterior (AP) view



(b) Posterior-anterior (PA) view

Figure 4.2: Patient Pat006 with 96 electrodes (organized in 12 strips of 8 electrodes) and the common mode sense (CMS) electrode

1 kHz sampling frequency with 16-bit resolution (except Pat002 where 500 Hz sampling frequency was used). The length of records was from three up to 30 minutes depending on the occurrence of the ectopic beats.

For each patient five ectopic beats were selected from the multichannel ECG records for further processing. The signals were processed using the software of the ProCardio 8 system. The raw ECG signals were stored in international **General Data Format** for biomedical signals (**GDF**) [228].

Pre-processing of the signals started with the following steps: recalculation of unipolar leads relative to the WCT and computation of standard bipolar leads, offset correction, filtration of the signal using Pipberger filter for removing excessive 50 Hz interference and high frequency noise. A reference lead was selected based on the distinct morphology and biggest amplitude of the ectopic complex. As a rule, one of the standard limb leads was selected. If a time marker was set in the reference lead, the same time marker was valid for all leads.

After selecting the reference lead the baseline correction in all leads was performed using the method described in section 3.2.2 (in two steps, using 2-point baseline correction). Example of two manually selected baseline time markers defining the processed interval in the reference lead is given in Fig. 4.3. After the baseline was set immediately before and after the selected PVC, the Zero-time defining the PVC onset (Fig. 4.4) was manually set and precised by the software using the method described in section 3.2.3.

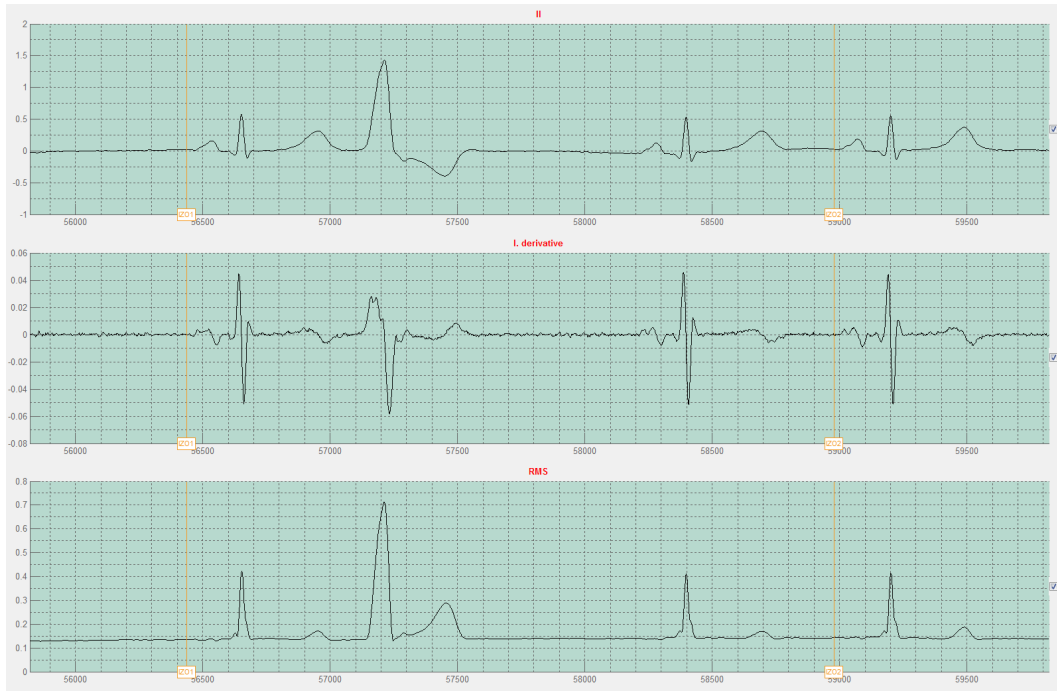


Figure 4.3: Initial manual selection of the processed interval. Orange lines mark selected baseline time markers **IZO1** and **IZO2**. **Upper graph:** standard lead II. **Middle graph:** Derivative of the lead II. **Lower graph:** RMS signal computed from all measured chest leads

Next, the time markers (Fig. 4.5) were set with 5 ms step to define sub-intervals of the selected initial 30 ms time interval. Using these time markers, sub-intervals were created for all possible combinations between them, resulting in 20 sub-intervals with duration of 5, 10, 15, 20 and 25 ms (Tab. 4.1).

Initial time instant	Duration					
	5 ms	10 ms	15 ms	20 ms	25 ms	30 ms
0 ms	0–5	0–10	0–15	0–20	0–25	0–30
5 ms	5–10	5–15	5–20	5–25	5–30	
10 ms	10–15	10–20	10–25	10–30		
15 ms	15–20	15–25	15–30			
20 ms	20–25	20–30				
25 ms	25–30					

Table 4.1: Twenty-one sub-intervals of the selected initial time interval 0–30 ms used to compute IBSPMs from each PVC

Finally, all of the 21 time intervals were used to compute IBSPMs (Fig. 4.6) for each out of five PVCs in each patient. As it was described in section 3.2, for the same selected 0–30 ms time interval TIBSPMs were computed for each time instant (with one millisecond time step). It resulted in 31 time instant BSP maps for each of the five

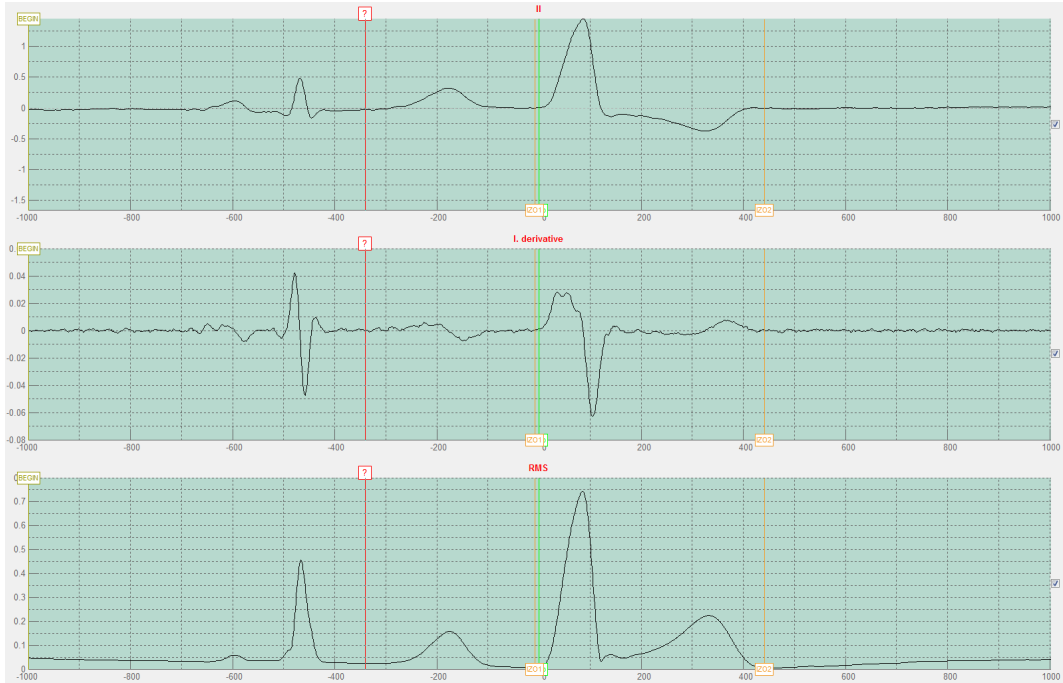


Figure 4.4: Redefinition of baseline times after first baseline correction (orange lines) and manual setting of the initial estimate of the PVC onset — **Zero-time** (green line). Red line with “?” label is a caliper, which is used to set the markers. **Upper graph:** standard lead II. **Middle graph:** Derivative of the lead II. **Lower graph:** RMS signal computed from all measured chest leads



Figure 4.5: Allocation of the final PVC onset (green line) set by the algorithm and six time markers (pink lines) defining sub-intervals of the selected initial 30 ms time interval. Orange lines mark selected baseline time markers **IZO1** and **IZO2**. **Upper graph:** standard lead II. **Middle graph:** Derivative of the lead II. **Lower graph:** RMS signal computed from all measured chest leads

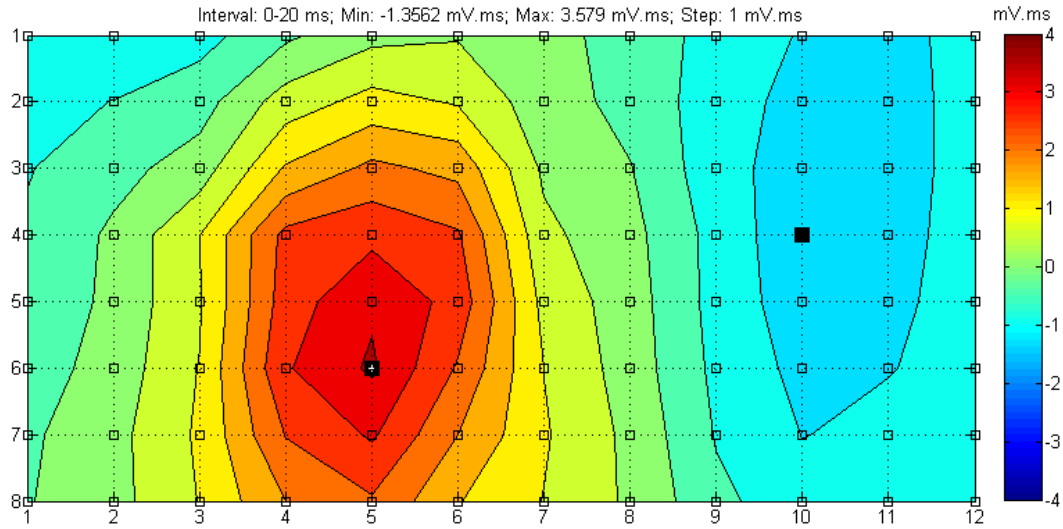


Figure 4.6: Integral body surface potential map of Pat006 for the 0–20 ms interval

ectopic beats in each patient. Therefore, there were 105 IBSPMs and 155 TIBSPMs for each patient used as the alternative input data for the inverse solution.

■ 4.2.2 CT data processing

After the multichannel ECG recording the patients with attached ECG electrodes underwent CT scanning of the whole chest (which is described in section 3.3) to obtain the patient-specific 3D configuration of the torso with its main electrical inhomogeneities as well as real positions of the measuring ECG electrodes on the torso surface (Fig. 4.7).

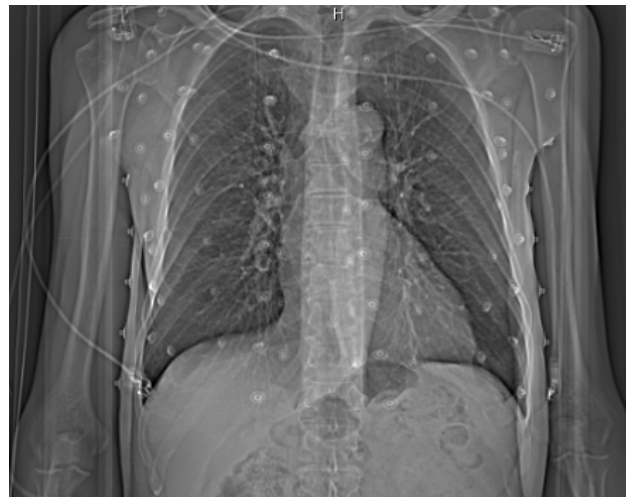


Figure 4.7: Anterior-posterior projection of the whole torso CT scan. Lighter dots indicate electrode positions

CT scanning was performed using Siemens Somatom Definition system. Contrast-enhanced cardiac CT angiography was performed with the slice thickness 0.3 mm. In order to create patient-specific torso models, the CT processing was performed using TomoCon PACS® software [229]. The software enables to perform automatic patient contouring based on the resolution setting. The contouring was performed for the following torso structures: torso, lungs, heart atria and ventricles (epi- and endocardial surfaces), aorta and pulmonary artery (Fig. 4.8).

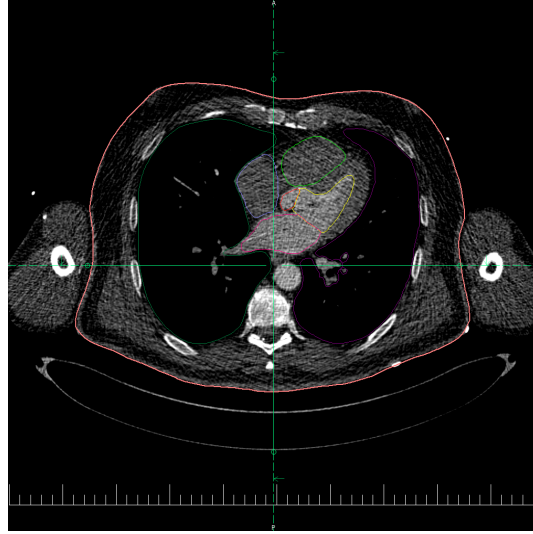


Figure 4.8: CT image with contours of the torso structures: pink — torso, grape — left lung, dark green — right lung, green — right ventricle, yellow — left ventricle, violet — right atrium, magenta — left atrium, blue — pulmonary artery, red — aorta

After obtaining the contours, each of them was manually corrected. In result, 3D volumes of all abovementioned torso structures were created. Example of the processed torso model with its internal inhomogeneities is given in Fig. 4.9a and the heart structures are presented in Fig. 4.9b-c. The surfaces of the torso structures were triangulated. The number of vertices and triangles was optimized to preserve sufficient geometry accuracy and to speed-up the inverse solution.



(a) 3D torso geometries (b) heart structures in AP projection (c) heart structures in PA projection

Figure 4.9: 3D structures of the Pat006 torso model. Colors display the following torso structures: pink – torso, grape — left lung, dark green — right lung, green — right ventricle, yellow — left ventricle, violet — right atrium, magenta — left atrium, blue — pulmonary artery, red — aorta

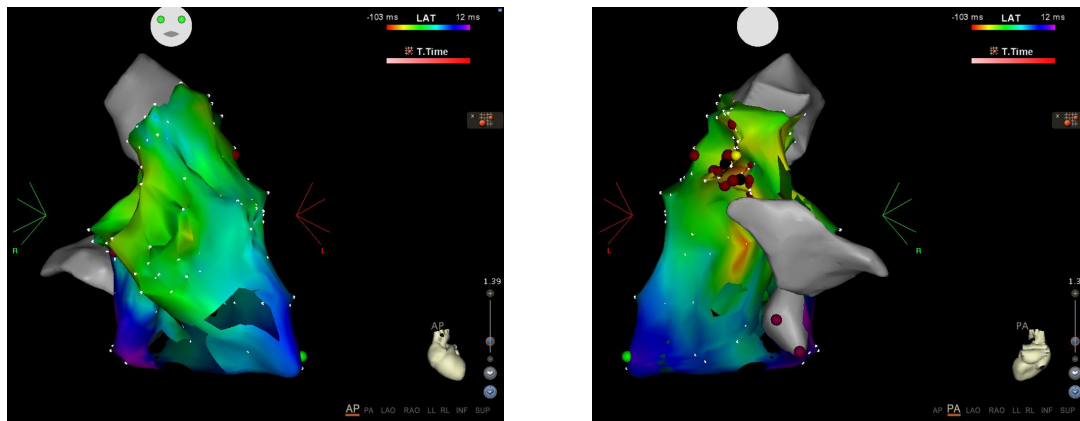
Three torso models with different level of complexity were created. The assumed conductivities were the same for the corresponding parts in all torso models. The conductivity of lungs was assumed four times lower than the conductivity of the torso; the conductivity of heart cavities, aorta and pulmonary artery structures was assumed three times higher than the conductivity of the torso [221].

■ 4.2.3 Electrophysiological study

After ECG measurement and CT scanning, the electrophysiological study and radiofrequency catheter ablation were performed on the same, or on the next day. Patients underwent the procedure under mild conscious sedation with fentanyl. Intravenous isoproterenol was infused as was deemed necessary for the induction of ectopy in patients with infrequent extrasystoles at the beginning of the procedure [J2].

Catheter ablation was performed using 3D electroanatomical mapping system CARTO® (Biosense Webster Inc). Endocardial bipolar and unipolar electrograms were recorded with bandpass filters (30–250 Hz for bipolar and 0.1–100 Hz for unipolar records) using the EP recording system LabSystem PRO™ (Boston Scientific). The right ventricle was mapped via standard femoral approach, and the left ventricle was mapped via transseptal or transaortal retrograde approach. Intracardiac echocardiographic system Vivid q™ (General Electric) was used to guide the transseptal puncture in patients with the PVC origin in the LV. These patients were anticoagulated with unfractionated heparin for activated clotting time of 250–300 s [J2].

After insertion of the mapping catheter a 3D model of the investigated cavity was created using the electroanatomical mapping system CARTO and merged with 3D model reconstructed from the CT scan, performed before the EP study. These procedures are described in more detail section 3.4. An example of the reconstructed endocardial surface of the right ventricle is presented in Fig. 4.10 and an example of the merged geometries is presented in Fig. 4.11.



(a) AP view

(b) PA view

Figure 4.10: Electroanatomic mapping (reconstruction) of the right ventricle of Pat004. The colors change according to the rainbow from red to blue/purple, where the red color represents the earliest activation and the blue/purple — the latest. Ablation points are marked in dark red/vine color

The target site for the radiofrequency ablation was determined by activation mapping and confirmed by pace mapping (requiring concordance of 11 out of 12 leads between the paced ECG signals and the clinical ECG during PVCs). After the target site was located, radiofrequency catheter ablation was performed using an open irrigated ablation catheter Thermocool Navistar (Biosense Webster Inc.) in the power-control mode (25–40 W, flow 15–20 ml/min, max. temperature 43°C). The position of the radiofrequency ablation was automatically marked on the intraoperative endocardial 3D model by the electroanatomical mapping system CARTO in dark red/vine color and labeled as ablation.

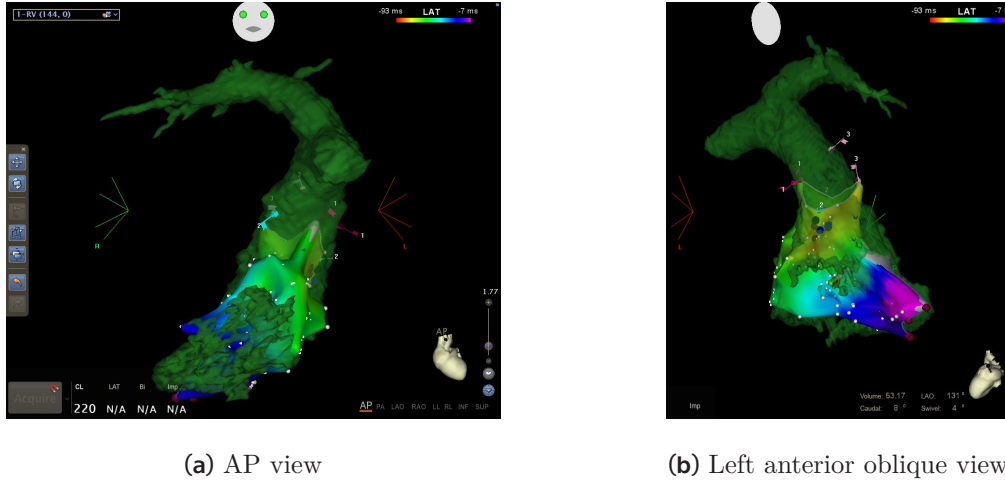


Figure 4.11: Right ventricle endocardium model (rainbow gradient color) in Pat007 obtained from the CARTO® mapping and navigation system by merging the intracardiac mapping with 3D model of the right ventricle and pulmonary artery geometry reconstructed from CT scan (moss color)

Patients were monitored for a minimum of 15 minutes with isoproterenol challenge after the last energy application to ensure complete abatement of the ventricular ectopy [J2].

After the EP study experienced clinician evaluated the location(s) of the ablation markers according to the suggested method described in section 3.4, and assigned it to the appropriate heart segment.

4.3 Inverse solution setting

In order to find the location of the PVC focus with a good accuracy, equivalent generator (selected in sec. 3.1.1) was computed for all positions in a dense regular 3 mm grid (sec. 3.1.4) throughout the modeled ventricular myocardium. The implementation of the SVD algorithm (described in 3.1.2) was developed in the Institute of Measurement Science SAS (Bratislava, Slovakia).

In each patient 5 PVCs were processed. For each ectopic beat 31 TIBSPMs and 21 IBSPMs from the initial 30 ms time interval (sec. 3.2.1, 3.2.3) were computed from multiple chest leads (selected in 3.1.3). Three torso models were modelled in each patient with different level of complexity (sec. 3.3). The inverse problem was solved for all possible **combinations** of the input parameters:

$$(31 \text{ TIBSPMs} + 21 \text{ IBSPMs}) \times 3 \text{ torso models} = 156 \text{ combinations.} \quad (4.1)$$

Summarizing, in each patient there were 156 combinations for each of 5 selected PVCs used as input data to solve the inverse problem using a single dipole model (representing the cardiac electrical generator) and a torso model (representing the volume conductor).

Chapter 5

Results

5.1 Selection of the relevant results using relative residual error criterion

As it was described in sec. 3.5.2, to evaluate the correctness/quality of the inverse solution in terms of single dipole — the relative residual error RRE value (Eq. (3.8)) less or equal to 0.3 is used as the main criterion to select the relevant results. There were 5309 (68%) relevant results in total for all combinations of the input parameters for all patients. A contingency table of the correct and incorrect relevant inverse results in each patient is given in Tab. 5.1. For better understanding the same information is presented in percentage in Fig. 5.1 and Fig. 5.2 (or in Fig. 5.3 in absolute values). Results of the inverse solutions for each patient are given in Appendixes D, E, F, G, H, I, J, K, L, M.

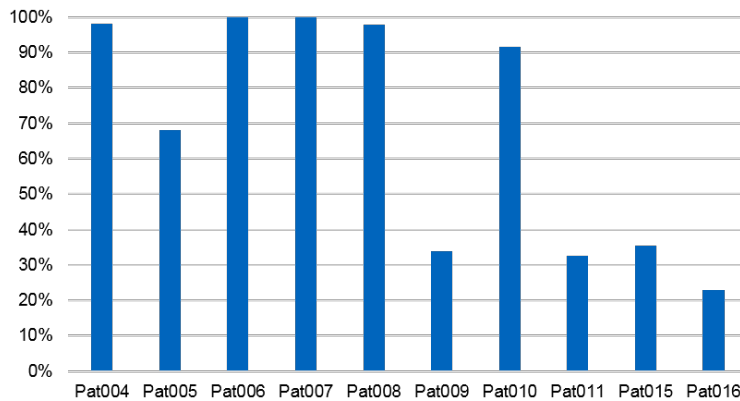


Figure 5.1: Percentage of the relevant inverse solutions with $RRE \leq 0.3$ in each patient

Patient	Correctness of the inverse solution		Total
	Incorrect	Correct	
Pat004	281	484	765
Pat005	291	240	531
Pat006	314	466	780
Pat007	519	261	780
Pat008	250	514	764
Pat009	121	144	265
Pat010	189	525	714
Pat011	255	0	255
Pat015	252	24	276
Pat016	179	0	179

Table 5.1: Contingency table showing how many correct/incorrect inverse results were observed among results with $RRE \leq 0.3$

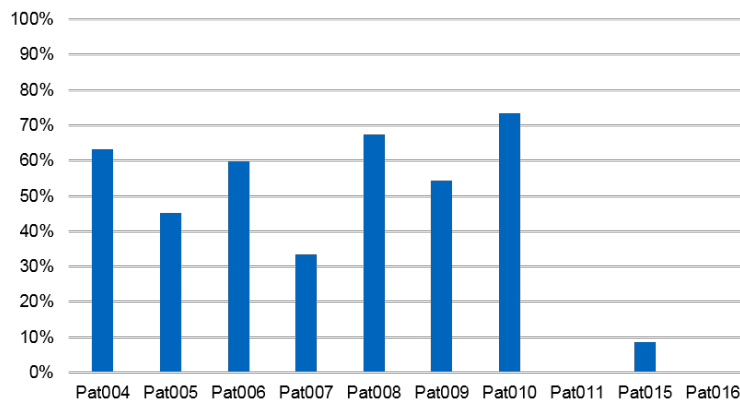


Figure 5.2: Percentage of the correct relevant inverse solutions out of all relevant solutions with $RRE \leq 0.3$ in each patient

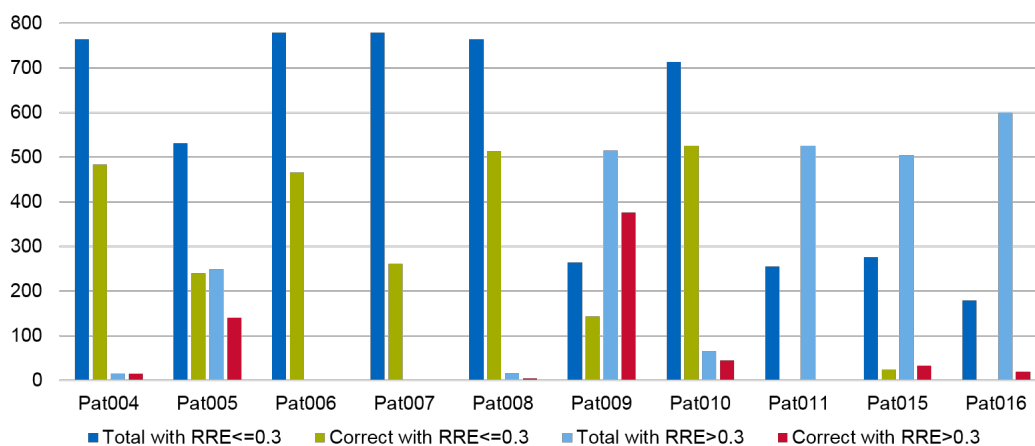


Figure 5.3: Correctness of the inverse solutions in each patient with respect to the RRE value. The first two columns show the results with $RRE \leq 0.3$ (relevant results), where the first column is the total number of relevant results, and the second column is the number of correct relevant results. Analogically, the next two columns show the results with $RRE > 0.3$, where the third column shows the total number of results and the fourth one the number of correct results

5.2 Evaluation of the input BSP maps impact on the inverse solution

The percentages of correct results depending on the used BSP maps are presented in Fig. 5.4. The evaluation of correct results in each patient is provided in Fig. 5.5 for the IBSPMs and in Fig. 5.6 for the TIBSPMs.

The contingency table describing the frequencies of correct and incorrect inverse results by BSP maps is given in Tab. C.1. Using the Eq. (3.11), a model of expected data can be calculated (Tab. C.2). Using the Eq. (3.12), we calculate the χ^2 :

$$\chi^2 = \sum \frac{(\text{observed}_{ij} - \text{expected}_{ij})^2}{\text{expected}_{ij}} = 162.101. \quad (5.1)$$

The observed chi-square value 162.101 is higher than the critical value of the chi-square for $df = 51$ (77.373, $p < 0.01$) and the null hypothesis is rejected. Therefore, the correctness of the inverse solution is dependent on the used BSP map.

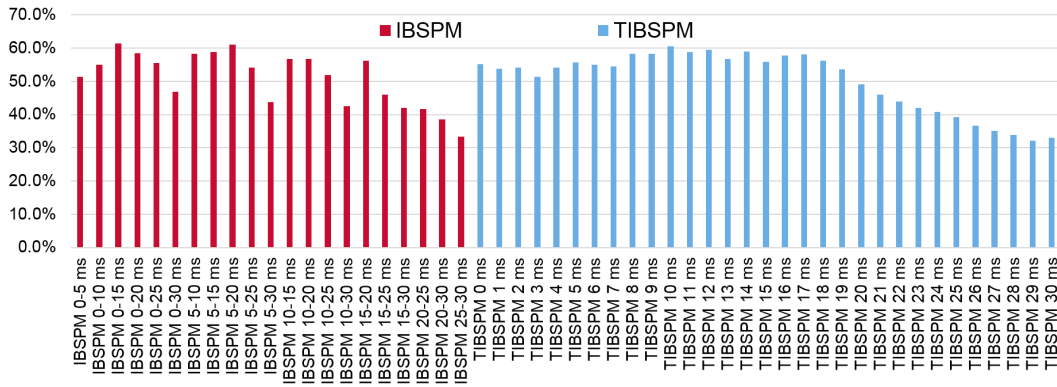


Figure 5.4: Percentage of correct inverse results for the selected 52 BSP maps. IBSPMs are presented in red color and TIBSPMs are presented in blue color

Since the null hypothesis is rejected, the second Person’s chi-square test is performed. This test differs from the first one in comparison of the BSP map, which provided the highest amount of the correct results versus all the other BSP maps. As can be seen from the Tab. C.1, the highest amount (in %) of the correct results was obtained for the IBSPM computed for the time interval 0–15 ms. Therefore, the contingency table has 2×2 size and is displayed in Tab. 5.2. Using the Eq. (3.11), we calculated the model of expected data and the results of these calculations are provided in the Tab. 5.3. Using the Eq. (3.12), we can determine the χ^2 :

$$\chi^2 = \sum \frac{(\text{observed}_{ij} - \text{expected}_{ij})^2}{\text{expected}_{ij}} = 4.77, \quad (5.2)$$

The observed chi-square value 4.77 is higher than the critical value of the chi-square for $df = 1$ (3.84, $p < 0.05$) and the null hypothesis is rejected. Therefore, the correctness of the inverse solution is dependent on the used body surface potential map and usage of the BSP map, obtained from the time interval 0–15 ms has 95% probability to provide highest amount of correct results.

Body surface potential map	Correctness of the inverse solution		Total
	Incorrect	Correct	
IBSPM 0-15 ms	36	57	93
All the other BSP maps	2615	2601	5216
Total	2651	2658	5309

Table 5.2: Contingency table showing how many correct inverse solutions were observed using IBSPM from 0–15 ms time interval versus all the other BSP maps

Body surface potential map	Correctness of the inverse solution		Total
	Incorrect	Correct	
IBSPM 0-15 ms	46	47	93
All the other BSP maps	2605	2611	5216
Total	2651	2658	5309

Table 5.3: Contingency table showing how many correct inverse solutions are expected (assuming independency of the inverse solution correctness from input BSP map) using IBSPM from 0–15 ms time interval versus all the other BSP maps

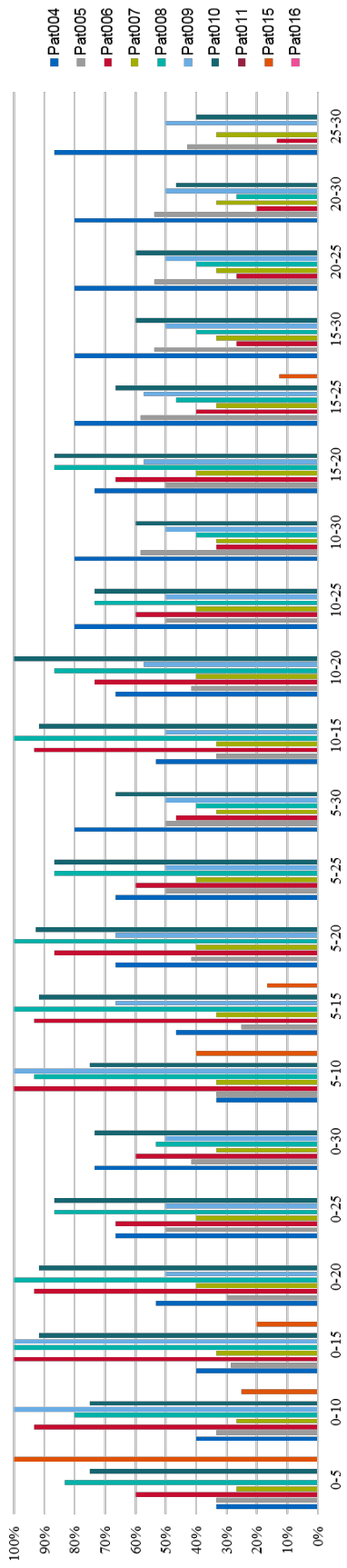


Figure 5.5: Percentage of the obtained correct inverse results from 21 input IBSPMs for each patient separately. Selected time interval of the defined initial 30 ms of the premature ventricular complex is given in milliseconds

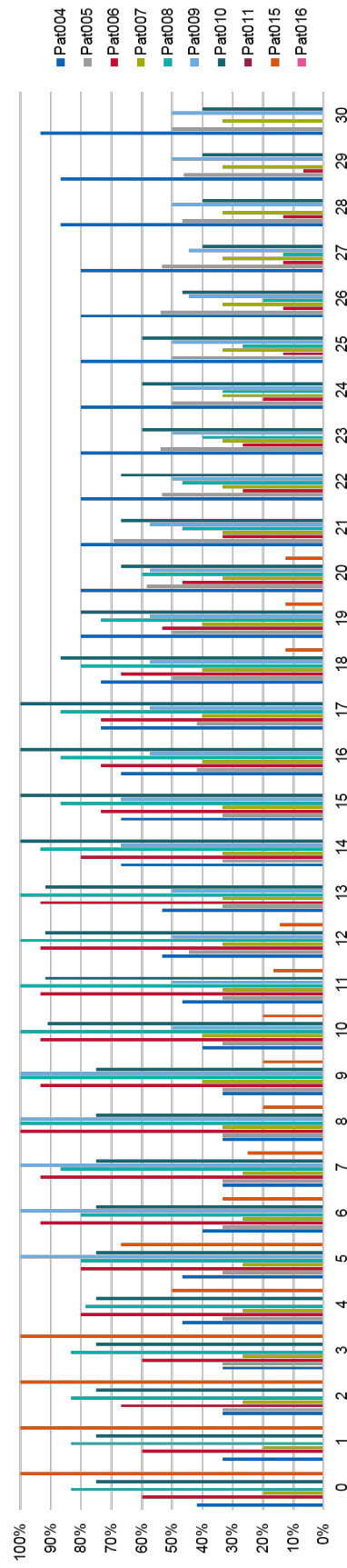


Figure 5.6: Percentage of the obtained correct inverse results from 31 input TBSPMs for each patient separately. Selected time instant of the defined initial 30 ms of the premature ventricular complex is given in milliseconds

5.3 Search of the patient-specific time instant for TIBSPM computation

As it was described in sec. 3.5.4, an approach to determine patient-specific time instant for computation of the TIBSPM was used. It was based on the correlations between all TIBSPMs, obtained from the selected 30 ms initial PVC time interval, for each of the 5 ectopic beats for each patient. The average of the correlation was calculated for each time instant for each beat separately. Results of these averaged correlations are presented in Fig. 5.7.

TIBSPM, which had the maximum averaged correlation between TIBSPMs from the selected initial 30 ms time interval, was used for inverse solution as input data in combination with each out of the three torso models of different complexity. Amount of the obtained relevant results of the inverse solutions using these TIBSPMs and amount of the correct relevant inverse results is given in Fig. 5.8 for each out of the three torso models with different complexity.

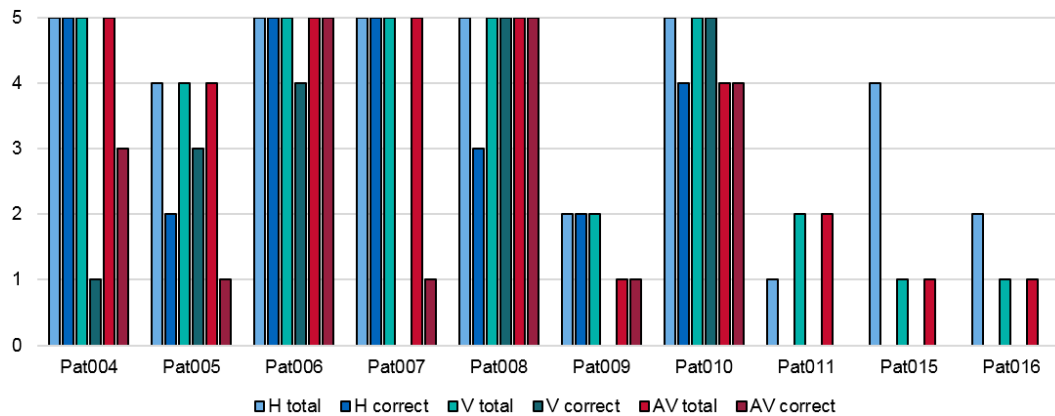


Figure 5.8: Number of the total and correct relevant inverse results obtained using TIBSPM with maximum averaged correlation between TIBSPMs of the selected initial 30 ms time interval in each out of five premature ventricular complexes and one of the torso models: homogeneous H, inhomogeneous V or inhomogeneous AV. Numbers of the total relevant inverse results are marked as “total”. Number of the correct relevant inverse results are marked as “correct”

From Fig. 5.8 it implies that the highest percentage of the correct relevant inverse results was obtained when TIBSPM with maximum averaged correlation was used in combination with homogeneous torso model H (68.4%), whereas using of the inhomogeneous torso models V and AV resulted in 51.4% and 60.6% success rate, respectively.

5.4 Evaluation of the impact of the torso model complexity on the inverse solution

The percentage of the number of correct relevant results depending on the torso model complexity are presented in Fig. 5.9. The same information regarding the percentage of the correct inverse results depending on the used torso model complexity in each patient is presented in Fig. 5.10. The contingency table describing frequencies of the correct and incorrect inverse results by torso model complexity is given in Tab. 5.4.

Using Eq. (3.11), we build a model of expected data (Tab. 5.5).

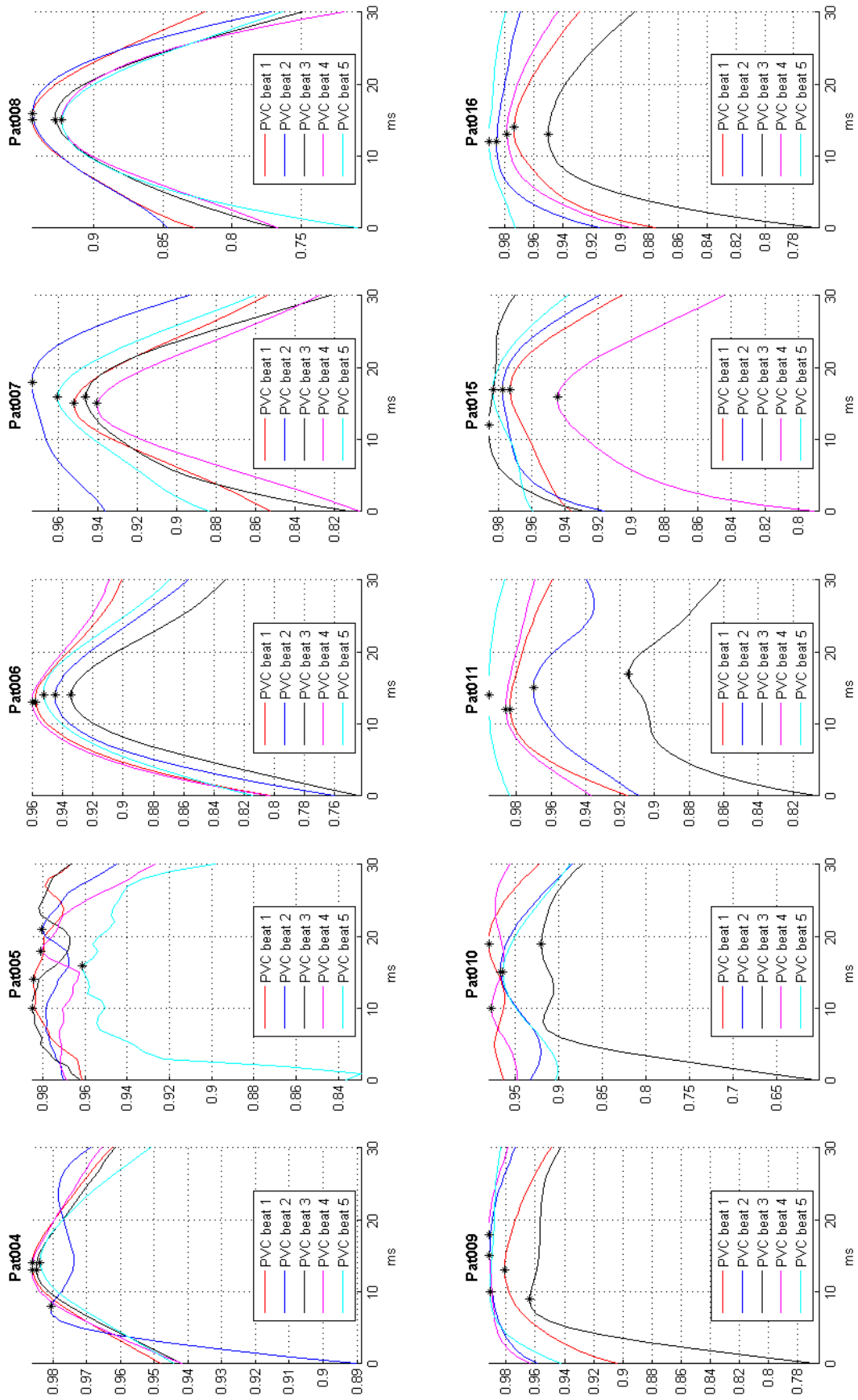


Figure 5.7: Averaged correlations of the TIBSPMs in each time instant for each of the five PVCs for each patient. Maximum is marked by asterisk *

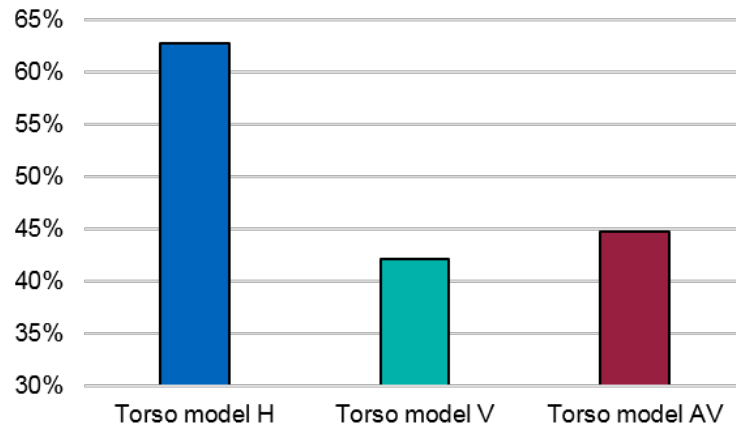


Figure 5.9: Amount of correct relevant inverse solutions (in %) obtained using integral and time instant BSP maps generated for five PVCs in each patient for three torso models with different inhomogeneities. H — homogeneous torso model, V — inhomogeneous torso model, AV — inhomogeneous torso model with highest level of complexity

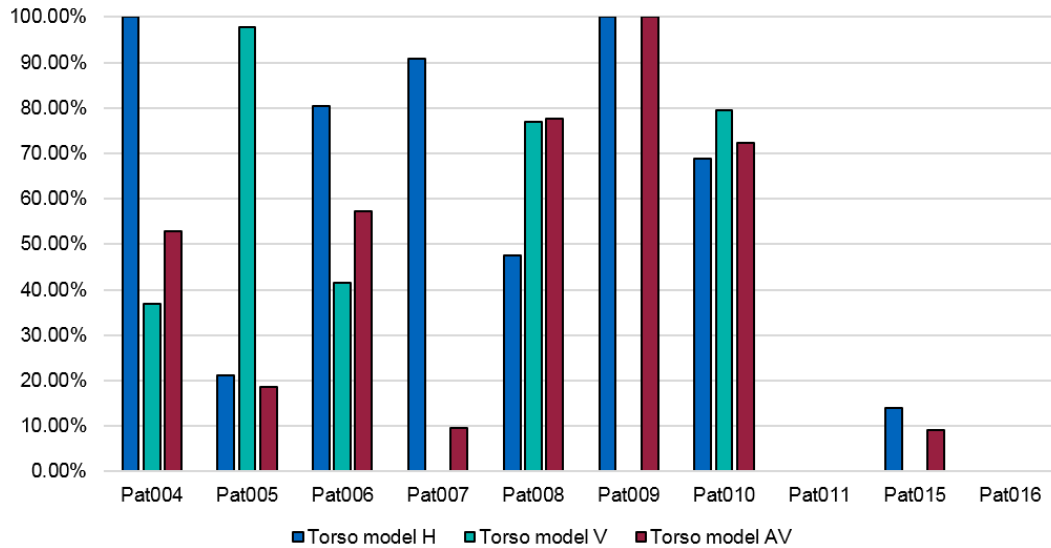


Figure 5.10: Percentage of obtained correct relevant inverse results for three levels of torso model complexity for each patient separately

Torso inhomogeneities	Correctness of the inverse solution		Total
	Incorrect	Correct	
Torso model H	676	1144	1820
Torso model V	1042	757	1799
Torso model AV	933	757	1690
Total	2651	2658	5309

Table 5.4: Contingency table showing how many correct relevant inverse solutions were observed using torso model with selected complexity

Using Eq. (3.12) we calculated the χ^2 :

$$\chi^2 = \sum \frac{(\text{observed}_{ij} - \text{expected}_{ij})^2}{\text{expected}_{ij}} = 183.81, \quad (5.3)$$

Torso inhomogeneities	Correctness of the inverse solution		Total
	Incorrect	Correct	
Torso model H	909	911	1820
Torso model V	898	901	1799
Torso model AV	844	846	1690
Total	2651	2658	5309

Table 5.5: Contingency table showing how many correct inverse solutions are expected (assuming independency of the inverse solution correctness from the torso model complexity) using torso model with selected complexity

The observed chi-square value 183.81 is higher than the critical value of the chi-square for $df = 2$ (9.21, $p < 0.01$) and the null hypothesis is rejected. Therefore, the correctness of the inverse solution is dependent on the complexity of the used torso model.

Since the null hypothesis is rejected, a new Person's chi-square test is performed to check whether the torso model, which gave the highest amount of the correct result, is better compared to the other two torso models joined in one category. The new contingency table is displayed in Tab. 5.6. The model of the expected data was calculated using Eq. (3.11) and is provided in Tab. 5.7.

Torso inhomogeneities	Correctness of the inverse solution		Total
	Incorrect	Correct	
Torso model H	676	1144	1820
Torso models V and AV	1975	1514	3489
Total	2651	2658	5309

Table 5.6: Contingency table showing how many correct relevant inverse solutions were observed using torso model with selected complexity

Torso inhomogeneities	Correctness of the inverse solution		Total
	Incorrect	Correct	
Torso model H	909	911	1820
Torso models V and AV	1742	1747	3489
Total	2651	2658	5309

Table 5.7: Contingency table showing how many correct inverse solutions are expected (assuming independency of the inverse solution correctness from the torso model complexity) using torso model with selected complexity

Calculations of the χ^2 value using the Eq. (3.12):

$$\chi^2 = \sum \frac{(\text{observed}_{ij} - \text{expected}_{ij})^2}{\text{expected}_{ij}} = 181.25, \quad (5.4)$$

The observed chi-square value 181.25 is significantly higher than the critical value of the chi-square for $df = 1$ (6.63, $p < 0.01$) and the null hypothesis is rejected. Therefore, the correctness of the highest amount of the inverse solution is dependent on the complexity of the used torso model.

5.5 Search of the best combination of the input data for the inverse solution

The frequencies of the correct relevant inverse results for the combinations, which had more than 60% correct inverse results, are displayed in Fig. 5.11. The contingency table describing frequencies of the correct and incorrect inverse results for all of the 156 combinations is given in Tab. C.3. Using the Eq. (3.11), a model of the expected data can be calculated. The results are presented in the Tab. C.4. Then, using Eq. (3.12) χ^2 is defined:

$$\chi^2 = \sum \frac{(\text{observed}_{ij} - \text{expected}_{ij})^2}{\text{expected}_{ij}} = 369.00, \quad (5.5)$$

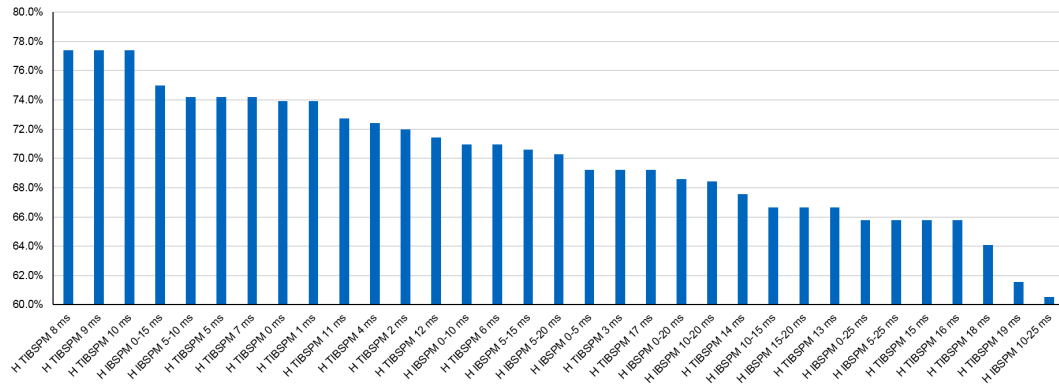


Figure 5.11: Percentage of the correct relevant inverse results for the combinations with more than 60% success. The first letter represents the used torso model: H — homogeneous torso model H. The second abbreviation represents the type of the used body surface potential map: IBSPM — integral, TIBSPM — time instant. The numbers represent the time interval or time instant

The observed chi-square value 369.00 is higher than the critical value of the chi-square for $df = 155$ (198.312, $p < 0.01$) and the null hypothesis is rejected. Therefore, the correctness of the inverse solution is dependent on the used combination of the input parameters of the inverse solution and there is a combination, yielding higher probability to obtain correct inverse result.

Since the null hypothesis is rejected, the further analysis is performed to define whether the combination of the input parameters for the inverse solution, which gave the highest amount of the correct result, is better compared to the other combinations joined in one category. According to the Tab. C.3, there are 3 combinations with highest amount of the correct inverse results. All combinations use the homogeneous torso model and a time instant map for the 8th, 9th or 10th ms. Therefore, the contingency table for the Person's chi-square test contains three best combinations and the remaining 153, joined into one category. The resulting table has 4×2 size and is displayed in Tab .5.8.

A model of the expected data is calculated using Eq. (3.11) and the results are provided in Tab. 5.9. The chi-square value χ^2 is defined using Eq. (3.12):

$$\chi^2 = \sum \frac{(\text{observed}_{ij} - \text{expected}_{ij})^2}{\text{expected}_{ij}} = 28.33, \quad (5.6)$$

The observed chi-square value 28.33 is higher than the critical value of the chi-square for $df = 3$ (11.34, $p < 0.01$) and the null hypothesis is rejected. Therefore, there are three

Combinations of the input parameters for the inverse solution	Correctness of the inverse solution		Total
	Incorrect	Correct	
H TIBSPM 8 ms	7	24	31
H TIBSPM 9 ms	7	24	31
H TIBSPM 10 ms	7	24	31
All other	2630	2586	5216
Total	2651	2658	5309

Table 5.8: Contingency table showing how many correct relevant inverse solutions were observed using the selected combination of the used body surface potential map and torso model with selected level of complexity

best combinations of the input parameters, using which there is a higher probability to obtain correct inverse result:

- 1) homogeneous torso model H and TIBSPM computed for 8 ms;
- 2) homogeneous torso model H and TIBSPM computed for 9 ms;
- 3) homogeneous torso model H and TIBSPM computed for 10 ms.

Combinations of the input parameters for the inverse solution	Correctness of the inverse solution		Total
	Incorrect	Correct	
H TIBSPM 8 ms	15.48	15.52	31
H TIBSPM 9 ms	15.48	15.52	31
H TIBSPM 10 ms	15.48	15.52	31
All other	15.48	15.52	5216
Total	2651	2658	5309

Table 5.9: Contingency table showing how many correct inverse solutions are expected (assuming independency of the inverse solution correctness from the used input combination) using the selected combination of the used body surface potential map and torso model with selected level of complexity

5.6 Evaluation of the stability of the inverse solution

For each input BSP map the inverse dipole is computed in each predefined position in the heart model and the position with the smallest RRE value is assumed as the best representative of the PVC origin. As it was described in sec. 3.5.7, two aspects of the stability of the inverse solution were assessed. First, analysis of the inverse solution spatial stability based on the minimal RRE value and best combination of input parameters is performed in sec. 5.6.1. Second, the spatial stability of the inverse solution in dependence on the input data variability was assessed for both input data — the BSP map (sec. 5.6.2) and the torso model (sec. 5.6.3).

5.6.1 Stability of the inverse solution using the best combination of input parameters based on the minimal RRE value

The best combination of input parameters (selected in sec. 5.5) consists of homogeneous torso model H and TIBSPM computed for the time instant 8 ms. The positions of the five dipoles of the inverse solution with the first five minimal, ascendingly sorted RRE values obtained from one input TIBSPM were examined. The assessment of the spatial stability of the inverse solution was based on calculations of the mean, standard deviation and quartiles of the distances between the positions of these five dipoles and their gravity center.

The mean and standard deviation of the distances between the positions of the dipoles and their gravity center for each of the patients were evaluated. Data range of the determined distances between the five dipoles and their gravity center for each patient is shown in box-and-whisker plot in Fig. 5.12. The smallest values were observed in Pat010 (2.4 ± 0.43 mm) and the highest values were in Pat011 (5.1 ± 2.37 mm). The results of the inverse solution for these two patients are depicted also in Fig. 5.13.

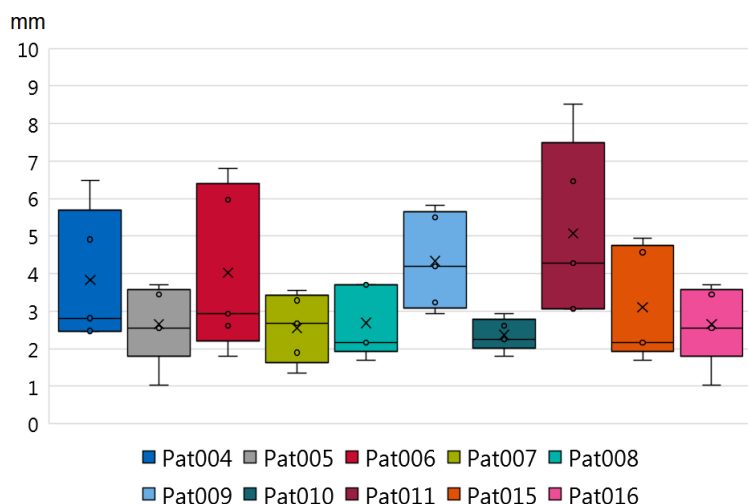
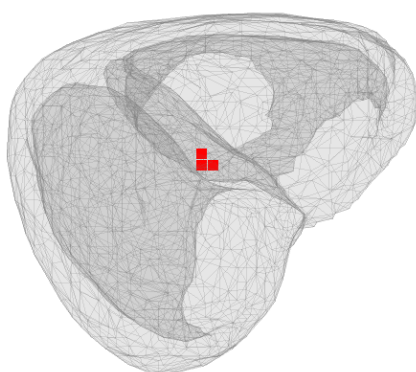
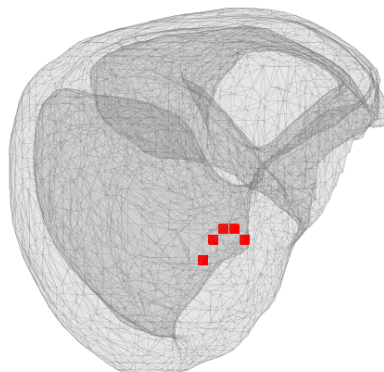


Figure 5.12: Box-and-whisker plot of the distances between the positions of the first five dipoles of the inverse solution with minimal RRE and their gravity center in each patient. Inverse solution was solved using the combination of the homogeneous torso model H and TIBSPM computed for time instant 8 ms. Five dipoles (instead of one) with minimal RRE were selected as the inverse solutions for one PVC



(a) Pat010 has the smallest values of the mean and SD of the distances between the dipole positions and their gravity center (2.4 ± 0.43 mm)



(b) Pat011 has the highest values of the mean and SD of the distances between the dipole positions and their gravity center (5.1 ± 2.37 mm)

Figure 5.13: Positions of the five dipoles of the inverse solutions with minimal RREs obtained for single PVC using TIBSPM in time instant 8 ms and homogeneous torso model H. Superior view

■ 5.6.2 Stability of the inverse solution in dependence on the BSP map variability

For evaluation of the spatial stability of the inverse solution in dependence on the BSP map variability, TIBSPMs in time instant 8 ms from five PVCs were used as input data of the inverse solution. For each of these 5 PVCs, five dipoles with minimal RRE were selected. Assessment of the distances between the positions of these twenty-five dipoles and their gravity center was performed for each patient. Data range of the determined distances between the twenty-five dipoles and their gravity center for each patient is shown in box-and-whisker plot in Fig. 5.14. The smallest values were obtained in Pat009 (3.9 ± 1.71 mm) and the highest values were in Pat011 (18.2 ± 14.17 mm). Results of the inverse solutions for these two patients are presented in Fig. 5.15.

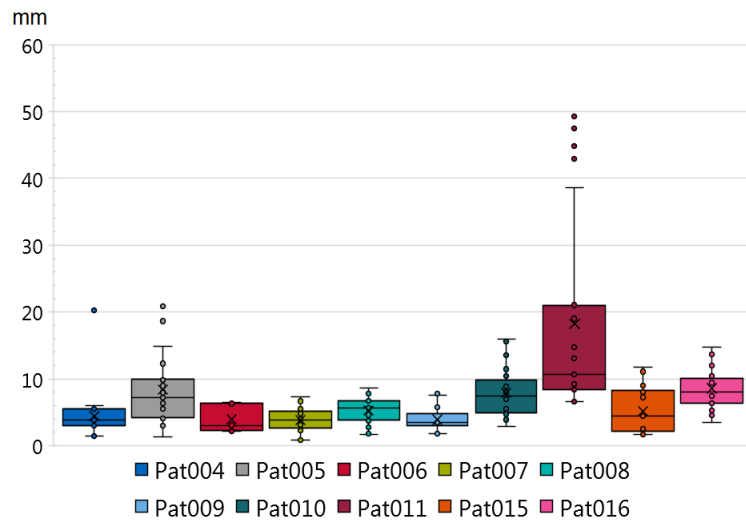


Figure 5.14: Box-and-whisker plot of the distances between the positions of the twenty-five dipoles of the inverse solutions and their gravity center in each patient. Inverse solution was solved using the combination of homogeneous torso model H and TIBSPM computed for time instant 8 ms. Five dipoles (instead of one) with minimal RRE were selected for each inverse solution for 5 PVCs

■ 5.6.3 Stability of the inverse solution in dependence on the torso model complexity

The spatial stability of the inverse solution in dependence on the torso model complexity was estimated using one of the BSP maps (IBSPM for the 0–15 ms time interval, which was selected in sec. 5.2) in combination with each of the three torso models (described in sec. 4.2.2). For each combination first five dipoles with minimal RRE values were selected. Evaluation of the distances between the positions of these five dipoles and their gravity center was performed for each combination in each of the ten patients. Mean and standard deviation of these distances in each patient are given in Fig. 5.16 and summarized for all patients — in Fig. 5.17.

In order to evaluate the dispersions of the obtained inverse results when the torso models of different complexity level are used, the F-test of equality of variances is used. As can be seen in Fig. 5.17, the smallest dispersion of the positions of the inverse results was gained when homogeneous torso model was used as input data for the inverse solution. The highest dispersion of the positions of the inverse results was obtained for the inhomogeneous torso model V, which was significantly higher ($p < 0.01$) than

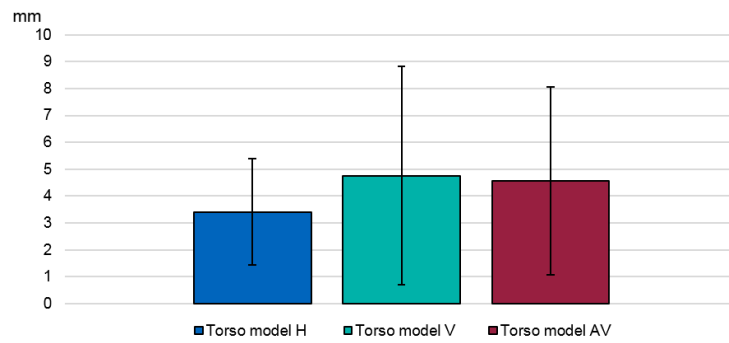


Figure 5.17: Mean and standard deviation of the positions of the five dipoles from their gravity center obtained for the inverse solutions with minimal RRE values computed for all 10 patients. Three combinations of the input data consisted of one BSP map (IBSPM for 0–15 ms time interval) and three torso models with different levels of complexity (torso model H — homogeneous, torso model V — inhomogeneous, torso model AV — refined inhomogeneous)

For detailed understanding of the variability of the evaluated distances between the inverse results positions and their gravity center when torso models with different level of complexity were used for the inverse solution, the box-and-whisker plots for all torso models are shown in Fig. 5.18 to Fig. 5.20.

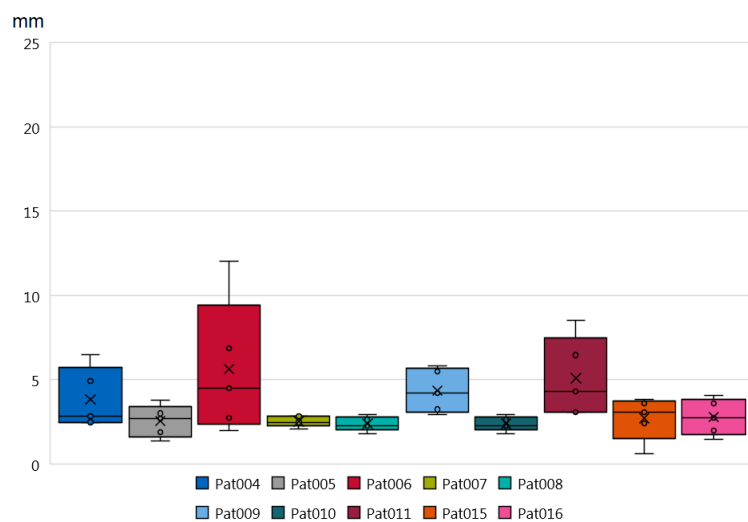


Figure 5.18: Box-and-whisker plot of the distances between the positions of the five dipoles of the inverse solution and their gravity center in each patient. Homogeneous torso model H and IBSPM 0–15 ms were used as input data for the inverse solution

When homogeneous torso model H was used as input data of the inverse solution, the smallest dispersion of the derived distances between the first five dipoles and their gravity center was observed in Pat008 and Pat010 (2.4 ± 0.43 mm), and the highest dispersion was observed in Pat006 (5.6 ± 4.04 mm). Obtained inverse results for these three patients are shown in Fig. 5.21.

When inhomogeneous torso model V was used as input data of the inverse solution, the smallest dispersion of the derived distances between the first five dipoles and their gravity center was observed in Pat015 (2.5 ± 0.96 mm), and the highest dispersion was observed in Pat009 (8.8 ± 7.03 mm). Obtained inverse results for these two patients are shown in Fig. 5.22.

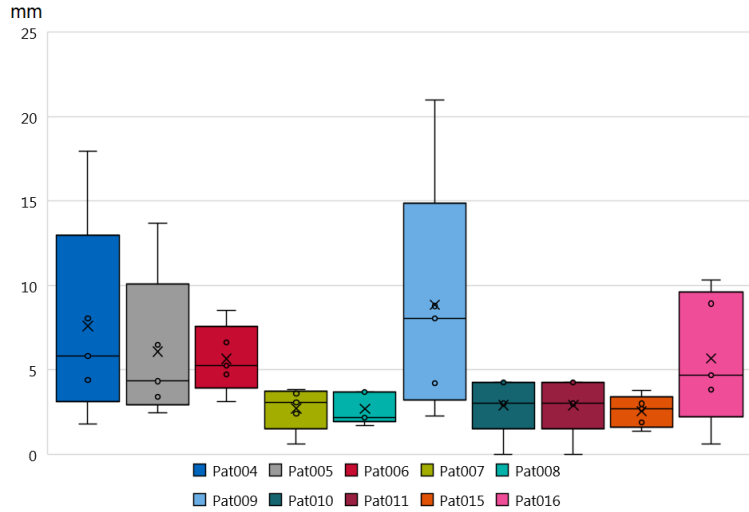


Figure 5.19: Box-and-whisker plot of the distances between the positions of the five dipoles of the inverse solution and their gravity center in each patient. Inhomogeneous torso model V and IBSPM 0–15 ms were used as input data for the inverse solution

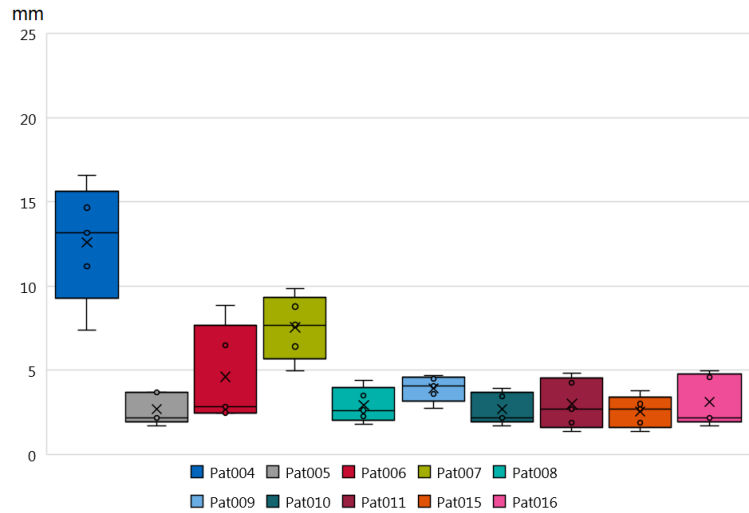
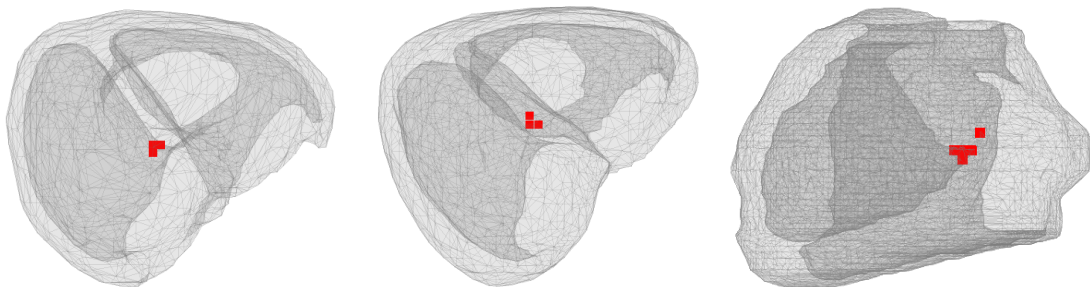
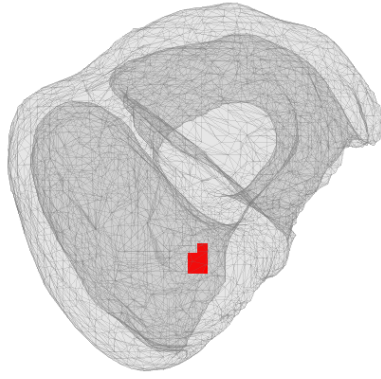


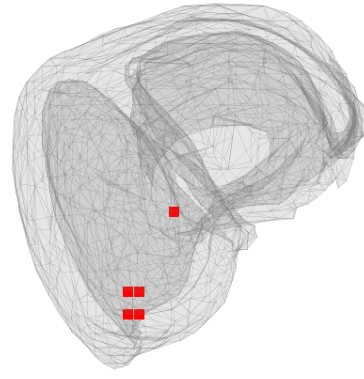
Figure 5.20: Box-and-whisker plot of the distances between the positions of the five dipoles of the inverse solution and their gravity center in each patient. Inhomogeneous torso model AV and IBSPM 0–15 ms were used as input data for the inverse solution



(a) Pat008. Superior view (b) Pat010. Superior view (c) Pat006. PA view
Figure 5.21: Positions of first five dipoles with minimal RRE value of the inverse solution for one BSP map (IBSPM 0–15 ms) and homogeneous torso model H



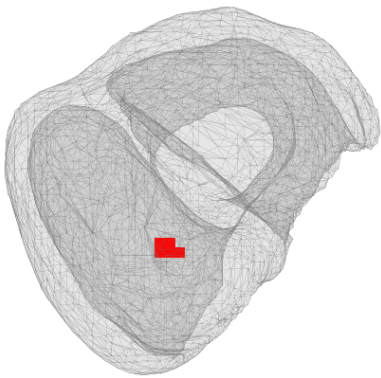
(a) Pat015. Superior view



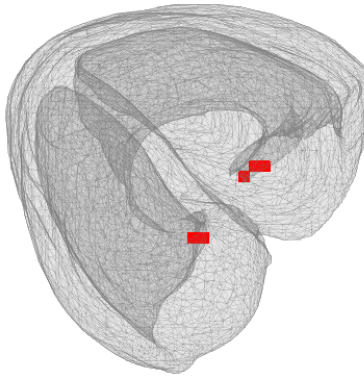
(b) Pat009. Superior view

Figure 5.22: Positions of first five dipoles with minimal RRE value of the inverse solution for one BSP map (IBSPM 0–15 ms) and inhomogeneous torso model V

When inhomogeneous torso model AV was used as input data of the inverse solution, the smallest dispersion of the derived distances between the first five dipoles and their gravity center was observed in Pat015 (2.5 ± 0.96 mm), and the highest dispersion was observed in Pat004 (12.6 ± 3.51 mm). Obtained inverse results for these two patients are shown in Fig. 5.23.



(a) Pat015. Superior view



(b) Pat004. Superior view

Figure 5.23: Positions of first five dipoles with minimal RRE value of the inverse solution for one BSP map (IBSPM 0–15 ms) and inhomogeneous torso model AV

In order to evaluate whether the gravity center of the determined inverse results shifts when torso model of different complexity is used, a distance between these three gravity centers was calculated (Fig. 5.24). The highest shift was observed in Pat007 between the gravity centers obtained from positions of the inverse solution with input data of homogeneous torso model H and inhomogeneous torso model V (21.4 mm), which is shown in Fig. 5.25. The smallest shift was observed in Pat016 between the gravity centers obtained from positions of the inverse solution with input data of homogeneous torso model H and inhomogeneous torso model AV (0.85 mm), which is shown in Fig. 5.26. Generally, the distances were higher between the homogeneous torso model H and the inhomogeneous torso model V or inhomogeneous torso model AV than between the two inhomogeneous torso models V and AV.

Chapter 6

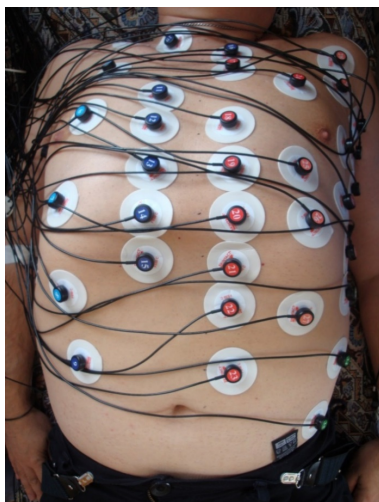
Discussion

6.1 Measurement-related issues

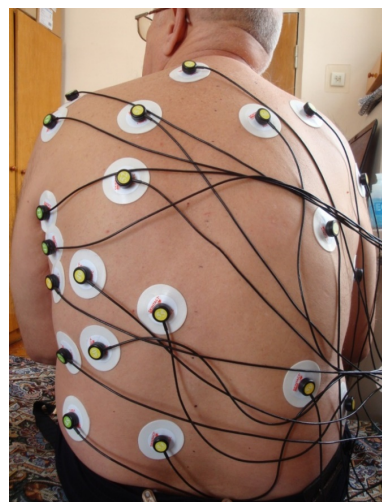
An accurate localization of the PVC focus before the invasive EP study and RFA can improve the success rate of the RFA and decrease the risks associated with the invasive EP procedure. Noninvasive localization of the PVC focus using BSP mapping and imaging modality (CT/MRI) can be achieved by solving the inverse problem.

A pilot study [J3] was performed in cooperation with the State Establishment “National M. Amosov Institute of Cardiovascular Surgery of the Academy of Medical Sciences of Ukraine” (Kyiv, Ukraine). The patient study group consisted of two male patients of 17 and 57 y.o.

The patients were measured using Amsterdam lead system with an irregular grid of 62 electrodes (Fig. 6.1). Therefore, each electrode had to be applied separately on the patient’s thorax. The procedure was very time consuming, impractical for the clinical use, and hard for the patients. That is why this lead system in this study was replaced by the 96 lead system with evenly distributed electrodes. It allowed using electrodes grouped in stripes. Currently, 12 stripes of the electrodes are placed in less than 5 minutes.



(a) AP view



(b) PA view

Figure 6.1: Patient P2 from a pilot study with Amsterdam lead system with an irregular grid of 62 electrodes. From [J3]

In this study, the patient group included male and female patients of different age varying 33–77 y.o. and torso geometry with body mass index 17.9–43.4. This variability in the group (from underweight to obese patients) resulted in a variability of the thorax structure models. In some female patients, the application of the stripes with electrodes was troublesome. The stripes had to be cut, in order to be placed on the upper part of

6.2 Golden truth of the PVC location and precision of the inverse solution

The correctness of the inverse solution was determined using agreement between the location of the inversely found equivalent dipole heart generator and assignment of area treated by the RFA to one of pre-defined segments of the heart by experienced clinician.

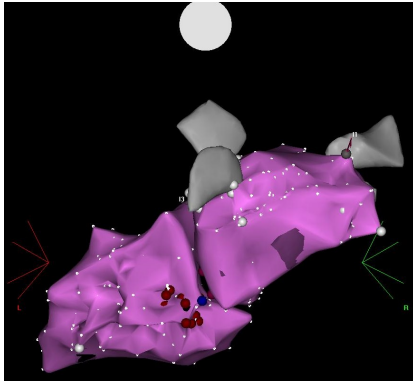
Obviously, the ideal way to evaluate the correctness and precision of the results would be the precise merging of the torso and heart models obtained from CT and during the EP study and measuring the distance between the location of the inverse result and location of the ablation point. Unfortunately, this was not possible in this work due to the following reasons:

- The software of the 3D navigational CARTO® system does not allow to import 3D models, created by another software. It means, that the heart model used for the inverse solution could not be imported to the 3D navigational CARTO® system to be used during the EP study and ablation. But, the CARTO® system allows to create 3D models from CT or MRI data using build-in tool. As it was already mentioned in sections 3.4 and 4.2.3, this/these 3D models are later merged/superposed with intracardial cavity model to provide clinician with additional and more reliable knowledge of the patient-specific heart anatomy.
- 3D models created by the 3D navigational CARTO® system from CT images are often distorted by the papillary muscles and are not smooth enough. Therefore, in spite of that these 3D models can be created long before the operation procedure and can be easily exported, they can not be used for the inverse problem computation as they will add numerical uncertainties and can hinder correct result.

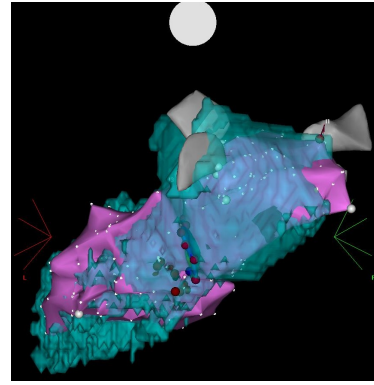
The only way in this situation would be to create two similar 3D models of the heart cavities from the same CT data using both software: the 3D navigational CARTO® system, and software used for CT images processing for the inverse problem — Tomo-Con PACS. This similar models of the heart cavities will be easily superposed thanks to the presence of reliable reference points (such as outflow tracts or coronary sinus) in both of them.

Since the ablation points are fixed only on the intracardial cavity model (Fig. 6.5a), this model should be merged with 3D heart model obtained from processed CT data using build-in tool of the CARTO® system. CARTO® system merging means that three reference points selected on the intracardial model are superposed with three reference points selected on the heart model from CT data. Thus, merging of the geometries implies not combination of two models into one, but alignment, resizing and rotation of the models to achieve minimal volume difference (Fig. 6.5b). In Fig. 6.6 is given an example of the merged geometries with used reference points, where can be seen how challenging it is to select the reliable reference points on the intracardial cavity model. Because intracardial cavity model has less reliable reference points the merging process should be performed during the EP study and its correctness should be checked by clinician invasively. It is also the reason why the intracardial cavity model can not be merged/superposed with the heart model used for the inverse solution straightaway.

Therefore, as it was already mentioned above, the heart cavity 3D model obtained from CT data using the build-in tool of the CARTO® navigation system should be merged/superposed with heart cavity 3D model obtained from the same CT data using the software for CT data processing for the inverse problem. Since both of the models will be created using the same CT images, there should be no significant difference be-

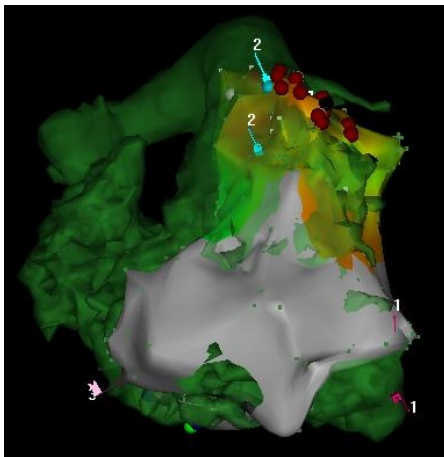


(a) Intraoperative endocardial geometry of the left atrium and left ventricle with ablation markers

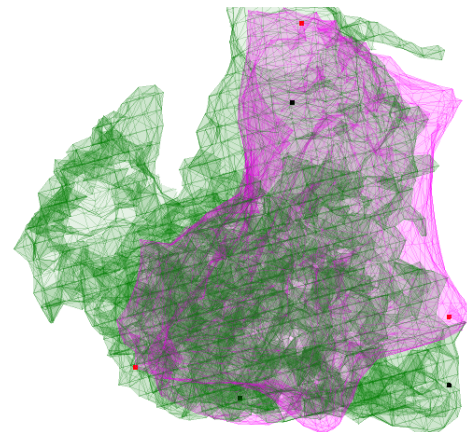


(b) merged/superposed geometries of the intraoperative endocardial geometries of the left cavities (pink) with 3D model of the left atrium and left ventricle reconstructed from CT images (cyan). Ablation markers are visible on intracardial model in vinous color

Figure 6.5: Geometries of the left cavities for Pat006 in PA projection



(a) view on 3D navigational CARTO® system. Reference points are marked with flags



(b) view in Matlab. Endocardial right ventricle model (pink color) reference points are marked by red squares and 3D model of right ventricle reconstructed from CT (green color) reference points are marked by black squares

Figure 6.6: Merged geometries of the intraoperative endocardial right ventricle with 3D model of the right ventricle reconstructed from CT of the Pat008. AP view

tween them. The result of this merging procedure is given in Fig. 6.7. These two merging procedures (intracardial cavity with heart cavity reconstructed using CARTO® system, heart cavity reconstructed using CARTO® system with heart cavity reconstructed using TomoCon PACS) allows to depict the ablation points from intracardial model in the heart cavity 3D model used for the inverse solution (Fig. 6.8).

This approach will be used in further studies after improvement of the merging algorithm. As can be seen in Fig. 6.7 there is a slight difference in the size of the 3D models heart cavities created using different software. The error is caused by the incorrect resizing value during the merging. When this issue will be solved, it would be

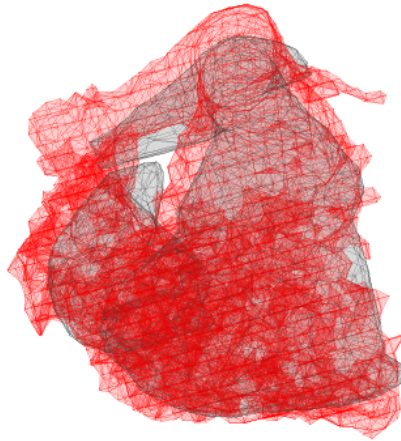
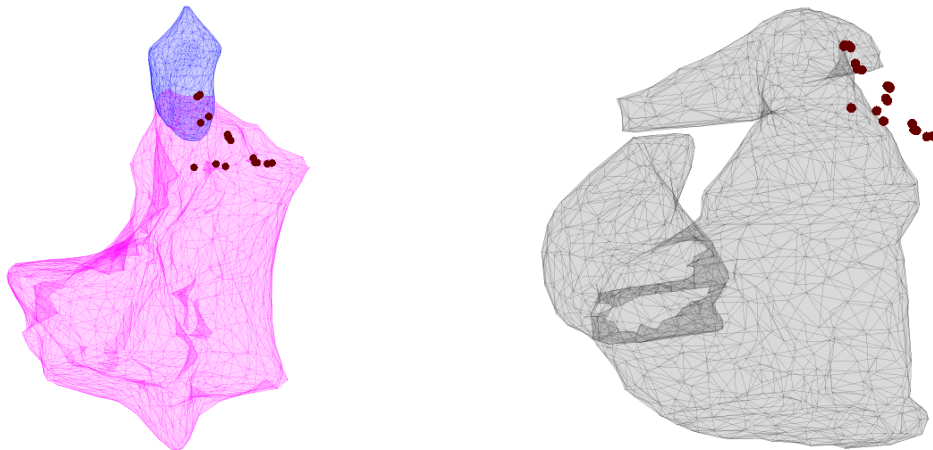


Figure 6.7: Right ventricle + right atrium + pulmonary artery 3D models of the Pat008. AP view. Grey color – 3D model reconstructed using CT data processing software (TomocCon PACS). Red color – 3D model reconstructed using build-in tool of the CARTO® system for CT data processing



(a) Intraoperative endocardial 3D model of the right ventricle (pink) with pulmonary artery (blue) with ablation points

(b) Joint 3D model of the right atrium, right ventricle and pulmonary artery used for the inverse solution with ablation points superposed after merging procedure

Figure 6.8: 3D models of the right ventricle with ablation points. AP view

possible to calculate the difference between the ablation lesion positions and location of the equivalent inverse dipole.

6.3 Analysis of the patients with small number of relevant results

All results were evaluated based on the RRE criterion (see sec. 3.5.2, Eq. (3.8)). In four patients, the percentage of relevant results was less than 40% (Fig. 5.1). As can be seen from Fig. 5.2, patients Pat011 and Pat016 did not have any correct relevant inverse results. This can be explained by the small amount of electrodes located in the heart region (Fig. 6.9). These examples prove that variability of the torso geometries and the location of the heart between the patients urges to make the protocol of the electrodes

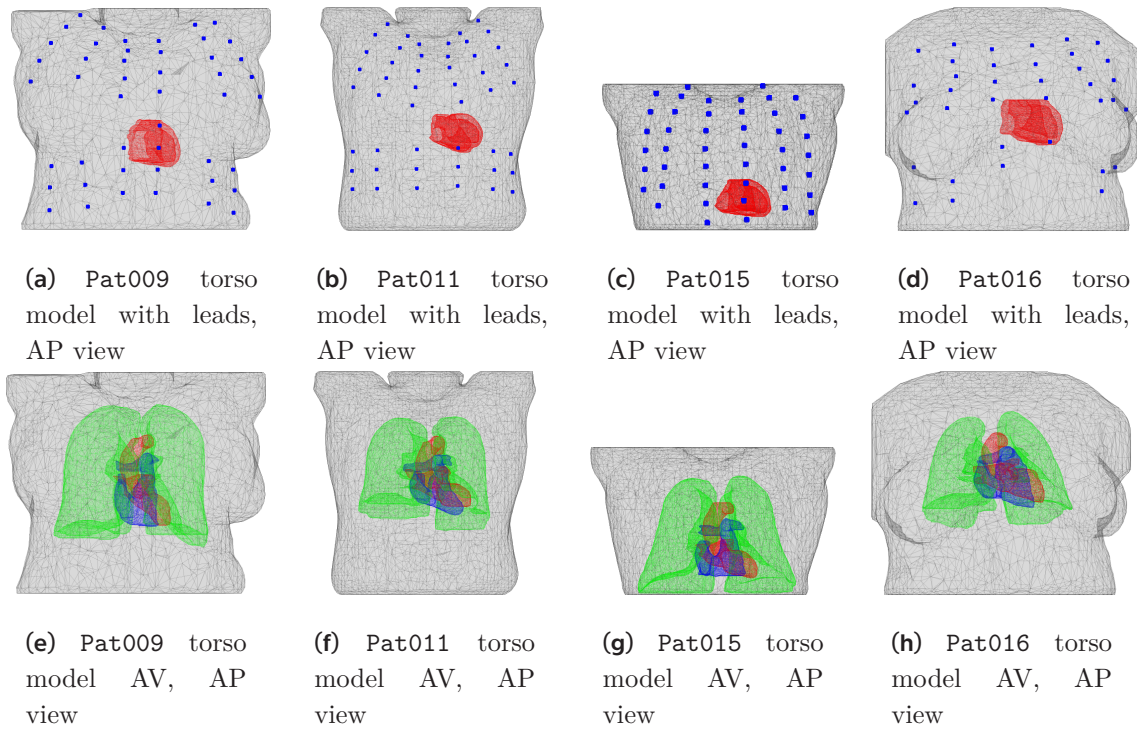


Figure 6.9: Torso models of the patients with RRE less than 40%

application more sophisticated. Currently, the procedure was based on placing the 28th electrode (it is forth electrode on the fourth stripe) on V_2 position.

In Pat015 patient the torso geometry ends exactly under the lungs but for numerical computations also lower part of the torso model should be present. In addition, as can be seen from the Fig.L.3 many incorrect dipoles were located in the neighboring segment. If they were considered as correct, the number of correct inverse results would drastically increase from 8.7% up to 100%.

In spite of the low percentage of the relevant inverse results in Pat009 patient, 73% of irrelevant inverse results were correct. High percentage of correct irrelevant inverse results was also observed in other two overweight female patients (Pat005 — 56.2%, Pat010 — 66.7%), which might signify/indicate of the need to increase the threshold for RRE in overweight and obese female patients. Fig. 6.10 represents mean and standard deviation of the RRE of the inverse solutions obtained using one of three torso models in combination with TIBSPM for male patient Pat006 and female patient Pat009, which were 0.15 ± 0.0242 (Pat006) and 0.32 ± 0.0411 (Pat009) for all combinations of the torso models and TIBSPMs.

There were variations of the RRE values when torso models with different level of complexity were taken into account (Fig. 6.10). Also, a tendency of the RRE decrease with increasing time was observed at the beginning of the observed interval in all patients. It was shown in [230] that RRE was higher and inverse solution results were not stable when the PVC focus was located in septum center, left ventricular apex or right ventricular posterior wall.

Thus, a thorough simulation study with confirmation in patients should be performed in order to evaluate the impact of the multiple factors on the RRE value: ECG noise presence, electrodes exclusion, position of the PVC focus, gender, overweight.

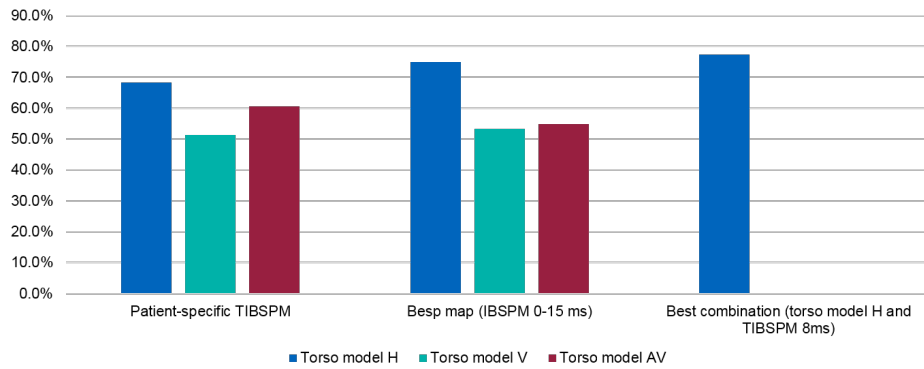


Figure 6.11: Percentage of correct relevant inverse results for one of the torso models (homogeneous H, inhomogeneous V, inhomogeneous AV) in combination with patient-specific TIBSPM or best map (IBSPM 0–15 ms, selected in sec. 5.3), and best combination of the input parameters (selected in sec. 5.5) — homogenous torso model H and TIBSPM 8 ms

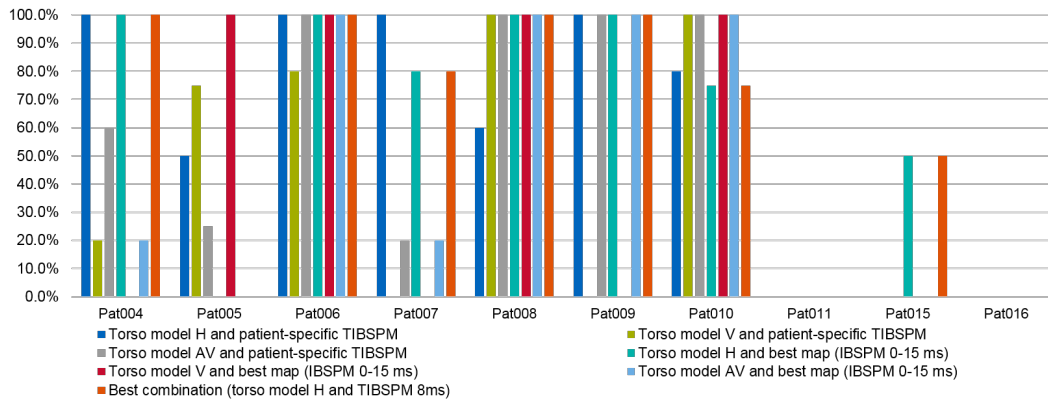


Figure 6.12: Percentage of obtained relevant inverse results for one of the torso models (homogeneous H, inhomogeneous V, inhomogeneous AV) in combination with patient-specific TIBSPM or best map (IBSPM 0–15 ms, selected in sec. 5.3), and best combination of input parameters (homogeneous torso model H and TIBSPM 8ms, selected in sec. 5.5) for each patient separately

6.5 Stability of the inverse solution

As it was mentioned before, the correctness of the results was not measured quantitatively, but qualitatively. Spatial stability of the inverse solution based on the minimal RRE criterion was merely estimated comparing the position of the “best” dipole with positions of the dipoles giving second to fifth best result and its dependency on fluctuation of input data was estimated using results from different beats or from using different torso models. Assessment of the spatial stability of the inverse solution depending on the torso model complexity showed that dispersion of the positions of the inverse results was smaller for homogeneous torso model H ($p < 0.01$) and is comparable with the 3 mm grid that determines the spatial resolution of the method. However, presence of high fluctuations in input BSP maps (e.g. in Pat011) can impair the stability.

Chapter 7

Conclusions

Noninvasive method for PVC focus localization was proposed using body surface potential mapping, and 3D model of the torso structure from a CT scan. The inverse solution was solved using a single dipole model (representing the heart generator), time instant/integral body surface potential map and a torso model.

Ten patients with frequent monomorphic PVCs underwent BSP mapping, a CT scanning and EP study with RFA. For each patient 5 PVCs were selected from ECG recordings from 96 chest leads. Semi-automatic method considering overall SNR was used to define the PVCs onset. For each PVC, 21 IBSPMs and 31 TIBSPMs were computed from initial 30 ms time interval.

Three torso models of different torso complexity were created from the CT scans: homogeneous torso model H (torso surface), inhomogeneous torso model V (torso, lungs, RV, LV); inhomogeneous torso model AV (torso, lungs, RA + RV + pulmonary artery, LA + LV + AO).

RFA was performed during an EP study to ablate the PVC focus. After successful RFA the clinician assigned the locations of the ablation lesion to one (or two in some cases) of predefined heart segments using a segment number according to AHA recommendations for the left ventricle division and its extension to the right ventricle, or using a 12-segment clock-like division for ablation lesions located in outflow tracts.

Inverse problem was solved for each of 5 PVCs for all 156 possible combinations of the input data: 21 IBSPMs and 31 TIBSPMs together with three levels of torso model complexity. Possible positions of the dipoles were specified in a 3 mm rectangular grid within the ventricular myocardium. The single dipole representing the PVC focus was selected based on the criterion of the relative residual error between the input BSP map and the map generated by the dipole. Only inverse solutions with RRE less or equal 0.3 were considered as relevant. Positions of the relevant inverse solution were compared with the locations of the ablation lesions obtained during EP study. If the segment assigned by clinician matched with the segment assigned to the position of the inverse solution, the solution was considered as correct.

Assessment of the inverse solution in terms of single dipole was based on the amount of correct inverse solutions. Evaluation of the obtained results can be summarized in the following points:

- The single dipole model representing the PVC focus can be used for the inverse solution for PVC focus localization.
- For all combinations of selected input parameters for all ten patients relevant results (with $RRE < 0.3$ suggesting that the real heart generator might be approximated by a dipole) were obtained in 68% cases.
- Threshold of the RRE criterion should be analyzed and specified more precisely in additional simulation study with confirmation in patients in order to evaluate the RRE dependence on multiple factors: ECG noise presence, electrodes exclusion, position of the PVC focus, gender, overweight.

Summary of achieved results and fulfillment of the goals

A noninvasive method for PVC focus localization was proposed using body surface potential mapping and 3D model of the torso structure obtained from a CT scan. The method is based on inverse solution using single dipole model as equivalent representation of the heat generator. The method was experimentally tested on a group of patients and influence of the selection and processing of input data on the correctness of obtained results and stability of the solution were analyzed.

Fulfillment of the goals of the thesis:

1. *Overview of existing noninvasive diagnostic methods for ventricular ectopic beat focus localization*

State of the art overview starts with presentation of medical fundamentals necessary for understanding of the thesis, which covers the heart anatomy (sec. 1.1), its electrical activity (sec. 1.2), types of cardiac arrhythmias (sec. 1.3) and their treatment (sec. 1.4). Chapter 1 describes also existing approaches to measurement (sec. 1.5), mapping (sec. 1.6) and modelling (sec. 1.7) of the cardiac electrical activity.

The existing noninvasive diagnostic methods based on solution of the inverse problem of electrocardiography and ECG imaging and their use for finding the pathological cardiac electrical generator models in ischemia, arrhythmias and particularly for the PVC focus localization are presented in the sec. 1.7.5, 1.7.6. ECG (sec. 1.5.2) remains to be the golden standard for the cardiac arrhythmia diagnostics. Nevertheless, ECG imaging shows promising results.

2. *Suggestion of a diagnostic method based on inverse solution and using appropriate electrical equivalent source, representing the pathological ventricular ectopic beat*

Proposal of the inverse method for PVC focus localization and its requirements were described in sec. 3.1. Single dipole model was selected to represent the small initially activated cardiac area during the pathological premature ventricular beat (sec. 3.1.1, 3.1.2).

Multichannel measuring system and ECG processing methods were suggested for obtaining the required distribution of the potential on the patient's torso in time (sec. 3.1.3, 3.2). CT scanning was selected to obtain the patient-specific torso geometry and structure as well as actual positions of the ECG electrodes (sec. 3.3). To verify the inverse solution correctness it was suggested to compare the with positions of the RFA lesions (sec. 3.4).

3. *Verification of the proposed method in patients*

Description of the measured patient group is presented (sec. 4.1). The patients with PVCs underwent BSP mapping (sec. 4.2.1), CT scanning (sec. 4.2.2), and EP

study with RFA (sec. 4.2.3). The inverse solution was computed using time integral or time instant BSP maps and patient-specific torso models with different levels of complexity. Behavior of the suggested method in patients with PVCs was tested by using different modifications of the input ECG and geometry data (156 combinations were used for evaluation of 5 selected PVCs in each patient 4.3). Results are presented in Chapter 5.

4. *Experimental study of the selection of the evaluated body surface potential map on stability and accuracy of the inverse solution*

The method proposed to study the BSP map interval impact on the inverse solution is described in sec. 3.5.3. Obtained results of the study are presented in sec. 5.2 and show that integral BSP map computed from the time interval 0–15 ms should be used as input for the inverse problem solution as it provides the highest amount of correct results ($p < 0.01$).

Patient-specific approach to selection of the input BSP data based on TIBSPM with the maximum correlation between the TIBSPMs from the whole studied 30 ms time interval was suggested (sec. 3.5.4). The use of patient-specific TIBSPM did not provide a significantly higher amount of correct inverse results 5.3.

Stability of the inverse solution and its dependence on the BSP fluctuations was assessed using the methods suggested in sec. 3.5.7 and evaluated in sec. 5.6.2.

5. *Study of the influence of torso model complexity on stability and accuracy of the inverse solution*

The proposed method for the study of the torso model complexity impact on the accuracy of the inverse solution was described in sec. 3.5.5 and the results are presented in sec. 5.4. It was shown that usage of the homogeneous torso model H provides the highest number of correct inverse solutions ($p < 0.01$).

Stability of the inverse solution in dependence of the selected torso model was analyzed using the approach suggested in sec. 3.5.7 and assessed in sec. 5.6.3.

In addition to goals 4 and 5, a method for finding the best combination of input parameters for the inverse solution (input BSP map and torso model) was suggested in sec. 3.5.6. Obtained results presented in sec. 5.5 show that homogeneous torso model H and TIBSPM computed for the time instant 8, 9 or 10 ms yield the highest probability to obtain correct results. Spatial stability of the inverse solution using this best combination was also assessed (sec. 5.6.1).

Based on the obtained results it can be stated, that after careful processing of the input ECG and CT data and evaluation of their quality, the proposed method for noninvasive localization of the PVC focus is able to supply pre-operative information identifying with high probability the proper heart segment with the PVC focus. Practical impact of using the method can be decreased time of the invasive EP study, higher safety, and reliability of the ablation therapy.



References

- [1] MALMIVUO, J., and R. PLONSEY. *Bioelectromagnetism*. New York, New York: Oxford University Press, 1995. ISBN 0-19-505823-2. ISSN 18255167.
- [2] DURRER, D., R. T. van DAM, G. E. FREUD, M. J. JANSE, F. L. MEIJLER, and R. C. ARZBAECHER. Total excitation of the isolated human heart. *Circulation*. 1970, Vol. 41, No. 6, pp. 899–912. ISSN 0009-7322. Available from DOI 10.1161/01.CIR.41.6.899.
- [3] CALAGHAN, S. C., J.-Y. LE GUENNEC, and E. WHITE. Cytoskeletal modulation of electrical and mechanical activity in cardiac myocytes. *Prog. Biophys. Mol. Biol.* jan, 2004, Vol. 84, No. 1, pp. 29–59. ISSN 0079-6107.
- [4] MACFARLANE, P. W., A. V. OOSTEROM, O. PAHLM, P. KLIGFIELD, M. JANSE, and J. CAMM. *Comprehensive electrocardiology*. London: Springer London, 2010. ISBN 978-1-84882-045-6. ISSN 1098-6596. Available from DOI 10.1007/978-1-84882-046-3.
- [5] OOSTEROM, A. van. Genesis of the T wave as based on an equivalent surface source model. *J. of Electrocardiol.* 2001, Vol. 34, No. 4, pp. 217–227. Available from DOI 10.1054/jelc.2001.28896.
- [6] PATTON, K. T., and G. A. THIBODEAU. *Anatomy & physiology*. Houston, Texas, USA: OpenStax College, 2010. ISBN 978-0-323-05532-1. <http://cnx.org/content/col11496/latest/>.
- [7] IAIZZO, P. A. *Handbook of cardiac anatomy, physiology, and devices*. Totowa, NJ: Humana Press, 2005. ISBN 1-59259-835-8.
- [8] CRANEFIELD, P. F., A. L. WIT, and B. F. HOFFMAN. Genesis of cardiac arrhythmias. *Circulation*. jan, 1973, Vol. 47, No. 1, pp. 190–204. ISSN 0009-7322. Available from DOI 10.1161/01.CIR.47.1.190.
- [9] ISSA, Z. F., J. M. MILLER, and D. P. ZIPES. *Clinical arrhythmology and electrophysiology: a companion to Braunwald's heart disease*. 7 ed. Philadelphia, USA: Saunders, 2007. ISBN 978-1-4160-5998-1.
- [10] ANTZELEVITCH, C., and A. BURASHNIKOV. Overview of basic mechanism of cardiac arrhythmia. *Card. Electrophysiol. Clinics*. 2011, Vol. 3, No. 1, pp. 23–45. Available from DOI 10.1016/j.ccep.2010.10.012.Overview.
- [11] BIEL, M. Cardiac HCN channels structure, function, and modulation. *Trends Cardiovasc. Med.* jul, 2002, Vol. 12, No. 5, pp. 206–213. ISSN 10501738. Available from DOI 10.1016/S1050-1738(02)00162-7.
- [12] BOLANOS, R., K. A. SELZMAN, L. JANTAC, and G. A. STOUFFER. *Hemodynamics of arrhythmias and pacemakers*. Chichester, UK: John Wiley & Sons, Ltd, 2017. ISBN 9781119066491. Available from DOI 10.1002/9781119066491.
- [13] BAMAN, T. S., D. C. LANGE, K. J. ILG, S. K. GUPTA, T.-Y. LIU, C. ALGUIRE, W. ARMSTRONG, E. GOOD, A. CHUGH, K. JONGNARANGSIN, F. PELOSI, T. CRAWFORD, M. EBINGER, H. ORAL, F. MORADY, and F. BOGUN. Relationship between



- burden of premature ventricular complexes and left ventricular function. *Heart Rhythm*. jul, 2010, Vol. 7, No. 7, pp. 865–9. ISSN 1556-3871. Available from DOI 10.1016/j.hrthm.2010.03.036.
- [14] CHA, Y. M., G. K. LEE, K. W. KLARICH, and M. GROGAN. Premature ventricular contraction-induced cardiomyopathy: a treatable condition. *Circ.-Arrhythmia Electrophysiol.* 2012, Vol. 5, No. 1, pp. 229–236. ISSN 19413149. Available from DOI 10.1161/CIRCEP.111.963348.
- [15] YOKOKAWA, M., E. GOOD, T. CRAWFORD, A. CHUGH, F. PELOSI, R. LATCHAMSETTY, K. JONGNARANGSIN, W. ARMSTRONG, H. GHANBARI, H. ORAL, F. MORADY, and F. BOGUN. Recovery from left ventricular dysfunction after ablation of frequent premature ventricular complexes. *Heart Rhythm*. feb, 2013, Vol. 10, No. 2, pp. 172–175. ISSN 15475271. Available from DOI 10.1016/j.hrthm.2012.10.011.
- [16] BAN, J.-E., H.-C. PARK, J.-S. PARK, Y. NAGAMOTO, J.-I. CHOI, H.-E. LIM, S.-W. PARK, and Y.-H. KIM. Electrocardiographic and electrophysiological characteristics of premature ventricular complexes associated with left ventricular dysfunction in patients without structural heart disease. *Europace*. may, 2013, Vol. 15, No. 5, pp. 735–741. ISSN 1099-5129. Available from DOI 10.1093/europace/eus371.
- [17] SADEK, M. M., and F. E. MARCHLINSKI. Ablation of ventricular arrhythmias. *Trends Cardiovasc. Med.* Elsevier, oct, 2014, Vol. 24, No. 7, pp. 296–304. ISSN 10501738. Available from DOI 10.1016/j.tcm.2014.07.002.
- [18] KNECHT, S., F. SACHER, M. WRIGHT, M. HOCINI, A. NOGAMI, T. ARENTZ, B. PETIT, R. FRANCK, C. DE CHILLOU, D. LAMAISON, J. FARRÉ, T. LAVERGNE, T. VERBEET, I. NAULT, S. MATSUO, L. LEROUX, R. WEERASOORIYA, B. CAUCHEMEZ, N. LELLOUCHE, N. DERVAL, S. M. NARAYAN, P. JAÏS, J. CLEMENTY, and M. HAÏSSAGUERRE. Long-term follow-up of idiopathic ventricular fibrillation ablation. *J. Am. Coll. Cardiol.* American College of Cardiology Foundation, aug, 2009, Vol. 54, No. 6, pp. 522–528. ISSN 07351097. Available from DOI 10.1016/j.jacc.2009.03.065.
- [19] DUKES, J. W., T. A. DEWLAND, E. VITTINGHOFF, M. C. MANDYAM, S. R. HECKBERT, D. S. SISCOVICK, P. K. STEIN, B. M. PSATY, N. SOTOODEHNIA, J. S. GOTTDIENER, and G. M. MARCUS. Ventricular ectopy as a predictor of heart failure and death. *J. Am. Coll. Cardiol.* 2015, Vol. 66, No. 2, pp. 101–109. ISSN 15583597. Available from DOI 10.1016/j.jacc.2015.04.062.
- [20] CLIFFORD, G. D., F. AZUAJE, and P. E. MCSHARRY. *Advanced methods and tools for ECG data analysis*. Norwood, MA, USA: Artech House, 2006. ISBN 978-1-58053-966-1.
- [21] LATCHAMSETTY, R., and F. BOGUN. Premature ventricular complex ablation in structural heart disease. *Card. Electrophysiol. Clinics*. 2017, Vol. 9, No. 1, pp. 133–140. ISSN 18779182. Available from DOI 10.1016/j.ccep.2016.10.010.
- [22] FOGOROS, R. N. *Antiarrhythmic drugs: a practical guide*. 2nd ed. ed. Oxford: Blackwell Futura, 2007. ISBN 978-1-4051-6351-4.
- [23] DAN, G.-A., A. MARTINEZ-RUBIO, S. AGEWALL, G. BORIANI, M. BORGGREFE, F. GAITA, I. van GELDER, B. GORENEK, J. C. KASKI, K. KJELDSSEN, G. Y. H. LIP, B. MERKELY, K. OKUMURA, J. P. PICCINI, T. POTPARA, B. K. POULSEN, M. SABA, I. SAVELIEVA, J. L. TAMARGO, C. WOLPERT, C. STICHERLING, J. R. EHRlich, R. SCHILLING, N. PAVLOVIC, T. DE POTTER, A. LUBINSKI, J. H. SVENDSEN, K.



- CHING, J. L. SAPP, C. CHEN-SCARABELLI, and F. MARTINEZ. Antiarrhythmic drugs—clinical use and clinical decision making: a consensus document from the European Heart Rhythm Association (EHRA) and European Society of Cardiology (ESC) Working Group on Cardiovascular Pharmacology, endorsed by the Heart Rhythm Society (HRS), Asia-Pacific Heart Rhythm Society (APHRs) and International Society of Cardiovascular Pharmacotherapy (ISCP). *EP Europace*. may, 2018, Vol. 20, No. 5, pp. 731–732an. ISSN 1099-5129. Available from DOI 10.1093/europace/eux373.
- [24] FOGOROS, R. N. *Electrophysiologic testing*. 4th ed. ed. Malden, Mass: Blackwell Futura, 2006. ISBN 9781405104784.
- [25] JOSEPHSON, M. E. *Clinical cardiac electrophysiology: techniques and interpretations*. 4 ed. Philadelphia: Wolters Kluwer Health/Lippincott Williams & Wilkins, 2008. ISBN 0781777399.
- [26] JOSEPH, J. P., and K. RAJAPPAN. Radiofrequency ablation of cardiac arrhythmias: past, present and future. *QJM*. apr, 2012, Vol. 105, No. 4, pp. 303–314. ISSN 1460-2725. Available from DOI 10.1093/qjmed/hcr189.
- [27] MURGATROYD, F. D., A. D. KRAHN, G. J. KLEIN, A. C. SKANES, and R. K. YEE. *Handbook of cardiac EP. Practical guide to invasive EP Studies and catheter ablation*. London, Great Britain: Remedica Publishing, 2002. ISBN 9781901346374.
- [28] FISHER, J. D., G. M. SCAVIN, J. A. ROTH, K. J. FERRICK, S. G. KIM, D. R. JOHNSTON, H. R. WILLIAMS, and R. FRAME. Direct current shock ablation: quantitative assessment of proarrhythmic effects. *PACE—Pacing Clin. Electrophysiol*. dec, 1991, Vol. 14, No. 12, pp. 2154–2166. ISSN 0147-8389. Available from DOI 10.1111/j.1540-8159.1991.tb06486.x.
- [29] WILBER, D. J., D. L. PACKER, and W. G. STEVENSON. *Catheter ablation of cardiac arrhythmias: basic concepts and clinical applications*. Malden, Massachusetts, USA: Blackwell Publishing, 2008. ISBN 978-1-4051-3117-9.
- [30] SCHMITT, C., I. DEISENHOFER, and B. ZRENNER. *Catheter ablation of cardiac arrhythmias*. Darmstadt: Steinkopff-Verlag, 2006. ISBN 3-7985-1575-1. Available from DOI 10.1007/3-7985-1576-X.
- [31] NATALE, A. *Handbook of cardiac electrophysiology*. London, UK: Informa Healthcare, 2007. ISBN 978 1 84184 620 0.
- [32] ECHT, D. S., P. R. LIEBSON, L. B. MITCHELL, R. W. PETERS, D. OBIASMANNO, A. H. BARKER, D. ARENSBERG, A. BAKER, L. FRIEDMAN, and H. L. GREENE. Mortality and morbidity in patients receiving encainide, flecainide, or placebo. The Cardiac Arrhythmia Suppression Trial. *N. Engl. J. Med*. mar, 1991, Vol. 324, No. 12, pp. 781–8. ISSN 0028-4793. Available from DOI 10.1056/NEJM199103213241201.
- [33] BURKART, F., M. PFISTERER, W. KIOWSKI, F. FOLLATH, and D. BURCKHARDT. Effect of antiarrhythmic therapy on mortality in survivors of myocardial infarction with asymptomatic complex ventricular arrhythmias: Basel antiarrhythmic study of infarct survival (BASIS). *J. Am. Coll. Cardiol*. dec, 1990, Vol. 16, No. 7, pp. 1711–1718. ISSN 07351097. Available from DOI 10.1016/0735-1097(90)90324-I.
- [34] CAIRNS, J. A., S. J. CONNOLLY, R. ROBERTS, and M. GENT. Randomised trial of outcome after myocardial infarction in patients with frequent or repetitive ventricular premature depolarisations: CAMIAT. Canadian Amiodarone Myocardial Infarction Arrhythmia Trial Investigators. *Lancet*. mar, 1997, Vol. 349, No. 9053, pp. 675–682. ISSN 0140-6736. Available from DOI 10.1016/S0140-6736(96)08171-8.

- [35] JULIAN, D. G., A. J. CAMM, G. FRANGIN, M. J. JANSE, A. MUNOZ, P. J. SCHWARTZ, and P. SIMON. Randomised trial of effect of amiodarone on mortality in patients with left-ventricular dysfunction after recent myocardial infarction: EMIAT. European Myocardial Infarct Amiodarone Trial Investigators. *Lancet*. mar, 1997, Vol. 349, No. 9053, pp. 667–674. ISSN 0140-6736.
- [36] SINGH, S. N., R. D. FLETCHER, S. G. FISHER, B. N. SINGH, H. D. LEWIS, P. C. DEEDWANIA, B. M. MASSIE, C. COLLING, and D. LAZZERI. Amiodarone in patients with congestive heart failure and asymptomatic ventricular arrhythmia. Survival Trial of Antiarrhythmic Therapy in Congestive Heart Failure. *N. Engl. J. Med.* jul, 1995, Vol. 333, No. 2, pp. 77–82. ISSN 0028-4793. Available from DOI 10.1056/NEJM199507133330201.
- [37] VORA, A., and S. KULKARNI. Pharmacotherapy to reduce arrhythmic mortality. *Indian Heart J.* Elsevier Ltd, 2014, Vol. 66, No. SUPPL. 1, pp. S113–S119. ISSN 00194832. Available from DOI 10.1016/j.ihj.2013.12.049.
- [38] HEINC, P. Kdy léčit komorové extrasystoly. *Interni medicina pro praxi*. 2007, Vol. 9, No. 10, pp. 448–452.
- [39] ZIPES, D. P., A. J. CAMM, M. BORGGREFE, A. E. BUXTON, B. CHAITMAN, M. FROMER, G. GREGORATOS, G. KLEIN, A. J. MOSS, R. J. MYERBURG, S. G. PRIORI, M. A. QUINONES, D. M. RODEN, M. J. SILKA, C. TRACY, J.-J. BLANC, A. BUDAJ, V. DEAN, J. W. DECKERS, C. DESPRES, K. DICKSTEIN, J. LEKAKIS, K. MCGREGOR, M. METRA, J. MORAIS, A. OSTERSPEY, J. L. TAMARGO, J. L. ZAMORANO, S. C. SMITH, A. K. JACOBS, C. D. ADAMS, E. M. ANTMAN, J. L. ANDERSON, S. A. HUNT, J. L. HALPERIN, R. NISHIMURA, J. P. ORNATO, R. L. PAGE, and B. RIEGEL. 2015 ESC Guidelines for the management of patients with ventricular arrhythmias and the prevention of sudden cardiac death. *Eur. Heart J.* 2015, Vol. 8, No. 9, pp. 746–837. ISSN 1099-5129. Available from DOI 10.1093/europace/eul108.
- [40] BOGUN, F., T. CRAWFORD, S. REICH, T. M. KOELLING, W. ARMSTRONG, E. GOOD, K. JONGNARANGSIN, J. E. MARINE, A. CHUGH, F. PELOSI, H. ORAL, and F. MORADY. Radiofrequency ablation of frequent, idiopathic premature ventricular complexes: comparison with a control group without intervention. *Heart Rhythm*. jul, 2007, Vol. 4, No. 7, pp. 863–867. ISSN 15475271. Available from DOI 10.1016/j.hrthm.2007.03.003.
- [41] EFREMIDIS, M., K. P. LETSAS, A. SIDERIS, and F. KARDARAS. Reversal of premature ventricular complex-induced cardiomyopathy following successful radiofrequency catheter ablation. *Europace*. apr, 2008, Vol. 10, No. 6, pp. 769–770. ISSN 1099-5129. Available from DOI 10.1093/europace/eun060.
- [42] TAKEMOTO, M., H. YOSHIMURA, Y. OHBA, Y. MATSUMOTO, U. YAMAMOTO, M. MOHRI, H. YAMAMOTO, and H. ORIGUCHI. Radiofrequency catheter ablation of premature ventricular complexes from right ventricular outflow tract improves left ventricular dilation and clinical status in patients without structural heart disease. *J. Am. Coll. Cardiol.* apr, 2005, Vol. 45, No. 8, pp. 1259–1265. ISSN 07351097. Available from DOI 10.1016/j.jacc.2004.12.073.
- [43] SENDEREK, T., J. BEDNAREK, and J. LELAKOWSKI. The effectiveness of RF ablation of ventricular ectopic beats made using selected mapping techniques. *Pol. Med. J.* nov, 2015, Vol. 39, No. 233, pp. 271–276. ISSN 1426-9686.
- [44] ADAMS, J. C., K. SRIVATHSAN, and W. K. SHEN. Advances in management of premature ventricular contractions. *J. Interv. Card. Electrophysiol.* nov, 2012, Vol. 35,



No. 2, pp. 137–49. ISSN 1572-8595. Available from DOI 10.1007/s10840-012-9698-x.

- [45] YAMADA, T., H. T. McELDERRY, H. DOPPALAPUDI, Y. MURAKAMI, Y. YOSHIDA, N. YOSHIDA, T. OKADA, N. TSUBOI, Y. INDEN, T. MUROHARA, A. E. EPSTEIN, V. J. PLUMB, S. P. SINGH, and G. N. KAY. Idiopathic ventricular arrhythmias originating from the aortic root prevalence, electrocardiographic and electrophysiologic characteristics, and results of radiofrequency catheter ablation. *J. Am. Coll. Cardiol.* jul, 2008, Vol. 52, No. 2, pp. 139–147. ISSN 1558-3597. Available from DOI 10.1016/j.jacc.2008.03.040.
- [46] BETENSKY, B. P., R. E. PARK, F. E. MARCHLINSKI, M. D. HUTCHINSON, F. C. GARCIA, S. DIXIT, D. J. CALLANS, J. M. COOPER, R. BALA, D. LIN, M. P. RILEY, and E. P. GERSTENFELD. The V2 transition ratio. *J. Am. Coll. Cardiol.* Elsevier Inc., may, 2011, Vol. 57, No. 22, pp. 2255–2262. Available from DOI 10.1016/j.jacc.2011.01.035.
- [47] STEVENSON, W. G., and K. SOEJIMA. Recording techniques for clinical electrophysiology. *J. Cardiovasc. Electrophysiol.* 2005, Vol. 16, No. 9, pp. 1017–1022. ISSN 10453873. Available from DOI 10.1111/j.1540-8167.2005.50155.x.
- [48] HUANG, S. K. S., and M. A. WOOD. *Catheter ablation of cardiac arrhythmias*. Philadelphia: Saunders/Elsevier, 2006. ISBN 1416003126.
- [49] BERBARI, E. Principles of electrocardiography. In: J. D. BRONZINO, ed. *The biomedical engineering handbook*. 2nd ed. Boca Raton, FL: CRC Press, 2000. pp. 525. ISBN 0-8493-0461-x. Available from DOI 10.1016/S0010-4825(01)00023-3.
- [50] SÖRNMO, L., and P. LAGUNA. *Bioelectrical signal processing in cardiac and neurological applications*. 1st ed. Boston, USA: Elsevier Academic Press, 2005. ISBN 9780124375529.
- [51] ASHLEY, E. A., and J. NIEBAUER. *Cardiology explained*. Chicago, IL, USA: Remedica Publishing, 2004. ISBN 978-1901346220.
- [52] BENNETT, D. H. *Bennett’s cardiac arrhythmia*. 8 ed. Oxford, UK: Wiley-Blackwell, 2013. ISBN 9780470674932.
- [53] TACCARDI, B. Distribution of heart potentials on the thoracic surface of normal human subjects. *Circulation Res.* apr, 1963, Vol. 12, No. 4, pp. 341–352. ISSN 0009-7330. Available from DOI 10.1161/01.RES.12.4.341.
- [54] ŠŤOVÍČEK, P. *Detection of global and local ischemic changes in electrical field of the heart*. Prague, Czech Republic: Charles University Prague, 2006. Ph.D. Thesis.
- [55] HOEKEMA, R., G. J. H. UIJEN, and A. van OOSTEROM. On selecting a body surface mapping procedure. *J. of Electrocardiol.* 1999, Vol. 32, No. 2, pp. 93–101.
- [56] TURZOVA, M., M. TYŠLER, and P. KNEPPO. A model study of the sensitivity of body surface potential distribution to variations of electrode placement. *J. of Electrocardiol.* jul, 1994, Vol. 27, No. 3, pp. 255–262. ISSN 00220736. Available from DOI 10.1016/S0022-0736(94)80010-3.
- [57] VANHEUSDEN, F. J., X. LI, G. S. CHU, T. P. ALMEIDA, G. A. NG, and F. S. SCHLINDWEIN. Analysis of spatial variability for the development of reduced lead body surface maps. In: *Computing in Cardiology Conference (CinC)*. Zaragoza, Spain: IEEE, 2013. pp. 535–538. ISBN 9781479908844. ISSN 23258861.

- [58] MEDTRONIC. *Medtronic CardioInsight mapping solution cleared by FDA*.
<http://newsroom.medtronic.com/phoenix.zhtml?c=251324&p=irol-newsArticle&ID=2241264>.
- [59] BARR, R. C., M. S. SPACH, and G. S. HERMAN-GIDDENS. Selection of the number and positions of measuring locations for electrocardiography. *IEEE Trans. Biomed. Eng.* mar, 1971, Vol. BME-18, No. 2, pp. 125–138. ISSN 0018-9294. Available from DOI 10.1109/TBME.1971.4502813.
- [60] LUX, R. L., C. R. SMITH, R. F. WYATT, and J. A. ABILDSKOV. Limited lead selection for estimation of body surface potential maps in electrocardiography. *IEEE Trans. Biomed. Eng.* 1978, Vol. BME-25, No. 3, pp. 270–276. ISSN 15582531. Available from DOI 10.1109/TBME.1978.326332.
- [61] LUX, R. L., M. J. BURGESS, R. F. WYATT, A. K. EVANS, G. M. VINCENT, and J. A. ABILDSKOV. Clinically practical lead systems for improved electrocardiography: comparison with precordial grids and conventional lead systems. *Circulation*. feb, 1979, Vol. 59, No. 2, pp. 356–363. ISSN 0009-7322. Available from DOI 10.1161/01.CIR.59.2.356.
- [62] FINLAY, D. D., C. D. NUGENT, M. P. DONNELLY, R. L. LUX, P. J. MCCULLAGH, and N. D. BLACK. Selection of optimal recording sites for limited lead body surface potential mapping: a sequential selection based approach. *BMC Med. Inform. Decis. Mak.* 2006, Vol. 6, pp. 1–9. ISSN 14726947. Available from DOI 10.1186/1472-6947-6-9.
- [63] DONNELLY, M. P., D. D. FINLAY, C. D. NUGENT, and N. D. BLACK. Lead selection: old and new methods for locating the most electrocardiogram information. *J. of Electrocardiol.* 2008, Vol. 41, No. 3, pp. 257–263. ISSN 00220736. Available from DOI 10.1016/j.jelectrocard.2008.02.004.
- [64] IDEKER, R. E., W. M. SMITH, S. M. BLANCHARD, S. L. REISER, E. V. SIMPSON, P. D. WOLF, and N. D. DANIELEY. The assumptions of isochronal cardiac mapping. *PACE—Pacing Clin. Electrophysiol.* mar, 1989, Vol. 12, No. 3, pp. 456–478. ISSN 0147-8389.
- [65] HSING, J., P. J. WANG, and A. AL-AHMAD. Electroanatomical mapping technologies. In: A. AL-AHMAD, D. J. CALLANS, H. HSIA, and A. NATALE, eds. *Electroanatomical mapping*. Oxford, UK: Blackwell Publishing, 2008. pp. 1–6. ISBN 978-1-4051-5702-5. Available from DOI 10.1002/9781444300284.
- [66] GEPSTEIN, L., H. GAL, and A. B.-H. SHLOMO. A novel method for nonfluoroscopic catheter-based electroanatomical mapping of the heart. *Circulation*. 1997, Vol. 95, No. 6, pp. 1611–1622.
- [67] WITTKAMPF, F. H., E. F. WEVER, R. DERKSEN, A. A. WILDE, H. RAMANNA, R. N. HAUER, and E. O. ROBLES DE MEDINA. LocaLisa: new technique for real-time 3-dimensional localization of regular intracardiac electrodes. *Circulation*. mar, 1999, Vol. 99, No. 10, pp. 1312–1317. ISSN 0009-7322.
- [68] GROOT, N. M. de, M. BOOTSMA, E. T. van der VELDE, and M. J. SCHALIJ. Three-dimensional catheter positioning during radiofrequency ablation in patients: first application of a real-time position management system. *J. Cardiovasc. Electrophysiol.* nov, 2000, Vol. 11, No. 11, pp. 1183–1192. ISSN 1045-3873.
- [69] VENTURA, R., T. ROSTOCK, H. U. KLEMM, B. LUTOMSKY, C. DEMIR, C. WEISS, T. MEINERTZ, and S. WILLEMS. Catheter ablation of common-type atrial flutter guided by three-dimensional right atrial geometry reconstruction and catheter



- tracking using cutaneous patches: a randomized prospective study. *J. Cardiovasc. Electrophysiol.* 2004, Vol. 15, No. 10, pp. 1157–1161. ISSN 10453873. Available from DOI 10.1046/j.1540-8167.2004.04064.x.
- [70] SCHALIJ, M. J., F. P. van RUGGE, M. SIEZENGA, and E. T. van der VELDE. Endocardial activation mapping of ventricular tachycardia in patients: first application of a 32-site bipolar mapping electrode catheter. *Circulation.* nov, 1998, Vol. 98, No. 20, pp. 2168–79. ISSN 0009-7322.
- [71] SCHILLING, R. J., N. S. PETERS, and D. W. DAVIES. Feasibility of a noncontact catheter for endocardial mapping of human ventricular tachycardia. *Circulation.* may, 1999, Vol. 99, No. 19, pp. 2543–2552. ISSN 0009-7322. Available from DOI 10.1161/01.CIR.99.19.2543.
- [72] MALKIN, R., N. KRAMER, B. SCHNITZ, M. GOPALAKRISHNAN, and A. L. CURRY. Advances in electrical and mechanical cardiac mapping. *Physiol. Meas.* feb, 2005, Vol. 26, No. 1, pp. R1–R14. ISSN 0967-3334. Available from DOI 10.1088/0967-3334/26/1/R01.
- [73] PACKER, D. L. Three-dimensional mapping in interventional electrophysiology: techniques and technology. *J. Cardiovasc. Electrophysiol.* oct, 2005, Vol. 16, No. 10, pp. 1110–1116. ISSN 1045-3873. Available from DOI 10.1111/j.1540-8167.2005.50161.x.
- [74] SKÁLA, T., and M. TÁBORSKÝ. Electromechanical mapping in electrophysiology and beyond. *Cor et Vasa.* 2015, Vol. 57, No. 6, pp. e470–e482. ISSN 18037712. Available from DOI 10.1016/j.crvasa.2015.10.002.
- [75] TYŠLER, M., J. ŠVEHLÍKOVÁ, V. ROSÍK, S. KARAS, E. HEBLÁKOVÁ, P. KNEPPO, J. MUZIK, M. KANIA, R. ZACZEK, and M. KOBYLECKA. Model-based method and instrumentation for noninvasive identification of local ischemic lesions in the heart. In: O. DÖSSEL, and W. C. SCHLEGEL, eds. *IFMBE Proc.* Munich, Germany: Springer, Berlin, Heidelberg, 2009. pp. 1403–1406. ISBN 9783642038815. ISSN 16800737. Available from DOI 10.1007/978-3-642-03882-2-372.
- [76] MEDVEGY, M., G. DURAY, A. PINTÉR, and I. PRÉDA. Body surface potential mapping: historical background, present possibilities, diagnostic challenges. *Ann. Noninvasive Electrocardiol.* apr, 2002, Vol. 7, No. 2, pp. 139–151. ISSN 1082-720X.
- [77] KORNREICH, F. Clinical utility of body surface potential mapping. *Cardiac Electrophysiol. Rev.* 1997, Vol. 3, pp. 304–307.
- [78] TYŠLER, M., V. ROSÍK, P. KAL’AVSKÝ, and G. BUKOR. Portable high resolution multichannel ECG measuring device. In: *Proc. of the 9th Int. Conf. MEASUREMENT 2013.* Smolenice, Slovakia: Institute of Measurement Science, 2013. pp. 161–164.
- [79] POTSE, M., A. C. LINNENBANK, and C. A. GRIMBERGEN. Automated generation of isochronal maps in the presence of activation block. *Int. J. of Bioelectromagnetism.* 2002, Vol. 4, No. 2, pp. 115–116.
- [80] DALY, M. J., D. D. FINLAY, P. J. SCOTT, C. D. NUGENT, A. A. J. ADGEY, and M. T. HARBINSON. Pre-hospital body surface potential mapping improves early diagnosis of acute coronary artery occlusion in patients with ventricular fibrillation and cardiac arrest. *Resuscitation.* jan, 2013, Vol. 84, No. 1, pp. 37–41. ISSN 1873-1570. Available from DOI 10.1016/j.resuscitation.2012.09.008.
- [81] FARINA, D., and O. DÖSSEL. Non-invasive model-based localization of ventricular ectopic centers from multichannel ECG. *Int. J. Appl. Electromagn. Mech.* 2009,




Vol. 30, No. 3-4, pp. 289–297. ISSN 13835416. Available from DOI 10.3233/JAE-2009-1029.

- [82] LAI, D., J. SUN, Y. LI, and B. HE. Usefulness of ventricular endocardial electric reconstruction from body surface potential maps to noninvasively localize ventricular ectopic activity in patients. *Phys. Med. Biol.* jun, 2013, Vol. 58, No. 11, pp. 3897–3909. ISSN 0031-9155. Available from DOI 10.1088/0031-9155/58/11/3897.
- [83] ROSÍK, V., S. KARAS, E. HEBLÁKOVÁ, M. TYŠLER, and S. FILIPOVÁ. Portable device for high resolution ECG mapping. *Meas. Sci. Rev.* 2007, Vol. 7, No. 6, pp. 57–61.
- [84] KANIA, M., R. MANIEWSKI, R. ZACZEK, M. KOBYLECKA, G. OPOLSKI, and L. KROLICKI. Exercise induced depolarization changes in BSPMs for assessment of ischemic heart disease. In: *Computing in Cardiology Conference (CinC)*. Nice, France: IEEE, 2015. pp. 945–948. ISBN 978-1-5090-0685-4. Available from DOI 10.1109/CIC.2015.7411068.
- [85] POTSE, M., A. C. LINNENBANK, and C. A. GRIMBERGEN. Software design for analysis of multichannel intracardial and body surface electrocardiograms. *Comput. Meth. Programs Biomed.* 2002, Vol. 69, No. 3, pp. 225–236. ISSN 01692607. Available from DOI 10.1016/S0169-2607(02)00014-7.
- [86] MOHAN, G. C., and S. DEVI. Forward problem in electrocardiogram: a review of certain approaches. *IOSR J. of Eng.* aug, 2013, Vol. 3, No. 8, pp. 21–24. ISSN 22788719. Available from DOI 10.9790/3021-03832124.
- [87] GULRAJANI, R. M. The forward and inverse problems of electrocardiography. *IEEE Eng. Med. Biol. Mag.* 1998, Vol. 17, No. 5, pp. 84–122. Available from DOI 10.1109/51.715491.
- [88] YAMASHITA, Y. Theoretical studies on the inverse problem in electrocardiography and the uniqueness of the solution. *IEEE Trans. Biomed. Eng.* 1982, Vol. BME-29, No. 11, pp. 719–725. Available from DOI 10.1109/TBME.1982.325002.
- [89] HELMHOLTZ, H. Ueber einige Gesetze der Vertheilung elektrischer Ströme in körperlichen Leitern, mit Anwendung auf die thierisch-elektrischen Versuche (Schluss.). *Annalen der Phys. und Chem.* 1853, Vol. 165, No. 7, pp. 353–377. ISSN 00033804. Available from DOI 10.1002/andp.18531650702.
- [90] TYŠLER, M. *Možnosti využití mapování a modelování elektrického pole srdce v kardiologické diagnostice.*
- [91] OOSTEROM, A. van. Source models in inverse electrocardiography. *Int. J. of Bioelectromagnetism.* 2003, Vol. 5, No. 1, pp. 211–214.
- [92] DÖSSEL, O. Inverse problem of electro-and magnetocardiography: review and recent progress. *Int. J. of Bioelectromagnetism.* 2000, Vol. 2, No. 2, pp. 1–43.
- [93] FARINA, D. *Forward and inverse problems of electrocardiography: clinical investigations.* Karlsruhe, Germany: Karlsruhe Institute of Technology (KIT) Institute of Biomedical Engineering, 2008. Ph.D. Thesis.
- [94] FUKUOKA, Y., T. F. OOSTENDORP, D. A. SHERMAN, and A. A. ARMOUNDAS. Applicability of the single equivalent moving dipole model in an infinite homogeneous medium to identify cardiac electrical sources: a computer simulation study in a realistic anatomic geometry torso model. *IEEE Trans. Biomed. Eng.* dec, 2006, Vol. 53, No. 12, pp. 2436–2444. ISSN 0018-9294. Available from DOI 10.1109/TBME.2006.880882.

- [95] SHOU, G., L. XIA, M. JIANG, F. LIU, and S. CROZIER. Forward and inverse solutions of electrocardiography problem using an adaptive BEM method. *Functional Imaging and Modeling of the Heart*. 2007, Vol. 4466, pp. 290–299. ISSN 03029743. Available from DOI 10.1109/TBME.2003.821027.
- [96] LAI, D., C. LIU, M. D. EGGEN, P. A. IAIZZO, and B. HE. Cardiac source localization by means of a single moving dipole solution during endocardial pacing in an animal model. In: *31st Annual International Conference of the IEEE Engineering in Medicine and Biology Society*. Minneapolis, Minnesota, USA: IEEE, 2009. pp. 1778–1780. ISBN 9781424432967. ISSN 1557-170X. Available from DOI 10.1109/IEMBS.2009.5334014.
- [97] LAI, D., C. LIU, M. D. EGGEN, P. A. IAIZZO, and B. HE. Equivalent moving dipole localization of cardiac ectopic activity in a swine model during pacing. *IEEE T. Inf. Technol. Biomed. Eng.* nov, 2010, Vol. 14, No. 6, pp. 1318–1326. ISSN 1089-7771. Available from DOI 10.1109/TITB.2010.2051448.
- [98] PULLAN, A. J., L. K. CHENG, M. P. NASH, C. P. BRADLEY, and D. J. PATERSON. Noninvasive electrical imaging of the heart: theory and model development. *Ann. Biomed. Eng.* oct, 2001, Vol. 29, No. 10, pp. 817–836. ISSN 0090-6964. Available from DOI 10.1114/1.1408921.
- [99] SHAHIDI, A. V., P. SAVARD, and R. NADEAU. Forward and inverse problems of electrocardiography: modeling and recovery of epicardial potentials in humans. *IEEE Trans. Biomed. Eng.* mar, 1994, Vol. 41, No. 3, pp. 249–256. ISSN 0018-9294. Available from DOI 10.1109/10.284943.
- [100] OOSTENDORP, T. F., P. F. H. M. van DESSEL, R. CORONEL, C. BELTERMAN, A. C. LINNENBANK, I. H. van SCHIE, A. van OOSTEROM, P. OOSTERHOFF, P. M. van DAM, and J. M. T. de BAKKER. Noninvasive detection of epicardial and endocardial activity of the heart. *Neth. Heart J.* nov, 2011, Vol. 19, No. 11, pp. 488–491. ISSN 1568-5888. Available from DOI 10.1007/s12471-011-0206-1.
- [101] GIFFARD-ROISIN, S., T. JACKSON, L. FOVARGUE, J. LEE, H. DELINGETTE, R. RAZAVI, N. AYACHE, and M. SERMESANT. Non-invasive personalisation of a cardiac electrophysiology model from body surface potential mapping. *IEEE Trans. Biomed. Eng.* sep, 2016, Vol. 64, No. 9, pp. 1–1. ISSN 0018-9294. Available from DOI 10.1109/TBME.2016.2629849.
- [102] RUDY, Y. The forward problem of electrocardiography revisited. *Circ.-Arrhythmia Electrophysiol.* jun, 2015, Vol. 8, No. 3, pp. 526–528. Available from DOI 10.1161/CIRCEP.115.003056.
- [103] BEAR, L. R., L. K. CHENG, I. J. LEGRICE, G. B. SANDS, N. A. LEVER, D. J. PATERSON, and B. H. SMAILL. Forward problem of electrocardiography: is it solved?. *Circ.-Arrhythmia Electrophysiol.* 2015, Vol. 8, No. 3, pp. 677–684. ISSN 19413084. Available from DOI 10.1161/CIRCEP.114.001573.
- [104] GRAAF, A. W. M. van der, P. BHAGIRATH, H. RAMANNA, Vincent J.H.M. van DRIEL, Jacques de HOOGE, Natasja M.S. de GROOT, and Marco J. W. GÖTTE. Noninvasive imaging of cardiac excitation: current status and future perspective. *Ann. Noninvasive Electrocardiol.* mar, 2014, Vol. 19, No. 2, pp. 105–113. ISSN 1082720X. Available from DOI 10.1111/anec.12140.
- [105] ARMOUNDAS, A. A., A. B. FELDMAN, R. MUKKAMALA, B. HE, T. J. MULLEN, P. A. BELK, Y. Z. LEE, and R. J. COHEN. Statistical accuracy of a moving equivalent dipole method to identify sites of origin of cardiac electrical activation. *IEEE*



- Trans. Biomed. Eng.* dec, 2003, Vol. 50, No. 12, pp. 1360–1370. ISSN 0018-9294. Available from DOI 10.1109/TBME.2003.819849.
- [106] KNEPPO, P., M. TYŠLER, and M. TURZOVA. Simulation study of possibilities of using limited lead mapping data for inverse solution based on multipole cardiac generator. In: *14th Annual International Conference of the IEEE Engineering in Medicine and Biology Society*. Paris, France: IEEE, 1992. pp. 2002–2003. ISBN 0-7803-0785-2. Available from DOI 10.1109/IEMBS.1992.5762140.
- [107] KNEPPO, P., J. SVEHLIKOVA, M. TINOVA, M. TURZOVA, and M. TYSLER. Multipolar generator capability to represent the heart activation process. In: *15th Annual International Conference of the IEEE Engineering in Medicine and Biology Society*. San Diego, CA, USA: IEEE, 1993. pp. 766–766. ISBN 0-7803-1377-1. ISSN 05891019. Available from DOI 10.1109/IEMBS.1993.978822.
- [108] TITOMIR, L. I., P. KNEPPO, V. G. TRUNOV, and E. A.-I. AIDU. *Biophysical fundamentals of electrocardiotopographic methods*. 1 ed. Moscow, RF: Fizmatlit, 2009. ISBN 978-5-9221-1162-1.
- [109] SKIPA, O. *Linear inverse problem of electrocardiography: epicardial potentials and transmbrane voltages*. Karlsruhe, Germany: Karlsruhe Institute of Technology (KIT) Institute of Biomedical Engineering, 2004. Ph.D. Thesis.
- [110] OOSTEROM, A. van. Solidifying the solid angle. *J. of Electrocardiol.* oct, 2002, Vol. 35, No. 4, pp. 181–192. Available from DOI 10.1054/jelc.2002.37176.
- [111] HENRIQUEZ, C. S. Simulating the electrical behavior of cardiac tissue using the bidomain model. *Crit. Rev. in Biomed. Eng.* 1993, Vol. 21, No. 1, pp. 1–77. ISSN 0278-940X.
- [112] POTSE, M., B. DUBE, J. RICHER, A. VINET, and R. M. GULRAJANI. A comparison of monodomain and bidomain reaction-diffusion models for action potential propagation in the human heart. *IEEE Trans. Biomed. Eng.* IEEE, dec, 2006, Vol. 53, No. 12, pp. 2425–2435. ISSN 0018-9294. Available from DOI 10.1109/TBME.2006.880875.
- [113] BISHOP, M. J., and G. PLANK. Bidomain ECG simulations using an augmented monodomain model for the cardiac source. *IEEE Trans. Biomed. Eng.* aug, 2011, Vol. 58, No. 8, pp. 2297–2307. ISSN 00189294. Available from DOI 10.1109/TBME.2011.2148718.
- [114] RUDY, Y. The electrocardiogram and cardiac excitation. In: N. SPERELAKIS, Y. KURACHI, A. TERZIC, and M. V. COHEN, eds. *Heart physiology and pathophysiology*. 4th ed. ed. San Diego, Calif.: Academic Press, 2001. pp. 138–148. ISBN 0126569754.
- [115] GULRAJANI, R. M., and G. E. MAILLOUX. A simulation study of the effects of torso inhomogeneities on electrocardiographic potentials, using realistic heart and torso models. *Circulation Res.* 1983, Vol. 52, No. 1, pp. 45–56. ISSN 0009-7330. Available from DOI 10.1161/01.RES.52.1.45.
- [116] ABOULAICH, R., N. FIKAL, E. EL GUARMAH, and N. ZEMZEMI. Stochastic finite element method for torso conductivity uncertainties quantification in electrocardiography inverse problem. *Math. Model. Nat. Phenom.* mar, 2016, Vol. 11, No. 2, pp. 1–19. Available from DOI 10.1051/mmnp/201611201.
- [117] KELLER, D. U. J., F. M. WEBER, G. SEEMANN, and O. DÖSSEL. Ranking the influence of tissue conductivities on forward-calculated ECGs. *IEEE Trans.*

- 
- Biomed. Eng.* jul, 2010, Vol. 57, No. 7, pp. 1568–1576. Available from DOI 10.1109/TBME.2010.2046485.
- [118] ARTHUR, R. M., S. WANG, and J. W. TROBAUGH. Changes in body-surface electrocardiograms from geometric remodeling with obesity. *IEEE Trans. Biomed. Eng.* jun, 2011, Vol. 58, No. 6, pp. 1565–1573. ISSN 0018-9294. Available from DOI 10.1109/TBME.2010.2104322.
- [119] SIMONYI, G. Electrocardiological features in obesity: the benefits of body surface potential mapping. *CardioRenal Med.* 2014, Vol. 4, No. 2, pp. 123–129. ISSN 16645502. Available from DOI 10.1159/000365012.
- [120] KUMAR, N. K. S., and M. R. REDDY. Non-invasive electrical imaging of heart: a patient specific approach. *Int. J. of Bioelectromagnetism.* 2004, Vol. 6, No. 1, pp. 1–7.
- [121] EREM, B., J. COLL-FONT, R. M. ORELLANA, P. ST'OVICEK, and D. H. BROOKS. Using transmural regularization and dynamic modeling for noninvasive cardiac potential imaging of endocardial pacing with imprecise thoracic geometry. *IEEE Trans. Med. Imaging.* mar, 2014, Vol. 33, No. 3, pp. 726–738. Available from DOI 10.1109/TMI.2013.2295220.
- [122] TYŠLER, M., and J. ŠVEHLÍKOVÁ. Noninvasive finding of local repolarization changes in the heart using dipole models and simplified torso geometry. *J. of Electrocardiol.* Elsevier Inc., 2013, Vol. 46, No. 4, pp. 284–288. ISSN 00220736. Available from DOI 10.1016/j.jelectrocard.2013.03.014.
- [123] CHENG, L. K., G.B. SANDS, and A.J. PULLAN. Construction of patient specific geometries suitable for the inverse problem of electrocardiography. In: *27th Annual Conference IEEE Engineering in Medicine and Biology.* Shanghai, China: IEEE, 2005. pp. 7201–7203. ISBN 0-7803-8741-4. ISSN 1557-170X. Available from DOI 10.1109/IEMBS.2005.1616170.
- [124] CLUITMANS, M. J. M., R. L. M. PEETERS, R. L. WESTRA, and P. G. A. VOLDERS. Noninvasive reconstruction of cardiac electrical activity: update on current methods, applications and challenges. *Neth. Heart J.* jun, 2015, Vol. 23, No. 6, pp. 301–311. ISSN 1568-5888. Available from DOI 10.1007/s12471-015-0690-9.
- [125] LENKOVÁ, J., J. ŠVEHLÍKOVÁ, and M. TYŠLER. Individualized model of torso surface for the inverse problem of electrocardiology. *J. of Electrocardiol.* Elsevier Inc., 2012, Vol. 45, No. 3, pp. 231–236. ISSN 00220736. Available from DOI 10.1016/j.jelectrocard.2012.01.006.
- [126] ŠVEHLÍKOVÁ, J., J. LENKOVÁ, M. TURZOVA, M. TYŠLER, M. KANIA, and R. MANIEWSKI. Influence of individual torso geometry on inverse solution to 2 dipoles. *J. of Electrocardiol.* Elsevier Inc., 2012, Vol. 45, No. 1, pp. 7–12. ISSN 00220736. Available from DOI 10.1016/j.jelectrocard.2011.07.012.
- [127] PFEIFER, B., F. F. HANSER, M. SEGER, G. FISCHER, R. MODRE-OSPRIAN, and B. TILG. Patient-specific volume conductor modeling for non-invasive imaging of cardiac electrophysiology. *Open Med. Inform. J.* oct, 2008, Vol. 2, pp. 32–41. Available from DOI 10.2174/1874431100802010032.
- [128] COCHET, H., R. DUBOIS, F. SACHER, N. DERVAL, M. SERMESANT, M. HOCINI, M. MONTAUDON, M. HAISSAGUERRE, F. LAURENT, and P. JAÏS. Cardiac arrhythmias: multimodal assessment integrating body surface ECG mapping into cardiac imaging. *Radiology.* apr, 2014, Vol. 271, No. 1, pp. 239–247. ISSN 0033-8419. Available from DOI 10.1148/radiol.13131331.

- [129] GILLETTE, K., J. TATE, B. KINDALL, P. M. van DAM, E. KHOLMOVSKI, and R. S. MACLEOD. Generation of combined-modality tetrahedral meshes. In: *Computing in Cardiology Conference (CinC)*. Nice, France: IEEE, 2015. pp. 953–956. ISBN 978-1-5090-0685-4. Available from DOI 10.1109/CIC.2015.7411070.
- [130] PRAKOSA, A., P. MALAMAS, S. ZHANG, F. PASHAKHANLOO, H. AREVALO, D. A. HERZKA, A. LARDO, H. HALPERIN, E. MCVEIGH, N. TRAYANOVA, and F. VADAKKUMPADAN. Methodology for image-based reconstruction of ventricular geometry for patient-specific modeling of cardiac electrophysiology. *Prog. Biophys. Mol. Biol.* Elsevier Ltd, aug, 2014, Vol. 115, No. 2-3, pp. 226–234. ISSN 00796107. Available from DOI 10.1016/j.pbiomolbio.2014.08.009.
- [131] RAHIMI, A., and L. WANG. Sensitivity of noninvasive cardiac electrophysiological imaging to variations in personalized anatomical modeling. *IEEE Trans. Biomed. Eng.* jun, 2015, Vol. 62, No. 6, pp. 1563–1575. Available from DOI 10.1109/TBME.2015.2395387.
- [132] TAKANO, N., H.-G. PUURTINEN, P. KAUPPINEN, J. HYTTINEN, and J. MALMIVUO. Effect of cardiac phases and conductivity inhomogeneities of the thorax models on ECG lead selection and reconstruction. In: *23rd Annual International Conference of the IEEE Engineering in Medicine and Biology Society*. Istanbul, Turkey: IEEE, 2001. pp. 367–370. ISBN 0-7803-7211-5. ISSN 04549244. Available from DOI 10.1109/IEMBS.2001.1018936.
- [133] RAMANATHAN, C., and Y. RUDY. Electrocardiographic imaging: II. Effect of torso inhomogeneities on noninvasive reconstruction of epicardial potentials, electrograms, and isochrones. *J. Cardiovasc. Electrophysiol.* feb, 2001, Vol. 12, No. 2, pp. 241–252. ISSN 1045-3873. Available from DOI 10.1046/j.1540-8167.2001.00241.x.
- [134] ZEMZEMI, N., C. DOBRZYNSKI, L. R. BEAR, M. POTSE, C. DALLET, Y.S COUDIERE, R. DUBOIS, and J. DUCHATEAU. Effect of the torso conductivity heterogeneities on the ECGI inverse problem solution. In: *Computing in Cardiology Conference (CinC)*. Nice, France: IEEE, 2015. pp. 233–236. ISBN 978-1-5090-0685-4. ISSN 2325887X. Available from DOI 10.1109/CIC.2015.7408629.
- [135] DIJK, W. A., P. M. van DAM, N. H. J. J. van der PUTTEN, A. C. MAAN, and M. J. J. de JONGSTE. Validation of infarct size and location from the ECG by inverse body surface mapping. In: *Computing in Cardiology Conference (CinC)*. Krakow, Poland: IEEE, 2012. pp. 337–340. ISBN 978-1-4673-2076-4. ISSN 23258861.
- [136] DAM, P.M. van, A. W. DIJK, N. H. VAN DER PUTTEN, A. C. MAAN, and M. J. J. DE JONGSTE. Estimating infarct severity from the ECG using a realistic heart model. *Comput. in Cardiol.* 2012, Vol. 39, pp. 333–336. ISSN 23258861.
- [137] JOHNSON, C. R. Computational and numerical methods for bioelectric field problems. *Crit. Rev. in Biomed. Eng.* 1997, Vol. 25, No. 1, pp. 1–81. ISSN 0278-940X. Available from DOI 10.1615/CritRevBiomedEng.v25.i1.10.
- [138] SACHSE, F. B. *Computational cardiology: modeling of anatomy, electrophysiology, and mechanics*. Lecture no ed. Berlin: Springer, 2004. ISBN 3-540-21907-2.
- [139] GULRAJANI, R. M. The forward problem of electrocardiography: from heart models to body surface potentials. In: *19th Annual International Conference of the IEEE Engineering in Medicine and Biology Society*. Chicago, IL, USA: IEEE, 1997. pp. 2604–2609. ISBN 0-7803-4262-3. ISSN 05891019. Available from DOI 10.1109/IEMBS.1997.756866.

-
- [140] XANTHIS, C. G., P. M. BONOVAS, and G. KYRIACOU. Inverse problem of ECG for different equivalent cardiac sources. *PIERS Online*. 2007, Vol. 3, No. 8, pp. 1222–1227. ISSN 1931-7360. Available from DOI 10.2529/PIERS070220144924.
- [141] GREENSITE, F. The mathematical basis for imaging cardiac electrical function. *Crit. Rev. in Biomed. Eng.* 1994, Vol. 22, No. 5-6, pp. 347–99. ISSN 0278-940X.
- [142] SERINAGAOGLU, Y., D. H. BROOKS, and R. S. MACLEOD. Combining numerical and physiological constraints in inverse electrocardiography. *Int. J. of Bioelectromagnetism*. 2003, Vol. 5, No. 1, pp. 215–217.
- [143] TITOMIR, L. I., and P. KNEPPO. On the possibility to determine integral characteristics of the cardiac electric generator from extracardiac electric and magnetic measurements. *IEEE Trans. Biomed. Eng.* apr, 1983, Vol. BME-30, No. 4, pp. 222–226. Available from DOI 10.1109/TBME.1983.325221.
- [144] MILANIČ, M., V. JAZBINŠEK, R. S. MACLEOD, D. H. BROOKS, and R. HREN. Assessment of regularization techniques for electrocardiographic imaging. *J. of Electrocardiol.* jan, 2014, Vol. 47, No. 1, pp. 20–28. ISSN 00220736. Available from DOI 10.1016/j.jelectrocard.2013.10.004.
- [145] BROOKS, D. H., G. F. AHMAD, R. S. MACLEOD, and G. M. MARATOS. Inverse electrocardiography by simultaneous imposition of multiple constraints. *IEEE Trans. Biomed. Eng.* jan, 1999, Vol. 46, No. 1, pp. 3–18. ISSN 0018-9294. Available from DOI 10.1109/10.736746.
- [146] POTYAGAYLO, D., E. G. CORTÉS, W. H. W. SCHULZE, and O. DÖSSEL. Binary optimization for source localization in the inverse problem of ECG. *Med. Biol. Eng. Comput.* sep, 2014, Vol. 52, No. 9, pp. 717–728. ISSN 0140-0118. Available from DOI 10.1007/s11517-014-1176-4.
- [147] SHOU, G., L. XIA, F. LIU, M. JIANG, and S. CROZIER. On epicardial potential reconstruction using regularization schemes with the L1-norm data term. *Phys. Med. Biol.* jan, 2011, Vol. 56, No. 1, pp. 57–72. ISSN 1361-6560. Available from DOI 10.1088/0031-9155/56/1/004.
- [148] CHAVEZ, C. E., F. ALONSO-ATIENZA, N. ZEMZEMI, Y. COUDIERE, and D. ALVAREZ. Inverse localization of ischemia in a 3D realistic geometry: a level set approach. In: *Computing in Cardiology Conference (CinC)*. Nice, France: IEEE, 2015. pp. 229–232. ISBN 978-1-5090-0685-4. ISSN 2325-8861. Available from DOI 10.1109/CIC.2015.7408628.
- [149] POTYAGAYLO, D., W. H. W. SCHULZE, and O. DÖSSEL. Local regularization of endocardial and epicardial surfaces for better localization of ectopic beats in the inverse problem of ECG. *Comput. in Cardiol.* 2014, pp. 837–840. ISSN 2325-8861.
- [150] BERGER, T., G. FISCHER, B. PFEIFER, R. MODRE, F. F. HANSER, T. TRIEB, F. X. ROITHINGER, M. STUEHLINGER, O. PACHINGER, B. TILG, and F. HINTRINGER. Single-beat noninvasive imaging of cardiac electrophysiology of ventricular pre-excitation. *J. Am. Coll. Cardiol.* nov, 2006, Vol. 48, No. 10, pp. 2045–2052. Available from DOI 10.1016/j.jacc.2006.08.019.
- [151] BARNES, J. P., and P. R. JOHNSTON. Application of robust generalised cross-validation to the inverse problem of electrocardiology. *Comput. Biol. Med.* Elsevier, feb, 2016, Vol. 69, pp. 213–225. ISSN 00104825. Available from DOI 10.1016/j.compbimed.2015.12.011.



- [152] TUBOLY, G., G. KOZMANN, and I. MAROS. Computational aspects of electrocardiological inverse solutions. *IFAC—PapersOnLine*. Elsevier B.V., 2015, Vol. 48, No. 20, pp. 48–51. ISSN 24058963. Available from DOI 10.1016/j.ifacol.2015.10.113.
- [153] COLL-FONT, J., B. EREM, P. ŠT’OVÍČEK, D. H. BROOKS, and P. M. van DAM. Quantitative comparison of two cardiac electrical imaging methods to localize pacing sites. In: *Computing in Cardiology Conference (CinC)*. Nice, France: IEEE, 2015. pp. 217–220. ISBN 978-1-5090-0685-4. ISSN 2325-8861. Available from DOI 10.1109/CIC.2015.7408625.
- [154] GHODRATI, A., D. H. BROOKS, G. TADMOR, and R. S. MACLEOD. Wavefront-based models for inverse electrocardiography. *IEEE Trans. Biomed. Eng.* sep, 2006, Vol. 53, No. 9, pp. 1821–1831. ISSN 0018-9294. Available from DOI 10.1109/TBME.2006.878117.
- [155] LIU, C., X. ZHANG, Z. LIU, S.M. POGWIZD, and B. HE. Three-dimensional myocardial activation imaging in a rabbit model. *IEEE Trans. Biomed. Eng.* IEEE, sep, 2006, Vol. 53, No. 9, pp. 1813–1820. ISSN 0018-9294. Available from DOI 10.1109/TBME.2006.873701.
- [156] LIU, C., N. D. SKADSBURG, S. E. AHLBERG, C. M. SWINGEN, P. A. IAIZZO, and B. HE. Estimation of global ventricular activation sequences by noninvasive three-dimensional electrical imaging: validation studies in a swine model during pacing. *J. Cardiovasc. Electrophysiol.* may, 2008, Vol. 19, No. 5, pp. 535–540. ISSN 1540-8167. Available from DOI 10.1111/j.1540-8167.2007.01066.x.
- [157] COLL-FONT, J., D. POTYAGAYLO, W. H. W. SCHULZE, O. DÖSSEL, and D. H. BROOKS. Comparison of temporal dimensionality reduction methods for constrained inverse in cardiac electrical imaging. In: *Computing in Cardiology Conference (CinC)*. Nice, France: IEEE, 2015. pp. 237–240. ISBN 978-1-5090-0685-4. Available from DOI 10.1109/CIC.2015.7408630.
- [158] COLL-FONT, J., B. PURCELL, J. XU, P. STOVICEK, D. H. BROOKS, and L. WANG. Evaluation of 2-norm versus sparsity regularization in spline-based joint reconstruction of epicardial and endocardial potentials from body-surface measurements. In: *Computing in Cardiology Conference (CinC)*. Nice, France: IEEE, 2015. pp. 957–960. ISBN 978-1-5090-0685-4. ISSN 2325-8861. Available from DOI 10.1109/CIC.2015.7411071.
- [159] ŠT’OVÍČEK, P., Š. HAVRÁNEK, J. ŠIMEK, M. ZBORNÍK, M. MLČEK, and O. KITTNAR. Isopotential ECG imaging correctly identified endocardial ectopic activation site in the case of arrhythmia from right ventricular outflow tract. In: O. DÖSSEL, and W. C. SCHLEGEL, eds. *IFMBE Proc.* Munich, Germany: Springer, Berlin, Heidelberg, 2009. pp. 1965–1968. ISBN 9783642038815. ISSN 16800737. Available from DOI 10.1007/978-3-642-03882-2_522.
- [160] JAMIL-COPLEY, S., R. BOKAN, P. KOJODJOJO, N. QURESHI, M. KOA-WING, S. HAYAT, A. KYRIACOU, B. SANDLER, A. SOHAIB, I. WRIGHT, D. W. DAVIES, Z. WHINNETT, N. S. PETERS, P. KANAGARATNAM, and P. B. LIM. Noninvasive electrocardiographic mapping to guide ablation of outflow tract ventricular arrhythmias. *Heart Rhythm*. Elsevier, apr, 2014, Vol. 11, No. 4, pp. 587–594. ISSN 15475271. Available from DOI 10.1016/j.hrthm.2014.01.013.
- [161] DUBOIS, R., A. J. SHAH, M. HOCINI, A. DENIS, N. DERVAL, H. COCHET, F. SACHER, L. R. BEAR, J. DUCHATEAU, P. JAIS, and M. HAISSAGUERRE. Non-invasive cardiac mapping in clinical practice: application to the ablation of car-

- diac arrhythmias. *J. of Electrocardiol.* Elsevier Inc., nov, 2015, Vol. 48, No. 6, pp. 966–974. Available from DOI 10.1016/j.jelectrocard.2015.08.028.
- [162] ARMOUNDAS, A. A., A. B. FELDMAN, D. A. SHERMAN, and R. J. COHEN. Applicability of the single equivalent point dipole model to represent a spatially distributed bio-electrical source. *Med. Biol. Eng. Comput.* sep, 2001, Vol. 39, No. 5, pp. 562–570. ISSN 0140-0118.
- [163] TYŠLER, M., V. ROŠÍK, and P. KNEPPO. Multichannel ECG measurement for non-invasive identification of heart regions with changed repolarisation. *XVIII IMEKO World Congress. Metrology for a Sustainable Development.* 2006, pp. 2216–2219.
- [164] TYŠLER, M., M. TURZOVA, M. TINOVA, J. ŠVEHLÍKOVÁ, E. HEBLÁKOVÁ, V. SZATHMARY, and S. FILIPOVÁ. Use of body surface potential maps for model-based assessment of local pathological changes in the heart. *Bull. Pol. Acad. Sci.* 2005, Vol. 53, No. 3, pp. 207–215.
- [165] ŠVEHLÍKOVÁ, J., M. POTSE, and M. TYŠLER. Inverse localization of the latest-activated areas in the ventricles from body surface potential maps. In: *Computing in Cardiology Conference (CinC)*. Cambridge, MA, USA: IEEE, 2014. pp. 129–132.
- [166] LAI, D., C. LIU, M. D. EGGEN, P. A. IAIZZO, and B. HE. Localization of endocardial ectopic activity by means of noninvasive endocardial surface current density reconstruction. *Phys. Med. Biol.* jul, 2011, Vol. 56, No. 13, pp. 4161–4176. ISSN 0031-9155. Available from DOI 10.1088/0031-9155/56/13/027.
- [167] PULLAN, A., D. PATERSON, and F. GREENSITE. Non-invasive imaging of cardiac electrophysiology. *Philosophical Trans. of the R. Soc. A: Math., Phys. and Eng. Sci.* 2001, Vol. 359, No. 1783, pp. 1277–1286. ISSN 1364-503X. Available from DOI 10.1098/rsta.2001.0835.
- [168] RUDY, Y., and B. J. MESSINGER-RAPPORT. The inverse problem in electrocardiography: solutions in terms of epicardial potentials. *Crit. Rev. in Biomed. Eng.* 1988, Vol. 16, No. 3, pp. 215–268. ISSN 0278-940X.
- [169] HORACEK, M. B., and J. C. CLEMENTS. The inverse problem of electrocardiography: a solution in terms of single- end double-layer sources on the epicardial surface. *Math. Biosci.* 1997, Vol. 144, No. 2, pp. 119–154. ISSN 00255564. Available from DOI 10.1016/S0025-5564(97)00024-2.
- [170] DAM, P. M. van, T. F. OOSTENDORP, A. C. LINNENBANK, and A. van OOSTEROM. Non-invasive imaging of cardiac activation and recovery. *Ann. Biomed. Eng.* sep, 2009, Vol. 37, No. 9, pp. 1739–1756. ISSN 0090-6964. Available from DOI 10.1007/s10439-009-9747-5.
- [171] DAM, P. M. van, R. TUNG, K. SHIVKUMAR, and M. M. LAKS. Quantitative localization of premature ventricular contractions using myocardial activation ECGI from the standard 12-lead electrocardiogram. *J. of Electrocardiol.* Elsevier Inc., nov, 2013, Vol. 46, No. 6, pp. 574–579. ISSN 00220736. Available from DOI 10.1016/j.jelectrocard.2013.08.005.
- [172] OOSTEROM, A. van. A comparison of electrocardiographic imaging based on two source types. *Europace.* nov, 2014, Vol. 16, No. suppl 4, pp. iv120–iv128. ISSN 1099-5129. Available from DOI 10.1093/europace/euu268.
- [173] HORACEK, M. B., C. J. PENNEY, and J. C. CLEMENTS. The inverse problem of electrocardiography in terms of epicardial potentials and their gradients. In: *Comput. in Cardiol.* Hannover, Germany, Germany: IEEE, 1999. pp. 197–200. ISBN 0-7803-5614-4. ISSN 02766574. Available from DOI 10.1109/CIC.1999.825940.



- Vol. 33, No. 9, pp. 1187–1201. ISSN 0090-6964. Available from DOI 10.1007/s10439-005-5537-x.
- [186] DE AMBROGGI, L., and A. D. CORLAN. Clinical use of body surface potential mapping in cardiac arrhythmias. *Anat. J. Cardiol.* 2007, Vol. 7 Suppl 1, No. 1, pp. 8–10. ISSN 1302-8723.
- [187] PLONSEY, R., and R. C. BARR. *Bioelectricity*. Boston, MA: Springer US, 2007. ISBN 978-0-387-48864-6. Available from DOI 10.1007/978-0-387-48865-3.
- [188] OOSTENDORP, T. F., and A. van OOSTEROM. Source parameter estimation in inhomogeneous volume conductors of arbitrary shape. *IEEE Trans. Biomed. Eng.* mar, 1989, Vol. 36, No. 3, pp. 382–91. ISSN 0018-9294. Available from DOI 10.1109/10.19859.
- [189] TYŠLER, M., and M. TINOVA. Representation of myocardium depolarization by simple models. In: *Proc. of Comp. in Cardiol. Conf.* London, UK: IEEE Comput. Soc. Press, 1993. pp. 703–706. ISBN 0-8186-5470-8. Available from DOI 10.1109/CIC.1993.378305.
- [190] STENROOS, M. The transfer matrix for epicardial potential in a piece-wise homogeneous thorax model: the boundary element formulation. *Phys. Med. Biol.* sep, 2009, Vol. 54, No. 18, pp. 5443–5455. ISSN 0031-9155. Available from DOI 10.1088/0031-9155/54/18/006.
- [191] ŠVEHLÍKOVÁ, J. *Identifikácia ischemických lézií z mnohozvodového merania elektrického poľa srdca na hrudníku*. Bratislava, Slovakia: Ústav merania SAV, 2011. Ph.D. Thesis.
- [192] ŠVEHLÍKOVÁ, J., M. TYŠLER, and M. TURZOVA. Multiple dipole heart model and its projection to the body surface potential map. *Lect. Notes of the ICB Seminar High Resolution ECG Mapping*. 2007, pp. 1–10.
- [193] LUX, R. L., R. S. MACLEOD, M. FULLER, L. S. GREEN, and F. KORNREICH. Estimating ECG distributions from small numbers of leads. *J. of Electrocardiol.* jan, 1995, Vol. 28, No. Sup., pp. 92–98. ISSN 00220736. Available from DOI 10.1016/S0022-0736(95)80032-8.
- [194] PUURTINEN, H. G., J. HYTTINEN, P. KAUPPINEN, N. TAKANO, P. LAARNE, and J. MALMIVUO. Application of lead field theory and computerized thorax modeling for the ECG inverse problem. In: *2001 Conf. Proc. of the 23rd Ann. Int. Conf. of the IEEE Eng. in Med. and Biol. Soc.* Istanbul, Turkey: IEEE, 2001. pp. 363–366. ISBN 0-7803-7211-5. ISSN 04549244. Available from DOI 10.1109/IEMBS.2001.1018935.
- [195] PUURTINEN, H. G., J. HYTTINEN, P. LAARNE, N. TAKANO, and J. MALMIVUO. Effect of number of electrodes, electrode displacement, and RMS measurement noise on the localization accuracy of ECG inverse problem. In: *Comput. in Cardiol.* Rotterdam, The Netherlands: IEEE, 2001. pp. 33–36. ISBN 0-7803-7266-2. ISSN 02766574. Available from DOI 10.1109/CIC.2001.977584.
- [196] GHODRATI, A., D. H. BROOKS, and R. S. MACLEOD. Methods of solving reduced lead systems for inverse electrocardiography. *IEEE Trans. Biomed. Eng.* feb, 2007, Vol. 54, No. 2, pp. 339–343. ISSN 0018-9294. Available from DOI 10.1109/TBME.2006.886865.
- [197] GHARBALCHI, F., Y. S. DOGRUSOZ, and G. W. WEBER. Lanczos bidiagonalization-based inverse solution methods applied to electrical imaging of the heart by using



- reduced lead-sets: a simulation study. *Cogent Math.* Cogent, nov, 2016, Vol. 3, No. 1, pp. 1–13. Available from DOI 10.1080/23311835.2016.1256461.
- [198] LI, G., X. ZHANG, J. LIAN, and B. HE. Noninvasive localization of the site of origin of paced cardiac activation in human by means of a 3-D heart model. *IEEE Trans. Biomed. Eng.* sep, 2003, Vol. 50, No. 9, pp. 1117–1120. ISSN 0018-9294. Available from DOI 10.1109/TBME.2003.816068.
- [199] GRAAF, A. W. M. van der, P. BHAGIRATH, J. de HOOGE, N. M. S. de GROOT, and M. J. W. GÖTTE. A priori model independent inverse potential mapping: the impact of electrode positioning. *Clin. Res. in Cardiol.* jan, 2016, Vol. 105, No. 1, pp. 79–88. ISSN 1861-0684. Available from DOI 10.1007/s00392-015-0891-7.
- [200] MIRI, R., I. M. GRAF, J. V. BAYARRI, and O. DÖSSEL. Applicability of body surface potential map in computerized optimization of biventricular pacing. *Ann. Biomed. Eng.* mar, 2010, Vol. 38, No. 3, pp. 865–875. ISSN 0090-6964. Available from DOI 10.1007/s10439-010-9944-2.
- [201] TILG, B., P. WACH, A. SIPPENSGROENEWEGEN, G. FISCHER, R. MODRE, F. ROITHINGER, M. MLYNASH, G. REDDY, T. ROBERTS, M. LESH, and P. STEINER. Closed-chest validation of source imaging from human ECG and MCG mapping data. In: *Proc. of the First Joint BMES/EMBS Conf. 1999 IEEE Eng. in Med. and Biol. 21st Ann. Conf. and the 1999 Ann. Fall Meeting of the Biomed. Eng. Soc.* Atlanta, GA, USA: IEEE, 1999. pp. 275. ISBN 0-7803-5674-8. Available from DOI 10.1109/IEMBS.1999.802345.
- [202] TILG, B., G. FISCHER, R. MODRE, F. HANSER, B. MESSNARZ, M. SCHOCKE, C. KREMSE, T. BERGER, F. HINTRINGER, and F. X. ROITHINGER. Model-based imaging of cardiac electrical excitation in humans. *IEEE Trans. Med. Imaging.* sep, 2002, Vol. 21, No. 9, pp. 1031–1039. ISSN 0278-0062. Available from DOI 10.1109/TMI.2002.804438.
- [203] MARCOMICHELAKIS, J., R. WITHERS, G. B. NEWMAN, K. O’BIEN, and R. EMANUEL. The relation of age to the thickness of the interventricular septum, the posterior left ventricular wall and their ratio. *Int. J. Cardiol.* nov, 1983, Vol. 4, No. 4, pp. 405–415. ISSN 01675273. Available from DOI 10.1016/0167-5273(83)90190-0.
- [204] LANG, R. M., M. BIERIG, R. B. DEVEREUX, F. A. FLACHSKAMPF, E. FOSTER, P. A. PELLIKKA, M. H. PICARD, M. J. ROMAN, J. SEWARD, J. S. SHANEWISE, S. D. SOLOMON, K. T. SPENCER, M. ST JOHN SUTTON, and W. J. STEWART. Recommendations for chamber quantification: a report from the american society of echocardiography’s guidelines and standards committee and the chamber quantification writing group, developed in conjunction with the European Association of Echocardiograph. *J. Am. Soc. Echocardiogr.* dec, 2005, Vol. 18, No. 12, pp. 1440–1463. ISSN 08947317. Available from DOI 10.1016/j.echo.2005.10.005.
- [205] KANSAL, S., D. ROITMAN, and L. T. SHEFFIELD. Interventricular septal thickness and left ventricular hypertrophy. An echocardiographic study. *Circulation.* nov, 1979, Vol. 60, No. 5, pp. 1058–1065. ISSN 0009-7322. Available from DOI 10.1161/01.CIR.60.5.1058.
- [206] STANFORD UNIVERSITY. *Left ventricle wall thickness.*
[https://web.stanford.edu/group/ccm_echocardio/cgi-bin/%0Amediawiki/index.php/Left_ventricle_wall_thickness.](https://web.stanford.edu/group/ccm_echocardio/cgi-bin/%0Amediawiki/index.php/Left_ventricle_wall_thickness)

- 
- [207] DHEIN, S. *Cardiac gap junctions: physiology, regulation, pathophysiology, and pharmacology*. Basel, Switzerland: Karger Medical and Scientific Publishers, 1998. ISBN 9783805565677.
- [208] DESPLANTEZ, T., E. DUPONT, N. J. SEVERS, and R. WEINGART. Gap junction channels and cardiac impulse propagation. *J. Membr. Biol.* aug, 2007, Vol. 218, No. 1-3, pp. 13–28. ISSN 0022-2631. Available from DOI 10.1007/s00232-007-9046-8.
- [209] SORNMO, L., and P. LAGUNA. Electrocardiogram (ECG) signal processing. In: M. AKAY, ed. *Wiley encyclopedia of Biomedical Engineering*. Hoboken, NJ, USA: John Wiley & Sons, Inc., 2006. pp. 1298–1313. ISBN 0471740365. Available from DOI 10.1002/9780471740360.
- [210] BUENDÍA-FUENTES, F., M. A. ARNAU-VIVES, A. ARNAU-VIVES, Y. JIMÉNEZ-JIMÉNEZ, J. RUEDA-SORIANO, E. ZORIO-GRIMA, A. OSA-SÁEZ, L. V. MARTÍNEZ-DOLZ, L. ALMENAR-BONET, and M. A. PALENCIA-PÉREZ. High-bandpass filters in electrocardiography: source of error in the interpretation of the ST segment. *ISRN Cardiol.* 2012, Vol. 2012, pp. 1–10. ISSN 2090-5599. Available from DOI 10.5402/2012/706217.
- [211] KLIFFIELD, P., L. S. GETTES, J. J. BAILEY, R. CHILDERS, B. J. DEAL, E. W. HANCOCK, G. VAN HERPEN, J. A. KORS, P. MACFARLANE, D. M. MIRVIS, O. PAHLM, P. RAUTAHARJU, and G. S. WAGNER. Recommendations for the standardization and interpretation of the electrocardiogram: Part I: The electrocardiogram and its technology: a scientific statement from the American Heart Association Electrocardiography and Arrhythmias Committee, Council on Clinical Cardiology; the American College of Cardiology Foundation; and the Heart Rhythm Society Endorsed by the International Society for Computerized Electrocardiology. *Circulation.* 2007, Vol. 115, No. 10, pp. 1306–1324. ISSN 00097322. Available from DOI 10.1161/CIRCULATIONAHA.106.180200.
- [212] MEDICAL INSTRUMENTATION Association for the Advancement of. *ANSI/AAMI EC11:1991/(R)2001 Diagnostic electrocardiographic devices*. Arlington, VA, USA: Association for the Advancement of Medical Instrumentation, 2001. ISBN 0910275505.
- [213] CENSI, F., G. CALCAGNINI, M. TRIVENTI, E. MATTEI, P. BARTOLINI, I. CORAZZA, and G. BORIANI. Effect of high-pass filtering on ECG signal on the analysis of patients prone to atrial fibrillation. *Annali dell'Istituto Superiore di Sanità.* dec, 2009, Vol. 45, No. 4, pp. 427–431. ISSN 0021-2571. Available from DOI 10.1590/S0021-25712009000400012.
- [214] KOSSMANN, C. E., D. A. BRODY, G. E. BURCH, H. H. HECHT, F. D. JOHNSTON, C. KAY, E. LEPESCHKIN, H. V. PIPBERGER, H. V. PIPBERGER, G. BAULE, A. S. BERSON, S. A. BRILLER, D. B. GESELOWITZ, L. G. HORAN, and O. H. SCHMITT. Recommendations for standardization of leads and of specifications for instruments in electrocardiography and vectorcardiography. *Circulation.* mar, 1967, Vol. 35, No. 3, pp. 583–602. ISSN 0009-7322. Available from DOI 10.1161/01.CIR.35.3.583.
- [215] BAILEY, J. J., A. S. BERSON, A. GARSON, L. G. HORAN, P. W. MACFARLANE, D. W. MORTARA, and C. ZYWIETZ. Recommendations for standardization and specifications in automated electrocardiography: bandwidth and digital signal processing. A report for health professionals by an ad hoc writing group of the Committee on Electrocardiography and Cardiac Electrophysiology of the Council on

- Clinical Cardiology, American Heart Association. *Circulation*. 1990, Vol. 81, No. 2, pp. 730–739. ISSN 0009-7322. Available from DOI 10.1161/01.CIR.81.2.730.
- [216] GARCÍA-NIEBLA, J., P. LLONTOP-GARCÍA, J. I. VALLE-RACERO, G. SERRA-AUTONELL, V. N. BATCHVAROV, and A. B. DE LUNA. Technical mistakes during the acquisition of the electrocardiogram. *Ann. Noninvasive Electrocardiol.* 2009, Vol. 14, No. 4, pp. 389–403. ISSN 1082720X. Available from DOI 10.1111/j.1542-474X.2009.00328.x.
- [217] KANIA, M., H. RIX, M. FERENIEC, D. JANUSEK, and R. MANIEWSKI. The effect of precordial leads displacement on P-wave morphology in body surface potential mapping. In: *Computing in Cardiology Conference (CinC)*. Zaragoza, Spain: IEEE, 2013. pp. 531–534. ISBN 978-1-4799-0884-4/2325-8861.
- [218] DAM, P. M. van, J. P. GORDON, and M. LAKS. Sensitivity of CIPS-computed PVC location to measurement errors in ECG electrode position: the need for the 3D Camera. *J. of Electrocardiol.* Elsevier, 2014, Vol. 47, No. 6, pp. 788–793. ISSN 00220736. Available from DOI 10.1016/j.jelectrocard.2014.08.005.
- [219] SVEHLIKOVA, J., J. LENKOVA, A. DRKOSOVA, M. FOLTIN, and M. TYSLER. ECG based assessment of the heart position in standard torso model. *IFMBE Proc.* 2011, Vol. 37, No. 1, pp. 474–477. ISSN 16800737. Available from DOI 10.1007/978-3-642-23508-5-123.
- [220] CUFFIN, B. N., and D. N. GESELOWITZ. Studies of the electrocardiogram using realistic cardiac and torso models. *IEEE Trans. Biomed. Eng.* may, 1977, Vol. BME-24, No. 3, pp. 242–252. ISSN 0018-9294. Available from DOI 10.1109/TBME.1977.326209.
- [221] HORACEK, M. B., J. W. WARREN, D. Q. FEILD, and C. L. FELDMAN. Statistical and deterministic approaches to designing transformations of electrocardiographic leads. *J. of Electrocardiol.* oct, 2002, Vol. 35, No. 4, pp. 41–52. ISSN 00220736. Available from DOI 10.1054/jelc.2002.37154.
- [222] CERQUEIRA, M. D., N. J. WEISSMAN, V. DILSIZIAN, A. K. JACOBS, S. KAUL, W. K. LASKEY, D. J. PENNELL, J. A. RUMBERGER, T. RYAN, M. S. VERANI, and American Heart Association Writing Group on Myocardial Segmentation and Registration for CARDIACIMAGING. Standardized myocardial segmentation and nomenclature for tomographic imaging of the heart. A statement for healthcare professionals from the Cardiac Imaging Committee of the Council on Clinical Cardiology of the American Heart Association. *Circulation*. jan, 2002, Vol. 105, No. 4, pp. 539–542. ISSN 1524-4539. Available from DOI 10.1161/01.CIR.0000060923.07573.F2.
- [223] FIELD, A. *Discovering statistics using SPSS*. 3 ed. Los Angeles, USA: SAGE Publications Ltd, 2009. ISBN 9781847879066.
- [224] FILLIBEN, J. J., and A. HECKERT. *F-test for equality of two standard deviations*. <http://atomic.phys.uni-sofia.bg/local/nist-e-handbook/e-handbook/eda/section3/eda359.htm>.
- [225] TYŠLER, M., V. ROŠÍK, and M. TURZOVA. Practical system for BSP mapping studies. In: I. PRÉDA, ed. *25th International Congress on Electrocardiology*. Budapest, Hungary; Singapore: World Scientific, 1998. pp. 81–84.
- [226] KADANEC, J., J. ZELINKA, G. BUKOR, and M. TYSLER. ProCardio 8 — system for high resolution ECG mapping. In: *2017 11th International Conference on Measurement*. Smolenice, Slovakia: IEEE, 2017. pp. 263–266. ISBN 978-80-972629-1-4. Available from DOI 10.23919/MEASUREMENT.2017.7983586.



- [227] KARAS, S., E. HEBLÁKOVÁ, V. ROSÍK, and M. TYŠLER. Multichannel high-resolution electrocardiograph developed in Matlab. In: *Tech. Comput. Prague. 16th Ann. Conf. Proc.* Prague, Czech Republic: Humusoft, 2008. pp. 55.
- [228] SCHLÖGL, A. "GDF - A general dataformat for biosignals". *Comput. Sci. - Digit. Lib.* aug, 2006, pp. 1–15.
<https://arxiv.org/abs/cs/0608052>.
- [229] TATRAMED S.R.O. *Software TomoCon PACS*.
<http://www.tatramed.sk/pacsItem?element=3&parentId=18&type=19>.
- [230] SVEHLIKOVA, J., M. TEPLAN, and M. TYSLER. Geometrical constraint of sources in noninvasive localization of premature ventricular contractions. *J. of Electrocardiol.* Elsevier Inc., may, 2018, Vol. 51, No. 3, pp. 370–377. ISSN 00220736. Available from DOI 10.1016/j.jelectrocard.2018.02.013.

Appendix A

Patient group description

Patient	Gender	Age, Yrs	Height, cm	Weight, kg	BMI	Comments
Pat001	Female	68	159	89	35.2	excluded: CT — bad quality
Pat002	Male	53	170	90	31.1	excluded: ECG — 500 Hz
Pat003	Female	64	165	70	25.7	excluded: no PVC
Pat004	Male	77	183	74	22.1	
Pat005	Female	43	158	74	29.6	
Pat006	Male	51	186	97	28	
Pat007	Female	54	159	54	21.4	
Pat008	Female	33	165	105	38.6	
Pat009	Female	74	170	78	27	
Pat010	Female	57	157	70	28.4	
Pat011	Female	71	173	85	28.4	
Pat012	Female	39	167	50	17.9	excluded: 3 PVCs
Pat013	Male	66	176	120	38.7	excluded: cancelled EP study
Pat014	Female	65	168	81	28.7	excluded: 3 PVCs
Pat015	Male	61	167	94	33.7	
Pat016	Female	47	165	95	34.9	
Pat017	Male	67	195	133	35	excluded: CT — bad quality
Pat018	Female	61	173	130	43.4	excluded: CT — did not fit into

Table A.1: Patient group description

Appendix B

Patient's informed consent protocol

Informace pro pacienta – informovaný souhlas

Vážená paní, vážený pane

rádi bychom Vám nabídli účast v klinické studii „**Stanovení lokalizace fokusu frekventních komorových extrasystol pomocí neinvazivního multipolárního povrchového EKG mapování**“.

Na základě kardiologického vyšetření Vám bylo doporučeno elektrofyziologické vyšetření spojené s radiofrekvenční ablací z důvodu přítomnosti komorových extrasystol. Informace o průběhu elektrofyziologického vyšetření jsou uvedeny v informovaném souhlasu s tímto výkonem. Komorové extrasystoly představují předčasný srdeční stah komor. Nalezení místa vzniku komorové extrasystoly není vždy nejjednodušší a v praxi se k tomu využívá trojrozměrného (3D) elektroanatomického mapování srdce. Spočívá to v tom, že pomocí elektrody zavedené do srdce cévou z třísla mapujeme postupně obě komory srdeční a jejich okolí (oblast aorty, oblast velkých srdečních žil) a hledáme místo vzniku komorových extrasystol. Po jeho nalezení toto místo zničíme aplikací radiofrekvenční energie, což vede k úplnému odstranění těchto pro Vás nepříjemných extrasystol. Tato metoda je sice velice účinná (účinnější než léky), ale může být časově dosti náročná tím, že je třeba zmapovat více srdečních oddílů. Proto bychom chtěli využívat neinvazivního multipolárního měření EKG, které by mohlo ještě před samotným výkonem pomoci k přesnější lokalizaci vzniku komorových extrasystol a tím snížit dobu výkonu a výkon by mohl být zacílen na daný oddíl a tím taktéž zkrácen.

V rámci naší studie bychom rádi zjistili, zda multipolární měření povrchového EKG může pomoci k přesnější lokalizaci komorových extrasystol. V současné době se z běžně dostupného 12 svodového povrchového EKG nedá přesně určit místo vzniku komorových extrasystol, lze jen podle určitých pravidel přibližně odhadnout oblast, odkud by signál mohl vycházet.

V případě vašeho souhlasu se zařazením do studie byste navíc absolvovala před elektrofyziologickým vyšetřením neinvazivní měření povrchového EKG multipolárním systémem spojeným s CT vyšetřením srdce. Na tělo pacienta se připevní stanovený počet elektrod (96-144) a provede se CT vyšetření za účelem zjistit přesné rozměry hrudníku a srdce. Z naměřeného EKG je poté získána integrační mapa, která se dále vyhodnocuje. Toto vyšetření trvá asi 45 min. Možná komplikace při tomto vyšetření je alergie na kontrastní látku, pokud jste alergický na jodovou kontrastní látku, tak vyšetření provedeno být nemůže. Dále je CT vyšetření spojeno s vystavením se radiační zátěži, která je 1-2 mSv a zhruba

Appendix C

Contingency tables

Body surface potential map	Correctness of the inverse solution		Total
	Incorrect	Correct	
IBSPM 0–5 ms	37	39	76
IBSPM 0–10 ms	40	49	89
IBSPM 0–15 ms	36	57	93
IBSPM 0–20 ms	42	59	101
IBSPM 0–25 ms	49	61	110
IBSPM 0–30 ms	59	52	111
IBSPM 5–10 ms	38	53	91
IBSPM 0–15 ms	40	57	97
IBSPM 0–20 ms	42	66	108
IBSPM 0–25 ms	51	60	111
IBSPM 0–30 ms	63	49	112
IBSPM 10–15 ms	45	59	104
IBSPM 10–20 ms	49	64	113
IBSPM 10–25 ms	54	58	112
IBSPM 10–30 ms	65	48	113
IBSPM 15–20 ms	49	63	112
IBSPM 15–25 ms	61	52	113
IBSPM 15–30 ms	65	47	112
IBSPM 20–25 ms	66	47	113
IBSPM 20–30 ms	67	42	109
IBSPM 25–30 ms	74	37	111
TIBSPM 0 ms	30	37	67
TIBSPM 1 ms	31	36	67
TIBSPM 2 ms	34	40	74
TIBSPM 3 ms	37	39	76
TIBSPM 4 ms	39	46	85
TIBSPM 5 ms	39	49	88
TIBSPM 6 ms	40	49	89
TIBSPM 7 ms	41	49	90
TIBSPM 8 ms	38	53	91
TIBSPM 9 ms	38	53	91
TIBSPM 10 ms	36	55	91
TIBSPM 11 ms	40	57	97
TIBSPM 12 ms	41	60	101
TIBSPM 13 ms	45	59	104
TIBSPM 14 ms	44	63	107
TIBSPM 15 ms	49	62	111
TIBSPM 16 ms	47	64	111
TIBSPM 17 ms	47	65	112
TIBSPM 18 ms	49	63	112
TIBSPM 19 ms	52	60	112
TIBSPM 20 ms	57	55	112
TIBSPM 21 ms	61	52	113
TIBSPM 22 ms	64	50	114
TIBSPM 23 ms	65	47	112
TIBSPM 24 ms	64	44	108

Continued on the next page

Table C.1: Contingency table showing how many correct inverse solutions were observed using BSP map generated for the selected time interval or time instant

Combinations of the input parameters for the inverse solution	Correctness of the inverse solution		Total
	Incorrect	Correct	
H IBSPM 0–5 ms	8	18	26
H IBSPM 0–10 ms	9	22	31
H IBSPM 0–15 ms	8	24	32
H IBSPM 0–20 ms	11	24	35
H IBSPM 0–25 ms	13	25	38
H IBSPM 0–30 ms	16	21	37
H IBSPM 5–10 ms	8	23	31
H IBSPM 5–15 ms	10	24	34
H IBSPM 5–20 ms	11	26	37
H IBSPM 5–25 ms	13	25	38
H IBSPM 5–30 ms	18	19	37
H IBSPM 10–15 ms	12	24	36
H IBSPM 10–20 ms	12	26	38
H IBSPM 10–25 ms	15	23	38
H IBSPM 10–30 ms	19	19	38
H IBSPM 15–20 ms	13	26	39
H IBSPM 15–25 ms	18	21	39
H IBSPM 15–30 ms	17	21	38
H IBSPM 20–25 ms	18	21	39
H IBSPM 20–30 ms	18	20	38
H IBSPM 25–30 ms	19	19	38
V IBSPM 0–5 ms	14	11	25
V IBSPM 0–10 ms	15	14	29
V IBSPM 0–15 ms	14	16	30
V IBSPM 0–20 ms	18	16	34
V IBSPM 0–25 ms	20	18	38
V IBSPM 0–30 ms	22	17	39
V IBSPM 5–10 ms	15	15	30
V IBSPM 5–15 ms	17	15	32
V IBSPM 5–20 ms	16	20	36
V IBSPM 5–25 ms	22	17	39
V IBSPM 5–30 ms	24	15	39
V IBSPM 10–15 ms	19	16	35
V IBSPM 10–20 ms	20	19	39
V IBSPM 10–25 ms	21	18	39
V IBSPM 10–30 ms	26	13	39
V IBSPM 15–20 ms	19	19	38
V IBSPM 15–25 ms	23	15	38
V IBSPM 15–30 ms	26	13	39
V IBSPM 20–25 ms	25	13	38
V IBSPM 20–30 ms	25	12	37
V IBSPM 25–30 ms	28	11	39
AV IBSPM 0–5 ms	15	10	25
AV IBSPM 0–10 ms	16	13	29
AV IBSPM 0–15 ms	14	17	31
AV IBSPM 0–20 ms	13	19	32
AV IBSPM 0–25 ms	16	18	34
AV IBSPM 0–30 ms	21	14	35
AV IBSPM 5–10 ms	15	15	30
AV IBSPM 5–15 ms	13	18	31
AV IBSPM 5–20 ms	15	20	35
AV IBSPM 5–25 ms	16	18	34
AV IBSPM 5–30 ms	21	15	36
AV IBSPM 10–15 ms	14	19	33
AV IBSPM 10–20 ms	17	19	36

Continued on the next page

Table C.3: Contingency table showing how many correct relevant inverse solutions were observed using selected combination of the input parameters (torso model and time interval or time instant for BSP map)

Combinations of the input parameters for the inverse solution	Correctness of the inverse solution		Total
	Incorrect	Correct	
AV IBSPM 10–30 ms	18	18	36
AV IBSPM 15–20 ms	17	18	35
AV IBSPM 15–25 ms	18	18	36
AV IBSPM 15–30 ms	17	18	35
AV IBSPM 20–25 ms	18	18	36
AV IBSPM 20–30 ms	17	17	34
AV IBSPM 25–30 ms	17	17	34
H TIBSPM 0 ms	11	12	23
H TIBSPM 1 ms	11	12	23
H TIBSPM 2 ms	12	13	25
H TIBSPM 3 ms	13	13	26
H TIBSPM 4 ms	14	15	29
H TIBSPM 5 ms	15	16	31
H TIBSPM 6 ms	15	16	31
H TIBSPM 7 ms	15	16	31
H TIBSPM 8 ms	15	16	31
H TIBSPM 9 ms	15	16	31
H TIBSPM 10 ms	15	16	31
H TIBSPM 11 ms	16	17	33
H TIBSPM 12 ms	17	18	35
H TIBSPM 13 ms	18	18	36
H TIBSPM 14 ms	18	19	37
H TIBSPM 15 ms	19	19	38
H TIBSPM 16 ms	19	19	38
H TIBSPM 17 ms	19	20	39
H TIBSPM 18 ms	19	20	39
H TIBSPM 19 ms	19	20	39
H TIBSPM 20 ms	19	20	39
H TIBSPM 21 ms	20	20	40
H TIBSPM 22 ms	19	19	38
H TIBSPM 23 ms	19	19	38
H TIBSPM 24 ms	18	18	36
H TIBSPM 25 ms	18	18	36
H TIBSPM 26 ms	18	19	37
H TIBSPM 27 ms	18	19	37
H TIBSPM 28 ms	19	19	38
H TIBSPM 29 ms	19	20	39
H TIBSPM 30 ms	19	20	39
V TIBSPM 0 ms	11	11	22
V TIBSPM 1 ms	11	11	22
V TIBSPM 2 ms	12	13	25
V TIBSPM 3 ms	12	13	25
V TIBSPM 4 ms	14	15	29
V TIBSPM 5 ms	14	15	29
V TIBSPM 6 ms	14	15	29
V TIBSPM 7 ms	15	15	30
V TIBSPM 8 ms	15	15	30
V TIBSPM 9 ms	15	15	30
V TIBSPM 10 ms	15	16	31
V TIBSPM 11 ms	16	17	33
V TIBSPM 12 ms	17	17	34
V TIBSPM 13 ms	17	18	35
V TIBSPM 14 ms	17	18	35
V TIBSPM 15 ms	18	19	37

Continued on the next page

Table C.4 Contingency table showing how many correct inverse solutions are expected (assuming independency of the inverse solution correctness from the used input combination) using combination of selected body surface potential map and torso model with selected level of complexity

Appendix D

Pat004

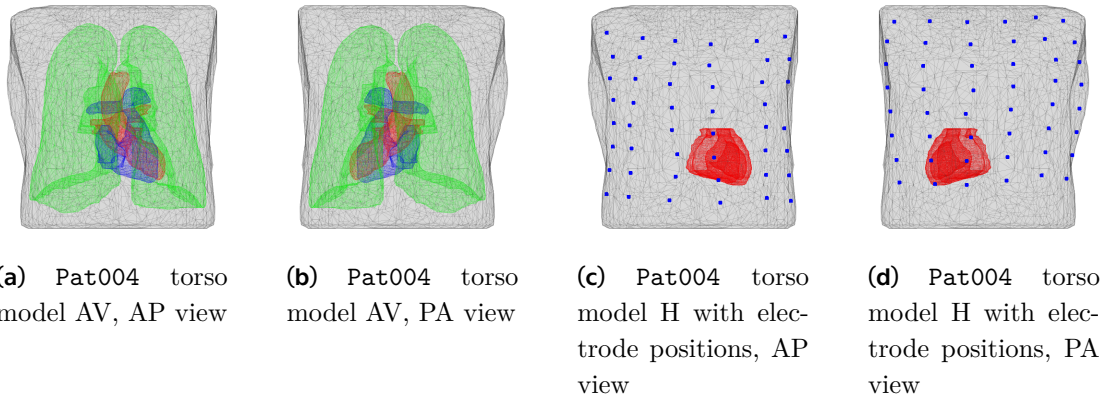


Figure D.1: Pat004. Torso model AV and torso model H with electrode positions

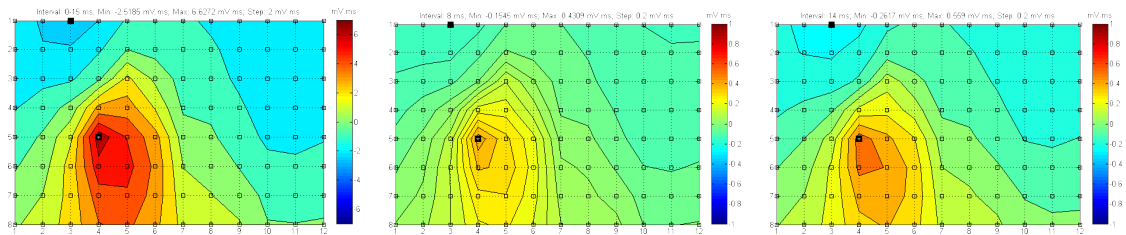


Figure D.2: BSP maps of patient Pat004

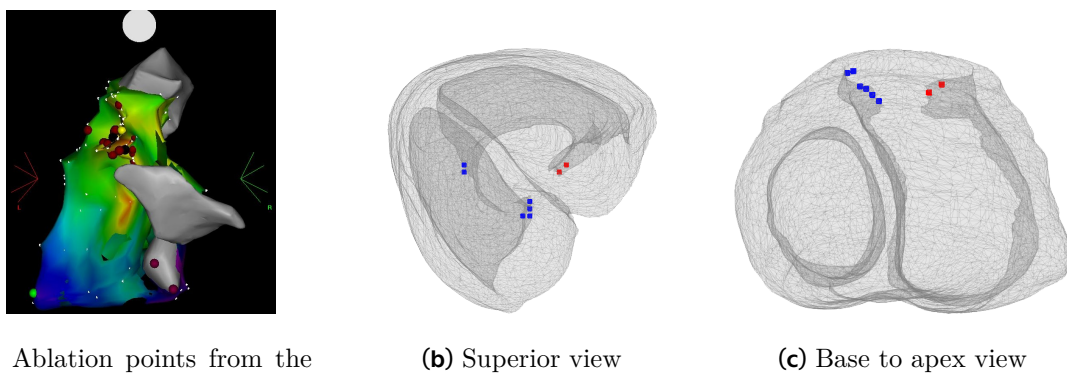


Figure D.3: Results of RFA and positions of all 780 inverse solutions for Pat004. Blue — correct results, Red — incorrect results



Figure D.4: Pat004. Positions of the inverse solutions for IBSPM 0–15 ms in combination with one of the torso models: homogeneous torso model H, or inhomogeneous torso model V, or inhomogeneous torso model AV (see sec. 3.5.3 and 5.2). Blue — correct results, Red — incorrect results



Figure D.5: Positions of the inverse solutions for torso model H and patient-specific TIBSPM (see sec. 3.5.4 and 5.3) for Pat004: PVC1 — TIBSPM 14 ms; PVC2 — TIBSPM 8 ms; PVC3 — TIBSPM 13 ms; PVC4 — TIBSPM 13 ms; PVC5 — TIBSPM 14 ms. Blue — correct results



Figure D.6: Positions of the inverse solutions for torso model V and patient-specific TIBSPM (see sec. 3.5.4 and 5.3) for Pat004: PVC1 — TIBSPM 14 ms; PVC2 — TIBSPM 8 ms; PVC3 — TIBSPM 13 ms; PVC4 — TIBSPM 13 ms; PVC5 — TIBSPM 14 ms. Blue — correct results, Red — incorrect results



Figure D.7: Positions of the inverse solutions for torso model AV and patient-specific TIBSPM (see sec. 3.5.4 and 5.3) for Pat004: PVC1 — TIBSPM 14 ms; PVC2 — TIBSPM 8 ms; PVC3 — TIBSPM 13 ms; PVC4 — TIBSPM 13 ms; PVC5 — TIBSPM 14 ms. Blue — correct results, Red — incorrect results



(a) Superior view (b) Base to apex view
Figure D.8: Positions of the inverse solutions for torso model H in combination with one of 52 BSP maps (see sec. 3.5.5 and 5.4) for Pat004: TIBSPM or IBSPM. Blue — correct results



(a) Superior view (b) Base to apex view
Figure D.9: Positions of the inverse solutions for torso model H and TIBSPM 8 ms (see sec. 3.5.6 and 5.5) for Pat004. Blue — correct results



(a) Superior view (b) Base to apex view
Figure D.10: Positions of the first five dipoles of the inverse solution with minimal RRE obtained for one TIBSPM 8 ms and homogeneous torso model H. Five dipoles (instead of one) with minimal RRE were selected for the inverse solution for one PVC (see sec. 3.5.7 and 5.6.1). Pat004



(a) Superior view (b) Base to apex view
Figure D.11: Positions of the twenty-five dipoles of the inverse solution with minimal RRE. Inverse solution was solved using the combination of homogeneous torso model H and TIBSPMs computed for 8 ms. Five dipoles (instead of one) with minimal RRE were selected for each inverse solution for 5 PVCs (see sec. 3.5.7 and 5.6.2) for Pat004



(a) Superior view (b) Base to apex view
Figure D.12: Positions of first five dipoles with minimal RRE value of the inverse solution for one BSP map (IBSPM 0–15 ms) and homogeneous torso model H (see sec. 3.5.7 and 5.6.3) for Pat004



(a) Superior view (b) Base to apex view
Figure D.13: Positions of first five dipoles with minimal RRE value of the inverse solution for one BSP map (IBSPM 0–15 ms) and inhomogeneous torso model V (see sec. 3.5.7 and 5.6.3) for Pat004



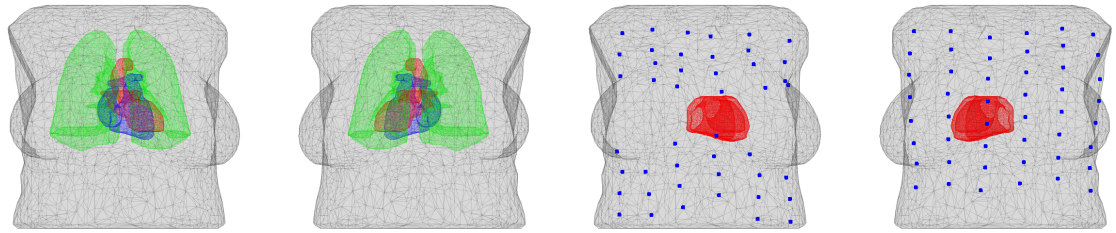
(a) Superior view (b) Base to apex view
Figure D.14: Positions of first five dipoles with minimal RRE value of the inverse solution for one BSP map (IBSPM 0–15 ms) and inhomogeneous torso model AV (see sec. 3.5.7 and 5.6.3) for Pat004



(a) Superior view (b) Base to apex view
Figure D.15: Gravity centers (see sec. 3.5.7 and 5.6.3) of the five dipoles positions derived for inverse solution for IBSPM 0–15 ms and each of the three input torso models in the ventricular myocardium of the Pat004. Blue — torso model H, Green — torso model V, Red — torso model AV

Appendix E

Pat005



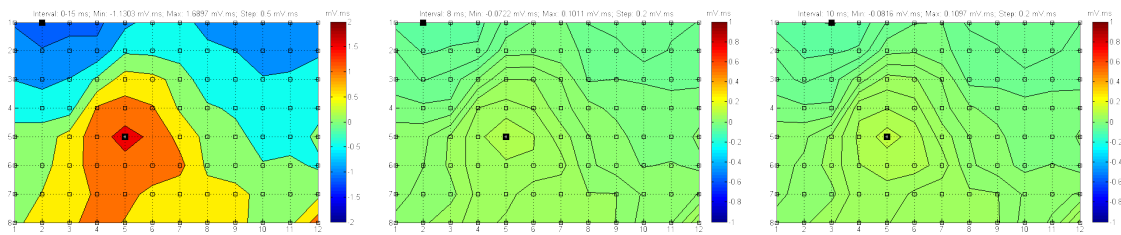
(a) Pat005 torso model AV, AP view

(b) Pat005 torso model AV, PA view

(c) Pat005 torso model H with electrode positions, AP view

(d) Pat005 torso model H with electrode positions, PA view

Figure E.1: Pat005. Torso model AV and torso model H with electrode positions

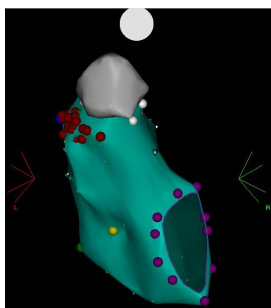


(a) IBSPM 0–15 ms

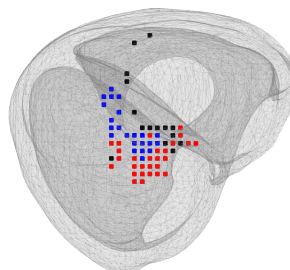
(b) TIBSPM 8 ms

(c) patient-specific TIBSPM 10 ms

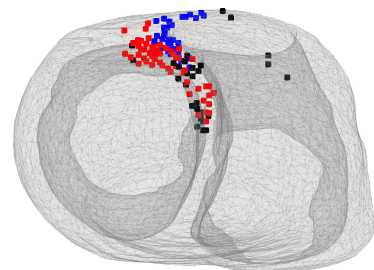
Figure E.2: BSP maps of patient Pat005



(a) Ablation points from the EP study. PA view



(b) Superior view



(c) Base to apex view

Figure E.3: Results of RFA and positions of all 780 inverse solutions for Pat005. Black — irrelevant results, Blue — correct results, Red — incorrect results

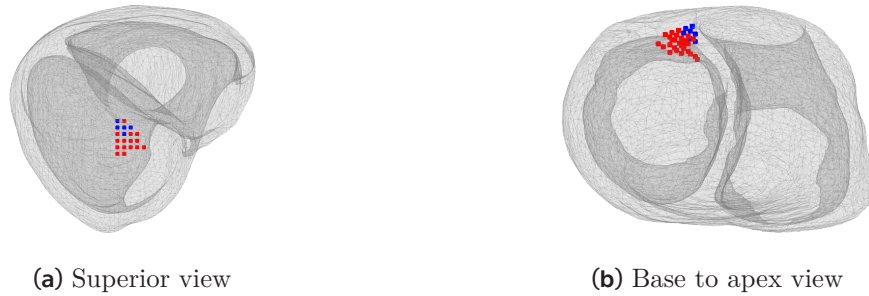


Figure E.8: Positions of the inverse solutions for torso model H in combination with one of 52 BSP maps (see sec. 3.5.5 and 5.4) for Pat005: TIBSPM or IBSPM. Blue — correct results, Red — incorrect results

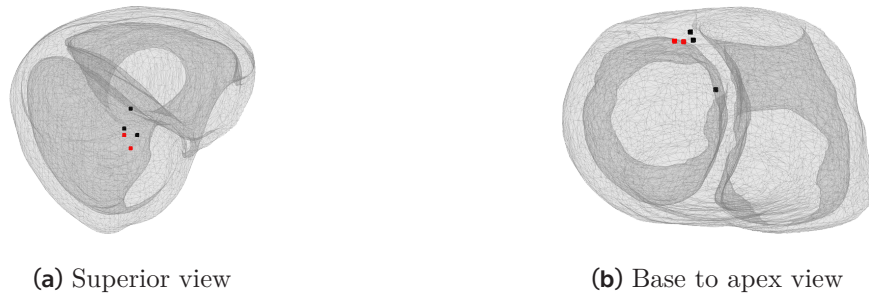


Figure E.9: Positions of the inverse solutions for torso model H and TIBSPM 8 ms (see sec. 3.5.6 and 5.5) for Pat005. Black — irrelevant results, Red — incorrect results

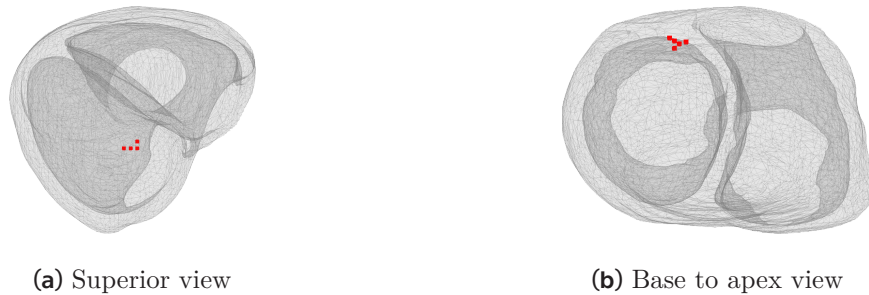


Figure E.10: Positions of the first five dipoles of the inverse solution with minimal RRE obtained for one TIBSPM 8 ms and homogeneous torso model H. Five dipoles (instead one) with minimal RRE were selected for the inverse solution for one PVC (see sec. 3.5.7 and 5.6.1). Pat005

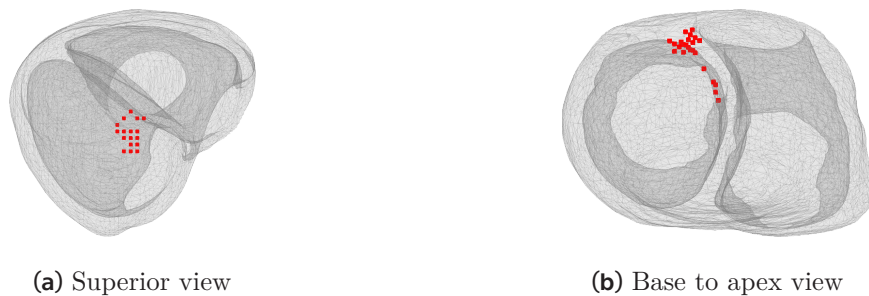
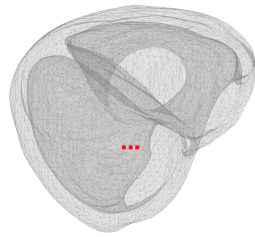
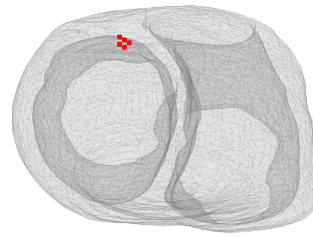


Figure E.11: Positions of the twenty-five dipoles of the inverse solution with minimal RRE. Inverse solution was solved using the combination of homogeneous torso model H and TIBSPMs computed for 8 ms. Five dipoles (instead one) with minimal RRE were selected for each inverse solution for 5 PVCs (see sec. 3.5.7 and 5.6.2) for Pat005

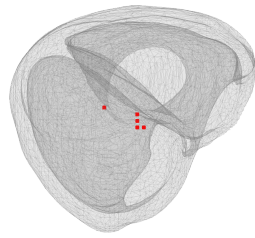


(a) Superior view

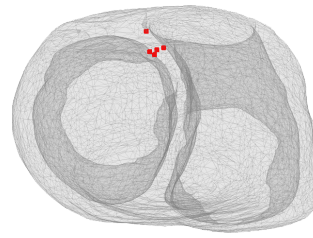


(b) Base to apex view

Figure E.12: Positions of first five dipoles with minimal RRE value of the inverse solution for one BSP map (IBSPM 0–15 ms) and homogeneous torso model H (see sec. 3.5.7 and 5.6.3) for Pat005

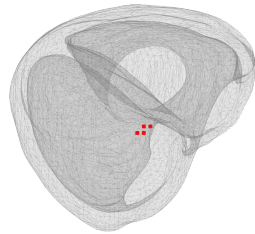


(a) Superior view

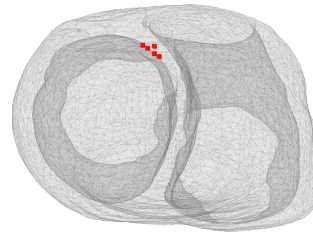


(b) Base to apex view

Figure E.13: Positions of first five dipoles with minimal RRE value of the inverse solution for one BSP map (IBSPM 0–15 ms) and inhomogeneous torso model V (see sec. 3.5.7 and 5.6.3) for Pat005

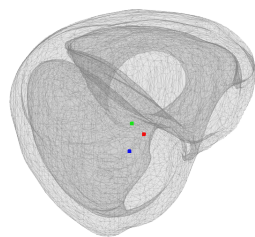


(a) Superior view

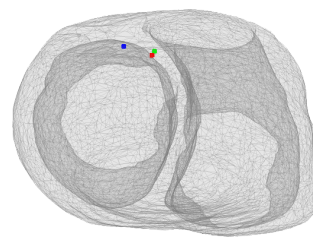


(b) Base to apex view

Figure E.14: Positions of first five dipoles with minimal RRE value of the inverse solution for one BSP map (IBSPM 0–15 ms) and inhomogeneous torso model AV (see sec. 3.5.7 and 5.6.3) for Pat005



(a) Superior view

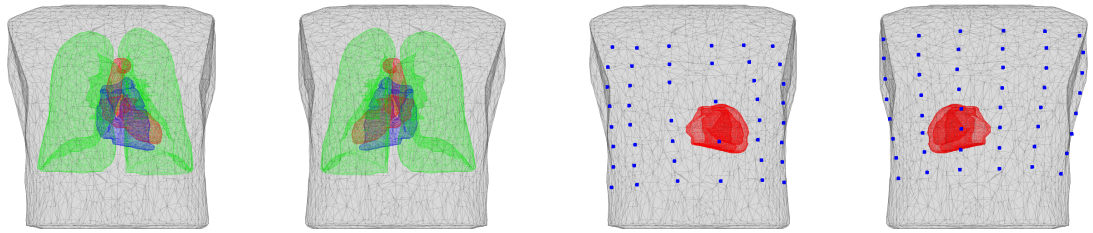


(b) Base to apex view

Figure E.15: Gravity centers (see sec. 3.5.7 and 5.6.3) of the five dipoles positions derived for inverse solution for IBSPM 0–15 ms and each of the three input torso models in the ventricular myocardium of the Pat005. Blue — torso model H, Green — torso model V, Red — torso model AV

Appendix F

Pat006



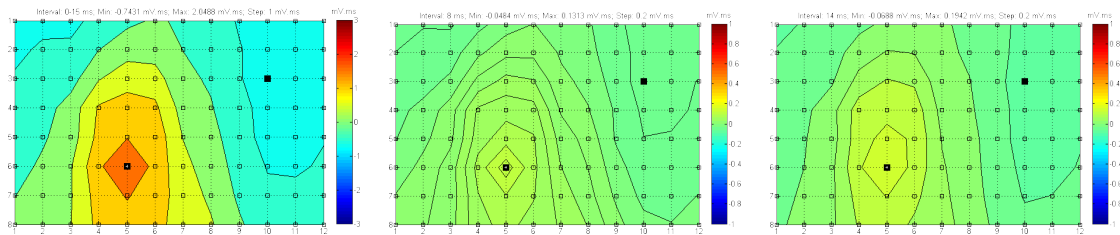
(a) Pat006 torso model AV, AP view

(b) Pat006 torso model AV, PA view

(c) Pat006 torso model H with electrode positions, AP view

(d) Pat006 torso model H with electrode positions, PA view

Figure F.1: Pat006. Torso model AV and torso model H with electrode positions

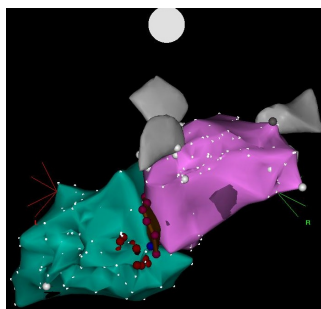


(a) IBSPM 0–15 ms

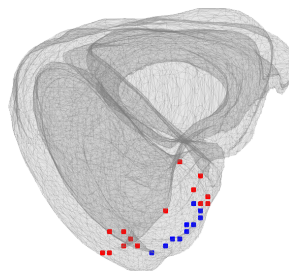
(b) TIBSPM 8 ms

(c) patient-specific TIBSPM 14 ms

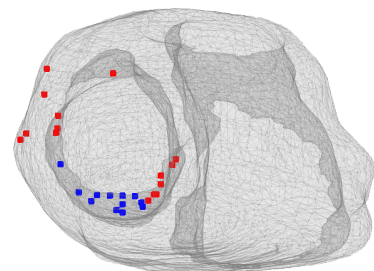
Figure F.2: BSP maps of patient Pat006



(a) Ablation points from the EP study. PA view



(b) Superior view



(c) Base to apex view

Figure F.3: Results of RFA and positions of all 780 inverse solutions for Pat006. Blue — correct results, Red — incorrect results



(a) Superior view (b) Base to apex view

Figure F.8: Positions of the inverse solutions for torso model H in combination with one of 52 BSP maps (see sec. 3.5.5 and 5.4) for Pat006: TIBSPM or IBSPM. Blue — correct results, Red — incorrect results



(a) Superior view (b) Base to apex view

Figure F.9: Positions of the inverse solutions for torso model H and TIBSPM 8 ms (see sec. 3.5.6 and 5.5) for Pat006. Blue — correct results



(a) Superior view (b) Base to apex view

Figure F.10: Positions of the first five dipoles of the inverse solution with minimal RRE obtained for one TIBSPM 8 ms and homogeneous torso model H. Five dipoles (instead one) with minimal RRE were selected for the inverse solution for one PVC (see sec. 3.5.7 and 5.6.1). Pat006



(a) Superior view (b) Base to apex view

Figure F.11: Positions of the twenty-five dipoles of the inverse solution with minimal RRE. Inverse solution was solved using the combination of homogeneous torso model H and TIBSPMs computed for 8 ms. Five dipoles (instead one) with minimal RRE were selected for each inverse solution for 5 PVCs (see sec. 3.5.7 and 5.6.2) for Pat006



(a) Superior view

(b) Base to apex view

Figure F.12: Positions of first five dipoles with minimal RRE value of the inverse solution for one BSP map (IBSPM 0–15 ms) and homogeneous torso model H (see sec. 3.5.7 and 5.6.3) for Pat006



(a) Superior view

(b) Base to apex view

Figure F.13: Positions of first five dipoles with minimal RRE value of the inverse solution for one BSP map (IBSPM 0–15 ms) and inhomogeneous torso model V (see sec. 3.5.7 and 5.6.3) for Pat006



(a) Superior view

(b) Base to apex view

Figure F.14: Positions of first five dipoles with minimal RRE value of the inverse solution for one BSP map (IBSPM 0–15 ms) and inhomogeneous torso model AV (see sec. 3.5.7 and 5.6.3) for Pat006



(a) Superior view

(b) Base to apex view

Figure F.15: Gravity centers (see sec. 3.5.7 and 5.6.3) of the five dipoles positions derived for inverse solution for IBSPM 0–15 ms and each of the three input torso models in the ventricular myocardium of the Pat006. Blue — torso model H, Green — torso model V, Red — torso model AV

Appendix G

Pat007

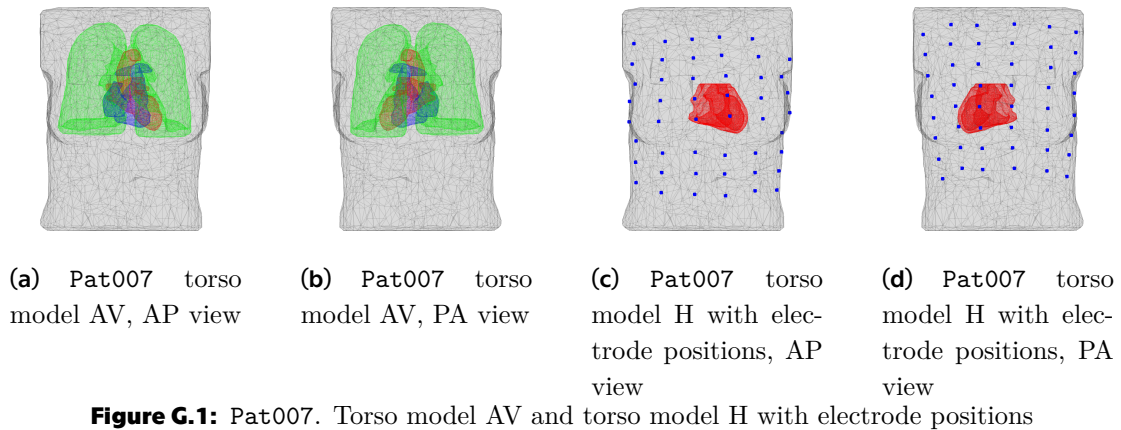


Figure G.1: Pat007. Torso model AV and torso model H with electrode positions

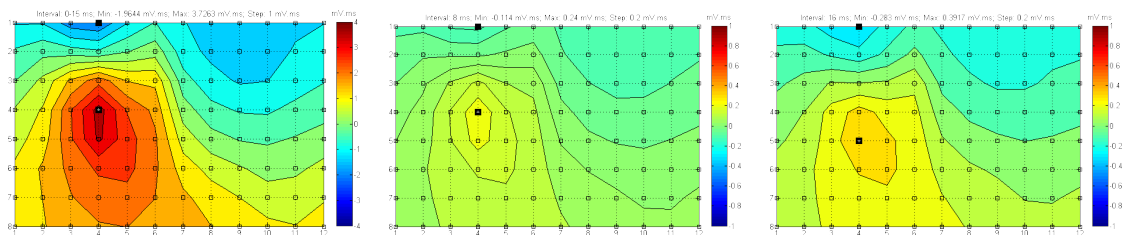


Figure G.2: BSP maps of patient Pat007

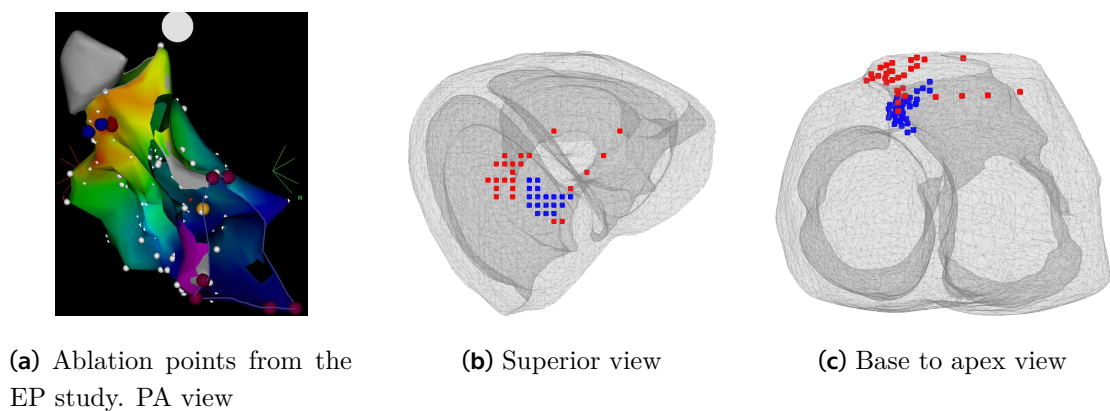


Figure G.3: Results of RFA and positions of all 780 inverse solutions for Pat007. Blue — correct results, Red — incorrect results



Figure G.4: Positions of the inverse solutions for IBSPM 0–15 ms in combination with one of the torso models: homogeneous torso model H, or inhomogeneous torso model V, or inhomogeneous torso model AV (see sec. 3.5.3 and 5.2) for Pat007. Blue — correct results, Red — incorrect results

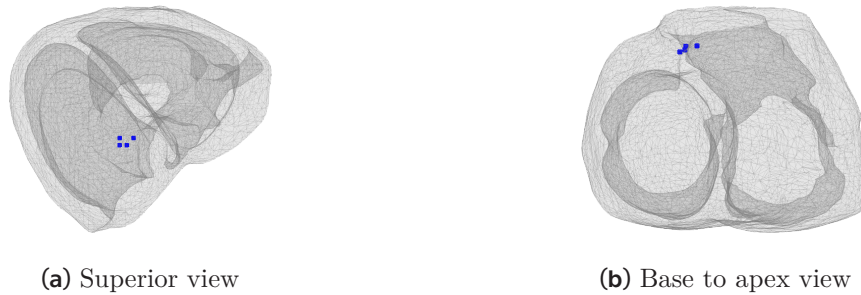


Figure G.5: Positions of the inverse solutions for torso model H and patient-specific TIBSPM (see sec. 3.5.4 and 5.3) for Pat007: PVC1 — TIBSPM 15 ms; PVC2 — TIBSPM 18 ms; PVC3 — TIBSPM 16 ms; PVC4 — TIBSPM 15 ms; PVC5 — TIBSPM 16 ms. Blue — correct results



Figure G.6: Positions of the inverse solutions for torso model V and patient-specific TIBSPM (see sec. 3.5.4 and 5.3) for Pat007: PVC1 — TIBSPM 15 ms; PVC2 — TIBSPM 18 ms; PVC3 — TIBSPM 16 ms; PVC4 — TIBSPM 15 ms; PVC5 — TIBSPM 16 ms. Red — incorrect results



Figure G.7: Positions of the inverse solutions for torso model AV and patient-specific TIBSPM (see sec. 3.5.4 and 5.3) for Pat007: PVC1 — TIBSPM 15 ms; PVC2 — TIBSPM 18 ms; PVC3 — TIBSPM 16 ms; PVC4 — TIBSPM 15 ms; PVC5 — TIBSPM 16 ms. Blue — correct results, Red — incorrect results



Figure G.8: Positions of the inverse solutions for torso model H in combination with one of 52 BSP maps (see sec. 3.5.5 and 5.4) for Pat007: TIBSPM or IBSPM. Blue — correct results, Red — incorrect results



Figure G.9: Positions of the inverse solutions for torso model H and TIBSPM 8 ms (see sec. 3.5.6 and 5.5) for Pat007. Blue — correct results, Red — incorrect results



Figure G.10: Positions of the first five dipoles of the inverse solution with minimal RRE obtained for one TIBSPM 8 ms and homogeneous torso model H. Five dipoles (instead one) with minimal RRE were selected for the inverse solution for one PVC (see sec. 3.5.7 and 5.6.1). Pat007



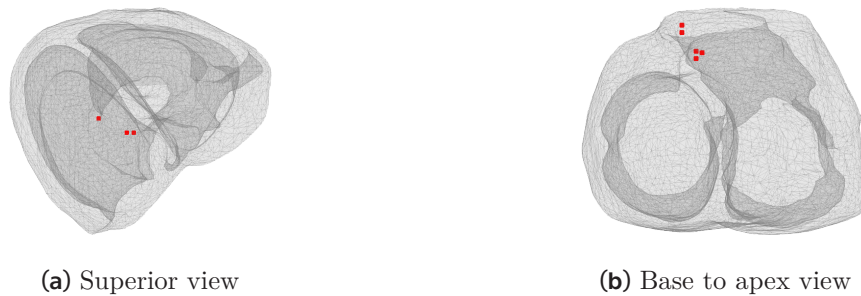
Figure G.11: Positions of the twenty-five dipoles of the inverse solution with minimal RRE. Inverse solution was solved using the combination of homogeneous torso model H and TIBSPMs computed for 8 ms. Five dipoles (instead one) with minimal RRE were selected for each inverse solution for 5 PVCs (see sec. 3.5.7 and 5.6.2) for Pat007



(a) Superior view (b) Base to apex view
Figure G.12: Positions of first five dipoles with minimal RRE value of the inverse solution for one BSP map (IBSPM 0–15 ms) and homogeneous torso model H (see sec. 3.5.7 and 5.6.3) for Pat007



(a) Superior view (b) Base to apex view
Figure G.13: Positions of first five dipoles with minimal RRE value of the inverse solution for one BSP map (IBSPM 0–15 ms) and inhomogeneous torso model V (see sec. 3.5.7 and 5.6.3) for Pat007



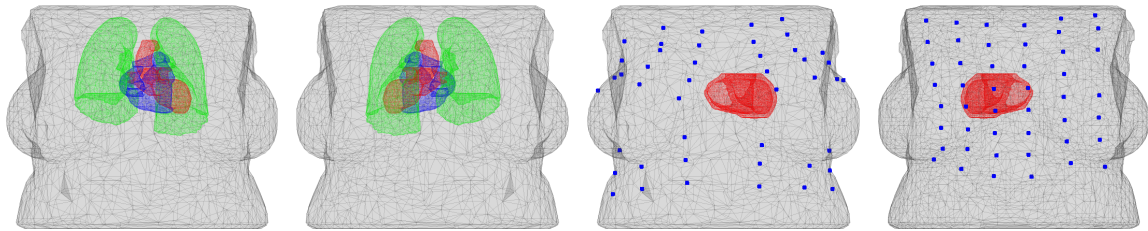
(a) Superior view (b) Base to apex view
Figure G.14: Positions of first five dipoles with minimal RRE value of the inverse solution for one BSP map (IBSPM 0–15 ms) and inhomogeneous torso model AV (see sec. 3.5.7 and 5.6.3) for Pat007



(a) Superior view (b) Base to apex view
Figure G.15: Gravity centers (see sec. 3.5.7 and 5.6.3) of the five dipoles positions derived for inverse solution for IBSPM 0–15 ms and each of the three input torso models in the ventricular myocardium of the Pat007. Blue — torso model H, Green — torso model V, Red — torso model AV

Appendix H

Pat008



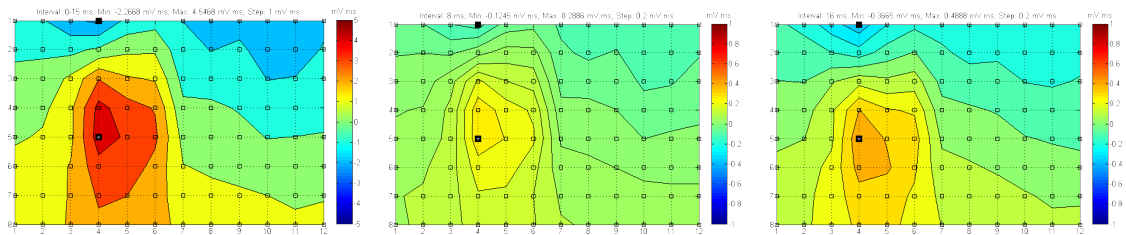
(a) Pat008 torso model AV, AP view

(b) Pat008 torso model AV, PA view

(c) Pat008 torso model H with electrode positions, AP view

(d) Pat008 torso model H with electrode positions, PA view

Figure H.1: Pat008. Torso model AV and torso model H with electrode positions

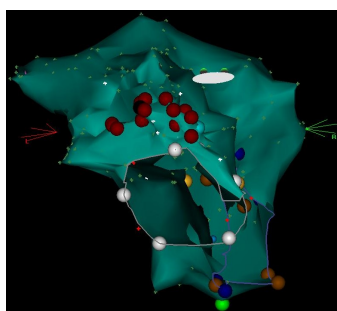


(a) IBSPM 0–15 ms

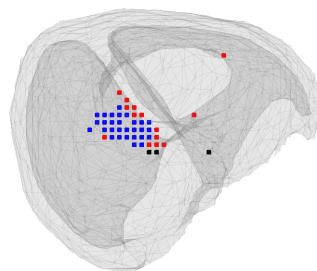
(b) TIBSPM 8 ms

(c) patient-specific TIBSPM 16 ms

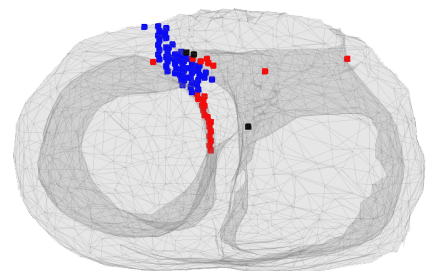
Figure H.2: BSP maps of patient Pat008



(a) Ablation points from the EP study. Superior view



(b) Superior view



(c) Base to apex view

Figure H.3: Results of RFA and positions of all 780 inverse solutions for Pat008. Black — irrelevant results, Blue — correct results, Red — incorrect results

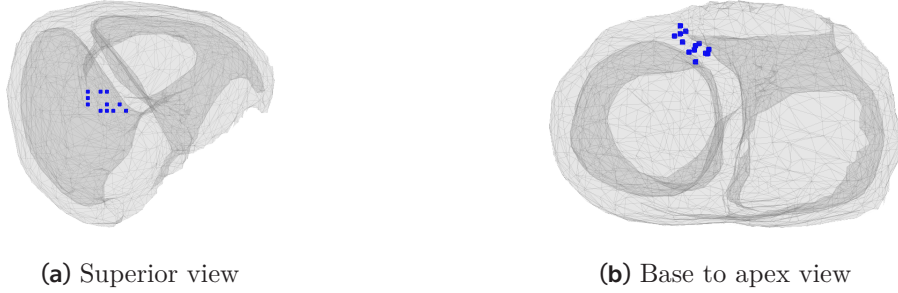


Figure H.4: Positions of the inverse solutions for IBSPM 0–15 ms in combination with one of the torso models: homogeneous torso model H, or inhomogeneous torso model V, or inhomogeneous torso model AV (see sec. 3.5.3 and 5.2) for Pat008. Blue — correct results

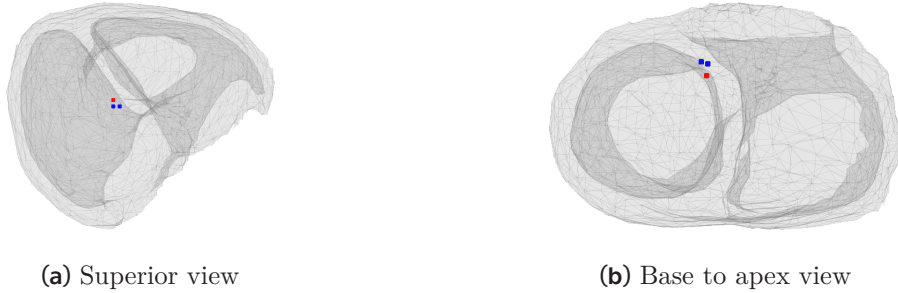


Figure H.5: Positions of the inverse solutions for torso model H and patient-specific TIBSPM (see sec. 3.5.4 and 5.3) for Pat008: PVC1 — TIBSPM 15 ms; PVC2 — TIBSPM 16 ms; PVC3 — TIBSPM 15 ms; PVC4 — TIBSPM 15 ms; PVC5 — TIBSPM 15 ms. Blue — correct results, Red — incorrect results

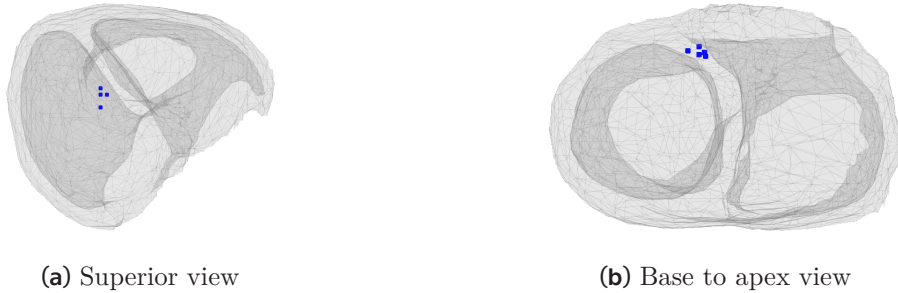


Figure H.6: Positions of the inverse solutions for torso model V and patient-specific TIBSPM (see sec. 3.5.4 and 5.3) for Pat008: PVC1 — TIBSPM 15 ms; PVC2 — TIBSPM 16 ms; PVC3 — TIBSPM 15 ms; PVC4 — TIBSPM 15 ms; PVC5 — TIBSPM 15 ms. Blue — correct results, Red — incorrect results

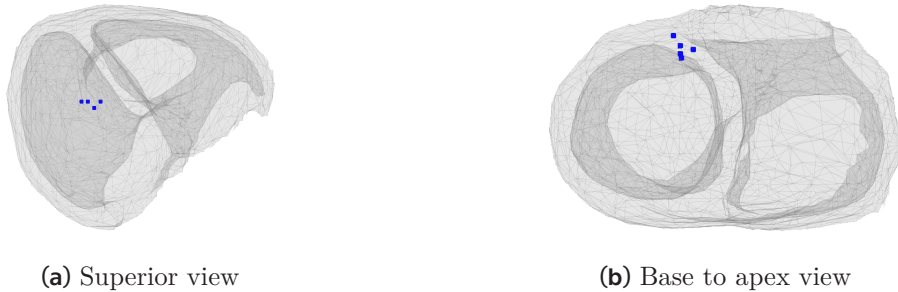


Figure H.7: Positions of the inverse solutions for torso model AV and patient-specific TIBSPM (see sec. 3.5.4 and 5.3) for Pat008: PVC1 — TIBSPM 15 ms; PVC2 — TIBSPM 16 ms; PVC3 — TIBSPM 15 ms; PVC4 — TIBSPM 15 ms; PVC5 — TIBSPM 15 ms. Blue — correct results

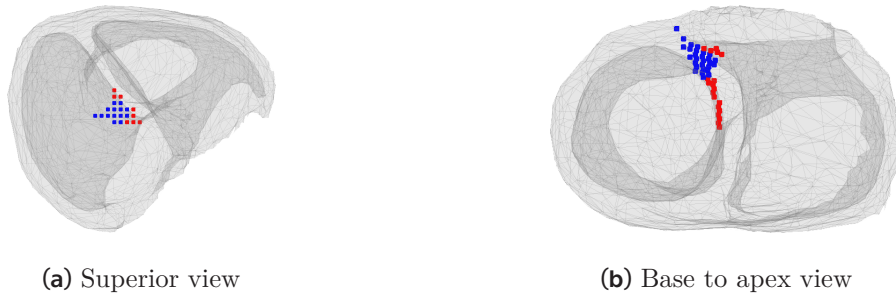


Figure H.8: Positions of the inverse solutions for torso model H in combination with one of 52 BSP maps (see sec. 3.5.5 and 5.4) for Pat008: TIBSPM or IBSPM. Blue — correct results, Red — incorrect results

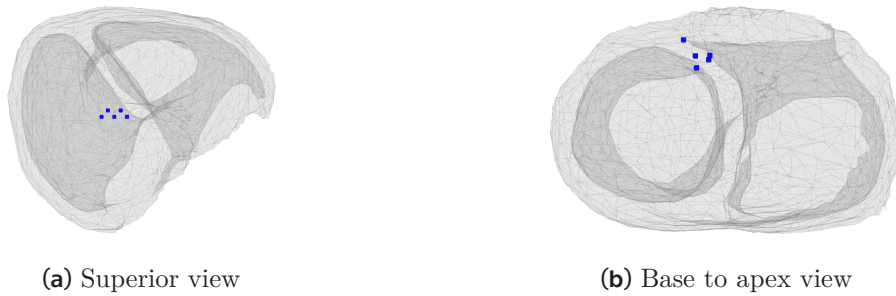


Figure H.9: Positions of the inverse solutions for torso model H and TIBSPM 8 ms (see sec. 3.5.6 and 5.5) for Pat008. Blue — correct results

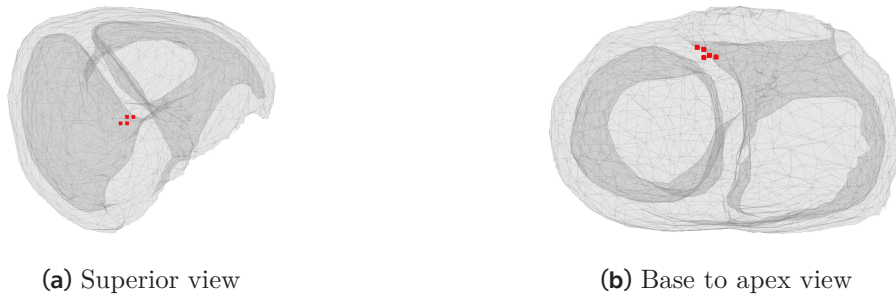


Figure H.10: Positions of the first five dipoles of the inverse solution with minimal RRE obtained for one TIBSPM 8 ms and homogeneous torso model H. Five dipoles (instead one) with minimal RRE were selected for the inverse solution for one PVC (see sec. 3.5.7 and 5.6.1). Pat008

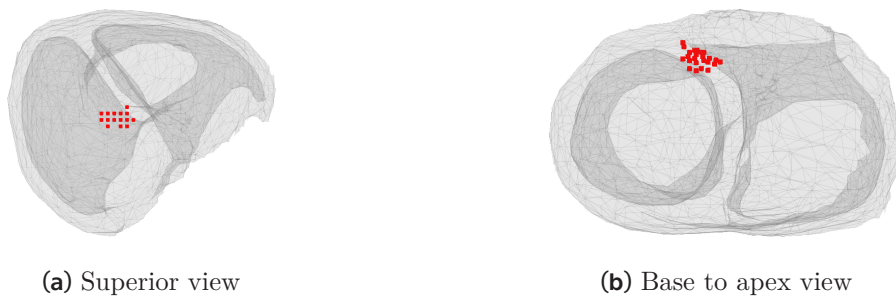


Figure H.11: Positions of the twenty-five dipoles of the inverse solution with minimal RRE. Inverse solution was solved using the combination of homogeneous torso model H and TIBSPMs computed for 8 ms. Five dipoles (instead one) with minimal RRE were selected for each inverse solution for 5 PVCs (see sec. 3.5.7 and 5.6.2) for Pat008

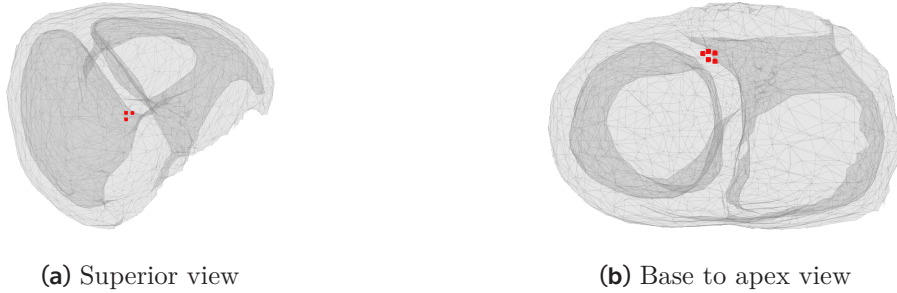


Figure H.12: Positions of first five dipoles with minimal RRE value of the inverse solution for one BSP map (IBSPM 0–15 ms) and homogeneous torso model H (see sec. 3.5.7 and 5.6.3) for Pat008

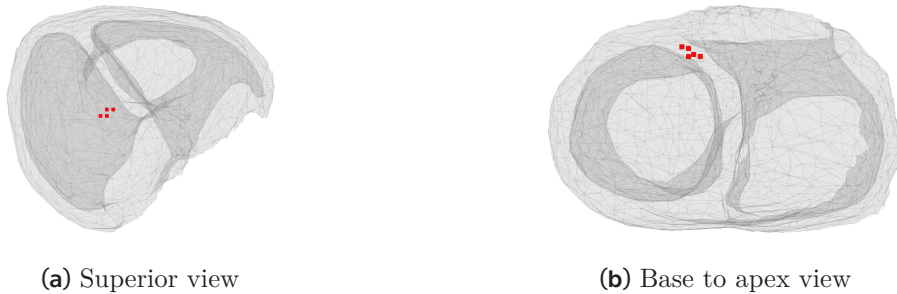


Figure H.13: Positions of first five dipoles with minimal RRE value of the inverse solution for one BSP map (IBSPM 0–15 ms) and inhomogeneous torso model V (see sec. 3.5.7 and 5.6.3) for Pat008

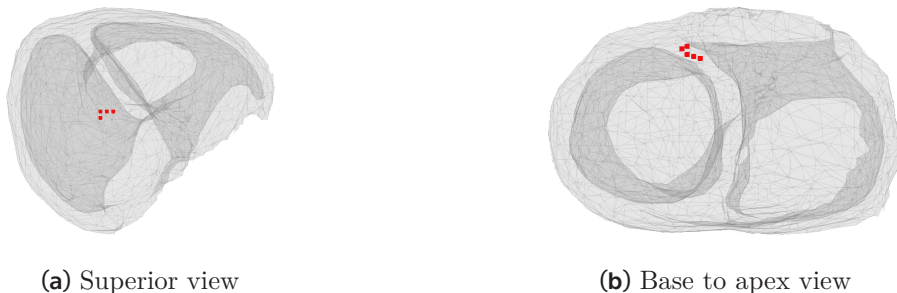


Figure H.14: Positions of first five dipoles with minimal RRE value of the inverse solution for one BSP map (IBSPM 0–15 ms) and inhomogeneous torso model AV (see sec. 3.5.7 and 5.6.3) for Pat008

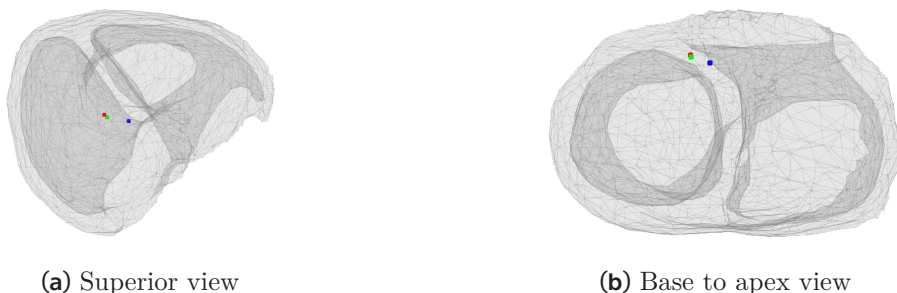
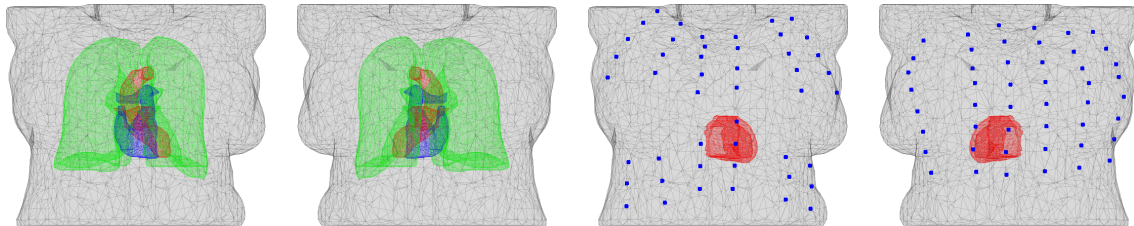


Figure H.15: Gravity centers (see sec. 3.5.7 and 5.6.3) of the five dipoles positions derived for inverse solution for IBSPM 0–15 ms and each of the three input torso models in the ventricular myocardium of the Pat008. Blue — torso model H, Green — torso model V, Red — torso model AV

Appendix

Pat009



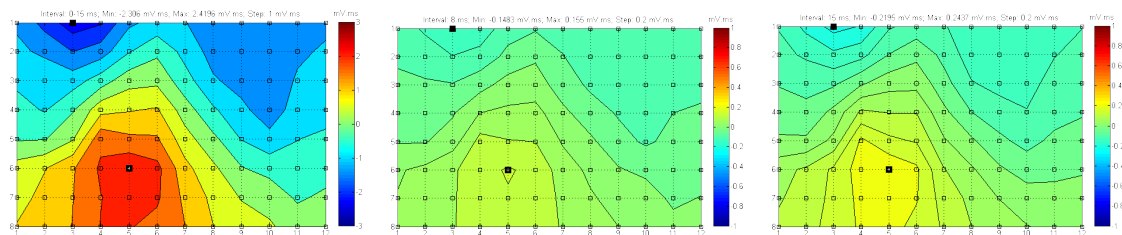
(a) Pat009 torso model AV, AP view

(b) Pat009 torso model AV, PA view

(c) Pat009 torso model H with electrode positions, AP view

(d) Pat009 torso model H with electrode positions, PA view

Figure I.1: Pat009. Torso model AV and torso model H with electrode positions

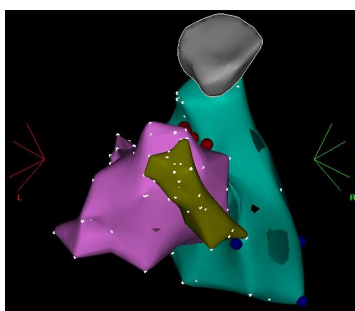


(a) IBSPM 0–15 ms

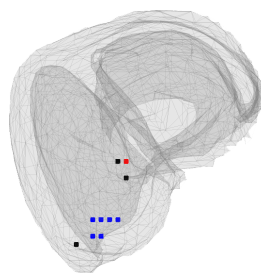
(b) TIBSPM 8 ms

(c) patient-specific TIBSPM 15 ms

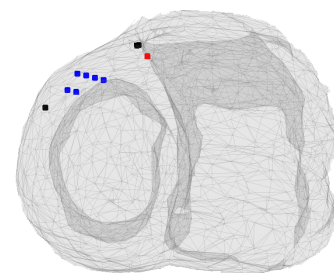
Figure I.2: BSP maps of patient Pat009



(a) Ablation points from the EP study. PA view



(b) Superior view



(c) Base to apex view

Figure I.3: Results of RFA and positions of all 780 inverse solutions for Pat009. Black — irrelevant results, Blue — correct results, Red — incorrect results



(a) Superior view

(b) Base to apex view

Figure I.4: Positions of the inverse solutions for IBSPM 0–15 ms in combination with one of the torso models: homogeneous torso model H, or inhomogeneous torso model V, or inhomogenous torso model AV (see sec. 3.5.3 and 5.2) for Pat009. Blue — correct results



(a) Superior view

(b) Base to apex view

Figure I.5: Positions of the inverse solutions for torso model H and patient-specific TIB-SPM (see sec. 3.5.4 and 5.3) for Pat009: PVC1 — TIBSPM 13 ms; PVC2 — TIB-SPM 15 ms; PVC3 — TIBSPM 9 ms; PVC4 — TIBSPM 18 ms; PVC5 — TIBSPM 10 ms. Blue — correct results



(a) Superior view

(b) Base to apex view

Figure I.6: Positions of the inverse solutions for torso model V and patient-specific TIB-SPM (see sec. 3.5.4 and 5.3) for Pat009: PVC1 — TIBSPM 13 ms; PVC2 — TIB-SPM 15 ms; PVC3 — TIBSPM 9 ms; PVC4 — TIBSPM 18 ms; PVC5 — TIBSPM 10 ms. Red — incorrect results



(a) Superior view

(b) Base to apex view

Figure I.7: Positions of the inverse solutions for torso model AV and patient-specific TIB-SPM (see sec. 3.5.4 and 5.3) for Pat009: PVC1 — TIBSPM 13 ms; PVC2 — TIB-SPM 15 ms; PVC3 — TIBSPM 9 ms; PVC4 — TIBSPM 18 ms; PVC5 — TIBSPM 10 ms. Blue — correct results



Figure I.8: Positions of the inverse solutions for torso model H in combination with one of 52 BSP maps (see sec. 3.5.5 and 5.4) for Pat009: TIBSPM or IBSPM. Blue — correct results



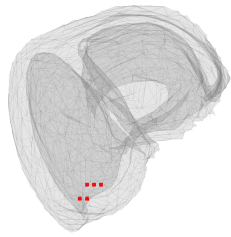
Figure I.9: Positions of the inverse solutions for torso model H and TIBSPM 8 ms (see sec. 3.5.6 and 5.5) for Pat009. Black — irrelevant results, Blue — correct results



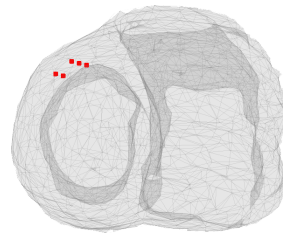
Figure I.10: Positions of the first five dipoles of the inverse solution with minimal RRE obtained for one TIBSPM 8 ms and homogeneous torso model H. Five dipoles (instead of one) with minimal RRE were selected for the inverse solution for one PVC (see sec. 3.5.7 and 5.6.1). Pat009



Figure I.11: Positions of the twenty-five dipoles of the inverse solution with minimal RRE. Inverse solution was solved using the combination of homogeneous torso model H and TIBSPMs computed for 8 ms. Five dipoles (instead of one) with minimal RRE were selected for each inverse solution for 5 PVCs (see sec. 3.5.7 and 5.6.2) for Pat009

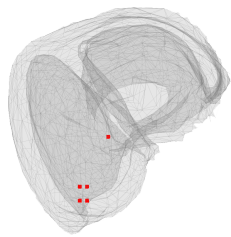


(a) Superior view

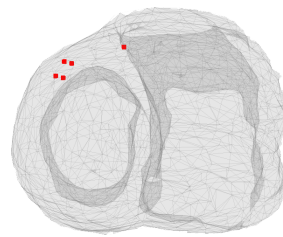


(b) Base to apex view

Figure I.12: Positions of first five dipoles with minimal RRE value of the inverse solution for one BSP map (IBSPM 0–15 ms) and homogeneous torso model H (see sec. 3.5.7 and 5.6.3) for Pat009

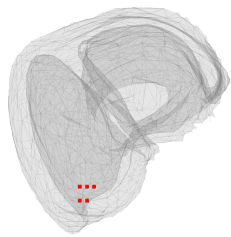


(a) Superior view

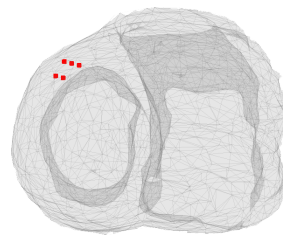


(b) Base to apex view

Figure I.13: Positions of first five dipoles with minimal RRE value of the inverse solution for one BSP map (IBSPM 0–15 ms) and inhomogeneous torso model V (see sec. 3.5.7 and 5.6.3) for Pat009

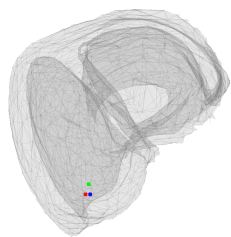


(a) Superior view

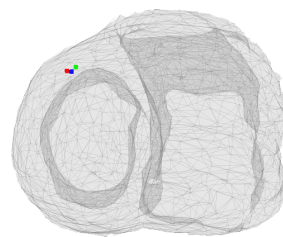


(b) Base to apex view

Figure I.14: Positions of first five dipoles with minimal RRE value of the inverse solution for one BSP map (IBSPM 0–15 ms) and inhomogeneous torso model AV (see sec. 3.5.7 and 5.6.3) for Pat009



(a) Superior view

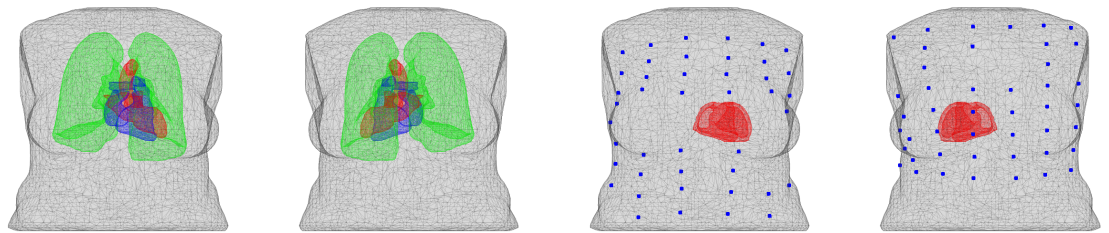


(b) Base to apex view

Figure I.15: Gravity centers (see sec. 3.5.7 and 5.6.3) of the five dipoles positions derived for inverse solution for IBSPM 0–15 ms and each of the three input torso models in the ventricular myocardium of the Pat009. Blue — torso model H, Green — torso model V, Red — torso model AV

Appendix J

Pat010



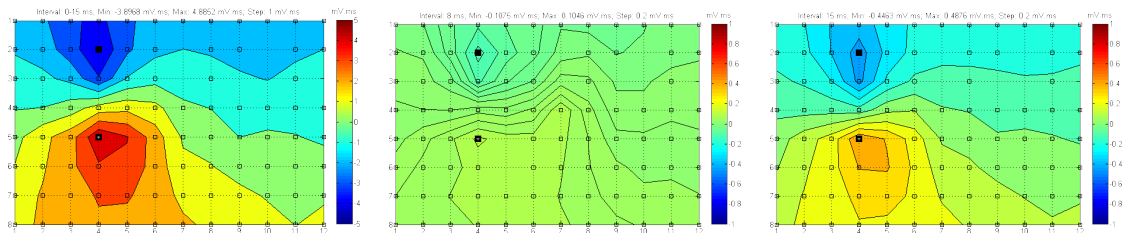
(a) Pat010 torso model AV, AP view

(b) Pat010 torso model AV, PA view

(c) Pat010 torso model H with electrode positions, AP view

(d) Pat010 torso model H with electrode positions, PA view

Figure J.1: Pat010. Torso model AV and torso model H with electrode positions

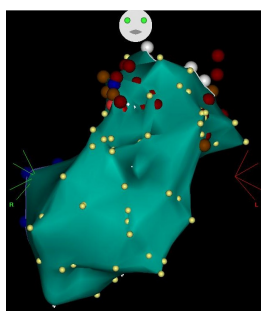


(a) IBSPM 0–15 ms

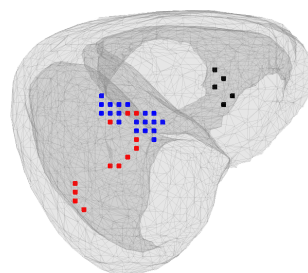
(b) TIBSPM 8 ms

(c) patient-specific TIBSPM 15 ms

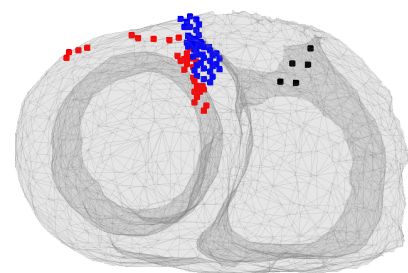
Figure J.2: BSP maps of patient Pat010



(a) Ablation points from the EP study. AP view



(b) Superior view



(c) Base to apex view

Figure J.3: Results of RFA and positions of all 780 inverse solutions for Pat010. Black — irrelevant results, Blue — correct results, Red — incorrect results

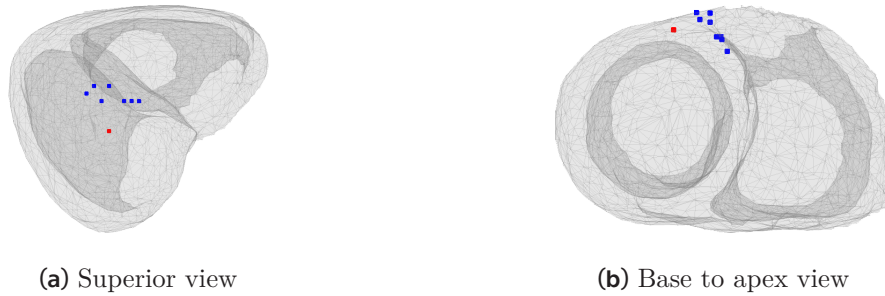


Figure J.4: Positions of the inverse solutions for IBSPM 0–15 ms in combination with one of the torso models: homogeneous torso model H, or inhomogeneous torso model V, or inhomogeneous torso model AV (see sec. 3.5.3 and 5.2) for Pat010. Blue — correct results, Red — incorrect results

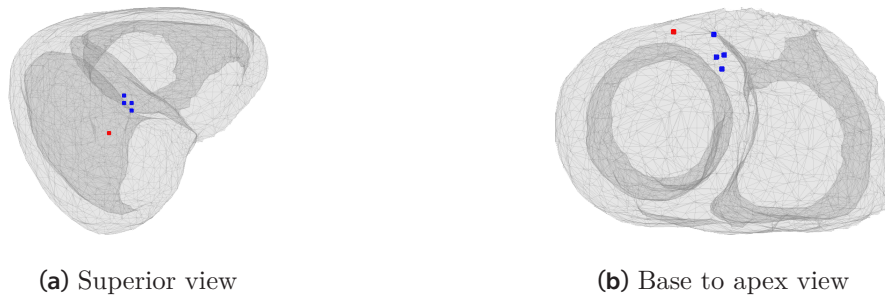


Figure J.5: Positions of the inverse solutions for torso model H and patient-specific TIBSPM (see sec. 3.5.4 and 5.3) for Pat010: PVC1 — TIBSPM 19 ms; PVC2 — TIBSPM 15 ms; PVC3 — TIBSPM 19 ms; PVC4 — TIBSPM 10 ms; PVC5 — TIBSPM 15 ms. Blue — correct results, Red — incorrect results

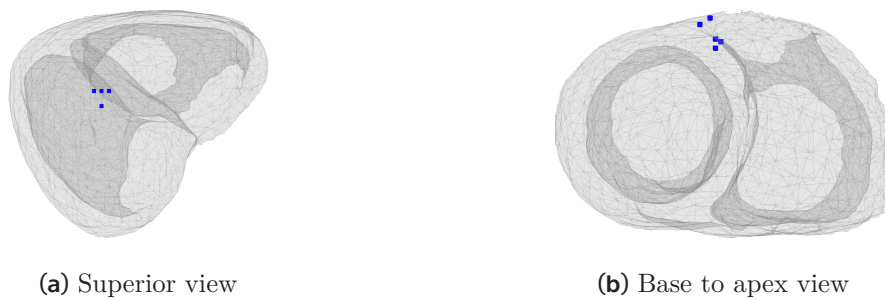


Figure J.6: Positions of the inverse solutions for torso model V and patient-specific TIBSPM (see sec. 3.5.4 and 5.3) for Pat010: PVC1 — TIBSPM 19 ms; PVC2 — TIBSPM 15 ms; PVC3 — TIBSPM 19 ms; PVC4 — TIBSPM 10 ms; PVC5 — TIBSPM 15 ms. Blue — correct results

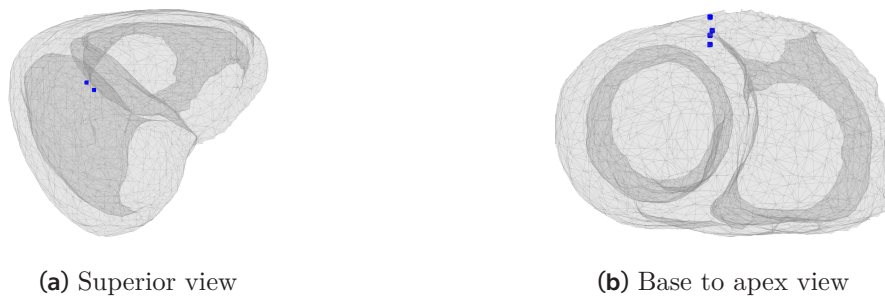


Figure J.7: Positions of the inverse solutions for torso model AV and patient-specific TIBSPM (see sec. 3.5.4 and 5.3) for Pat010: PVC1 — TIBSPM 19 ms; PVC2 — TIBSPM 15 ms; PVC3 — TIBSPM 19 ms; PVC4 — TIBSPM 10 ms; PVC5 — TIBSPM 15 ms. Blue — correct results

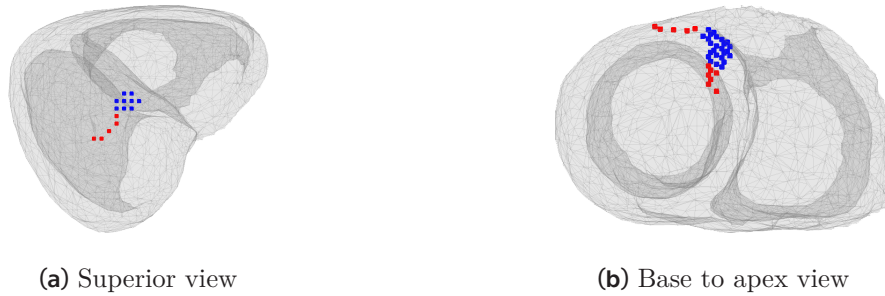


Figure J.8: Positions of the inverse solutions for torso model H in combination with one of 52 BSP maps (see sec. 3.5.5 and 5.4) for Pat010: TIBSPM or IBSPM. Blue — correct results, Red — incorrect results



Figure J.9: Positions of the inverse solutions for torso model H and TIBSPM 8 ms (see sec. 3.5.6 and 5.5) for Pat010. Black — irrelevant results, Blue — correct results, Red — incorrect results

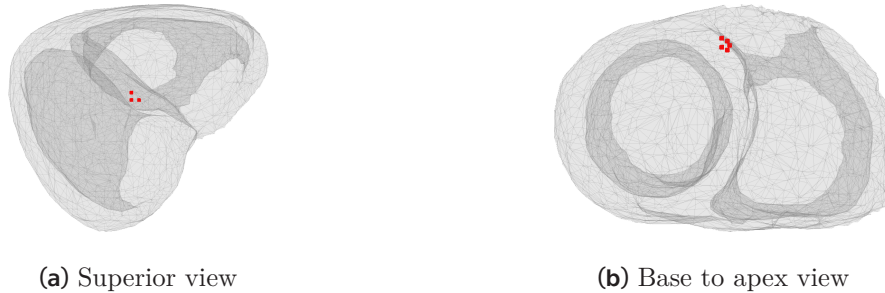


Figure J.10: Positions of the first five dipoles of the inverse solution with minimal RRE obtained for one TIBSPM 8 ms and homogeneous torso model H. Five dipoles (instead one) with minimal RRE were selected for the inverse solution for one PVC (see sec. 3.5.7 and 5.6.1). Pat010

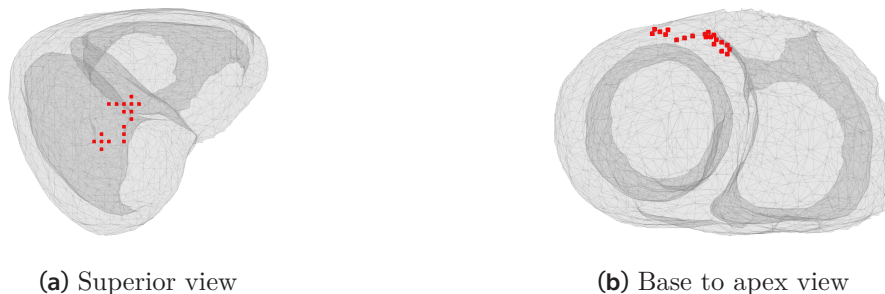
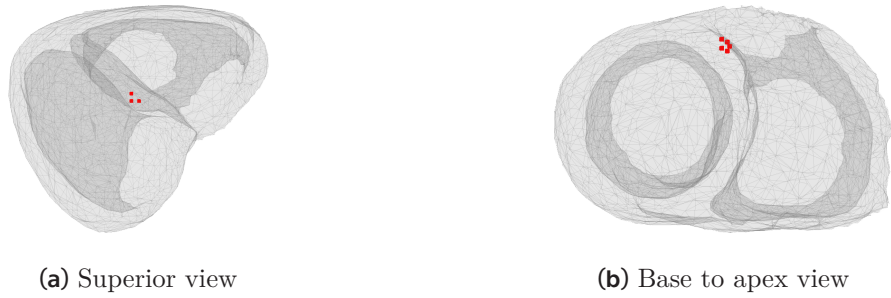
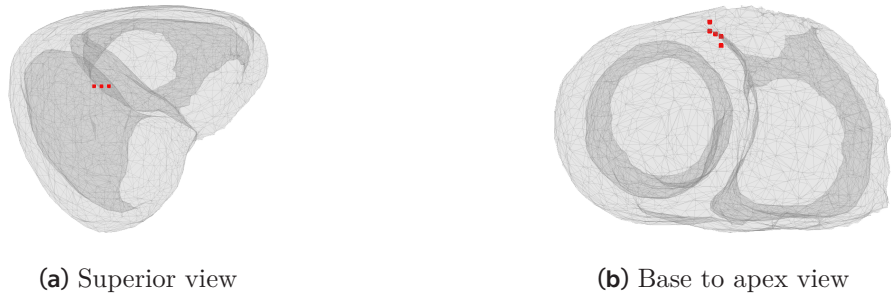


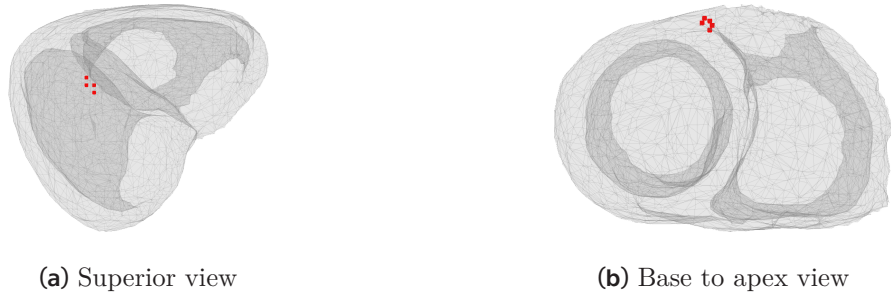
Figure J.11: Positions of the twenty-five dipoles of the inverse solution with minimal RRE. Inverse solution was solved using the combination of homogeneous torso model H and TIBSPMs computed for 8 ms. Five dipoles (instead one) with minimal RRE were selected for each inverse solution for 5 PVCs (see sec. 3.5.7 and 5.6.2) for Pat010



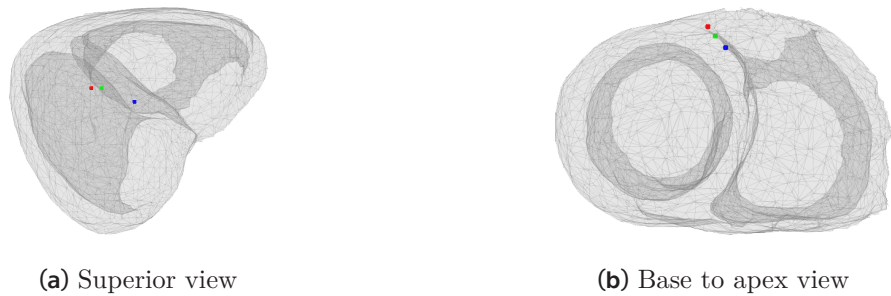
(a) Superior view (b) Base to apex view
Figure J.12: Positions of first five dipoles with minimal RRE value of the inverse solution for one BSP map (IBSPM 0–15 ms) and homogeneous torso model H (see sec. 3.5.7 and 5.6.3) for Pat010



(a) Superior view (b) Base to apex view
Figure J.13: Positions of first five dipoles with minimal RRE value of the inverse solution for one BSP map (IBSPM 0–15 ms) and inhomogeneous torso model V (see sec. 3.5.7 and 5.6.3) for Pat010



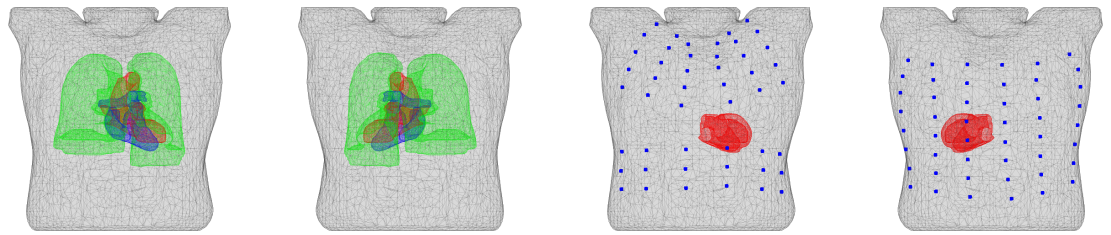
(a) Superior view (b) Base to apex view
Figure J.14: Positions of first five dipoles with minimal RRE value of the inverse solution for one BSP map (IBSPM 0–15 ms) and inhomogeneous torso model AV (see sec. 3.5.7 and 5.6.3) for Pat010



(a) Superior view (b) Base to apex view
Figure J.15: Gravity centers (see sec. 3.5.7 and 5.6.3) of the five dipoles positions derived for inverse solution for IBSPM 0–15 ms and each of the three input torso models in the ventricular myocardium of the Pat010. Blue — torso model H, Green — torso model V, Red — torso model AV

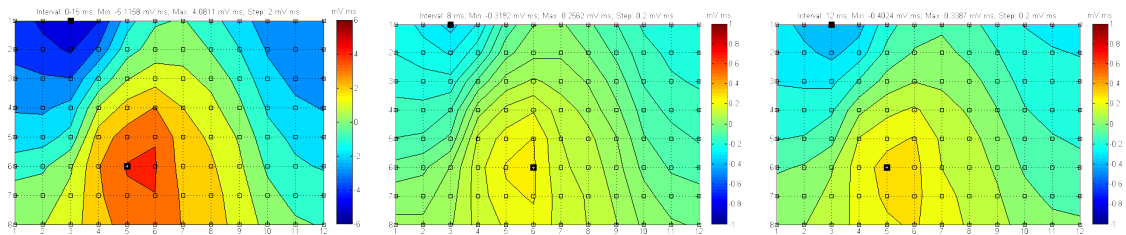
Appendix K

Pat011



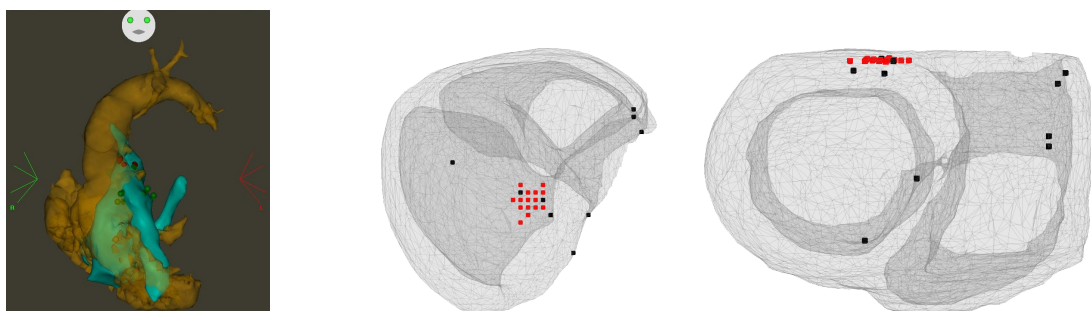
(a) Pat011 torso model AV, AP view (b) Pat011 torso model AV, PA view (c) Pat011 torso model H with electrode positions, AP view (d) Pat011 torso model H with electrode positions, PA view

Figure K.1: Pat011. Torso model AV and torso model H with electrode positions



(a) IBSPM 0–15 ms (b) TIBSPM 8 ms (c) patient-specific TIBSPM 12 ms

Figure K.2: BSP maps of patient Pat011



(a) Ablation points from the EP study. AP view (b) Superior view (c) Base to apex view

Figure K.3: Results of RFA and positions of all 780 inverse solutions for Pat011. Black — irrelevant results, Red — incorrect results

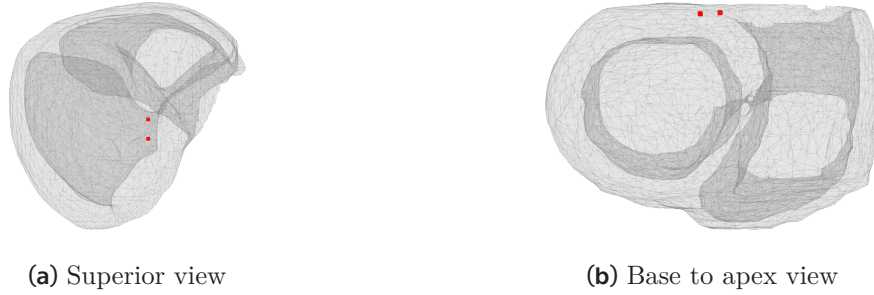


Figure K.4: Positions of the inverse solutions for IBSPM 0–15 ms in combination with one of the torso models: homogeneous torso model H, or inhomogeneous torso model V, or inhomogenous torso model AV (see sec. 3.5.3 and 5.2) for Pat011. Red — incorrect results

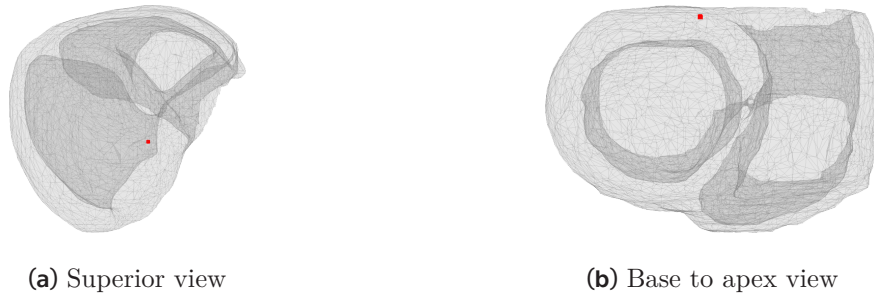


Figure K.5: Positions of the inverse solutions for torso model H and patient-specific TIBSPM (see sec. 3.5.4 and 5.3) for Pat011: PVC1 — TIBSPM 12 ms; PVC2 — TIBSPM 15 ms; PVC3 — TIBSPM 17 ms; PVC4 — TIBSPM 12 ms; PVC5 — TIBSPM 14 ms. Red — incorrect results

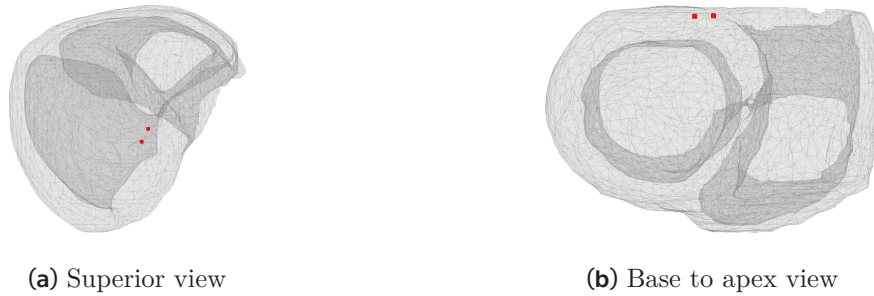


Figure K.6: Positions of the inverse solutions for torso model V and patient-specific TIBSPM (see sec. 3.5.4 and 5.3) for Pat011: PVC1 — TIBSPM 12 ms; PVC2 — TIBSPM 15 ms; PVC3 — TIBSPM 17 ms; PVC4 — TIBSPM 12 ms; PVC5 — TIBSPM 14 ms. Red — incorrect results



Figure K.7: Positions of the inverse solutions for torso model AV and patient-specific TIBSPM (see sec. 3.5.4 and 5.3) for Pat011: PVC1 — TIBSPM 12 ms; PVC2 — TIBSPM 15 ms; PVC3 — TIBSPM 17 ms; PVC4 — TIBSPM 12 ms; PVC5 — TIBSPM 14 ms. Red — incorrect results

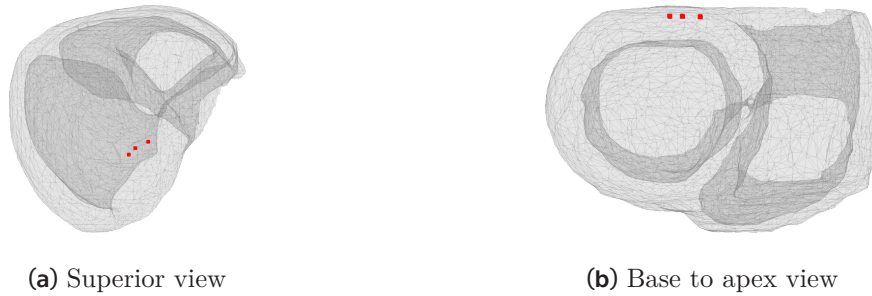


Figure K.8: Positions of the inverse solutions for torso model H in combination with one of 52 BSP maps (see sec. 3.5.5 and 5.4) for Pat011: TIBSPM or IBSPM. Red — incorrect results

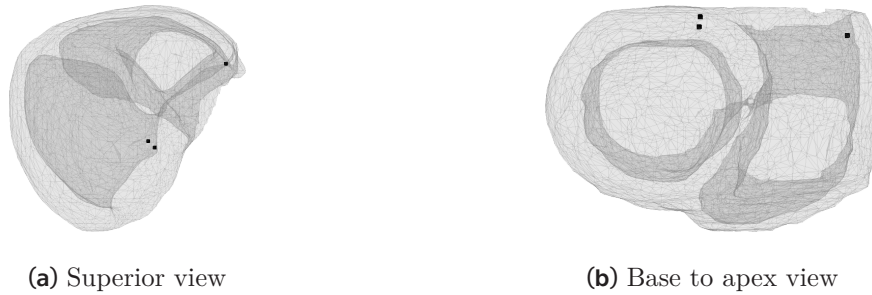


Figure K.9: Positions of the inverse solutions for torso model H and TIBSPM 8 ms (see sec. 3.5.6 and 5.5) for Pat011. Black — irrelevant results



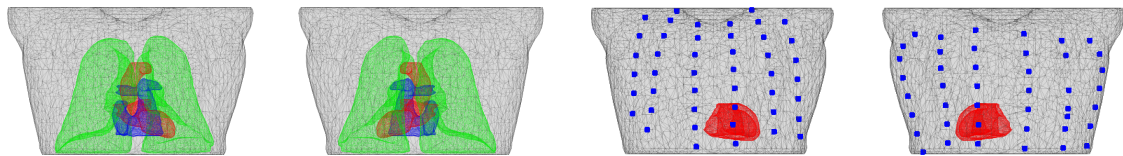
Figure K.10: Positions of the first five dipoles of the inverse solution with minimal RRE obtained for one TIBSPM 8 ms and homogeneous torso model H. Five dipoles (instead one) with minimal RRE were selected for the inverse solution for one PVC (see sec. 3.5.7 and 5.6.1). Pat011



Figure K.11: Positions of the twenty-five dipoles of the inverse solution with minimal RRE. Inverse solution was solved using the combination of homogeneous torso model H and TIBSPMs computed for 8 ms. Five dipoles (instead one) with minimal RRE were selected for each inverse solution for 5 PVCs (see sec. 3.5.7 and 5.6.2) for Pat011

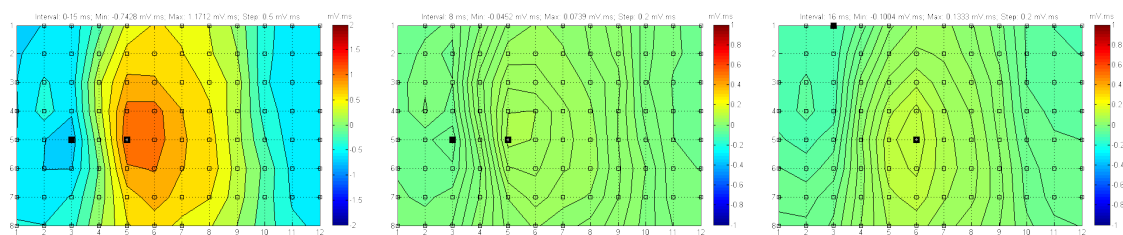
Appendix L

Pat015



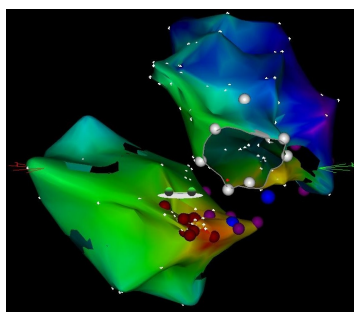
(a) Pat015 torso model AV, AP view (b) Pat015 torso model AV, PA view (c) Pat015 torso model H with electrode positions, AP view (d) Pat015 torso model H with electrode positions, PA view

Figure L.1: Pat015. Torso model AV and torso model H with electrode positions

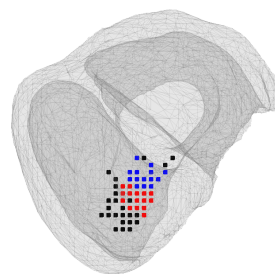


(a) IBSPM 0–15 ms (b) TIBSPM 8 ms (c) patient-specific TIBSPM 16 ms

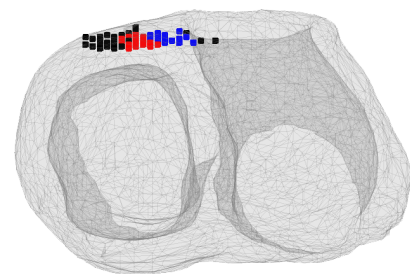
Figure L.2: BSP maps of patient Pat015



(a) Ablation points from the EP study. Superior view

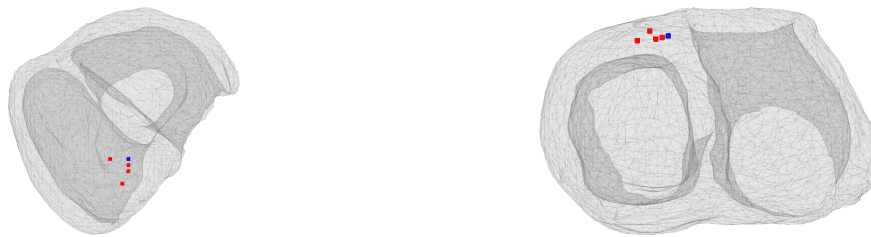


(b) Superior view



(c) Base to apex view

Figure L.3: Results of RFA and positions of all 780 inverse solutions for Pat015. Black — irrelevant results, Blue — correct results, Red — incorrect results



(a) Superior view

(b) Base to apex view

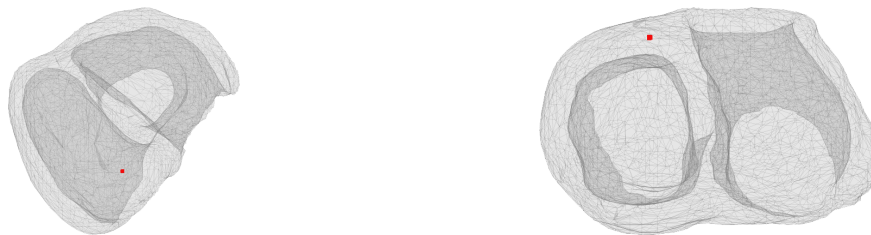
Figure L.4: Positions of the inverse solutions for IBSPM 0–15 ms in combination with one of the torso models: homogeneous torso model H, or inhomogeneous torso model V, or inhomogeneous torso model AV (see sec. 3.5.3 and 5.2) for Pat015. Blue — correct results, Red — incorrect results



(a) Superior view

(b) Base to apex view

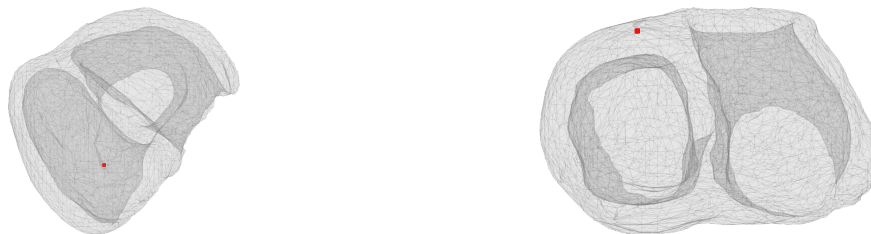
Figure L.5: Positions of the inverse solutions for torso model H and patient-specific TIBSPM (see sec. 3.5.4 and 5.3) for Pat015: PVC1 — TIBSPM 17 ms; PVC2 — TIBSPM 17 ms; PVC3 — TIBSPM 12 ms; PVC4 — TIBSPM 16 ms; PVC5 — TIBSPM 17 ms. Red — incorrect results



(a) Superior view

(b) Base to apex view

Figure L.6: Positions of the inverse solutions for torso model V and patient-specific TIBSPM (see sec. 3.5.4 and 5.3) for Pat015: PVC1 — TIBSPM 17 ms; PVC2 — TIBSPM 17 ms; PVC3 — TIBSPM 12 ms; PVC4 — TIBSPM 16 ms; PVC5 — TIBSPM 17 ms. Red — incorrect results



(a) Superior view

(b) Base to apex view

Figure L.7: Positions of the inverse solutions for torso model AV and patient-specific TIBSPM (see sec. 3.5.4 and 5.3) for Pat015: PVC1 — TIBSPM 17 ms; PVC2 — TIBSPM 17 ms; PVC3 — TIBSPM 12 ms; PVC4 — TIBSPM 16 ms; PVC5 — TIBSPM 17 ms. Red — incorrect results

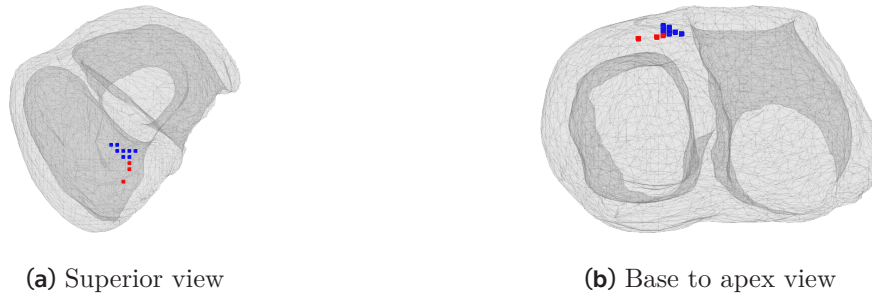


Figure L.8: Positions of the inverse solutions for torso model H in combination with one of 52 BSP maps (see sec. 3.5.5 and 5.4) for Pat015: TIBSPM or IBSPM. Blue — correct results, Red — incorrect results

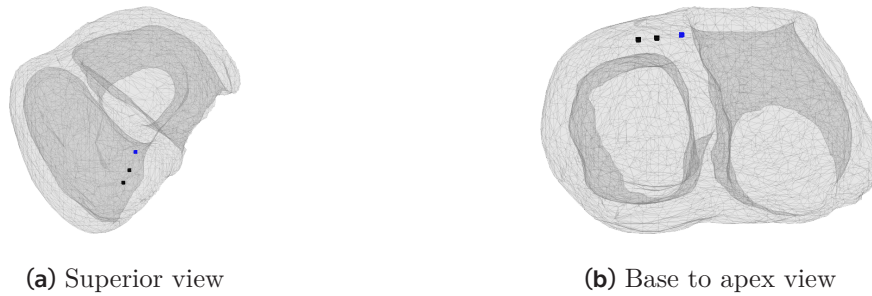


Figure L.9: Positions of the inverse solutions for torso model H and TIBSPM 8 ms (see sec. 3.5.6 and 5.5) for Pat015. Black — irrelevant results, Blue — correct results

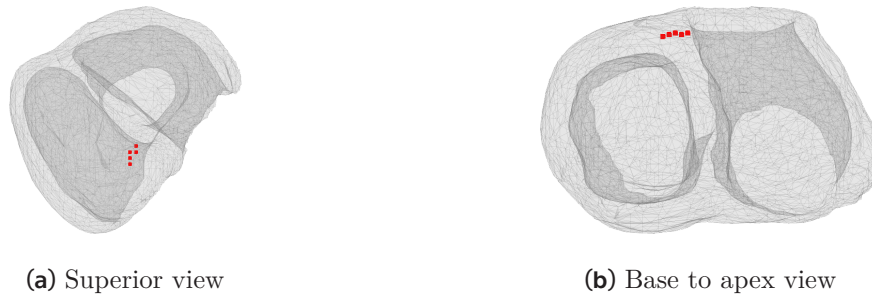


Figure L.10: Positions of the first five dipoles of the inverse solution with minimal RRE obtained for one TIBSPM 8 ms and homogeneous torso model H. Five dipoles (instead one) with minimal RRE were selected for the inverse solution for one PVC (see sec. 3.5.7 and 5.6.1). Pat015

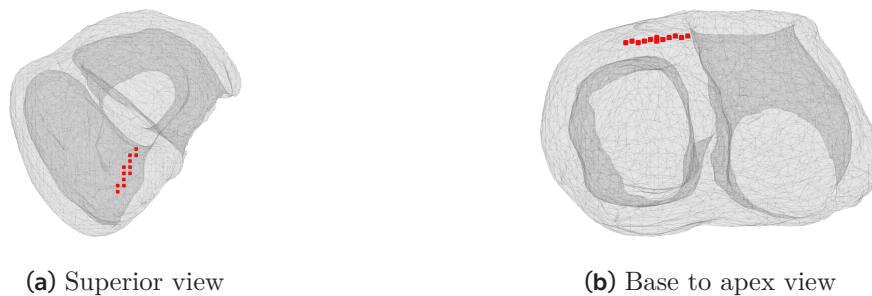
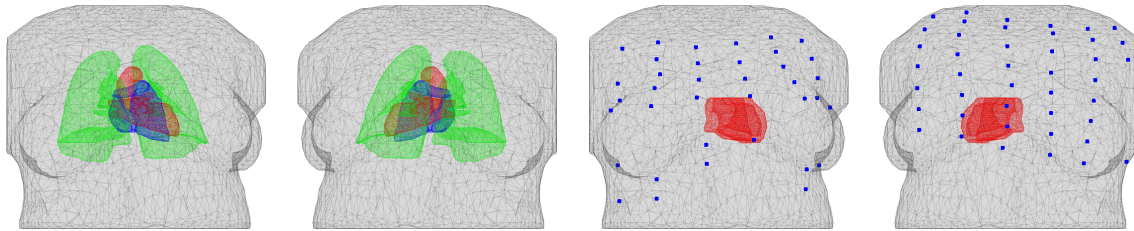


Figure L.11: Positions of the twenty-five dipoles of the inverse solution with minimal RRE. Inverse solution was solved using the combination of homogeneous torso model H and TIBSPMs computed for 8 ms. Five dipoles (instead one) with minimal RRE were selected for each inverse solution for 5 PVCs (see sec. 3.5.7 and 5.6.2) for Pat015

Appendix M

Pat016



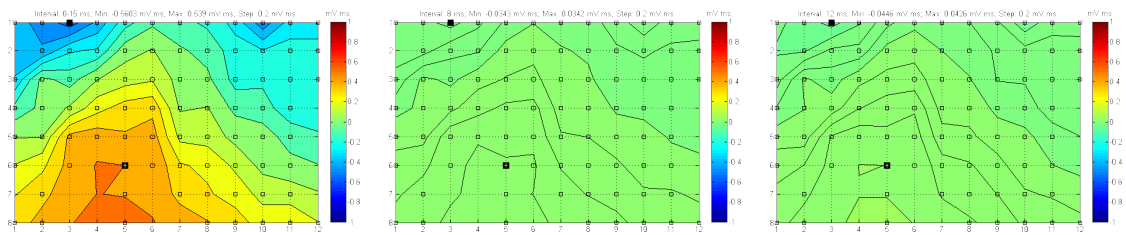
(a) Pat016 torso model AV, AP view

(b) Pat016 torso model AV, PA view

(c) Pat016 torso model H with electrode positions, AP view

(d) Pat016 torso model H with electrode positions, PA view

Figure M.1: Pat016. Torso model AV and torso model H with electrode positions

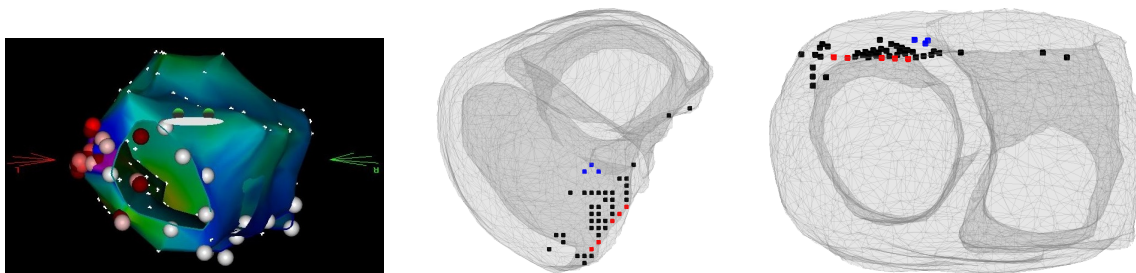


(a) IBSPM 0–15 ms

(b) TIBSPM 8 ms

(c) patient-specific TIBSPM 12 ms

Figure M.2: BSP maps of patient Pat016

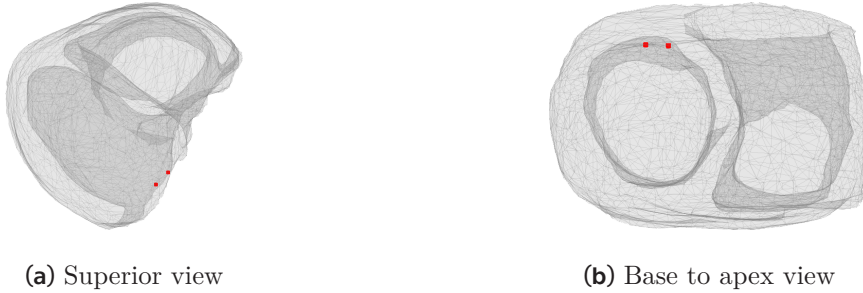


(a) Ablation points from the EP study. Superior view

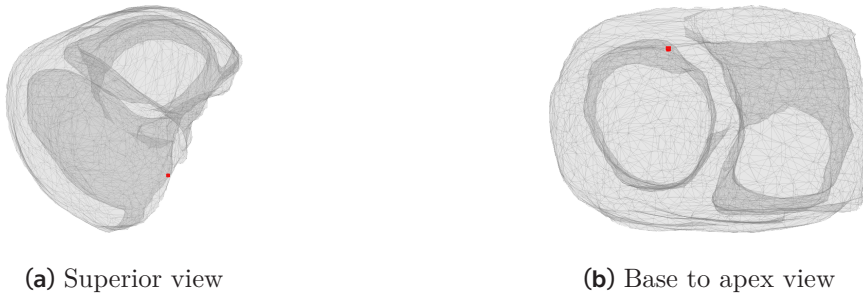
(b) Superior view

(c) Base to apex view

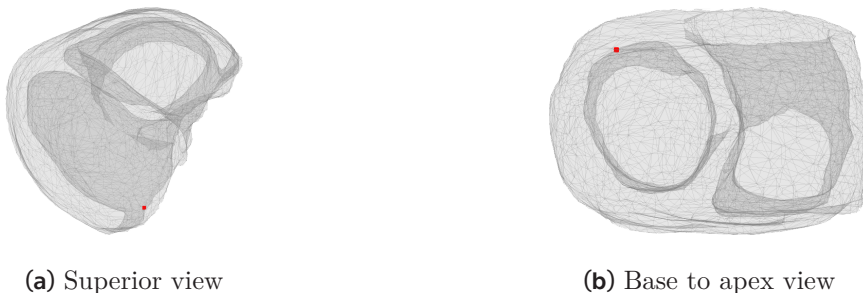
Figure M.3: Results of RFA and positions of all 780 inverse solutions for Pat016. Black — irrelevant results, Blue — correct results, Red — incorrect results



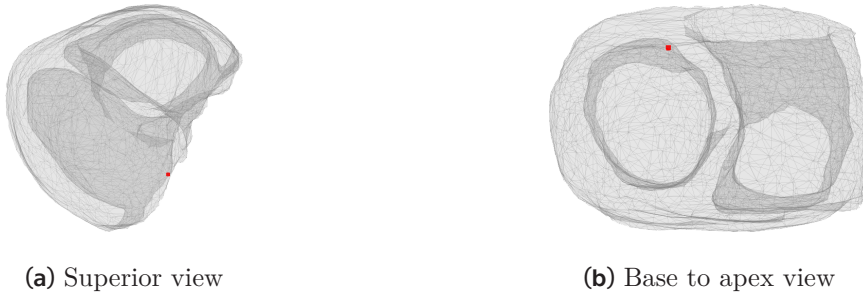
(a) Superior view (b) Base to apex view
Figure M.4: Positions of the inverse solutions for IBSPM 0–15 ms in combination with one of the torso models: homogeneous torso model H, or inhomogeneous torso model V, or inhomogeneous torso model AV (see sec. 3.5.3 and 5.2) for Pat016. Red — incorrect results



(a) Superior view (b) Base to apex view
Figure M.5: Positions of the inverse solutions for torso model H and patient-specific TIBSPM (see sec. 3.5.4 and 5.3) for Pat016: PVC1 — TIBSPM 14 ms; PVC2 — TIBSPM 12 ms; PVC3 — TIBSPM 13 ms; PVC4 — TIBSPM 13 ms; PVC5 — TIBSPM 12 ms. Red — incorrect results



(a) Superior view (b) Base to apex view
Figure M.6: Positions of the inverse solutions for torso model V and patient-specific TIBSPM (see sec. 3.5.4 and 5.3) for Pat016: PVC1 — TIBSPM 14 ms; PVC2 — TIBSPM 12 ms; PVC3 — TIBSPM 13 ms; PVC4 — TIBSPM 13 ms; PVC5 — TIBSPM 12 ms. Red — incorrect results



(a) Superior view (b) Base to apex view
Figure M.7: Positions of the inverse solutions for torso model AV and patient-specific TIBSPM (see sec. 3.5.4 and 5.3) for Pat016: PVC1 — TIBSPM 14 ms; PVC2 — TIBSPM 12 ms; PVC3 — TIBSPM 13 ms; PVC4 — TIBSPM 13 ms; PVC5 — TIBSPM 12 ms. Red — incorrect results



Figure M.8: Positions of the inverse solutions for torso model H in combination with one of 52 BSP maps (see sec. 3.5.5 and 5.4) for Pat016: TIBSPM or IBSPM. Red — incorrect results

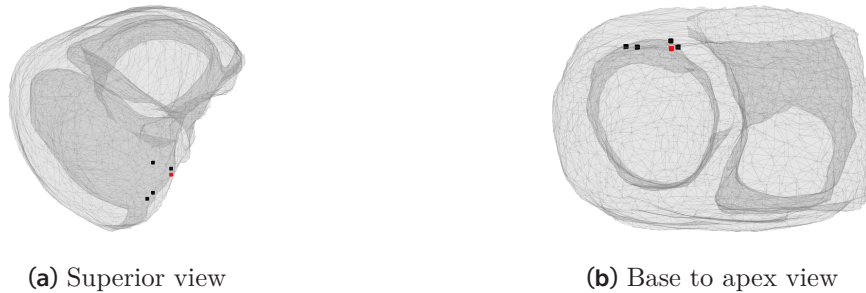


Figure M.9: Positions of the inverse solutions for torso model H and TIBSPM 8 ms (see sec. 3.5.6 and 5.5) for Pat016. Black — irrelevant results, Red — incorrect results

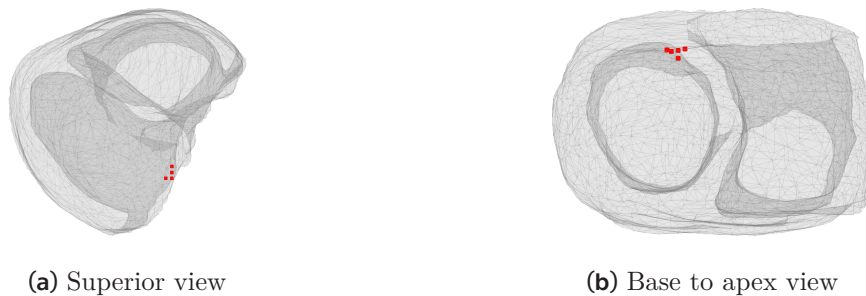


Figure M.10: Positions of the first five dipoles of the inverse solution with minimal RRE obtained for one TIBSPM 8 ms and homogeneous torso model H. Five dipoles (instead one) with minimal RRE were selected for the inverse solution for one PVC (see sec. 3.5.7 and 5.6.1). Pat016

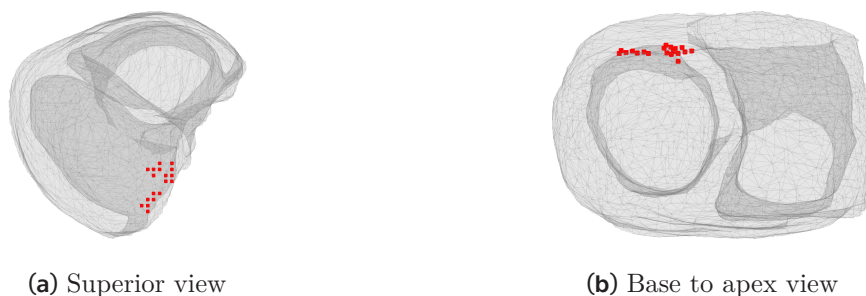


Figure M.11: Positions of the twenty-five dipoles of the inverse solution with minimal RRE. Inverse solution was solved using the combination of homogeneous torso model H and TIBSPMs computed for 8 ms. Five dipoles (instead one) with minimal RRE were selected for each inverse solution for 5 PVCs (see sec. 3.5.7 and 5.6.2) for Pat016



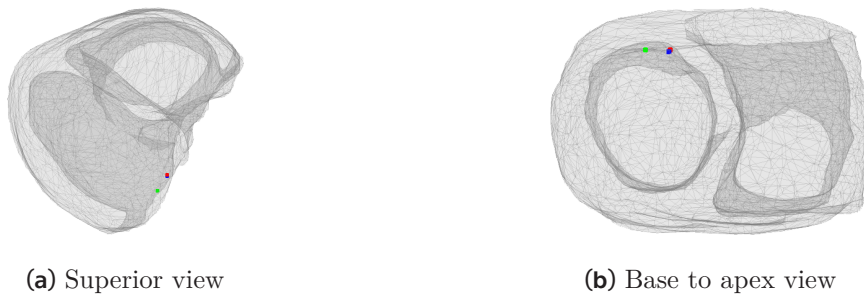
(a) Superior view (b) Base to apex view
Figure M.12: Positions of first five dipoles with minimal RRE value of the inverse solution for one BSP map (IBSPM 0–15 ms) and homogeneous torso model H (see sec. 3.5.7 and 5.6.3) for Pat016



(a) Superior view (b) Base to apex view
Figure M.13: Positions of first five dipoles with minimal RRE value of the inverse solution for one BSP map (IBSPM 0–15 ms) and inhomogeneous torso model V (see sec. 3.5.7 and 5.6.3) for Pat016



(a) Superior view (b) Base to apex view
Figure M.14: Positions of first five dipoles with minimal RRE value of the inverse solution for one BSP map (IBSPM 0–15 ms) and inhomogeneous torso model AV (see sec. 3.5.7 and 5.6.3) for Pat016



(a) Superior view (b) Base to apex view
Figure M.15: Gravity centers (see sec. 3.5.7 and 5.6.3) of the five dipoles positions derived for inverse solution for IBSPM 0–15 ms and each of the three input torso models in the ventricular myocardium of the Pat016. Blue — torso model H, Green — torso model V, Red — torso model AV

Appendix N

List of author's publications

Papers in journals related to the Thesis

- [J1] TYŠLER, M., **O. PUNSHCHYKOVA**, J. ŠVEHLÍKOVÁ, P. OSMANČÍK, J. ŽĎÁRSKÁ, and P. KNEPPO. Noninvasive identification of local disorders of electrogenesis in ventricular arrhythmias. *Cardiology Letters*. 2017, Vol. 26, No. 1, pp. 39–46. (SJR 2017 = 0.121)
- [J2] **PUNSHCHYKOVA, O.**, J. ŠVEHLÍKOVÁ, M. TYŠLER, R. GRÜNES, K. SEDOVA, P. OSMANČÍK, J. ŽĎÁRSKÁ, D. HEŘMAN, and P. KNEPPO. Influence of torso model complexity on the noninvasive localization of ectopic ventricular activity. *Measurement Science Review*. 2016, Vol. 16, No. 2, pp. 96–102. (JRC 2017 IF = 1.345)
- [J3] **PUNSHCHYKOVA, O.**, J. ŠVEHLÍKOVÁ, P. KNEPPO, V. MAKSYMENKO, and M. TYŠLER. Noninvasive localization of the ectopic focus using time integral ECG mapping. *Experimental and Clinical Cardiology*. 2014, Vol. 20, No. 7, pp. 1564–1570. (SJR 2017 = 0.111)
- [J4] TYŠLER, M., J. ŠVEHLÍKOVÁ, **O. PUNSHCHYKOVA**, and J. LENKOVÁ. Influence of torso model accuracy on the noninvasive localization of heart pathologies. *Acta Mechanica Slovaca*. 2013, Vol. 17, No. 3, pp. 18–25.
- [J5] **PUNSHCHYKOVA, O.**, P. KNEPPO, and M. TYŠLER. Noninvasive system for localization of small repolarization changes in the heart. *Clinician and Technology*. 2012, Vol. 42, No. 2, pp. 7–10.
- [J6] **PUNSHCHYKOVA, O.**, P. KNEPPO, V. MAKSYMENKO, M. TYŠLER, and M. SYCHYK. Surface mapping using multichannel ECG for arrhythmia localization determination. *The yearbook of scientific works of Ukrainian Society of Cardiovascular Surgery*. 2012, Vol. 20, No. 1, pp. 414–417.
- [J7] **DEUTSCH, E.**, M. TYŠLER, J. ŠVEHLÍKOVÁ, and P. KNEPPO. Impact of the position of ectopic ventricular activation origin on its noninvasive assessment: a simulation study. *Acta Mechanica Slovaca*. 2018, Vol. 22, No. 1, pp. 16–23. (accepted)

Conference contributions related to the Thesis

- [C1] **DEUTSCH, E.**, J. SVEHLIKOVA, M. TYSLER, and P. KNEPPO. The accuracy of noninvasive localization of ectopic focus: simulation study of the impact of focus position and used ECG leads. In: *45th International Congress on Electrocardiology, 18th Congress of the International Society for Holter and Noninvasive Electrocardiology in conjunction with the 38th Congress of the Japanese Society for*

Holter and Noninvasive Electrocardiology (JASHNE) and the 33rd Annual Conference of the Japanese Society for Computerized Electrocardiology (JSCE). Chiba, Japan, 2018.

- [C2] TYSLER, M., J. SVEHLIKOVA, **E. DEUTSCH**, P. OSMANCIK, and R. HATALA. Noninvasive imaging of the origin of premature ventricular activity. In: *World Congress on Medical Physics and Biomedical Engineering 2018. IFMBE Proceedings 68/1*, Prague: Springer Nature Singapore Pte Ltd., 2019, pp. 97–101.
- [C3] **DEUTSCH, E.**, J. SVEHLIKOVA, M. TYSLER, P. OSMANCIK, J. ZDARSKA, and P. KNEPPO. Effect of elimination of noisy ECG leads on the noninvasive localization of the focus of premature ventricular complexes. In: *World Congress on Medical Physics and Biomedical Engineering 2018. IFMBE Proceedings 68/1*, Prague: Springer Nature Singapore Pte Ltd., 2019, pp. 75–79.
- [C4] TYŠLER, M., **O. PUNSHCHYKOVA**, J. ŠVEHLÍKOVÁ, P. OSMANČÍK, J. ŽĎÁRSKÁ, and P. KNEPPO. Impact of the number of ECG leads on the noninvasive localization of premature ventricular activity. In: *Trendy v biomedicínském inženýrství. 12. Česko-slovenská konference*. Horní Lomná, ČR: VŠB — TU Ostrava, 2017.
- [C5] TYSLER, M., **O. PUNSHCHYKOVA**, J. SVEHLIKOVA, P. OSMANCIK, J. ZDARSKA, and P. KNEPPO. Evaluation of using reduced number of mapping leads for noninvasive localization of ectopic ventricular activity. In: *44th International Congress on Electrocardiology, 17th Congress of the International Society for Holter and Noninvasive Electrocardiology*. Portland, Oregon USA, 2017, p. 8.
- [C6] **PUNSHCHYKOVA, O.**, J. SVEHLIKOVA, M. TYSLER, and P. KNEPPO. Accuracy of noninvasive PVC focus localization depending on its position in the ventricles: a simulation study. In: *11th International Conference on Measurement 2017*. Smolenice, Slovakia: IEEE, 2017, pp. 209–212.
- [C7] ŠVEHLÍKOVÁ, J., **O. PUNSHCHYKOVA**, K. KROMKOVÁ, M. TYŠLER, and R. HATALA. First experience with PVC localization from clinical data. In: *11th International Conference on Measurement 2017*. Smolenice, Slovakia: IEEE, 2017, pp. 213–216.
- [C8] **PUNSHCHYKOVA, O.**, J. ŠVEHLÍKOVÁ, M. TYŠLER, R. GRÜNES, K. SEDOVA, P. OSMANČÍK, J. ŽĎÁRSKÁ, D. HEŘMAN, and P. KNEPPO. Vliv nehomogenit modelu torza na neinvazivní lokalizaci komorových extrasystol. In: *XIV. České a slovenské sympozium o arytmiích a kardiostimulaci*. Olomouc, ČR, 2016.
- [C9] TYSLER, M., **O. PUNSHCHYKOVA**, J. SVEHLIKOVA, P. OSMANCIK, J. ZDARSKA, and P. KNEPPO. Noninvasive localization of ectopic ventricular activity using homogeneous and inhomogeneous torso models. In: *43st International Congress on Electrocardiology*. Palma, 2016, pp. 49–50.
- [C10] **PUNSHCHYKOVA, O.**, J. ŠVEHLÍKOVÁ, M. TYŠLER, P. KNEPPO, R. GRÜNES, K. SEDOVA, B. SENYSH, P. OSMANČÍK, J. ŽĎÁRSKÁ, and D. HEŘMAN. Neinvazívna lokalizácia ektoptickej komorovej activity s použitím rôzne presných modelov torza získaných z CT hrudníka. In: *Lekárska fyzika a biofyzika na ziaciaku 21. storocia 2: Aplikácie fyziky v medicíne*. Bratislava, Slovakia: Univerzita Komenského v Bratislave, 2015, p. 40.
- [C11] **PUNSHCHYKOVA, O.**, J. ŠVEHLÍKOVÁ, P. KNEPPO, R. GRÜNES, K. SEDOVA, B. SENYSH, P. OSMANČÍK, J. ŽĎÁRSKÁ, D. HEŘMAN, and M. TYŠLER. Influence of modeled heart cavities on the noninvasive localization of ectopic ventric-

